LASER THOMSON SCATTERING MEASUREMENTS OF THE PLASMA STRUCTURE IN THE FRONT POLE REGION OF A MAGNETICALLY-SHIELDED HALL EFFECT THRUSTER

A Dissertation
Presented to
The Academic Faculty

By

Jean Luis Suazo Betancourt

In Partial Fulfillment
of the Requirements for the Degree
Doctor of Philosophy in the
Daniel Guggenheim School of
Aerospace Engineering

Georgia Institute of Technology

May 2024

© Jean Luis Suazo Betancourt 2024

LASER THOMSON SCATTERING MEASUREMENTS OF THE PLASMA STRUCTURE IN THE FRONT POLE REGION OF A MAGNETICALLY-SHIELDED HALL EFFECT THRUSTER

Thesis committee:

Dr. Mitchell L. R. Walker, Advisor
Aerospace Engineering
Georgia Institute of Technology

Dr. Wenting Sun
Aerospace Engineering
Georgia Institute of Technology

Dr. Adam M. Steinberg, Advisor
Aerospace Engineering
Georgia Institute of Technology

Dr. Lukas Graber
Electrical and Computer Engineering
Georgia Institute of Technology

Dr. Sedina Tsikata
Aerospace Engineering
Georgia Institute of Technology

Date approved: 4/16/2024

Se lo dedico’ a mi querida familia.

De Bani pa’l mundo con Dios mediante.

ACKNOWLEDGMENTS

Primeramente, gracias a Dios. No soy ni sere nada ni nadie sin la gracia y la bendicion que me ha dado Dios. Segundamente, gracias a mi madre, mi padre, y mis hermanos. Sin su apoyo yo le hubiera dado banda a todo esto hace años.

To my loved ones in the DMV, thanks for the love, support and patience. I know I've missed a lot being in grad school. Excited to slide back around the way and make up for lost time.

A mis seres queridos en RD, gracias por su paciencia, su apoyo, y su amor. Ahora es que nos vamos a desacatar de verdad con Dios mediante.

To my friends in Atlanta, I wouldn't have survived without being able to escape into the real world with y'all and not think about the lab. From the bottom of my hear, thank you.

Thank you to the grad students past. My man Cheong, watching you effortlessly move in the lab my first day here really made it clear how much I had to learn to be successful. Nathan and Connie, thanks for showing me what you had to offer when you weren't sprinting to the finish line. To my man Jovel, I'll always chuckle at that first convo we had when I was on the way to the lab my first day as I watch you climb and become CEO of EP. There's no one I would have rather have been shooting in the gym with those early days when things were bleak. I'll carry all the good moments we had together in my heart for the rest of my life and I wish you and your new family nothing but the best out west.

To my guys Muhannad and Adrian, thanks for all the love. The catharsis of the time we spent shooting the [redacted] outside of the lab is part of the reason I didn't quit every single time I was going to (which was pretty often). To the Thomson team, I quite literally wouldn't have been here without all the grinding we had to do to make these systems work. To my man Hwi, I wouldn't have ever figured out how to align those filters without the time we spent together at TAMU and when you came to GT. So close to LTS and so far

from LTS at the same time. So weird. I'll owe you a round every time we link up and I'm looking forward to the next time. Julian, I'm glad our interests aligned enough for us to get to know each other as well as we did during this last year of testing. I'm excited to link up in the DMV and get a drink. Naia, thanks for everything you've done to help me in the lab and even more so for everything you've done for me outside of the lab – I'll be grateful to you forever and I'll spend the duration of our friendship making sure you know it! Chhavi, I look at the pics from when we were grinding studying for quals and laugh. We thought it was the end of the world, little did we know how insane it would get after quals and after proposal lol. I'm glad your thesis tests are coming up and you're about to be slidng out of here as well.

To the newer students, keep grinding. As I sit here writing this, although it's been forever since I started it does still feel like it's flown by now that it's over I guess. Arega, I remember when I walked into the lab during the IHI tests on my first day and you were moving and grooving. I was like man, she really knows what's up in here. Those carbon nanotubes aren't gonna know what hit them. Jacob, I appreciate that during the pandemic you were working and Busek and still took time to answer some of my texts as I had finished quals and needed to learn labview. You know a lot and you help a lot, I have zero doubt that the rest of your journey at GT is gonna smooth. Will, your work ethic is unparalleled. Those 'how is your stuff going?' on the catwalk have meant a lot, even if my answer was always 'taking it one day at a time', haha. Janice, you have big shoes to fill with (JJ)EFE, but watching you administer the JANUS stuff makes it clear that that won't be a problem.

Thanks to my committee for thoroughly examining my work. Special shotout to my advisors Drs. Walker and Steinberg. Dr. Steinberg, you were always available to help and guide me with the laser and paper stuff, and if I had a reasonable case for (thinking) I needed anything I got it. Your contribution to my development is appreciated. Dr. Walker, thanks for identifying my boundaries and limits and pushing (and keeping) me beyond them.

TABLE OF CONTENTS

Acknowledgments iv

List of Tables xii

List of Figures xiv

List of Acronyms xxii

Summary xxiii

Chapter 1: Introduction, Motivation, and Proposed Work 1

1.1 Overview of Electric Propulsion 1

1.1.1 Prominence of Electric Propulsion 1

1.1.2 Overview of Hall effect thrusters 3

1.1.3 Hall effect thruster Performance Quantification and Plasma Property Measurements 5

1.2 Electric Propulsion Background and Motivation 7

1.2.1 Predictive Models and Simulations in EP 8

1.2.2 EP-Relevant Laser Based Plasma Measurements 9

1.2.3 Hall Effect Thruster Thermalized Magnetic Field Line Model 13

1.3 Thesis Question, Goals, Objectives, and Outline 15

1.3.1 Thesis Goal and Questions 15

1.3.2 Thesis Objectives 16

1.3.3 Thesis Outline 17

Chapter 2: Plasma and Hall Effect Thruster Background 18

2.1 Introduction 18

2.2 Overview of Fundamental Plasma Physics 18

2.2.1 Governing Equations of a Plasma 18

2.2.2 Plasma Parameters 21

2.3 Potential Profiles in Hall Effect Thrusters 24

2.4 Magnetically Shielded Hall Effect Thrusters 27

2.5 Magnetically Shielded Thruster Pole Erosion 28

Chapter 3: Laser Thomson Scattering Physics and Signal Analysis via Least Squares and Bayesian Inference 31

3.1 Introduction 31

3.2 Scattering of Electromagnetic Radiation 31

3.2.1 Rotational Raman Scattering 33

3.2.2 Incoherent Thomson Scattering 36

3.2.3 Maxwellian, Druyvesteyn and Generalized Single Dimensional Electron Velocity Distribution Function Submodels 38

3.3 Matrix Optics, Solid Angle, and Spatial Resolution 41

3.4 Model Parameters and Synthetic Spectra 44

3.5 Pre-Processing of Raw laser Thomson and Raman Signals 46

3.6 Nonlinear Least Squares 50

3.7 Bayesian Inference and Model Selection 53

3.7.1 Background and Bayes' Equation 53

3.7.2 Likelihood and Prior PDFs 55

3.7.3 Sampling from and Approximating the Posterior PDF 56

3.7.4 Bayesian Model Selection 58

3.8 Distinguishing Velocity Distribution Functions with Bayesian Model Selection 60

3.8.1 Synthetic Data, Priors, and Test Matrix 60

3.8.2 Effects of Prior Uncertainty 62

3.8.3 Effects of Prior Inaccuracy 65

3.8.4 Interactions of Inaccuracy and Uncertainty 66

3.8.5 Transdimensional Model Selection 69

3.9 Application of Bayesian LTS Methods to ns-Pulsed Plasmas 71

3.9.1 Experimental Setup 72

3.9.2 Bayesian Inference and Model Selection 74

3.10 Summary 86

Chapter 4: Discharge Voltage Effects on the Spatial Distribution of the Electron Number Density and Temperature in a ns-Pulsed Plasma; Detection Limit Estimates and Spatial Resolution Investigations 88

4.1 Experimental Layout 88

4.1.1 Vacuum Test Cell and Electrodes 88

4.1.2 Cell Electrical Configuration 93

4.1.3 Interrogation Optical Beam System 96

4.1.4 Collection and Detection System 103

4.2 Effects of Pressure, Voltage, and Phase Delay On Plasma Discharge Properties 108

4.3 External Discharge Voltage Boundary Condition Effect on the Spatially Resolved Electron Temperature and Density Profiles 115

4.3.1 Spatial Resolution and Discharge Study Test Matrix 115

4.3.2 Confirmation of Statistical Stationality of the Plasma Pulse 116

4.3.3 Results, Spatial Resolution Limitations and System Improvements . 117

4.3.4 Summary 120

Chapter 5: Large Vacuum Test Facility Thomson Scattering Measurements in the Krypton Plume of a Lanthanum Hexaboride Hollow Cathode . . 121

5.1 Introduction 121

5.2 Experimental Setup 121

5.2.1 Vacuum Test Facility 121

5.2.2 Cathode Discharge, Cathode Discharge Mounting and Relative Movement 123

5.2.3 Internal and External Interrogation Beam Optical Systems and their Alignment 124

5.2.4 Internal and External Light Collection and Detection Systems and Their Alignment 132

5.2.5 Fine Temporal, Polarization and Fiber Alignment and Chamber Compression Movement Correction 142

5.3 Cathode Discharge Test Matrices and Results 148

5.4 Discussion 152

5.4.1 Quantitative Comparison with Similar LTS Systems 152

5.4.2 Qualitative and Quantitative Comparison of the Electron Property Profiles 157

5.5 Summary 158

Chapter 6: Large Vacuum Test Facility Measurements in the Near Field Plume of a High Current Density Magnetically Shielded Hall Effect Thruster 160

6.1 Introduction . . . 160

6.2 Experimental Setup . . . 160

6.2.1 Vacuum Test Facility . . . 160

6.2.2 Thruster Discharge and Relative Motion . . . 162

6.2.3 Interrogation Optical System . . . 165

6.2.4 Collection and Detection Optical Systems . . . 169

6.3 Raman Scattering Calibration, Least Squares and Bayesian Inference Analysis . . . 174

6.4 Stray Light Correction . . . 175

6.5 Discharge Channel and Cathode Centerline Axial Measurements . . . 179

6.5.1 Normalized Axial Measurement Locations and Thruster Discharge Telemetry . . . 179

6.5.2 Spatially-normalized Axial Electron Temperature and Density Profiles . . . 181

6.6 Discharge Channel, Front Pole and Cathode Grid Measurements . . . 187

6.6.1 Normalized Grid Measurement Locations and Thruster Discharge Telemetry . . . 187

6.6.2 Spatially-Normalized Discharge Channel, Front Pole and Cathode Grid Electron Properties . . . 191

6.6.3 Discharge Channel and Front Pole Analysis . . . 194

6.7 Magnetic Field Line Measurements . . . 196

6.7.1 Normalized Axial Measurement Locations and Thruster Discharge Telemetry . . . 196

6.7.2 Electron Temperature and Density Profiles Along Magnetic Field Lines . . . 197

6.7.3 Magnetic Field Measurement Analysis 199

6.8 Summary 202

Chapter 7: Conclusions, Contributions, and Future Work 205

7.1 Conclusions and Contributions 205

7.2 Implications and Future Work 208

7.2.1 Implications 208

7.2.2 Future Work 209

References 211

LIST OF TABLES

1.1 Sample of recent missions with electric propulsion elements. 2

3.1 Units and descriptions for the parameters used in the LRS models presented in Subsection 3.2.1. The values in this table were used to generate the synthetic spectrum presented in Figure 3.2. 44

3.2 Units and descriptions for the parameters used in the LTS models presented in Subsection 3.2.2. The values in this table were used to generate the synthetic spectrum presented in Figure 3.3. 45

3.3 Description of the different plasma submodel QoI and nuisance parameter vectors used for Bayesian model selection. M_1 and M_2 describe single Maxwellian and Druyvesteyn submodels. M_3 and M_4 describe single and distinct temperature sums of Maxwellian and Druyvesteyn submodels. . . . 45

3.4 Signals present during LRS acquisiton. 48

3.5 Signals present during LTS acquisiton. 48

3.6 Description of the $3\sigma_{\mathrm{x},i}$ ranges for the submodel parameters used in the synthetic LTS prior distributions. 60

3.7 Description of the $3\sigma_{\mathrm{x},i}$ ranges for the LRS case at 7 Torr. 80

3.8 Description of the $3\sigma_{\mathrm{x},i}$ ranges for the LTS case at 7 Torr neutral background pressure 10 kV. 83

4.1 System timing configuration. 96

4.2 Master optical diagram for the system. 97

4.3 Interrogation beam optical parameters. 97

4.4 Detection system optical parameters. 105

4.5 Detection system collection parameters. 108

4.6 Pressure sweep test matrix. 109

4.7 Phase delay sweep test matrix. 110

4.8 Leading edge phase delay test matrix. 111

4.9 Spatially resolved voltage sweep test matrix. 115

5.1 Interrogation beam optical parameters. 128

5.2 Detection system optical parameters. 141

5.3 Cathode experiment LRS test matrix. 148

5.4 Cathode discharge test matrix. 151

5.5 Detection system collection parameters. 152

6.1 Interrogation beam optical parameters. 167

6.2 Detection system optical parameters. 173

6.3 Description of the $3\sigma_{\mathrm{x},i}$ ranges used for the LRS cases. 174

6.4 Description of the $3\sigma_{\mathrm{x},i}$ ranges used for the LTS cases. 175

LIST OF FIGURES

1.1 Notional operational diagram of an US-type HET with center mounted cathode. 3

1.2 Notional field topology diagram of a traditional US versus MS HET. 5

1.3 Notional diagram of a typical LTS system. 10

2.1 Notional illustration of Debye shielding and plasma sheaths in a plasma. . . 22

2.2 Notional HET potential profiles form the anode in dark cyan to the discharge channel exit plane in cyan. Electric field lines in blue point in the notional direction of ion acceleration. 25

2.3 Notional effect of magnetically shielding the channel walls. 28

3.1 General scattering wave orientation in a scattering experiment. 31

3.2 Synthetic LRS spectra for air and nitrogen. 47

3.3 Synthetic LTS spectra using the four models. 47

3.4 $\ln(B_{2,1})$ versus SNR over priors with increasing misinformation: (a) $\kappa_{\mathrm{x},i}^{\mathrm{stretch}}$ = 0, (b) $\kappa_{\mathrm{x},i}^{\mathrm{stretch}}$ = 100, and (c) $\kappa_{\mathrm{x},i}^{\mathrm{stretch}}$ = 300. Synthetic data generated from model M1 is in blue, and synthetic data generated from model M2 is in purple. Dots indicate the calculated value of $\ln(B_{i,j})$, and lines indicate a line of best fit. $|\ln(B_{i,j})|$ substantially greater than zero indicates that the Bayesian framework is able to correctly identify the right model. 63

3.5 $\ln(B_{2,1})$ versus γ_{MD} at varying SNR levels over decreasingly certain priors for model M_3: (a) $\kappa_{\mathrm{x},i}^{\mathrm{stretch}}$ = 0, (b) $\kappa_{\mathrm{x},i}^{\mathrm{stretch}}$ = 100, and (c) $\kappa_{\mathrm{x},i}^{\mathrm{stretch}}$ = 300. Dots indicate the calculated value of $\ln(B_{i,j})$, and lines indicate a line of best fit. γ_{MD} characterizes how "Maxwellian" the plasma is. 64

3.6 $\ln(B_{2,1})$ versus SNR for decreasingly accurate priors: (a) $\kappa_{\mathrm{x},i}^{\mathrm{shift}}$ = 1, (b) $\kappa_{\mathrm{x},i}^{\mathrm{shift}}$ = 20, and (c) $\kappa_{\mathrm{x},i}^{\mathrm{shift}}$ = 30. Synthetic data generated from model M1 is in blue, and synthetic data generated from model M2 is in purple. Dots indicate the calculated value of $\ln(B_{i,j})$, and lines indicate a line of best fit. $|\ln(B_{i,j})|$ substantially greater than zero indicates that the Bayesian framework is able to correctly identify the right model. 66

3.7 $\ln(B_{2,1})$ versus γ_{MD} at varying SNR levels over decreasingly informative priors with Model M_3: (a) $\kappa_{\mathrm{x},i}^{\mathrm{shift}}$ = 1, (b) $\kappa_{\mathrm{x},i}^{\mathrm{shift}}$ = 20, and (c) $\kappa_{\mathrm{x},i}^{\mathrm{shift}}$ = 30. Dots indicate the calculated value of $\ln(B_{i,j})$, and lines indicate a line of best fit. γ_{MD} characterizes how "Maxwellian" the plasma is. 67

3.8 $\ln(B_{2,1})$ versus SNR over decreasingly informative priors: (a) $(\kappa_{\mathrm{x},i}^{\mathrm{stretch}},\ \kappa_{\mathrm{x},i}^{\mathrm{shift}}) = (10,\ 2)$, (b) $(\kappa_{\mathrm{x},i}^{\mathrm{stretch}},\ \kappa_{\mathrm{x},i}^{\mathrm{shift}}) = (25,\ 5)$, and (c) $(\kappa_{\mathrm{x},i}^{\mathrm{stretch}},\ \kappa_{\mathrm{x},i}^{\mathrm{shift}}) = (100,\ 20)$. Synthetic data generated from model M1 is in blue, and synthetic data generated from model M2 is in purple. Dots indicate the calculated value of $\ln(B_{i,j})$, and lines indicate a line of best fit. $|\ln(B_{i,j})|$ substantially greater than zero indicates that the Bayesian framework is able to correctly identify the right model. 68

3.9 $\ln(B_{2,1})$ versus γ_{MD} at varying SNR levels over decreasingly informative priors: (a) $(\kappa_{\mathrm{x},i}^{\mathrm{stretch}},\ \kappa_{\mathrm{x},i}^{\mathrm{shift}}) = (10,\ 2)$, (b) $(\kappa_{\mathrm{x},i}^{\mathrm{stretch}},\ \kappa_{\mathrm{x},i}^{\mathrm{shift}}) = (25,\ 5)$, and (c) $(\kappa_{\mathrm{x},i}^{\mathrm{stretch}},\ \kappa_{\mathrm{x},i}^{\mathrm{shift}}) = (100,\ 20)$. Dots indicate the calculated value of $\ln(B_{i,j})$, and lines indicate a line of best fit. γ_{MD} characterizes how "Maxwellian" the plasma is. 69

3.10 $\ln(B_{i,j})$ versus SNR over several data generation cases; (a) data generated with M_1, (b) data generated with M_2, (c) data generated with M_3, and (d) data generated with M_4. $\ln(B_{2,1})$ (blue), $\ln(B_{3,1})$ (orange), $\ln(B_{4,1})$ (red). Dots indicate the calculated value of $\ln(B_{i,j})$, and lines indicate a line of best fit. 70

3.11 A nanosecond pulsed discharge setup and a sample discharge image as well as the diagram of the collection system optical setup . The interrogation laser beam propagates in the $\mathbf{x}$ direction, is polarized in the $\mathbf{y}$ direction, and the scattering is collected in the $\mathbf{z}$ direction. M, l, HWP and BNF are acronyms for mirrors, lenses, half wave plates, and Bragg notch filters, respectively. 73

3.12 Raman least-squares fit at two background pressures; (a) p_{g} = 10 Torr, and (b) p_{g} = 7 Torr. The data and rejected data lines are presented in black and black-dashed. The estimated center wavelength is presented with a purple-dashed line, and the rejected data region is presented with red-dashed lines. 76

3.13 Raman least-squares inferred parameters versus p_{g} ; (a) η, and (b) λ_{i}. 77

3.14 Thomson least-squares fit at two discharge voltages; (a) V_{D} = 5 kV and (b) V_{D} = 10 kV. The data and rejected data lines are presented in black and black-dashed. The estimated center wavelength is presented with a purple-dashed line, and the rejected data region is presented with red-dashed lines. The SNR estimates using the Maxwellian and Druyvesteyn submodels are 4 and 5 in (a) and 15 and 14 in (b), respectively. 78

3.15 Individual elements of the Thomson QoI $\mathbf{x}_{\mathrm{LS}}^{\mathrm{T}}$ versus V_{D}. The Maxwellian submodel inversion is shown in (a) with a circle marker, and the Druyvesteyn submodel in (b) with a square marker. 79

3.16 LRS marginal and joint posterior distribution functions for all LRS model inputs along with the prior and least squares posterior estimates. Samples from the prior are in orange, and the Bayesian and LS posteriors in steel blue and red. 81

3.17 LRS marginal and joint posterior distribution functions for all LRS model inputs along with the prior and least squares posterior estimates. The Bayesian and LS posteriors are presented in steel blue and red. 82

3.18 LTS marginal and joint posterior distribution functions for all LTS model inputs along with the prior and least squares posterior estimates. Samples from the prior are in green, the Bayesian posteriors for the Maxwellian and Druyvesteyn submodels in blue and orange, respectively as well as the posterior estimates of the LS inference in purple and red, respectively. . . . 84

3.19 LTS marginal and joint posterior distribution functions for all LTS model inputs along with the prior and least squares posterior estimates. The Bayesian posteriors for the Maxwellian and Druyvesteyn submodels are in blue and orange, respectively as well as the posterior estimates of the LS inference in purple and red, respectively. 85

4.1 Isometric and front views of the plasma cell. 89

4.2 Vacuum cell electrodes and brewster window. 91

4.3 Vacuum cell pressure control section. 91

4.4 Vacuum cell vacuum pulling section. 93

4.5 Vacuum cell electrical configuration. 94

4.6 First and second legs of the interrogation beam optical system. 99

4.7 Third leg of the interrogation beam optical system. 100

4.8 Collection system optical diagram. 104

4.9 Spatial variation in electron properties versus pressure. 109

4.10 Variation in electron properties versus phase delay. 110

4.11 Spatially resolved electron properties at a 40-ns delay with respect to the leading edge of the plasma pulse. 112

4.12 Spatially resolved electron properties at a 50-ns delay with respect to the leading edge of the plasma pulse. 112

4.13 Spatially resolved electron properties at a 60-ns delay with respect to the leading edge of the plasma pulse. 113

4.14 Spatially resolved electron properties at a 70-ns delay with respect to the leading edge of the plasma pulse. 113

4.15 Individual and averaged discharge current signals at several discharge voltages. Individual oscilloscopelines are plotted with thin soft colored lines, and the average oscilloscopesignal is plotted with a dark colored line. The 8, 12, and 20 kV cases used 100 oscilloscope traces, the 16 kV case used 21 oscilloscope traces. 116

4.16 Spatially resolved electron properties at discharge voltage of 20 kV. 117

4.17 Spatially resolved electron properties at discharge voltage of 16 kV. 118

4.18 Spatially resolved electron properties at discharge voltage of 12 kV. 118

4.19 Spatially resolved electron properties at discharge voltage of 8 kV. 119

5.1 Cathode discharge mounted to the axial and radial stages inside of VTF-2. . 124

5.2 Notional diagram of the relative location of the external optical system with respect to the vacuum test facility. IOAR and DOAR area acronyms for interrogation optical axis rails and detection optical axis rails respectively . 125

5.3 Master optical diagram for the interrogation, collection and detection systems. The vacuum interface is represented as the large thick red dashed line. 127

5.4 A photo of the internal optical rail structure that supports the last leg of the interrogation optical axis and the collection optical axis. The internal interrogation optical axis and the collection optical axis are shown in green. 130

5.5 A previous iteration of the internal rail structure with the HET in place during alignment. The focus of the interrogation beam is clearly visible. The collection optical axis and its intersection with the focus of the beam is shown in green. A second view is presented in the bottom right before the collection optics were added and before the collection optical rail was placed at the necessary angle with respect to the chamber axes. 131

5.6 Brewster window and fiber flange feedthrough. 133

5.7 Notional diagram of the blocked versus unblocked solid angle cases. 136

5.8 Detection system optical diagram. 140

5.9 Pictures of the internal optical structure movement tests. 145

5.10 Least squares fitted results for the rotational Raman inversion; (a) and (b) show the raw ($\mathbf{b}$), truncated ($\mathbf{b}|_{\mathrm{trunc}}$) with rejection regions and model spectra ($P_{\lambda}^{\mathrm{R}}\left(\mathbf{x}_{\mathrm{LS}}^{\mathrm{R}}\right)$) at 105 Torr and 5.6 Torr, respectively. 149

5.11 Least squares fitted results for the rotational Raman inversion; (a) shows the system efficiency constant versus background pressure, and (b) estimated center wavelength versus background pressure. 150

5.12 Picture of the final configuration of the interrogation and collection system at atmospheric chamber pressure. 151

5.13 Picture of the interrogation system and cathode discharge at vacuum. 151

5.14 Diagram of the radial locations probed relative to the HET from a top and side view. 152

5.15 Least squares fitted results for the laser Thomson scattering inversion; (a) and (b) show the raw ($\mathbf{b}$), truncated ($\mathbf{b}|_{\mathrm{trunc}}$) with rejection regions and model spectra for both a Maxwellian ($P_{\lambda}^{\mathrm{TM}}\left(\mathbf{x}_{\mathrm{LS}}^{\mathrm{TM}}\right)$) and Druyvesteyn spectra distribution function ($P_{\lambda}^{\mathrm{TD}}\left(\mathbf{x}_{\mathrm{LS}}^{\mathrm{TD}}\right)$). Figures (a) and (b) correspond to absolute number densities of 1.074×10^{18} and 1.85×10^{17} m^{-3} respectively. Figure (a) and (b) were taken along the center line at $z_{\mathrm{beam-cathode}}$ = 2 mm and $z_{\mathrm{beam-cathode}}$ = 8 mm, respectively. 153

5.16 Axially resolved electron properties calculated using Maxwellian and Druyvesten spectral distribution functions at two different radii. At a radius of $r_{\mathrm{beam-cathode}}$ = 2 mm, the signal at $z_{\mathrm{beam-cathode}}$ = 8 mm was very low and, as a result, was not included. 154

5.17 Least squares fitted results for the laser Thomson scattering inversion; (a) and (b) show the raw ($\mathbf{b}$), truncated ($\mathbf{b}|_{\mathrm{trunc}}$) with rejection regions and model spectra for both a Maxwellian ($P_{\lambda}^{\mathrm{TM}}\left(\mathbf{x}_{\mathrm{LS}}^{\mathrm{TM}}\right)$) and Druyvesteyn spectra distribution function ($P_{\lambda}^{\mathrm{TD}}\left(\mathbf{x}_{\mathrm{LS}}^{\mathrm{TD}}\right)$). Figures (a) and (b) correspond to absolute number densities of 1.074×10^{18} and 1.85×10^{17} m^{-3} respectively. Figure (a) and (b) were taken along the center line at $z_{\mathrm{beam-cathode}}$ = 3 mm and $z_{\mathrm{beam-cathode}}$ = 7 mm, respectively. 155

6.1 Annotated picture with all of the relevant basis vectors. 164

6.2 Notional diagram of the relative location of the external optical system with respect to the vacuum test facility. IOAR and DOAR area acronyms for interrogation optical axis rail and detection optical axis rail respectively . . 165

6.3 Master optical diagram for the interrogation, collection and detection systems. The vacuum interface is represented as the large thick red dashed line. 166

6.4 A photo of the internal optical rail structure that supports the last leg of the interrogation optical axis and the collection optical axis. 168

6.5 Detection system optical diagram. 172

6.6 Least squares fitted spectrum for the rotational Raman inversion showing the raw and truncated ($\mathbf{b}$ and $\mathbf{b}|_{\mathrm{trunc}}$) spectra with rejection regions and model spectra ($P_{\lambda}^{\mathrm{R}}\left(\mathbf{x}^{\mathrm{R}}\right)$) at 5.2 Torr. 176

6.7 LRS marginal and joint posterior distribution functions for all LRS model inputs along with least squares posterior estimates. The Bayesian and LS posterior samples are presented in steel blue and red, respectively. For the sake of clarity, each joint posterior displays a single Mahalanobis contour containing the most probable 11.8% of the distribution. 177

6.8 Correction of the $C_{\mathrm{T}} - D_{\mathrm{T}}|_{\mathrm{raw}}$ spectrum. 178

6.9 Correction of the $A_{\mathrm{T}} - (B_{\mathrm{T}} + (C_{\mathrm{T}} - D_{\mathrm{T}}))$ spectrum. 179

6.10 Normalized discharge channel and cathode axial measurement locations. The thruster boundaries are represented in grey, the front pole cover in light grey, and the cathode keeper body in black. 180

6.11 Individual and mean thruster discharge telemetry scans for the cathode and channel centerline axial measurements. 180

6.12 Individual thruster discharge telemetry power spectra for the cathode and channel centerline axial measurements. 181

6.13 Spatially-normalized electron temperature and density profiles at the cathode centerline using a Maxwellian submodel. 182

6.14 Spatially-normalized axial profile of the Bayes' factor for the Maxwellian and Druyvesteyn submodels $\ln(B_{2,1})$. 182

6.15 Spatially-normalized electron temperature and density profiles at the channel centerline using a Maxwellian submodel. 183

6.16 Discharge channel centerline normalized magnetic field strength. 185

6.17 Channel centerline electron temperature and density profiles at 300 V and 15 A. 185

6.18 Electron temperature and density versus notional discharge current at the channel center line at a normalized axial location of z/r_{o} = .0133. 187

6.19 Normalized discharge channel, front pole and and cathode grid measurement locations. The thruster boundaries are represented in grey, the front pole cover in light grey, and the cathode keeper body in black. 188

6.20 Individual and mean thruster discharge telemetry scans for the cathode grid measurements. 189

6.21 Individual thruster discharge telemetry power spectra for the for the cathode grid measurements. 189

6.22 Individual and mean thruster discharge telemetry scans for the channel and front pole grid measurements. 190

6.23 Individual and mean thruster discharge telemetry power spectra for the channel and front pole grid measurements. 190

6.24 Spatially normalized electron temperature and density profiles for the cathode grid. 191

6.25 Spatially normalized electron temperature and density profiles for the channel and front pole grid. 193

6.26 Discharge channel centerline normalized magnetic field strength at several radii approaching the front pole region. 193

6.27 Spatial heat map of the channel and front pole grid electron pressure. 195

6.28 Electron pressure profiles in the channel and front pole grid. 196

6.29 Normalized magnetic field line measurement locations in blue. The field lines are numbered one to two from left to right, and the magnetic field line points are numbered one to nine from top to bottom on each respective field line. The thruster boundaries are represented in grey, the front pole cover in light grey, and the cathode keeper body in black. 197

6.30 Individual and mean thruster discharge telemetry scans. 198

6.31 Individual thruster discharge telemetry power spectra. 198

6.32 Electron temperature and density profiles along the outlined magnetic field lines. The field lines (B_{i}) are numbered from left to right, and the point along each field line $\hat{s}_{\mathrm{j}}$ are numbered from top to bottom along each field line in Figure 6.29. 199

6.33 Electron pressure along each magnetic field line. 200

6.34 Estimated gradient of the electrostatic potential along the each probed magnetic field line. 201

SUMMARY

Laser Thomson scattering (LTS) is a diagnostic that provides direct access to electron properties in a plasma. This diagnostic is calibrted via laser Raman scattering (LRS). The goal of this thesis was to probe the electron properties in the near field plasma plume of a magnetically shielded (MS) Hall effect thruster (HET), a type of electrostatic electric propulsion device (EP), to provide insight into the applicability of the isothermal magnetic field line model and a notional description of the electron-property-predicted plasma structure traversing the front pole region from the discharge to cathode centerline. To this end, this thesis provides the following contributions:

1. Implementation of a Bayesian analysis and model selection framework for LRS-calibrated LTS diagnostics.

2. Detailed design and implementation of a discharge plasma cell and LTS system for near plasma boundary and laser plasma and laser neutral interactions.

3. Detailed design and implementation of a large vacuum test facility LTS system for measurements in live EP devices benchmarked on a hollow cathode.

4. Detailed upgrade to the large vacuum test facility LTS system for measurements in the near field discharge of a high current density MS HET. Specifically, axially resolved electron property measurements along the discharge channel centerline, spatially resolved method traversing the front pole region from the channel centerline to the cathode centerline, and measurements along two distinct magnetic field lines.

CHAPTER 1

INTRODUCTION, MOTIVATION, AND PROPOSED WORK

This chapter presents a brief overview of electric propulsion (EP) that sets the general context and motivation for this study. The motivation for the specific work is then presented after a brief of the literature. Then, the research questions are proposed as a starting point for the investigation to follow. The chapter ends with an overview of the document.

1.1 Overview of Electric Propulsion

1.1.1 Prominence of Electric Propulsion

Spacecraft motion is subject to Newton's laws. The sum of the external forces and the change in momentum due to the acceleration and expulsion of propellant from a thruster, is equal to the momentum change of the spacecraft. The motion of a spacecraft of mass and velocity m_{s} and $\mathbf{v}_{\mathrm{s}}$, subject to external forces $\mathbf{F}_{\mathrm{ext}}$, expelling propellant of velocity $\mathbf{v}_{\mathrm{e}}$ can be described by [33, 38, 91]

$$\mathbf{F}_{\mathrm{ext}} + \mathbf{T} = \frac{\mathrm{d}}{\mathrm{dt}}(m_{\mathrm{s}}\mathbf{v}_{\mathrm{s}}). \tag{1.1}$$

The thrust is defined as the change in momentum due to the expulsion of propellant m_{p} at a given velocity, $\mathbf{v}_{\mathrm{p}}$ by the relationship $\mathbf{T} \equiv \frac{\mathrm{d}}{\mathrm{dt}}(m_{\mathrm{p}}\mathbf{v}_{\mathrm{p}})$. Projecting along $\mathbf{v}_{\mathrm{e}}$ in Equation 1.1, assuming a constant propellant speed, and neglecting external forces (due to drag, radiation pressure, gravity, etc.) leads to the following expression for the change in the velocity of the spacecraft

$$\Delta v_{\mathrm{s}} = v_{\mathrm{p}} \log\left(1 + \frac{m_{\mathrm{p}}}{m_{\mathrm{s}}}\right). \tag{1.2}$$

Equation 1.2 shows that, in order to increase Δv_{s}, a spacecraft can either exhaust propellant at a larger relative speed or burn more propellant. EP devices are advantageous in this regard because they have exhaust velocities that are at least an order of magnitude higher than the exhaust velocities of typical chemical propulsion devices [91]. Because chemical propulsion devices accelerate propellant through the release of energy stored in chemical bonds, their exhaust velocities are energy-limited to a few km/s. In contrast, EP devices use energy provided by external sources like external power supplies to accelerate propellant and can therefore reach exhaust velocities on the order of tens to hundreds of km/s. These savings in propellant, and therefore spacecraft mass, have been illustrated several times. One such example is Dawn's NSTAR gridded ion engine (GIE) achieving a Δv_{s} of 11 km/s with less than 500 kg of propellant, as opposed to the projected 6000 kg of propellant that would have been required to achieve the same velocity increment if Dawn used a chemical propulsion device [83, 142]. These high exhaust velocities and ISP come at the expense of thrust, with a typical high power Hall effect thruster (HET) producing about 400 mN of thrust [97].

The mass-saving capabilities of EP devices have extended their possible range of applications from station keeping and orbit raising, which are simple spacecraft orbit maintenance and adjustment maneuvers, to main propulsion elements for deep space exploration. Between 1964 and 2018, eight deep space missions were launched with EP. From 1964 to 2018, 24 small satellite missions were launched with EP [131]. A sample of some recent missions after 2015 illustrating the future prevalence of EP devices is shown in Table 1.1 [83, 120, 129, 136, 151, 159].

Table 1.1: Sample of recent missions with electric propulsion elements.

Mission	**Launch Year**	**EP Device**	**Number of EP Devices**
Dawn	2015	Ion thruster	1
BepiColombo	2018	Ion thruster	4
Psyche	2022	Hall effect thruster	1
Starlink	2015-2022	Hall effect thruster	Over 2000

To date, more than 2,600 satellites have been launched that leverage EP. Endeavors like the Psyche mission [164] will use HETs to perform rendezvous and orbit maneuvers with the largest metal asteroid in the solar system pushing the boundaries of how EP is leveraged. To support future missions, EP thruster development, spacecraft integration, and ground testing have been major areas of research over the last decade.

1.1.2 Overview of Hall effect thrusters

EP devices accelerate propellant through electrical heating and/or the direct application of electromagnetic fields [33]. EP thrusters can be categorized by their acceleration mechanism as electrothermal, electrostatic, or electromagnetic. Electrothermal EP thrusters directly heat propellant that is then ionized through DC or AC electric fields and accelerated through nozzle expansion, examples of which are resistojet and arcjet thrusters. Electromagnetic thrusters accelerate ionized propellant through the direct application of electric and magnetic body forces, and include pulsed plasma and magnetoplasmadynamic thrusters. Electrostatic EP thrusters accelerate ionized propellant through the direct application of electric body forces, and include electrospray, ion, and HETs. HETs are the subject of this work.

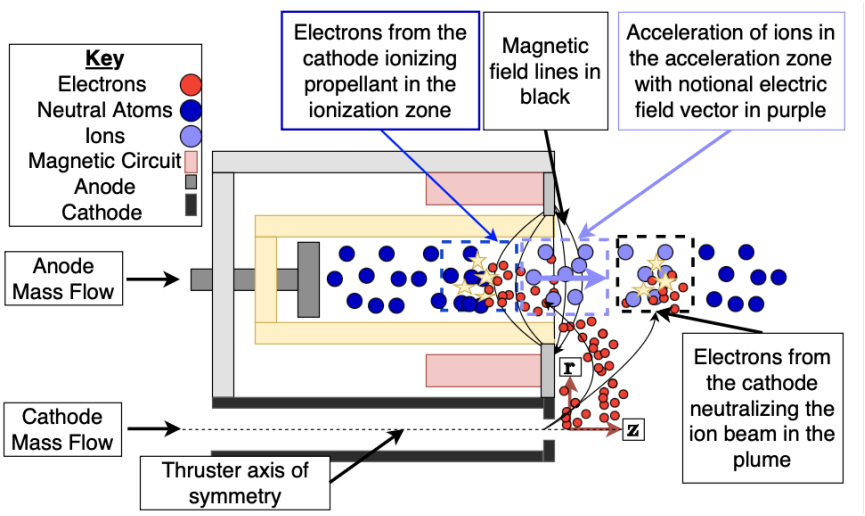

Figure 1.1: Notional operational diagram of an US-type HET with center mounted cathode.

Although Section 2.2 further details the plasma physics of HET operation, a brief overview is presented here, referencing Figure 1.1. HETs are electrostatic devices that create thrust through the acceleration of ions produced by neutral propellant ionization with magnetized electrons from a hollow cathode electron source [8, 10, 33, 38]. They are typically cylindrical in shape with a single discharge channel, although the effect of non-cylindrical and multi-channel thrusters has been the subject of several studies [29, 34, 114], and reviewed in [169]. The propellant that is fed through an annular anode, also acting as the propellant distributor, is ionized and then accelerated and finally recombines in the plasma plume. The electrons that ionize the propellant are magnetized via a standing magnetic field that acts to delay the time for the electrons to accelerate through the potential well between the anode and cathode, acting as a magnetic confinement mechanism for efficient ionization of propellant in the annular channel of a typical HET.

HETs are typically classified into two types: HETs with non-conducting discharge channel walls, typically known as stationary plasma thrusters (SPTs) or thrusters without anode layers, and thrusters with conducting channel walls, known as thrusters with anode layers (TALs) [13]. The fundamental difference is in the location and extent of the region where the bulk of the ion acceleration and thrust generation occurs. HETs, both SPT and TAL, have flown and been continuously developed since the 1970s. However, many details about their plasma processes over several length and time scales that factor into their time-and-space averaged efficiency and performance are not well understood at this time [42, 67, 138].

For the remainder of this work, we consider HETs without conducting walls as the test article for the main experiments in this work outlined in Chapter 6 is an SPT type HET. Subcategories of this type of HET, such as unshielded (US) and magnetically shielded (MS) HETs, exist. The main difference between US and MS thrusters lies in their magnetic field topology and channel wall chamfering, as seen in Figure 1.2. MS thrusters leverage a specially designed magnetic field topology that deviates from the US radial magnetic field

in the discharge channel to enforce equipotentialization of the magnetic field lines near the wall [78]. Equipotentialization of magnetic field lines near the wall shields the walls from ion bombardment and reduce erosion rates by orders of magnitude. Details on MS, MS HETs, and pole erosion are outlined in Section 2.3 and Section 2.4.

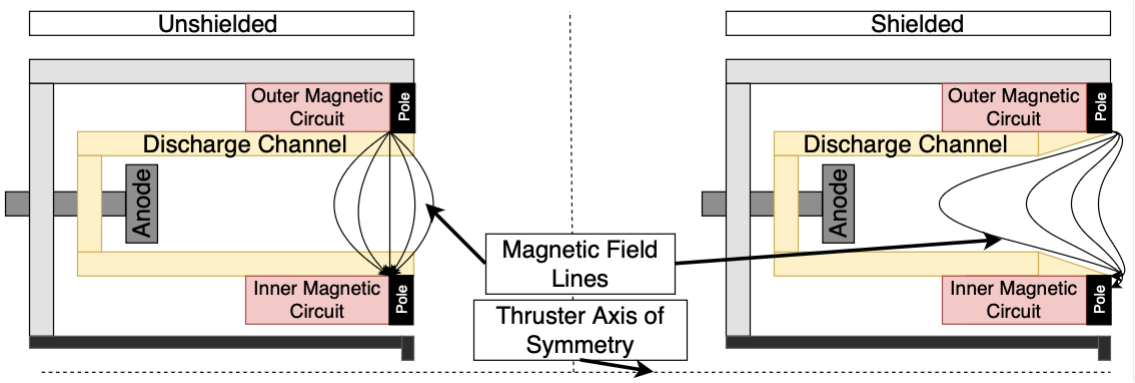

Figure 1.2: Notional field topology diagram of a traditional US versus MS HET.

1.1.3 Hall effect thruster Performance Quantification and Plasma Property Measurements

Several figures of merit are used to quantify the performance of HETs. The total impulse is defined as

$$I \equiv \int_{t_o}^{t_f} |\mathbf{T}| \mathrm{dt} = \int_{t_o}^{t_f} \frac{\mathrm{d}}{\mathrm{dt}}(m_s|\mathbf{v}_s|)\mathrm{dt} \approx v_e \Delta m_s = v_e \Delta m_p. \tag{1.3}$$

In this context, the total impulse quantifies the possible Δv capabilities of a thruster. Equation 1.3 illustrates that the same total impulse can be achieved by two means: a large magnitude change force applied over a short time duration or a small magnitude force applied over a long time duration. The specific impulse quantifies the efficiency of a thruster in terms of its fuel consumption and exhaust velocity,

$$I_{sp} \equiv \frac{I}{g_o \int_{t_o}^{t_f} \dot{m}_p \mathrm{dt}} = \frac{I}{g_o \Delta m_p} \approx \frac{v_e \Delta m_p}{g_o \Delta m_p} = \frac{v_e}{g_o}. \tag{1.4}$$

As previously stated, ionization is a key feature of EP thrusters. Not all of the propellant

is ionized and used to produce thrust, which leads to the following definition for propellant utilization efficiency as

$$\alpha \equiv \frac{\dot{m}_{\mathrm{i}}}{\dot{m}_{\mathrm{p}}} = \frac{I_{\mathrm{b}} M}{e \dot{m}_{\mathrm{p}}}, \tag{1.5}$$

with $\dot{m}_{\mathrm{i}}, \dot{m}_{\mathrm{p}}$, I_{b}, M,and e being the ion and propellant mass flow rates, ion beam current, propellant atomic mass, and electron charge, respectively. This definition only accounts for singly-charged ions but can be easily corrected [91].

Thrust efficiency is defined as the ratio of the mechanical to electrical power inputs to the thruster,

$$\eta_{\mathrm{thrust}} \equiv \frac{P_{\mathrm{mech}}}{P_{\mathrm{elect}}} = \frac{\dot{m}_{\mathrm{p}} v_{\mathrm{p}}^2}{2 P_{\mathrm{elect}}} \approx \frac{T^2}{2 \dot{m}_{\mathrm{p}} P_{\mathrm{elect}}}, \tag{1.6}$$

with P_{mech} and P_{elect} being the mechanical and electrical power inputs to the thruster. Reaching high thruster efficiency, as demonstrated in Equation 1.6, requires that the losses – stemming from ionization losses, velocity spreads, beam divergences, and power deposition and radiation – be minimized [38, 91]. The effect of loss mechanisms on thruster efficiency and predictive modeling of these loss mechanisms for thruster development is one of the driving factors behind emerging thruster diagnostic technologies like high-speed electrostatic and non-invasive laser diagnostics.

Quantification of HET performance based on metrics outlined in this subsection requires several kinds of measurements to be taken, including thrust and plasma property measurements in the plume of HETs. HET performance campaign design typically begins with the selection of an adequate ground-based testing facility. Variations from facility to facility in terms of size, pumping capabilities, electrostatic probe design, and processes for data acquisition and inversion lead to efforts for standardization of methodologies used in EP testing [94, 96, 98, 107, 110, 111]. Along with thrust measurements from various types of thrust stands, plasma property measurements have traditionally and reliably been

performed with electrostatic plasma probes; the most widely used is the Langmuir probe. Under several sets of assumptions, Langmuir probe measurements provide electron number density, electron temperature, and the electron energy distribution function. Additional assumptions can also lead to ion properties [107]. These probes and their limitations are well understood, and their use in the EP community has led to great advancements in the research, design, and testing of HETs. However, the very presence of an electrostatic probe in a plasma perturbs the plasma. These perturbations are exacerbated in the near-field plume of HETs [88]. In the case of MS HETs, where the channel wall shielding is driven by equipotentialized magnetic field lines, the presence of electrostatic probes has the potential to interfere with plasma process investigations. Laser-based diagnostics provide a path forward for investigating the plasma processes in the near-field plume of HETs due to their minimally invasive nature.

1.2 Electric Propulsion Background and Motivation

EP researchers aim to understand how the applied electromagnetic fields, mass flow rates, thruster geometry, cathode placement, and external boundary conditions like the ground facility and the thruster electrical configuration with respect to the ground facility affect the performance of EP devices like HETs. These input conditions affect the plasma processes in the discharge channel, as well as in the near-field and far-field plume of the HETs. Several transient phenomena and their roles in thruster performance and stability have been investigated for decades, most notably the HET breathing mode discharge oscillation as well as anomalous electron mobility [89, 122, 123, 130] . Recently, previously identified and new phenomena on these transient time scales and their effect on HET performance and stability have begun to be investigated with the help of high-speed electrostatic probes and laser-based diagnostics [40, 45, 68, 82, 118, 139, 143, 158].

In the last decade, emerging optical technologies have facilitated the aggressive development of laser-based diagnostics in EP-relevant plasmas with low densities – among

them being laser induced fluorescence (LIF), terahertz time- domain spectroscopy (THz-TDS), and laser Thomson scattering (LTS) [6, 9, 28, 43, 61, 69, 99, 112, 124, 128]. This manuscript will focus on LTS, which can provide non-invasive probing of the electron temperature, density and bulk drift velocity. LTS provides an avenue for reliable electron property measurements in the near-field plume of HETs, data that can calibrate and validate closure models and HET plasma simulations.

1.2.1 Predictive Models and Simulations in EP

The fundamental qualitative physical processes that govern the operation of HETs are outlined in Subsection 1.1.2. The physics are described via highly nonlinear coupled partial differential equations that require physics-based closures, simplifications, and many assumptions before they can be applied tractably to HETs. There are several different general classes of HET simulation models: kinetic models, fluid/hybrid models, and particle-in-cell models [37, 95].

Kinetic models use full direct numerical simulations of the Boltzmann/Vlasov equations for all species. These models reduce the dimensionality of the domain, oftentimes to 1D, in order to include inertial terms in the electron momentum equations [146]. Quasineutral fluid models assume fluid conservation equations for electrons, ions, and neutrals. Electrons are typically modeled with the continuity equation, momentum conservation equation, and energy conservation equations. Ions are modeled with continuity and momentum conservation. Neutral atoms are described with fluid equations, the functional form of which takes on a much simpler form given the limited extent of neutral atom interactions given their possible collision mechanisms. Quasineutrality is enforced via the continuity equations for the ions and electrons [41]. Hybrid models treat electrons as fluids and many ions as single superparticles. Neutral atoms are treated as simple fluids or as superparticles. Physics sub-models and closures are included to study not well-understood phenomena like cross-field anomalous electron transport [19]. Particle-in-cell (PIC) models treat all species

as super-particles, or treat only a small number of particles over a limited domain and are typically used to understand and quantify anomalous transport due to turbulence and instabilities in HETs [115].

HET simulations are built on many physics-based models. Models are confined and tuned/calibrated through measurements to be accurate in certain parts of the thruster over a given operational regime, and oftentimes, models that help to close the governing equations have scalings that depend on critical plasma parameters like the local magnetic field strength, electron temperature, and density. Therefore, validating and calibrating these simulations, especially in the near-field plume and pole region of an MS HET, is very challenging. This is due to spatial variations in quantities that would validate or invalidate certain models occur over small length scales that are difficult to resolve accurately with electrostatic probes in the harsh environment within a few tens of mm from the thruster discharge channel without perturbing the plasma [88, 134]. Accurate validation and calibration of predictive MS HET simulations will require minimally invasive investigations in the near-field plume.

1.2.2 EP-Relevant Laser Based Plasma Measurements

Lasers have been used to measure plasma properties beginning in the 1960s [69] . LTS is the elastic electromagnetic scattering of incident radiation from unbounded charged particles and can be coherent or incoherent. Sections 2.2 and 2.4 in References [28, 140], respectively, discuss the cases in which the experimental setup and plasma conditions meet the conditions for coherent LTS. In this work, we implement only incoherent LTS, but we discuss coherent LTS measurements as they are relevant. LTS has been a popular method for probing plasmas because LTS spectral measurements are directly proportional to the 1-D electron velocity distribution function (EVDF), giving direct access to electron property information. State-of-the-art LTS setups for EP-relevant investigations consist of a high-energy interrogation laser beam incident on a plasma, high throughput collection and relay

optical systems with strong stray light rejection via volume Bragg grating (VBG) notch filters, and compact spectrographs with powerful intensified or electron-multiplying detectors for spectrum collection [44, 55, 117]. Figure 1.3 illustrates a notional LTS detection system.

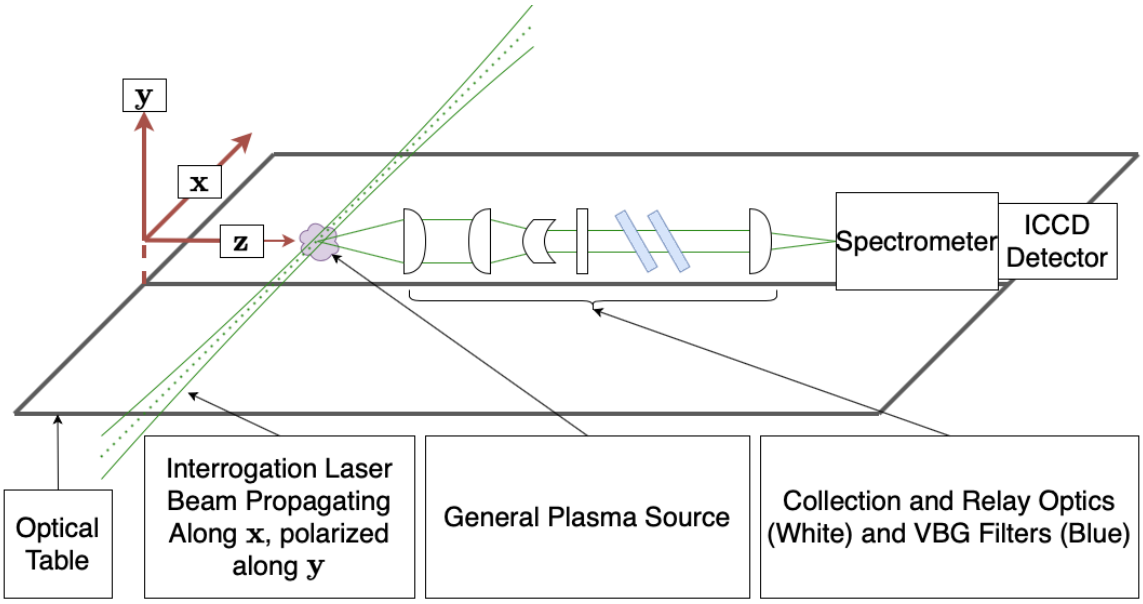

Figure 1.3: Notional diagram of a typical LTS system.

A calibration diagnostic is necessary to relate the absolute intensity detected to the electron density in an LTS experiment. This method of calibration was typically Rayleigh scattering up until the early 2000s, when system throughput and stray light rejection methods – including several different kinds of filters – were able to allow for the detection of rotational Raman lines close to the laser wavelength; since this time, Rayleigh and/or rotational Raman scattering have been used for calibration, although care must be taken when using Rayleigh as the calibration method of choice given that reflections from the test volume saturate the detection branch leading to an unreliable calibration [17, 39]. In this work, rotational Raman scattering is used to calibrate the absolute number density.

With the advancement in available system throughput and laser technology, phase-resolved LTS and LRS measurements became feasible outside of a fusion environment

[27]. During the same time period, temporally and spatially resolved electrostatic probe measurements via high-speed dual Langmuir probes were being leveraged to investigate breathing mode dynamics. However, studies conducted were able to show several systematic deviations between Langmuir probe measurements and other optical diagnostics. These deviations were attributed to the more restrictive assumptions necessary to process Langmuir probe data and, for example, optical emission spectroscopy (OES) measurements as compared to LTS [53]. Measurements were also being conducted on weakly ionized discharges and atmospheric plasmas jets, further pushing the detection limits of LTS systems [49, 70, 74].

During this same time period, in the early 2010s, laser-based measurements on live EP devices were being conducted; LTS was leveraged to measure xenon plasma properties in an ion thruster and a Hall effect thruster, while LIF was leveraged with a novel photon-counting method to measure phase-resolved plasma properties in a stabilized discharge [61, 62, 68]. Additionally, ion and neutral dynamics during ionization collisions were studied with LIF [82]. It is important to note that time-resolved and phase-resolved are often used interchangeably. Phase-resolved measurements are measurements in which a system is either stabilized or periodic fluctuations are assumed to be constant, and measurements are taken by changing the relative phase of the probing time window versus the time window of the phenomena of interest. Time-resolved measurements are measurements in which high-repetition-rate probing methods are used to collect single-to-multi-shot measurements of a phenomenon whose periodic fluctuations may or may not be assumed to be constant. One of the first instances of true time-resolved optical measurements of a transient phenomenon in an EP device was performed during a study using a high-speed camera to capture two discharge modes in a high-power 6-kW HET [75]. A similar study was performed on the NASA HERMeS thruster with high-speed imaging [89].

Advancements in optical filters, specifically volume Bragg gratings, allowed for notch filtering within a few wavenumbers of the laser wavelengths with high throughput out-

side of the filter top-hat, allowing for the almost complete collection of rotational Raman measurements near an excitation wavelength, further enabling rotational Raman as both a calibration measurement for LTS and a standalone measurement for gas temperature in several CO_2 based plasma based experiments [55, 80, 85].

During the late 2010s, several advancements in high-power high-repetition-rate lasers and higher repetition rate cameras as well as cavity-enhanced methods, enabled more optical-based studies of EP devices. These studies ranged from passive imaging of instabilities, such as ion acoustic turbulence, using high-speed cameras to LIF measurements of anomalous electron mobility in high-power HETs, as well as plasma perturbation by the wide-spread use of high-power lasers on several different kinds of plasma sources [100, 101]. In 2018 and 2019, several experiments leveraging LTS and LRS were conducted to study spatially and phase-resolved equilibrium and non-equilibrium discharges in HETs, DC discharges, and HiPMS argon discharges [116, 117, 125, 128, 139]. These studies were enabled by many of the technologies mentioned earlier in this sub-section.

Incoherent LTS measurements on a low-power MS and US HET were performed in the near-field plume as well as in the plume of a 5 A cathode in 2019 and 2020 [126, 141, 152]. These spatially resolved studies were aimed at understanding the impact of the thruster input configuration had on the spatial distribution of the electron temperature and density as well as determining the effect the cathode emitter material temperature had on the resulting spatial distribution of these same quantities. Additionally, the cathode results were compared to a numerical code, which showed good agreement. Around the same time, tomographic methods were leveraged with optical emission spectroscopy to determine the spatial distribution of the electron temperature [135]. Non-physical results stemmed from the collisional radiative model and the angular sampling rate used in the tomographic method, further showing how highly model-based methods that require many assumptions to invert data have severe disadvantages as compared to LTS.

Time-resolved studies via LIF and electrostatic probes were used to study abrupt mode

transitions in a mid-power HET. The mechanisms behind these abrupt changes in discharge modes and efficiency losses are still not well understood, although the authors did make correlations to anomalous electron mobility [122, 123, 130]. Several other authors have studied this phenomenon from the perspective of plasma turbulence and azimuthal discharge instabilities. Coherent LTS has been leveraged to study these azimuthal instabilities in HETs [138]. The same group used coherent and incoherent LTS to study several discharge modes and their contribution to anomalous electron mobility in HETs. Recently, spatially and phase-resolved electron temperature and number density measurements at 100-kHz in a pulsed DC discharge were performed [153, 158]. Similar single-shot measurements were performed using a pulse-burst laser in a quiescent plasma by another group of researchers [128]. Additionally, phase-resolved ion velocity measurements with transfer function techniques have been performed [143].

Recently, LTS was used to study axial variation in electron properties and electron mach Number hollow cathodes, as well as heat flux and electron diffusion in the plume of a high Power HET [160, 165, 166, 172, 176]. These measurements solidify the state of the art in EP-relevant LTS diagnostics as large-vacuum test facility implementations of LTS systems for measurements in live HET test articles.

1.2.3 Hall Effect Thruster Thermalized Magnetic Field Line Model

As mentioned in Section 1.1, a critical element to the operation of a HET is the electric field that stands accelerates ions out of the discharge channel to generate thrust. However, in addition to accelerating the bulk of ions out of the channel, potential structures stand up in the discharge channel HETs that accelerate ions towards the insulating walls of the channel, causing channel erosion [95]. Channel erosion is the life-limiting factor for US HETs because of large sheath potential drops due to the high near-wall electron temperature. The equipotentialized field lines in MS HETs keep near-wall electron temperatures low, minimizing the sheath potential drop therefore almost effectively eliminating erosion via

ion bombardment.

Early models predicted a thermalized potential structure, in which electron mobility along the magnetic field lines compared with restricted mobility across them lead to magnetic field lines that are isothermal and a constant thermalized electrostatic potential along the field lines. [8, 10, 11]. Studies conducted on the potential structures in HETs have been active since their inception. In the early 2000s, the potential structure was investigated at constant discharge voltage and varying current to study the location of the acceleration region in a conventional HET, showing the sensitivity of the beginning of the acceleration region to discharge current [14]. Studies on the effect of segmented electrodes placed along the outer radius of the ceramic channel showed a significant influence on the acceleration and ionization regions due to changes in the potential structure of the thruster. A 2D hydrodynamic model and a high-speed emissive probe were used to measure and explain the potential structure change due to the segmented electrodes [21]. However, these investigations were conducted with probes that bring into question the validity of the measurements in this region.

Thrusters leveraging more complex magnetic field topologies, like those present in magnetically shielded HETs, bring into question the validity of the thermalized potential model in near field discharge MS HETs. This isothermal magnetic field line model is widely used in MS HET plasma simulations [78, 87]. Recent extension of MS HET operation at high and ultra-high current densities motivate investigating the validity of the isothermal magnetic field line model in the near field discharge of a high current density magnetically shielded HET [150, 156, 168].

Radial and axial magnetic field line gradients and gradients in the temperature distribution can lead to a potential structure that differs greatly from that of the predicted thermalized potential model. Models that explicitly include temperature gradients, generalizing the thermalized potential model, were developed and experimentally verified [26]. However, the role of deviation from thermalized magnetic field lines in complex magnetic field

topologies like those present in MS HETs has not received extensive study.

1.3 Thesis Question, Goals, Objectives, and Outline

1.3.1 Thesis Goal and Questions

Near-field plume plasma simulations for high-power MS HETs rely on a thermalized magnetic field line model. However, measurements along magnetic field lines in the near-field thruster discharge region have not been performed. Additionally, near-field measurements traversing the front pole region that directly probe the electron properties have not been performed in a high-power HET. Electrostatic probes, even on high-speed translation stages, are expected to affect the potential structures in the near-field plume plasma due to the perturbative nature of the probes, requiring minimally invasive laser diagnostics for such investigations.

Previous near-field investigations have been made with minimally-perturbative optical diagnostics like OES and LIF. OES is a typically line-averaged measurement that requires the development of a collisional radiative model to estimate the electron properties and tomographic techniques to provide spatial resolution [135]. LIF is a spatially resolved measurement, but it targets the ion population, not the electrons [113]. LTS is a spatially-resolved, minimally-invasive diagnostic that can directly probe electron properties that has recently been implemented in large vacuum test facilities where high current density high-power MS HETs are tested [152]. Therefore, LTS is chosen as the diagnostic for this work due to its ability to provide spatially resolved electron property measurements.

The overall goal of this thesis is to probe the electron properties in the near field plume of a MS HET using LTS in order to provide insight into the applicability of the isothermal magnetic field line model, and provide a notional description of the electron-property-predicted plasma structure in the near field plume of an MS HET. To this end, this thesis is aims to answer the following questions:

1. *Are the magnetic field lines isothermal in the near field discharge of an MS HET operating at high current densities?*

2. *Do the electron temperature and density profiles traversing the inner front pole region from the discharge channel centerline to the cathode centerline produce an electron pressure profile that agrees with ion velocity erosion measurements that indicate ions are accelerated from the core and beam edge region to the front pole region?*

3. *How do the axial electron temperature and density profiles along the discharge channel channel centerline compare to available state-of-the-art HET plasma simulations?*

1.3.2 Thesis Objectives

The first objective of this thesis is to make LTS measurements of electron temperature and density along two distinct magnetic field lines in the near field discharge plasma of a MS HET operating at high current density. Analysis of this data will help address the first question above.

The second objective of this thesis is to take radially and axially resolved measurements of electron temperature and density that traverse the front pole region from the discharge channel centerline to the cathode centerline, to provide insight into whether ions can be accelerated from the discharge channel to the front pole region. Analysis of this data will help to address the second question above.

The third objective of this thesis is to take axially resolved electron temperature and density measurements to compare to available simulations of this thruster and provide data for future simulation calibration efforts. Analysis and comparison of this data will help to address the third question above.

To this end, the following has been accomplished. First, the relevant LTS and LRS models have been outlined as they were necessary to invert the signals of interest and

extract electron temperature and density. Second, a Bayesian uncertainty framework has been built around these models that is reliable even in the case of low signal to noise ratios and has been benchmarked against previous uncertainty methods. Low signal to noise ratios of less than two were encountered as the region between the discharge channel centerline and the cathode centerline were traversed. Reliable uncertainty quantification allowed us to observe and comment on trends outside of the error bars with confidence.

With reliable signal inversion and uncertainty quantification in hand, we needed the ability to detect LRS and LTS. Therefore, a tabletop LTS system was implemented in order to understand LRS and LTS techniques and quantify the notional number density detection limits using the purchased capital equipment. This bought down risk before the large-scale vacuum test facility implementation was attempted.

With an understanding of the techniques, the LTS system was scaled and implemented in a large vacuum test facility and tested on a source with expected number densities exceeding the expected detection limits of our equipment. Finally, the system was adapted to make measurements in the near field discharge region of a high current density MS HET.

1.3.3 Thesis Outline

This thesis is organized in the following way. This chapter presented a brief review of the relevant literature that motivated the thesis questions that guide this work. Chapter 2 provides a brief overview of plasmas relevant to the understanding of the operation of MS HETs and pole erosion. Chapter 3 outlines the LTS and LRS models, data pre-processing, and signal inversion via least squares and Bayesian inference. Chapter 4 outlines the implementation of the tabletop plasma cell and LTS system used to estimate the number density detection limit. Chapter 5 outlines the implementation of the large vacuum test facility LTS system and its benchmarking using a hollow cathode plasma source. Chapter 6 outlines the modification of the large vacuum test facility LTS system and the data collected to answer the thesis question. Chapter 7 concludes the thesis and provides avenues for future work

CHAPTER 2
PLASMA AND HALL EFFECT THRUSTER BACKGROUND

2.1 Introduction

This chapter details the background required to understand the operation of MS HETs. First is an overview of fundamental plasma physics. Then, the physics of MS HETs are discussed.

2.2 Overview of Fundamental Plasma Physics

2.2.1 Governing Equations of a Plasma

A plasma is, on average, a quasi-neutral ensemble of charged particles that exhibit collective behavior [81]. Plasmas have the tendency to, on time scales much larger than the perturbation of interest and on length scales larger than the Debye length, maintain quasi-neutrality and shield out any and all perturbations to the bulk plasma via a plasma sheath. These phenomena are formalized in Subsubsection 2.2.2 after the governing equations are defined.

The collective behavior of plasmas arises from short-range interactions, on the length scales of the collision cross-sections, via collisions among the particles and long-range electromagnetic interactions, on the order of the Debye length, that depends on the instantaneous behavior of each individual charged particle in the plasma [81].

To precisely determine the state of a plasma, the configuration of the system of particles, each denoted by i in the volume of interest V must be known and propagated forward using Newton's second law and the Lorentz force, making each i^{th} individual particle's configuration in time, t, a function of every other particle's configuration. This is often expressed as

$$\mathbf{x}_i(t), \mathbf{u}_i(t) = f\left(\mathbf{B}\left(\mathbf{x}_i(t), \mathbf{u}_i(t)\right), \mathbf{E}\left(\mathbf{x}_i(t), \mathbf{u}_i(t)\right)\right) \; \forall i \in V, \tag{2.1}$$

with $\mathbf{x}_i(t)$, $\mathbf{u}_i(t)$, $\mathbf{B}(\mathbf{x}_i(t), \mathbf{u}_i(t))$ and $\mathbf{E}(\mathbf{x}_i(t), \mathbf{u}_i(t)))$ being the position and velocity of each particle, respectively and the resulting electric and magnetic fields resulting from the position and velocity of each particles configuration. For a system of more than a few hundred particles, this kinetic approach becomes intractable. Instead, a statistical approach, characterizing the density of particles at each point in space as a function of time, provides a more tractable framework and forms the basis upon which plasmas are studied. The function that describes this density of each class of particles denoted by α is the distribution function, $f_\alpha(\mathbf{x}, \mathbf{u}, t)$. The number of particles in the phase space volume, or point in space-time, $\mathbf{x} + \mathbf{dx}, \mathbf{v} + \mathbf{dv}$ at time t is $f_\alpha(\mathbf{x}, \mathbf{u}, t)\mathrm{d}\mathbf{x}\mathrm{d}\mathbf{u}$ [32, 109]. The species distribution functions provide a more detailed description than a fluid approach, which involves statistical moments over the distribution functions, but provides a less detailed description than the kinetic approach in Equation 2.1. In EP, the fundamental quantities of interest are the species distribution functions [33, 38]. These functions form the basis for all other desired quantities of interest, like species temperature and number density, T_α and n_α, for example.

The relationship that describes the time rate change of the species distribution function is known as the Boltzmann equation,

$$\frac{\partial}{\partial t} f_\alpha(\mathbf{x}, \mathbf{u}, t) + \mathbf{u}_\alpha \cdot \frac{\partial}{\partial t} f_\alpha(\mathbf{x}, \mathbf{u}, t) + \mathbf{a}_\alpha \cdot \frac{\partial}{\partial t} f_\alpha(\mathbf{x}, \mathbf{u}, t) = \sum_{\sigma_i} C_{\alpha/\sigma_i}(f_{\alpha_i}). \tag{2.2}$$

This relationship states that the total time derivative in phase space for the particle species α is equal to the sum of the effect of the collisions on particles α from all other particles σ_i, quantified via the collision operator $\sum_{\sigma_i} C_{\alpha/\sigma_i}(f_{\alpha_i})$. The collision operator in the Boltzmann equation has several different models and must adhere to several constraints,

all detailed in Chapter 2 of [32]. However, the a fluid-like approach via velocity moments of the Boltzmann equation yield equations that are more tractable for the understanding of the relevant HET processes. Velocity moments of the Boltzmann equation lead to a set of fluid equations for each species. In this context, a velocity moment is the integral over velocity space of the product of the Boltzmann equation and the velocity raised to the k^{th} power. The detailed derivation of the fluid equations can be can be found in [32]. The zeroth velocity moment of the Boltzmann equation yields the continuity equation,

$$\frac{\partial}{\partial t} n_\alpha + \nabla \cdot (n_\alpha \mathbf{u}_\alpha) = 0, \tag{2.3}$$

the first velocity (tensor) moment yields the momentum equation,

$$m_\alpha [\frac{\partial}{\partial t}(n_\alpha \mathbf{u}_\alpha) + \mathbf{u}_\alpha \nabla \cdot (n_\alpha \mathbf{u}_\alpha)] = n_\alpha q_\alpha [\mathbf{E} + \mathbf{u}_\alpha \times \mathbf{B}] - \nabla \cdot (\mathbf{P} - \mathbf{T}_{\alpha/\sigma}), \tag{2.4}$$

and the second scalar moment yields the energy equation, the unclosed version of which we will ignore for the moment. A general property of these moments is that each k^{th} moment contains a $(k+1)^{\text{th}}$ moment.

The forms presented above are unclosed. Assuming a thermalized, isotropic pressure closure for the pressure tensor, $\mathbf{P}$, and modeling the viscosity tensor, $\mathbf{T}_{\alpha/\sigma}$, using a frictional-like collision that is dependent on the collision frequencies between species and their relative velocities yields the final forms of our governing equations,

$$\nabla \cdot \mathbf{P} = \nabla P = \nabla (n_\alpha k_{\text{b}} T_\alpha) \tag{2.5}$$

$$\nabla \cdot \mathbf{T}_{\alpha/\sigma} \equiv \mathbf{R}_{\alpha/\sigma} = \sum_\sigma \nu_{\alpha/\sigma} m_\alpha m_\alpha (\mathbf{u}_\alpha - \mathbf{u}_\sigma) \tag{2.6}$$

$$\frac{\partial}{\partial t} n_\alpha + \nabla \cdot (n_\alpha \mathbf{u}_\alpha) = 0, \tag{2.7}$$

$$m_\alpha n_\alpha [\frac{\partial}{\partial t}(\mathbf{u}_\alpha) + \mathbf{u}_\alpha \cdot \nabla(\mathbf{u}_\alpha)] = n_\alpha q_\alpha [\mathbf{E} + \mathbf{u}_\alpha \times \mathbf{B}] - \nabla P - \mathbf{R}_{\alpha/\sigma}, \tag{2.8}$$

and

$$\frac{3}{2} q_\alpha n_\alpha \frac{\partial}{\partial t} T_\alpha + \frac{3}{2} \nabla \cdot (q_\alpha n_\alpha \mathbf{u}_\alpha T_\alpha) - \frac{3}{2} q_\alpha T_\alpha \nabla \cdot (n_\alpha \mathbf{u}_\alpha) + q_\alpha n_\alpha T_\alpha \nabla \cdot (\mathbf{u}_\alpha) - \nabla \cdot (k_\alpha \nabla T_\alpha) = \sum_\sigma Q_{\alpha/\sigma}, \tag{2.9}$$

with $Q_{\alpha/\sigma} = -\mathbf{R}_{\alpha/\sigma} \cdot (\mathbf{u}_\alpha - \mathbf{u}_\sigma)$. In these equations, $k_\mathrm{b}, m_\alpha, n_\alpha, q_\alpha$ and T_α are the Boltzmann constant, mass, number density, charge, and equilibrium temperature of the species α. Additionally, $\nu_{\alpha/\sigma}$ is the collision frequency of the species α with species σ.

These governing equations, along with Maxwell's equations,

$$\nabla \cdot \mathbf{E} = \frac{\rho}{\epsilon_\mathrm{o}} \tag{2.10}$$

$$\nabla \times \mathbf{E} = -\frac{\partial}{\partial t} \mathbf{B} \tag{2.11}$$

$$\nabla \cdot \mathbf{B} = 0 \tag{2.12}$$

$$\nabla \times \mathbf{B} = \frac{1}{c^2} \frac{\partial \mathbf{E}}{\partial t} + \mu_\mathrm{o} \mathbf{J} \tag{2.13}$$

form the basis for phenomena of interest including thermalized potential, Debye shielding and plasma sheaths. In Maxwell's equations, $\rho, \epsilon_\mathrm{o}, \mu_\mathrm{o}, c$ and $\mathbf{J}$ are the charge density, vacuum permittivity, vacuum permeability, speed of light, and the current density, respectively.

2.2.2 Plasma Parameters

Several parameters are necessary to define the state of each species in a plasma, α , as seen in the equations presented in Subsection 2.2.1. However, these parameters do not describe the collective behavior of a plasma. In order to describe collective plasma behavior and observable phenomena/structures in confined plasmas, such as Debye shielding and plasma sheaths, definitions of Debye length and plasma frequency are necessary. Figure 2.1

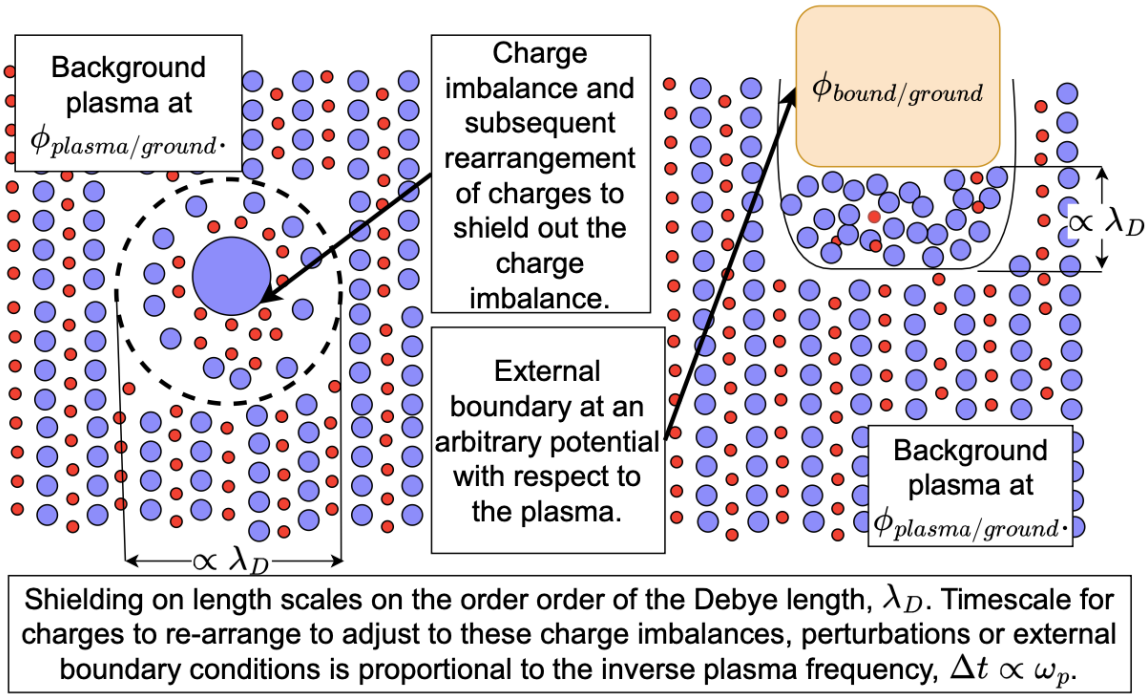

Figure 2.1: Notional illustration of Debye shielding and plasma sheaths in a plasma.

illustrates the Debye shielding phenomenon with a notionally uniform background plasma, whereupon there is a charge imbalance (left) and external boundary (right). In the charge imbalance case, the charges rearrange to shield out the imbalance from the bulk plasma. In the external boundary case, a sheath forms to shield the bulk plasma from the external boundary [86].

Debye Length, Plasma Frequency and Quasineutrality

Debye shielding is the tendency of a plasma to shield out charge imbalances and external boundary conditions via the rearrangement of its charged particles. The phenomena happen over a characteristic length scale known as the Debye length. See Appendix A.1 of [86] for a full derivation. Expressing the charge density in the plasma as the sum of the individual charge densities of each species as yields a relationship between the charge density and the electrostatic potential, ϕ, as

$$\nabla^2\phi = -\frac{1}{\epsilon_o}\sum^{\alpha}(q_\alpha n_\alpha). \tag{2.14}$$

The integral of Equation 2.23 substituted into Equation 2.14 with a Taylor expansion in the resulting exponential term yields

$$\nabla^2\phi = \sum^{\alpha}\left(\frac{n_{\alpha_o}q_\alpha^2}{\epsilon_{\rm o}k_{\rm b}T_\alpha}\right)\phi. \tag{2.15}$$

The term in the parenthesis has units of length^{-2} and is used to define the Debye length as

$$\lambda_{\rm D} \equiv \sqrt{\sum^{\alpha}\lambda_{{\rm D}_\alpha}^2}, \tag{2.16}$$

which contains the sum of the contributions from all species,

$$\lambda_{{\rm D}_\alpha} \equiv \sqrt{\frac{\epsilon_{\rm o}k_{\rm b}T_\alpha}{n_{\alpha_o}q_\alpha^2}}. \tag{2.17}$$

In the literature, Debye length is often synonymous with the electron Debye length, $\lambda_{{\rm D}_e}$.

Charges rearrange in order to maintain quasi-neutrality on time scales greater than the inverse of characteristic frequencies, known as the plasma frequencies. Typically, the fastest of these frequencies is the electron plasma frequency. Assuming a collisionless plasma with no pressure gradients, using Equation 2.7 and Equation 2.8 for the electron population, Equation 2.10, and introducing a perturbation to the number density as $n_\alpha = n_{\alpha_o} + \Delta n_\alpha$ yields a linear ordinary differential equation in time that takes the form of an undamped harmonic oscillator for Δn_α as

$$\frac{\partial^2}{\partial t^2}\Delta n_\alpha + \frac{n_{\alpha_o}q_\alpha^2}{m_\alpha\epsilon_o^2}\Delta n_\alpha = 0 \tag{2.18}$$

The characteristic frequency for the perturbation to the number density is defined as the plasma frequency for species α,

$$\omega_{p_\alpha} \equiv \sqrt{\frac{n_{\alpha_o}q_\alpha^2}{m_\alpha\epsilon_o^2}}. \tag{2.19}$$

The formulation in Equation 2.18 is physically akin to displacing a slab of electrons in a plasma ever so slightly; the result would be a slab of electrons oscillating in the relatively stationary ion background [86].

When the time scales of the phenomena of interest are larger than the inverse plasma frequency, and when the length scales of interest are much larger than the Debye length, the plasma quickly shields out charge imbalances via externally imposed boundary conditions or perturbations and the bulk plasma is quasineutral,

$$\sum^{\alpha} n_\alpha q_\alpha = 0. \tag{2.20}$$

Quasineutrality is maintained away from plasma boundaries. However, near debye shielded boundaries plasmas sheaths form. The plasma sheath is the name given to the non-quasineutral layer that forms at the Debye-shielded boundary of a confined plasma [86]. The sheath separates and forms the plasma transition from the bulk plasma to the boundary. Plasma sheaths form at the non-plasma boundaries of HETs like the walls of the discharge channel and the front pole covers. Because the plasma sheath is non quasineutral, electric fields accelerate charges to and from the relevant non-plasma boundary. See Section 2.2 of Reference [86] for a detailed description.

2.3 Potential Profiles in Hall Effect Thrusters

Figure 2.2 illustrates notional potential profiles in an US HET. The potential contours begin at the anode, with the darkest magenta line, and get lighter, illustrating the drop in the magnitude of the potential contours. Arrows, indicating the electric field direction as the gradient of an assumed electrostatic potential (Equation 2.22).

As mentioned in Section 1.2, the plasma processes that govern HET performance are highly dependent on the potential profile in the vicinity of the exit plane of a HET [14]. The spatial structure and magnitude of the potential profile influence the beginning and

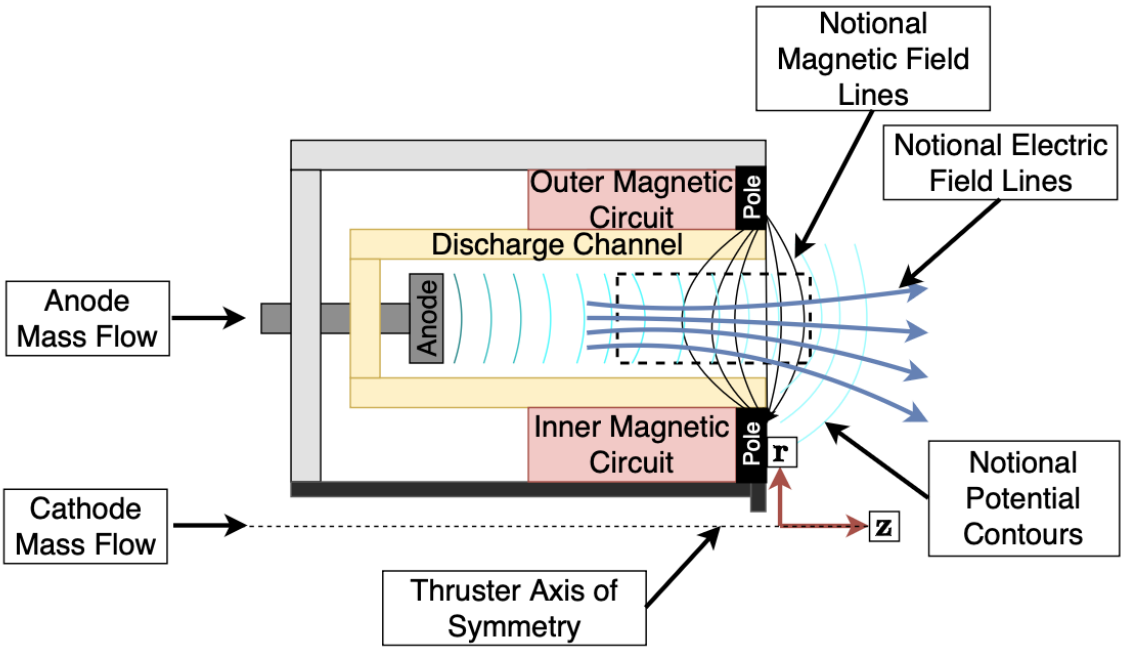

Figure 2.2: Notional HET potential profiles form the anode in dark cyan to the discharge channel exit plane in cyan. Electric field lines in blue point in the notional direction of ion acceleration.

end, extent, and uniformity of the acceleration region. These profiles, as in [14] have been traditionally measured with electrostatic probes. However, as shown in [21], segmented electrodes placed in the near field plume significantly affect the plasma potential profiles, in turn affecting the plasma plume divergence angle. A two-fluid-based plasma model with thermalized potential helped to explain the observed phenomena in the vicinity of these segmented electrodes, that was also in the vicinity of approximately radial electric fields.

For the electron population, assuming a collisionless plasma with negligible electron momentum in 1D along a magnetic field line, the electron momentum conservation equation, Equation 2.8, becomes

$$\mathbf{E} = \frac{1}{q_e n_e} \nabla P_e \tag{2.21}$$

Assuming no temperature gradients along the magnetic field line and an electrostatic electric field such that

$$-\mathbf{E} = \nabla\phi, \tag{2.22}$$

yields

$$\nabla\phi = -\frac{k_\mathrm{b}T_\mathrm{e}}{e}\frac{\nabla n_\mathrm{e}}{n_\mathrm{e}}. \tag{2.23}$$

Equation 2.23 is the quantitative relationship between the number density gradient and the isothermal magnetic lines of force. In the low temperature case, the field lines are expected to be lines of constant temperature and approximately constant potential. The validity of these assumptions has been shown to break down with small deviations from radial magnetic field lines. Temperature gradients along these non-radial magnetic field lines lead to electron current along the field lines that form electron temperature contours that do not track the magnetic field contours and can therefore not be isothermal [26]. Reference [64] discusses the domain of applicability for the thermalized potential model, concluding that in the case of non-uniform magnetic fields or non-constant temperature field lines, the thermalized potential model is not applicable.

To date, evidence of erosion of the front-facing magnetic pole region of magnetically shielded HETs has been observed, but models that reproduce a thermalized potential via approximately isothermal magnetic field lines fail to predict accurate erosion rates without calibration. These models have been used since the discovery of the magnetic shielding effect detailed in Section 2.4. During qualification life tests of the BPT-4000 thruster, discharge channel erosion rates were found to have stopped after 5600 hours of testing [52]. Investigations of the cause of this phenomenon using thermalized potential-based 2D simulation on a magnetically field-aligned mesh led to the discovery of the magnetic shielding effect [52, 60].

2.4 Magnetically Shielded Hall Effect Thrusters

The allure of HETs for space missions stems from their mass utilization efficiency. However, US HETs suffer from channel erosion as their life-limiting factor. High electron temperature plasma close to the wall, and deviation from equipotentialization perpendicular to the channel walls accelerate ions into the channel via potential gradients that form along magnetic field lines and through the channel wall sheath potential [36, 144]. The erosion of the channel walls in US HETs exposes the interior of the HETs to the plasma, destroying the magnetic circuit that is critical for operation. This effectively limits the useful life of US thrusters to about 10,000 hours. Magnetic shielding reduces these erosion rates by 2-3 orders of magnitude [66, 121].

The design of the magnetic field lines near the walls of MS HETs preserves equipotentialization at potentials near the discharge potential, reducing ion bombardment. This equipotentialization of the magnetic field lines of force in the channel keeps the plasma potential in the channel near the discharge potential and the electron temperature low due to the topology of the wall grazing magnetic field lines; this leads to induced electric field lines that are approximately perpendicular to the wall, minimizing ion bombardment [77, 78]. This is different from other attempts at leveraging magnetic fields to shield the channel walls, including magnetic mirrors [50]. The MS HET theory presented in [78] was validated in a companion paper that detailed the experiments on a retrofit of the H6 US thruster into the H6MS, a magnetically shielded H6 variant [73].

The wall grazing magnetic field lines, which extend into the anode region with low electron temperature keeps the electron temperature along the wall low and the potential high, near the discharge potential. This leads to an almost fully perpendicular electric field near the wall. Given that the grazing field line is parallel to the wall, the electric field / potential shields the wall from high-energy ions. Figure 2.3 details the phenomena described above.

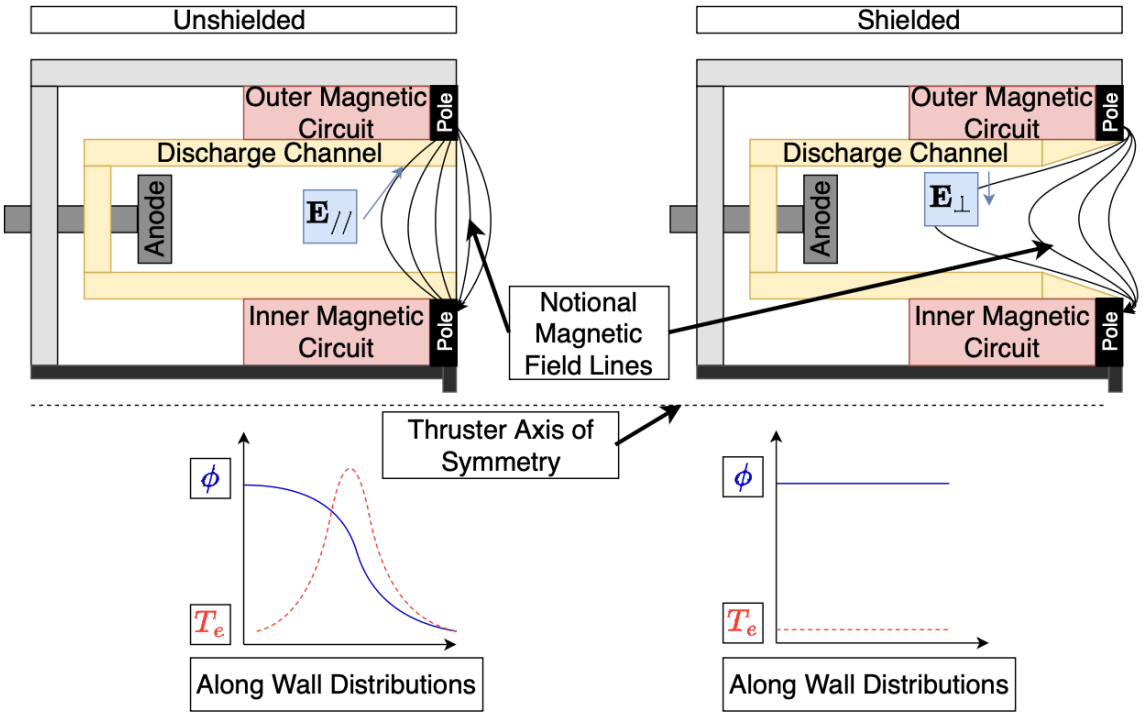

Figure 2.3: Notional effect of magnetically shielding the channel walls.

Thermalized potential in the thruster discharge channel is a key design goal of magnetically shielded HETs [51, 57, 59]. However, the validity of the thermalized potential model outside the discharge channel, specifically near the discharge channel exit plane, has not been studied extensively.

2.5 Magnetically Shielded Thruster Pole Erosion

Pole erosion is the wear of the front-facing inner pole region due to ion bombardment. MS HETs effectively shield the channel walls from ion bombardment, reducing the rate of channel erosion and effectively eliminate channel erosion as the life-limiting factor for MS HETs. However, this leads secondary mechanisms, such as pole erosion that occur at much slower rates, to emerge as the primary life-limiting concern.

Pole erosion was first observed after unexpected sputtering of the magnetic pole during wear tests of the H6MS [65]. Investigations have shown that the largest surface topography changes occurred at the point where the field lines terminate near the front magnetic pole,

as measured by electrostatic probes [71]. However, the mechanisms that caused the ions to accelerate towards the pole were contested between a potential that can accelerate ions to the pole from the discharge region or near pole plasma heating due to plasma instabilities. LIF, surface mounted and translating probes confirmed the acceleration of ions towards the pole [90]. The ion flux was found to originate in the vicinity immediately adjacent to the pole, being comprised of low-velocity ions that were not accelerated with the bulk of the beam ions, validating predictions made in [79]. LIF measurements and comparisons with numerical simulations in [147] confirm that plasma conditions in the near pole region can excite instabilities in the lower hybrid frequency (LHF) range. An idealized model developed to scale the ion velocity distribution function (IVDF) with the LHF brought erosion rates at the inner pole close to wear test measurements, indicating that instabilities may play a role in the erosion of the front pole.

It was speculated, but not confirmed, in [90] that a lower population of higher energy ions was also accelerated towards the pole with high kinetic energy due to shifts in the acceleration region caused by magnetic shielding. A 2D plasma simulation predicted that plasma potential contours at the channel edge can accelerate high-energy ions from the edge of the acceleration region to the pole surface [133]. It was also predicted that pole erosion is not unique to MS thrusters but a phenomenon in all HETs. However, larger potentials due to MS at the thruster exit plane as a result of the movement of the acceleration zone are predicted to exacerbate the pole erosion in MS HETs [157].

Bimodal IVDFs, measured with time-averaged LIF, confirmed the sensitivity of the location acceleration region to discharge voltage, background pressure and magnetic field strength. Changing the location of the acceleration zone affects front pole erosion by changing the location of high and low-energy ions that can be accelerated to the pole [113]. Time-resolved LIF measurements of IVDFs using a transfer function averaging method were used to investigate these complex IVDFs in the beam edge region of an MS HET, were the pole-erosion-causing ions are believed to originate [143].

At present, state-of-the-art near-field measurements leverage laser-based diagnostics, mostly LIF, due to the large perturbations introduced to the discharge characteristics by virtue of electrostatic probes [88]. LIF has been shown to provide accurate spatially and temporally resolved measurements of the ion dynamics in the near-field plume of MS HETs. However, the role electrons play in the near-field plasma dynamics has not been investigated extensively. Incoherent LTS in two low-power HET architectures, MS and US, confirmed the shift of the acceleration region in the MS thruster case and observed larger-than-expected electron temperatures that can be linked to plasma instabilities [152]. Despite this, the role that electrons play in the potential structures that accelerate ions toward the front pole in high-power MS HETs is still unclear. High electron temperatures and densities in this region prohibit accurate investigations using electrostatic probes. Instead, incoherent LTS will be used to measure the electron properties in the near-field plume of a high-power MS HET. Fundamentals of incoherent LTS are presented in Section 3.2

CHAPTER 3

LASER THOMSON SCATTERING PHYSICS AND SIGNAL ANALYSIS VIA LEAST SQUARES AND BAYESIAN INFERENCE

3.1 Introduction

This chapter presents the physics of LTS and LRS as well as the model equations necessary to invert pre-processed LRS and LTS spectra. First, the models are presented. Matrix optics and the general procedure for sizing the collection and detection optics are presented as well as determining the system solid angle. Then, the appropriate parameterizations for least squares inversion and Bayesian inference are presented. Then, least squares inversion and uncertainty quantification are presented. Then, the Bayesian inference and model selection framework is presented.

3.2 Scattering of Electromagnetic Radiation

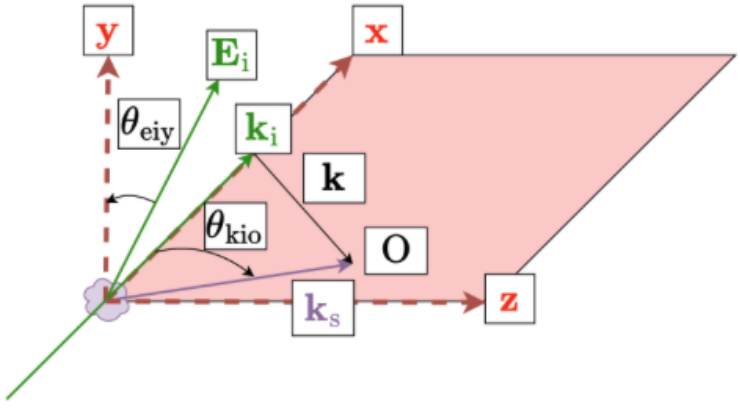

Figure 3.1: General scattering wave orientation in a scattering experiment.

Incident radiation interacts with matter, accelerating the charges in the matter, which leads to the re-radiation, consistent with the differential scattering cross-section of the mat-

ter for the scattering process of interest. Scattered power intensity is directional, and the characteristics of the scattered radiation are dependent on the reference frame and direction of observation, all of which are wrapped into the differential scattering cross-section. Figure 3.1 depicts the scattering configuration with all relevant angles and vector orientations that appear in the description of our scattering model equations.

We are interested in the spectrally-distributed total scattered power per pulse/shot of incident radiation, averaged over an accumulation of shots. For detailed derivations, see Refs. [7, 20, 30, 47, 58, 105]. The general equation representing the spectrally distributed total scattering signal in units of counts per nm is

$$P_\lambda = \underbrace{\underbrace{\underbrace{\eta \frac{\lambda_\mathrm{i}}{hc} \Delta\Omega \, L \, E_\mathrm{i}}_{\mathrm{I}} \, n \frac{\partial\sigma}{\partial\Omega}(\lambda)}_{\mathrm{II}} \, S(\lambda)}_{\mathrm{III}}, \tag{3.1}$$

where η is the intensified photoelectron to scattered photon calibration constant, λ_i is the incident wavelength, h is the Planck constant, c is the speed of light, $\Delta\Omega$ is the solid angle of collection, L is the length of the probe volume, E_i is incident laser energy, n is the scatterer number density, $\partial\sigma/\partial\Omega$ is the scattering cross section per unit solid angle, and S is the spectral redistribution function. λ_i/hc gives the photons per joule at the incident wavelength. The braces denote (I) the leading constants that are often grouped as "system calibration constant", C_sys; (II) the magnitude of the scattered power, and (III) the total scattered power, which is redistributed spectrally due to broadening mechanisms. The differential scattering cross section per unit solid angle contains all of the physics of the scattering of interest. The wavelength dependence of the scattering cross section and spectral distribution function is explicitly stated in Equation 3.1, but is omitted in the rest for compactness. We discuss the relevant rotational Raman and Thomson scattering in the following subsections.

3.2.1 Rotational Raman Scattering

Laser rotational Raman scattering (LRS) is necessary in order to calibrate the absolute electron number density measurements in an LTS experiment. LRS is the inelastic scattering of incident radiation from polyatomic molecules as the result of a net exchange of energy from the incident radiation and the internal energy modes of the molecule[20, 105]. For a diatomic molecule, its rotational selection rules for the possible transitions in the rotational quantum number J follow $J' = J \rightarrow J \pm 2$ for Stokes (+) and anti-Stokes (-) transitions, respectively. [12, 25]. It can be shown (see Refs. [2, 20]) that the rotational Raman scattering cross section is the sum of the Stokes and anti-Stokes cross sections as

$$\frac{\partial \sigma^{\mathrm{R}}}{\partial \Omega} = \sum_{J} \frac{\partial \sigma^{\mathrm{R}}}{\partial \Omega}_{\text{ Stokes}} + \sum_{J} \frac{\partial \sigma^{\mathrm{R}}}{\partial \Omega}_{\text{ anti-Stokes}}. \tag{3.2}$$

The Stokes and anti-Stokes cross sections, $\frac{\partial \sigma}{\partial \Omega}_{J'}$, relate the perpendicular scattering cross sections $\frac{\partial \sigma}{\partial \Omega}^{\perp}_{J'}$, to the population faction $\frac{n_J}{n_{\mathrm{g}}}$, through

$$\frac{\partial \sigma}{\partial \Omega}_{J'} = \frac{n_J}{n_{\mathrm{g}}} \left\{ (1-\rho) \cos^2(\zeta) \left[1 - \cos^2(\theta_{\mathrm{kio}}) \sin^2(\theta_{\mathrm{eiz}}) \right] + \rho \right\} \frac{\partial \sigma}{\partial \Omega}^{\perp}_{J'}. \tag{3.3}$$

In Equation 3.3, ρ, ζ, θ_{kio}, and θ_{eiz} are the depolarization ratio, the angle between the polarization of the scattered Raman radiation and the incident radiation, the angle between the incident radiation propagation direction and the direction of scattering observation, and the angle between the incident radiations polarization and the $\mathbf{z}$ axis, in Figure 3.1, respectively.

The ratio of the Jth population level (n_J) to the total number density of particles (n_{g}) is quantified through the partition function as

$$\frac{n_J}{n_{\mathrm{g}}} = \frac{1}{Q_{\mathrm{g}}} g_J (2J+1) \exp\left[-\frac{\epsilon_J(J)}{k_{\mathrm{B}} T_{\mathrm{g}}} \right]. \tag{3.4}$$

The perpendicular Raman cross section, $(\partial\sigma/\partial\Omega)^{\perp}_{J'}$, is

$$\frac{\partial\sigma}{\partial\Omega}^{\perp}_{J'} = \frac{64\pi^4}{45}\frac{\gamma^2}{\epsilon_{\mathrm{o}}^2}\frac{b_{J'}}{\lambda_{J'}^4}, \tag{3.5}$$

with g_J being the nuclear spin degeneracy and depends on whether the value of J is even or odd. For nitrogen, g_{J} is equal to 3 and 6 when J is odd or even, respectively. Similarly, for oxygen, g_{J} is equal to 1 and 0 when J is odd or even, respectively.

The anisotropy of the molecular polarizability tensor, $\gamma^2/\epsilon_{\mathrm{o}}^2$, is linearly interpolated from experimental measurements at the frequency of interest, as is typical in Refs. [2, 28, 140]. The rotational energy mode, rotational partition function, ideal gas law, Placzek-Teller coefficients, and Raman scattering wavelengths are

$$\epsilon_J(J) = hc\left[B_{\mathrm{g}}J\left(J+1\right) - D_{\mathrm{g}}J^2\left(J+1\right)^2\right], \tag{3.6}$$

$$Q_{\mathrm{g}} = \frac{\left(2I_{\mathrm{g}}+1\right)^2 k_{\mathrm{B}}\,T_{\mathrm{g}}}{2B_{\mathrm{g}}hc}, \tag{3.7}$$

$$p_{\mathrm{g}} = n_{\mathrm{g}}\,k_{\mathrm{B}}\,T_{\mathrm{g}}, \tag{3.8}$$

$$b_{J'}(J) = \frac{3}{8}\frac{(2J+1\pm1)(2J+1\pm3)}{(2J+1)(2J+1\pm2)}, \tag{3.9}$$

and

$$\lambda_{J'}(J) = \lambda_{\mathrm{i}} \pm \lambda_{\mathrm{i}}^2 B_{\mathrm{g}}(4J+2\pm4), \tag{3.10}$$

respectively. B_{g} and D_{g} are the molecular rotation constant and centrifugal distortion constants, respectively, and they both depend on the gas species. $B_{\mathrm{g}} = 199$ m^{-1} for nitrogen and 143.8 m^{-1} for oxygen. $D_{\mathrm{g}} = 5.7{\times}10^{-4}$ m^{-1} for nitrogen and 4.8×10^{-4} m^{-1} for oxygen. T_{g} and k_{b} are the equilibrium scattering gas temperature and Boltzmann constant.

In the case of rotational Raman scattering, we assume the only relevant source of spectral redistribution is due to the finite detection optics, spectrometer, and detection system –

commonly referred to as the instrument function – because Doppler and pressure broadening are negligible. We assume that this (integral normalized) function can be modeled by a Gaussian probability density function, resulting in a spectral redistribution function

$$S^{\mathrm{R}}(\lambda_{J'}, \lambda_{\mathrm{i}}, \tau) = \frac{1}{\sqrt{2\pi}\sigma_{\mathrm{if}}(\tau)} \exp\left[-\frac{1}{2}\left(\frac{\lambda_{\mathrm{i}} - \lambda_{J'}}{\sigma_{\mathrm{if}}(\tau)}\right)^2\right]. \tag{3.11}$$

Traditionally, instrument functions are described with full-width half maximums (FWHM), τ. Here, τ is one of the parameters fit using least squares to the LRS spectrum (see below) and is not independently measured. We can relate this to the Gaussian instrument function width σ_{if} via

$$\sigma_{\mathrm{if}}(\tau) = \frac{\tau}{2\sqrt{2\log(2)}}. \tag{3.12}$$

In the Raman case, given that we model this as the only source of broadening, the redistribution operation becomes a simple convolution. However, given that each Raman transition produces a single intensity at the particular Raman wavelength, we are mathematically convolving a Gaussian with a Dirac delta function at each transition. As such, the convolution is simply the peak intensity of the Raman line multiplied by the instrument function Gaussian centered at that Raman transition wavelength. Hence, we can explicitly state the expected Raman signal, in photon counts per nm, for a single species indexed by χ_j, as

$$P_{\lambda}^{\mathrm{R}}|_{\chi_j} = \eta \frac{\lambda_{\mathrm{i}}}{hc} \Delta\Omega \, L \, E_{\mathrm{i}} \, n_{\chi_j}(T, p_{\chi_j}) \left[\sum_J \frac{\partial \sigma^{\mathrm{R}}}{\partial \Omega}_{J'}\right]_{\chi_j} S_{\lambda}^{\mathrm{R}}(\lambda_{J'}, \tau)\,, \tag{3.13}$$

We are interested in LRS from air and pure nitrogen. For the case of air (modeled as a

two-component mixture of N_2 and O_2),

$$P_\lambda^{\mathrm{R}}\left(\mathbf{x}^{\mathrm{R}}, \boldsymbol{\theta}^{\mathrm{R}}\right) = \eta \frac{\lambda_{\mathrm{i}}}{hc}\, \Delta\Omega\, L\, E_{\mathrm{i}}\, n_{\mathrm{g}}(T_{\mathrm{g}}, p_{\mathrm{g}}) \left[\gamma_{\mathrm{N}_2} \left[\sum_J \frac{\partial \sigma^{\mathrm{R}}}{\partial \Omega}_{J'} \right]_{N_2} + \gamma_{\mathrm{O}_2} \left[\sum_J \frac{\partial \sigma^{\mathrm{R}}}{\partial \Omega}_{J'} \right]_{O_2} \right] S_\lambda^{\mathrm{R}}(\lambda_{J'}, \tau)\,, \tag{3.14}$$

with $\gamma_{\mathrm{N}_2} = .79$ and $\gamma_{\mathrm{O}_2} = 0.21$. In the case of only nitrogen, $\gamma_{\mathrm{N}_2} = 1$ and $\gamma_{\mathrm{O}_2} = 0$ Here, we explicitly call out the dependencies of P_λ^{R} on the quantities of interest (QoI) in our calibration measurements ($\mathbf{x}^{\mathrm{R}}$) and so-called nuisance parameters (θ^{R}) that influence the scattered power but are not of primary interest to the measurement, via

$$\mathbf{x}^{\mathrm{R}} = [\eta, \lambda_{\mathrm{i}}]^\top \quad \text{and} \quad \theta^{\mathrm{R}} = [T_{\mathrm{g}}, p_{\mathrm{g}}, \tau]^\top . \tag{3.15}$$

In this formulation, the neutral gas temperature is estimated from the fit to the data using the width of the LRS spectrum, the FWHM is fit with respect to the width of the LRS linewidths, the efficiency constant is fit to the amplitude of the LRS spectrum and the data, and finally, the center wavelength is fit with respect to the center of the spectrum.

3.2.2 Incoherent Thomson Scattering

LTS is the elastic electromagnetic scattering of incident radiation from unbounded charged particles and can be coherent or incoherent. Sections 2.2 and 2.4 in Refs. [28, 140] respectively discuss the cases in which the experimental setup and plasma conditions meet the conditions for coherent Thomson scattering. In this work, we consider only incoherent LTS.

For LTS, the wavelengths of the scattered radiation are consistent with the Doppler shifted motion of the individual electrons along the scattering wave vector $\mathbf{k}$; see Chapters 1 and 4 of Ref. [47] and Chapter 2 of Ref. [140] for details. It can be shown that the electron

Thomson scattering cross section is

$$\frac{\partial \sigma^{\mathrm{T}}}{\partial \Omega} = r_{\mathrm{e}}^2 \left[1 - \cos^2(\theta_{\mathrm{kio}}) \sin^2(\theta_{\mathrm{eiy}})\right], \tag{3.16}$$

with the classical electron radius being approximately 2.8179×10^{-15} m. For LTS, the redistribution of the total scattered power is dominated by two wavelength shifts caused by the relative motion of each scattering electron with respect to the observer of the scatter [47]. This is directly linked to the relative velocity of the observer and the scattering electron along the scattering wave vector, $\mathbf{k} \equiv \mathbf{k}_{\mathrm{i}} - \mathbf{k}_{\mathrm{s}}$, with $\mathbf{k}_{\mathrm{i}}$ being the incident propagation wave vector and $\mathbf{k}_{\mathrm{s}}$ being the wave vector along the direction from the scattering volume to the observer. To avoid confusion, the spectral distribution function is explicitly labeled with k to indicate that it is along the direction of the scattering wavevector, in whatever unit vector basis is used to define these vectors. For an ensemble of electrons, this spectral distribution shape function is directly related to the EVDF along the scattering wave vector, f_k. This distribution happens over tens of nm, an order of magnitude or greater than that of the instrument function broadening, justifying why that contribution to the broadening is often neglected, as is done here. Given this, the total scattered power is redistributed over the electron velocity distribution function along the scattering wave vector. The relationship between the spectral distribution function along the scattering wave vector and the velocity distribution function is $S_{\mathrm{k}}(\lambda) = \frac{1}{k} f_{\mathrm{v_k}}(\lambda)$. For a plasma whose electron population is in thermal equilibrium, $S_{\mathrm{k}}(\lambda)$ corresponds to a Maxwellian electron velocity distribution function (EVDF) that can be related to the equilibrium electron temperature T_{e} . In the case of a non-equilibrium plasma, there are several analytical models that can be applied, including bi-Maxwellian and Druyvesteyn distributions. A brief description of these candidate submodels is presented below.

3.2.3 Maxwellian, Druyvesteyn and Generalized Single Dimensional Electron Velocity Distribution Function Submodels

As stated above, electrons adopt a Maxwellian EVDF in the thermal equilibrium case. This is a solution to the Boltzmann equation in which the net effect of any collisional process between like and unlike molecules is zero, regardless of the collision mechanism [3]. This is encountered in plasmas with high degrees of ionization and collisionality [140]. In this case, the classical electron temperature is the full descriptor for the shape of the distribution. The Druyvesteyn EVDF is a non-equilibrium distribution that describes plasmas where the low degree of ionization and non-constant collision frequency among the electrons. In the Druyvesteyn case, the effective electron temperature is defined from a mean energy calculation determined from moments of the EVDF distribution function.

In the more general case, a cumulative energy distribution function (CEDF) that interpolates between the Maxwellian and Druyvesteyn distributions parameterized by d, T_{eV} and a function of the electron energy in eV [5, 46, 93, 103] is

$$F(E_{\mathrm{eV}}) = c_1(d)\, T_{\mathrm{eV}}^{-3/2} \sqrt{E_{\mathrm{eV}}} \exp\left\{ \left[-c_2(d) \left(\frac{E_{\mathrm{eV}}}{T_{\mathrm{eV}}} \right)^d \right] \right\}, \tag{3.17}$$

with c_1 and c_2 being functions of gamma functions of d.

This CEDF has been used extensively to assess the degree of departure from a Maxwellian distribution in electrostatic probe data, quantified through the parameter d. At $d = 1$, Equation 3.17 is the CEDF of a Maxwellian, and at $d = 2$ it is one of a Druyvesteyn. The conversion between this CEDF, and the PDF function required in order to cast the spectral distribution function from the eV domain to the nm domain, with the label G representing the generalized distribution, is

$$S_{\mathrm{k}}^{\mathrm{G}}(\lambda) = \frac{\partial E_{\mathrm{eV}}}{\partial \lambda} S_{\mathrm{k}} \left(E_{\mathrm{eV}}(\lambda) \right), \tag{3.18}$$

with

$$S_{\mathrm{k}}^{\mathrm{G}}(E_{\mathrm{eV}}(\lambda)) = \frac{1}{k}\left[\frac{\partial}{\partial\lambda_{\mathrm{s}}}F\left(E_{\mathrm{eV}}(\lambda_s) = \frac{1}{2}m_{\mathrm{e}}v(\lambda)^2\right)\right], \tag{3.19}$$

with, as implicitly stated in the S_k equations above,

$$v = \frac{1}{k}(\omega_{\mathrm{i}}(\lambda_{\mathrm{i}}) - \omega(\lambda) - kv_{\mathrm{d}}^2). \tag{3.20}$$

The somewhat arbitrary nature of the functional form of Equation 3.17 (see Ref. [5]), and ambiguity in the dimensionality of E_{eV} makes solving Equation 3.18 and Equation 3.19 ill-posed. Instead, there is good support in the literature building distributions as weighted sums of other distribution functions, with the most recognizable being the Bi-Maxwellian distribution function [18, 56, 93]. To this end, instead of resolving Equation 3.18 and Equation 3.19, a generalized function is defined as a superposition of Maxwellian and Druyvesteyn spectral distribution functions, with

$$P_{\lambda}^{\mathrm{T}}\left(\mathbf{x}^{\mathrm{T}}, \boldsymbol{\theta}^{\mathrm{T}}\right) = \eta\frac{\lambda_{\mathrm{i}}}{hc}\Delta\Omega\, L\, E_{\mathrm{i}}\, n_{\mathrm{e}}\frac{\partial\sigma^{\mathrm{T}}}{\partial\Omega}S_{\mathrm{k},\lambda}^{\mathrm{T}}\left(\mathbf{x}^{\mathrm{T}}, \lambda_{\mathrm{i}}\right), \tag{3.21}$$

and the spectral distribution function as,

$$S_{\mathrm{k},\lambda}^{\mathrm{T}}\left(\mathbf{x}^{\mathrm{T}}, \boldsymbol{\theta}^{\mathrm{T}}\right) = \frac{1}{n_{\mathrm{e}}}\left[\sum_{i=1}^{N_{\mathrm{M}}} n_{\mathrm{e},i}^{\mathrm{M}}\, S_{\mathrm{k},\lambda}^{\mathrm{M}}\left(n_{\mathrm{e},i}^{\mathrm{M}}, T_{\mathrm{e},i}^{\mathrm{M}}\right) + \sum_{i=1}^{N_{\mathrm{D}}} n_{\mathrm{e},i}^{\mathrm{D}}\, S_{\mathrm{k},\lambda}^{\mathrm{D}}\left(n_{\mathrm{e},i}^{\mathrm{D}}, T_{\mathrm{e},i}^{\mathrm{D}}\right)\right]. \tag{3.22}$$

This function is parameterized by the following QoI and nuisance parameter vectors,

$$\mathbf{x}^{\mathrm{T}} = \left[\mathbf{T}^{\mathrm{M}}; \mathbf{n}^{\mathrm{M}}; \mathbf{T}^{\mathrm{D}}; \mathbf{n}^{\mathrm{D}}, v_{\mathrm{d}}\right], \boldsymbol{\theta}^{\mathrm{T}} = \left[\eta, \lambda_{\mathrm{i}}\right]^{\top}. \tag{3.23}$$

With $\mathbf{n}$ and $\mathbf{T}$ are electron number density and temperature vectors. Superscripts indicate a Maxwellian or Druyvesteyn distribution. Using this system, an equilibrium plasma corresponds to the model $N_{\mathrm{M}} = 1$, $N_{\mathrm{D}} = 0$, and $\mathbf{x}^{\mathrm{T}} = [T_{\mathrm{e}}, n_{\mathrm{e}}, v_{\mathrm{d}}]^{\top}$. For simplicity, the superposition is limited to the cases where N_{M} and N_{D} are both less than or equal to one. For

convenience, we define a distribution fraction for binary Maxwellian–Druyvesteyn plasmas ($N_{\rm M} = N_{\rm D} = 1$):

$$\gamma_{\rm MD} = \frac{n_{\rm e}^{\rm M}}{n_{\rm e}^{\rm M} + n_{\rm e}^{\rm D}} = \frac{n_{\rm e}^{\rm M}}{n_{\rm e}}. \tag{3.24}$$

For the Maxwellian and Druyvesteyn distribution functions described above, the spectral distribution functions parameterized by frequency (see Ref. [140] for a full set of derivations) are given by

$$S_{\rm k,\omega}^{\rm M} = \frac{1}{\sqrt{2\pi}} \frac{1}{k_\sigma \sigma} \exp\left[-\frac{1}{2} \left(\frac{\omega_{\rm i} - \omega - k_\sigma v_{\rm d}}{k_\sigma \sigma} \right)^2 \right], \tag{3.25}$$

and

$$S_{\rm k,\omega}^{\rm D} = \beta \frac{1}{k_\sigma \sigma} {\rm erfc}\left[\alpha \left(\frac{\omega_{\rm i} - \omega - k_\sigma v_{\rm d}}{k_\sigma \sigma} \right)^2 \right], \tag{3.26}$$

The incident and scattered frequencies, the magnitude of the scattering wavevector, and σ are represented by

$$\omega_{\rm i} = \frac{2\pi c}{n} \frac{1}{\lambda_{\rm i}}, \omega_{\rm s} = \frac{2\pi c}{n} \frac{1}{\lambda}, \tag{3.27}$$

$$k_{\rm i} = \frac{2\pi}{\omega_{\rm i}}, k = \frac{2\pi}{\omega}, \tag{3.28}$$

$$k_\sigma \equiv |\mathbf{k}| = \sqrt{k_{\rm i}^2 + k^2 - 2k_{\rm i} k \cos\theta_{\rm kio}} \approx 2k_{\rm i} \sin\left(\frac{\theta_{\rm kio}}{2} \right), \tag{3.29}$$

and

$$\sigma \equiv \sqrt{\frac{k_{\rm B} T_{\rm e}}{m_{\rm e}}}. \tag{3.30}$$

Finally, as presented, the distributions were derived on the frequency ω domain. To be proper PDF functions on the wavelength domain (in nm), a change of variables is required for a proper mathematical redistribution of the scattered power. This is paramount for accurate estimates of the LTS electron number density. In this case, the analytical expression is

$$\frac{\partial \omega}{\partial \lambda} = \frac{2\pi c}{n} \frac{1}{\lambda^2}, \tag{3.31}$$

such that

$$S_{\mathrm{k},\lambda}(\lambda) = \frac{\partial \omega}{\partial \lambda} S_{\mathrm{k},\omega}(\omega(\lambda)). \tag{3.32}$$

3.3 Matrix Optics, Solid Angle, and Spatial Resolution

Proper alignment of the detection and spectroscopic equipment is necessary for proper imaging of objects relaying your scattered light. In a free-space optical system, like those in a benchtop plasma experiment, the object being imaged is typically the interrogation beam scattering volume itself. In the case of LTS and LRS in a large vacuum test facility, the object being imaged is typically a fiber that has relayed the scattered light from inside of the large vacuum test facility. In both cases, proper alignment and sizing of detection optics as well as their relative distances, are critical in order to optimize spatial resolution, laser line blocking and system throughput.

An understanding of the choice of optical components, their relative placement and size will dictate some key parameters necessary for inferring the parameters of interest from the model equations in the previous subsection. This subsection presents the basic geometrical optics necessary to calculate the imaging properties of the optical layout used to detect the scattered radiation. Because typical collection systems consist of two or more lenses in general, we approach the problem of determining the magnification and solid angle of our detection system with ray matrices. This is appropriate in the wavelength region of interest near 532 nm. In other cases, it may be necessary to use Gaussian optics software.

The goal of our detection system is, in general, to create a magnified image of the center plane of the object that is emanating the scattered light of interest. This will vary depending on the optical configuration. To do this, we use some collection of optics with relative distances chosen to be consistent with the specific needs of the optical system. In our case, we must spectrally filter the light transmitted (either free space or fiber) from our object with a notch filter to remove stray light reflections and Rayleigh scattered light, then spectrally decompose this light with the spectrometer in order to detect a spectrum at

our detector. We use several lenses and a notch filter to create this image of interest onto the slit plane of the spectrometer. The relative distances and sizes of these components, as well as other intentionally placed apertures, serve to limit the field of view into the region of interest and the brightness of the image created on the slit plane of the spectrometer and, therefore, the intensity of the light at the detector plane [4, 108]. In order to robustly calculate the parameters of interest, namely the detection length L and the collection solid angle, $\Delta\Omega$, we turn to matrix optics.

We treat the scattered light being scattered by the interrogation beam as paraxial rays characterized by their height off the optical axis and their angle with respect to the optical axis as

$$r(z) = \begin{bmatrix} y(z) \\ \theta(z) \end{bmatrix} \tag{3.33}$$

We are interested in the following optical elements: thin lenses, apertures, and free space propagation of rays. We treat notch filters as effective apertures that limit light throughput when they are misaligned (i.e., not filtering). When they are filtering, these filters simply act as reflecting elements for the intended wavelength to be filtered. The filters in their filtering mode are not considered in the numerical aperture and, therefore, solid angle calculation. When their effective size is acting as an aperture, the filters can act as a limiter on the maximum angle collected from the image plane. The ray matrices for a lens ($O_{\text{l}}(f)$) and free space propagation of a ray ($O_{\text{fs}}(\Delta z)$) are

$$O_{\text{l}}(f) = \begin{bmatrix} 1 & 0 \\ \frac{1}{f_{\text{l}}} & 1 \end{bmatrix}, O_{\text{fs}}(\Delta z) = \begin{bmatrix} 1 & \Delta z \\ 0 & 1 \end{bmatrix} \tag{3.34}$$

In a free space optical system imaging the interrogation volume directly, the collection solid angle, spatial resolution, and size of the interrogation volume is set directly by the detection optical system. In the case of a detection system imaging a fiber that has one end collecting scattered light and another end transmitting it to the detection system, they can

be set by the fiber numerical aperture, the vacuum side relay optics, or some combination.

To determine the maximum collection solid angle through the numerical aperture, we must calculate the maximum collection angle from the optical axis at the object plane in the expected configuration of our optical collection system. In the free space case, the object plane is the interrogation volume plane, and the image plane is the spectrometer slit plane. In the fibered case, the object plane is the fiber plane and the image plane is again the spectrometer plane. To determine the detection length, width and solid angle, we define two rays, the marginal and chief rays at the object plane as

$$r^{\mathrm{m}}(0) = \begin{bmatrix} 0 \\ \theta_{\max} \end{bmatrix}, r^{\mathrm{c}}(0) = \begin{bmatrix} d_{\mathrm{object}}/2 \\ \theta_{\max} \end{bmatrix}, \tag{3.35}$$

where d_{object} is the diameter of the object being imaged, assuming it is coaxial with the detection optical axis. We can define an equivalent matrix for the entire optical train from the object plane to the spectrometer slit plane with a matrix product and use this matrix product to optimize our system for the maximum marginal ray angle $\theta_{\max}$ that meets all of the aperture requirements for our system, making our collection lens the limiting aperture. We can then calculate the solid angle for a cone of half angle $\theta_{\max}$ as

$$\Delta\Omega = 2\pi(1 - \cos(\theta_{\max})). \tag{3.36}$$

The detection length and width, $L_{\mathrm{det}}, W_{\mathrm{det}}$, are related to the magnification of the interrogation volume onto the face of the image plane. Generally, a detection system will magnify the object at the image plane, that is the slit plane in our case. To determine the magnification, M, we need to calculate the height of the chief ray at the slit plane. The ratio of the height of the chief ray at the object plane and the image plane gives the magnification, M. Having M, the detection length and detection height are related to the interrogation length

and width by

$$L = \frac{L_{\text{int}}}{M}, W_{\text{det}} = \frac{W_{\text{int}}}{M}. \tag{3.37}$$

The spatial resolution of the measurement is given by $L_{\text{det}} \times W_{\text{det}}$. The magnification can be calculated as the ratio of the height of the chief ray at the object plane versus the height of the chief ray at the image plane. With these tools, we can express the collection solid angle and detection length as functions of the detection system that detection system optical elements. These will be described for each independent experiment in the following chapters.

3.4 Model Parameters and Synthetic Spectra

Table 3.1: Units and descriptions for the parameters used in the LRS models presented in Subsection 3.2.1. The values in this table were used to generate the synthetic spectrum presented in Figure 3.2.

Parameter	Unit	Value	Description
p_{g}	Torr	5	Measured neutral gas pressure
T_{g}	K	275	Neutral gas temperature
τ	nm	0.153	LRS spectral linewidth FWHM
η	–	1	System efficiency constant
λ_{i}	nm	532	Incident laser wavelength,
E_{i}	mJ	500	Measured incident laser energy per pulse
$\gamma^2/\epsilon_{\text{o}}^2$	m^6	0.505 $\times 10^{-60}$	Polarizability tensor anisotropy from Ref. [[2]]
ζ	rad	0	Raman polarization angle
$\Delta\Omega$	sr	0.05	Calculated system solid angle
L	mm	2	Interrogation volume length
θ_{eiy}	rad	$\pi/2$	Incident polarization to lab-frame $\mathbf{y}$ angle
θ_{kio}	rad	$\pi/2$	Incident polarization to collection $\mathbf{k}$ angle
ρ	–	3/4	Depolarization ratio from Ref. [[2]]
I_{g}	–	1	Nuclear spin quantum number from Ref. [[2]]
B_{g}	m^{-1}	198.973	Rotational energy constant from Ref. [[2]]
D_{g}	m^{-1}	5.7 $\times 10^{-4}$	Centrifugal distortion constant from Ref. [[124]]
$g_{J=\text{even}}$	–	6	Nuclear spin degeneracy from Ref. [[2]]
$g_{J=\text{odd}}$	–	3	Nuclear spin degeneracy from Ref. [[2]]

One LRS model and four plasma models are considered in this work. The plasma

Table 3.2: Units and descriptions for the parameters used in the LTS models presented in Subsection 3.2.2. The values in this table were used to generate the synthetic spectrum presented in Figure 3.3.

Parameter	Unit	Value	Description
γ_{MD}		0.5	Maxwellian–Druyvesteyn distribution fraction
$n_{\mathrm{e}}^{\mathrm{M}}$	m^{-3}	1×10^{17}	Maxwellian number density
$n_{\mathrm{e}}^{\mathrm{D}}$	m^{-3}	1×10^{17}	Druyvesteyn number density
$T_{\mathrm{e}}^{\mathrm{M}}$	eV	5	Maxwellian electron temperature
$T_{\mathrm{e}}^{\mathrm{D}}$	eV	4	Druyvesteyn electron temperature.
v_{d}	km s^{-1}	0	Bulk drift velocity
η		1	System efficiency constant
λ_{i}	nm	532	Incident laser wavelength
E_{i}	mJ	500	Measured incident laser energy per pulse
n		1	Refractive index
$\Delta\Omega$	sr	0.05	Calculated system solid angle.
L	mm	2	Interrogation volume length
θ_{eiy}	rad	$\pi/2$	Incident polarization to lab-frame $\mathbf{y}$ angle
θ_{kio}	rad	$\pi/2$	Incident polarization to collection $\mathbf{k}$ angle
r_{e}	m	2.8179×10^{-15}	Classical electron radius from Ref. [[140]]

models are specified in Table 3.3. Note that model M_3 features a binary Maxwellian–Druyvesteyn plasma with a constant electron temperature, i.e., $T_{\mathrm{e}} = T_{\mathrm{e}}^{\mathrm{M}} = T_{\mathrm{e}}^{\mathrm{D}}$, whereas M_4 contains two distinct temperatures. For Thomson scattering, the QoI are given by Equation 3.23, which differs depending on the model, defined by N_{M}, N_{D}, v_{d}, and the vector of nuisance parameters from the Raman inference. Simulated Thomson spectra based on M_1–M_4, using the parameters listed in Table 3.2, are shown in Figure 3.3.

Table 3.3: Description of the different plasma submodel QoI and nuisance parameter vectors used for Bayesian model selection. M_1 and M_2 describe single Maxwellian and Druyvesteyn submodels. M_3 and M_4 describe single and distinct temperature sums of Maxwellian and Druyvesteyn submodels.

Model	$\mathbf{x}^{\mathrm{T}}$	$\boldsymbol{\theta}^{\mathrm{T}}$
M_1	$\left[T_{\mathrm{e}}^{\mathrm{M}}, n_{\mathrm{e}}^{\mathrm{M}}, v_{\mathrm{d}}\right]^{\top}$	$\left[\eta, \lambda_{\mathrm{i}}\right]^{\top}$
M_2	$\left[T_{\mathrm{e}}^{\mathrm{D}}, n_{\mathrm{e}}^{\mathrm{D}}, v_{\mathrm{d}}\right]^{\top}$	$\left[\eta, \lambda_{\mathrm{i}}\right]^{\top}$
M_3	$\left[T_{\mathrm{e}}, n_{\mathrm{e}}, \gamma^{\mathrm{MD}}, v_{\mathrm{d}}\right]^{\top}$	$\left[\eta, \lambda_{\mathrm{i}}\right]^{\top}$
M_4	$\left[T_{\mathrm{e}}^{\mathrm{M}}, T_{\mathrm{e}}^{\mathrm{D}}, n_{\mathrm{e}}, \gamma^{\mathrm{MD}}, v_{\mathrm{d}}\right]^{\top}$	$\left[\eta, \lambda_{\mathrm{i}}\right]^{\top}$

The LRS and LTS models presented in Eqs. Equation 3.14 and Equation 3.21 produce an intensity at each wavelength, λ. A measured spectrum can be represented in vector form,

$$\mathbf{b} = \left[P_{\lambda_1}, P_{\lambda_2}, \ldots, P_{\lambda_{N_\lambda}} \right]^\top, \tag{3.38}$$

where N_λ is the number of spectral resolution elements. It is oftentimes necessary to reject those parts of a spectrum that straddle the laser wavelength. Therefore, when evaluating experimental data, elements of $\mathbf{b}$ within 4τ of the laser wavelength are eliminated from the comparison. In what follows, we use both real data, synthetic data, and modeled data. Synthetic data are indicated with a tilde, e.g.,

$$\widetilde{\mathbf{b}} = \left[\widetilde{P}_{\lambda_1}, \widetilde{P}_{\lambda_2}, \ldots, \widetilde{P}_{\lambda_{N_\lambda}} \right]^\top, \tag{3.39}$$

and modeled data are indicated with a hat, e.g.,

$$\hat{\mathbf{b}}(\mathbf{x}) = \left[P_{\lambda_1}(\mathbf{x}), P_{\lambda_2}(\mathbf{x}), \ldots, P_{\lambda_{N_\lambda}}(\mathbf{x}) \right]^\top. \tag{3.40}$$

3.5 Pre-Processing of Raw laser Thomson and Raman Signals

Collected signals during a Raman or Thomson scattering acquisition are the sum of several desired and undesired signals that make their way to the detector during acquisition. Additionally, signals may be shifted slightly from their expected wavelength positions due to internal misalignment of the spectrograph and image of the object on the slit plane and therefore detector face. These facts must be accounted for in order to properly estimate our parameters of interest.

In our case, we will collect LTS scattered light from plasmas that are created by ionizing Kr, which are monatomic molecules. Our detection system will be calibrated by collecting

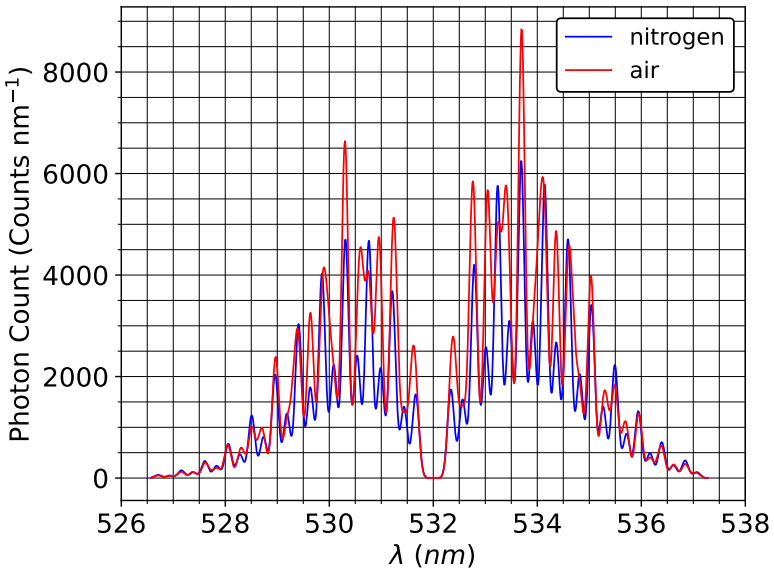

Figure 3.2: Synthetic LRS spectra for air and nitrogen.

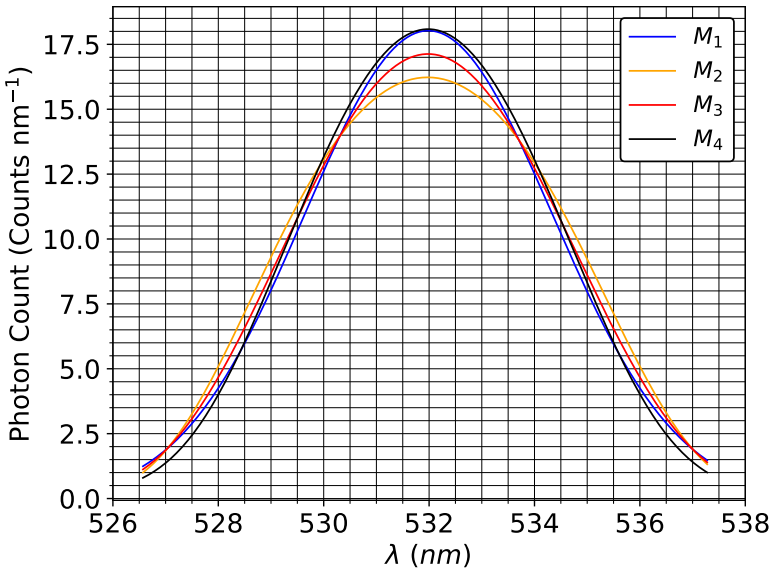

Figure 3.3: Synthetic LTS spectra using the four models.

LRS from neutral air or nitrogen, both of which can be modeled as a (sum of) diatomic molecule(s). Given this, the expected signals are tabulated in Table 3.4 and Table 3.5. The O and B in the P (pressure) column correspond to the operational and base pressures, respectively. Note that noise is present in all signals and is not individually tabulated.

Filtering elements are necessary in an LTS detection system. In order to detect both

Table 3.4: Signals present during LRS acquisiton.

Tag	P	Laser	Raman	Rayleigh	Reflections	Background
A_{R}	O	On	Yes	Yes	Yes	Yes
B_{R}	B	On	Yes	Yes	Yes	Yes
C_{R}	O/B	Off	No	No	No	Yes

Table 3.5: Signals present during LTS acquisiton.

Tag	P	Laser	Plasma	Thomson	Emissions	Rayleigh	Reflect	Background
A_{T}	O	On	On	Yes	Yes	Yes	Yes	Yes
B_{T}	O	Off	On	No	Yes	No	No	Yes
C_{T}	O	On	Off	No	No	Yes	Yes	Yes
D_{T}	O	Off	Off	No	No	No	No	Yes

LRS and LTS, Rayleigh scattered light and reflections at and very close to the laser wavelength must be blocked from reaching the detector using filtering elements. In our case, Optigrate BNF-532-OD4 BNF filters of several sizes are used. When they are well aligned, they are OD4 filters for the center wavelength and have a throughput of about 80% for all other wavelengths [44, 55]. Without filtering elements, stray light saturate the chip count at 532 nm and redistribute light in the vicinity of the laser wavelength on the chip, which makes it impossible to resolve the LRS or LTS signals.

Assuming an appropriate set of filtering elements, finite optics, slight misalignments and and the finite size of the beam blocking region [162] will lead to a trace amount of Rayleigh and reflections that make their way to the detector. This assumption is good for a well-aligned free space optical system that is directly imaging the laser beam interrogation volume in a finite-sized vessel. Because of the vessel walls, reflections make their way through the system to the detector that are off plane of the object plane. These levels are, however on the order of the LRS and LTS scattered light when the filter is well and allow us to resolve the LRS and LTS signals. For systems that relay the scattered light through a fiber, the fiber face forms an almost perfect plane from which to image. An appropriately

sized rejection ring image relative to the object image will filter the undesired stray light almost perfectly in this case.

In the general case, for a given optical configuration, including a grating element, it is best practice to collect LRS scattered light at several operating pressures (A_{R}) and at least one time at base pressure (B_{R}) in order to capture the desired LRS signals as well as the reflections and background. This ensures multiple points for number density calibration of the detection system using LRS. Similarly, when collecting LTS signals, every point of interest must obviously have a LTS raw signal (A_{T}) collected. The collection of B_{T} and C_{T} are highly dependent on the interrogation volume location relative to any surfaces that may add additional reflections or fluoresce, leading to strong laser line stray light and broadband stray light around the laser wavelength that may overtake the LRS and in particular LTS signals, see the discussions on stray light in [140] for more information. Finally, background scans B_{T} are required. With the scans in hand, the data to be processed can be recovered from simple subtraction of the signals of interest. In the LRS case, the preliminary data vector is recovered

$$\mathbf{b} = A_{\mathrm{R}} - B_{\mathrm{R}}. \tag{3.41}$$

In the LTS case,

$$\mathbf{b} = A_{\mathrm{T}} - (B_{\mathrm{T}} + (C_{\mathrm{T}} - D_{\mathrm{T}})). \tag{3.42}$$

Vestiges of stray light at the center wavelength are removed manually by defining a rejection,

$$\lambda_{\mathrm{min,max}}^{\mathrm{rej}} \notin \lambda_{\mathrm{s}}^{\mathrm{rej}} \equiv \lambda_{\mathrm{i_o}} \pm c_\tau \frac{\tau}{2.0}. \tag{3.43}$$

After having isolated the LTS signal, and with η and λ_{i} in hand from the LRS fit to the data, the LTS quantities of interest in can be estimated.

The least squares method for fitting the signals using the models and quantifying uncertainty in these fitted parameters are presented in Section 3.6. This is the standard for

quantifying uncertainty in LTS experiments due to its simple implementation. Howevever, it suffers from robustness issues due to the tiered nature of the signal inversion. The LRS calibration diagnostic, which relies on at least one measured quantity that itself is subject to uncertainty, produces quantities of interest that are then used in the LTS signal inversion. Under these circumstances, the propagation of uncertainty in the variables of interest may not produce accurate uncertainty distributions of correlations between variables. Section 3.7 introduces a Bayesian inference signal inversion technique that robustly accounts for the uncertainty in measured and inferred variables in an LRS-calibrated LTS diagnostic. The resulting uncertainty distributions are compared to provide guidance for when a least squares inversion is sufficient.

3.6 Nonlinear Least Squares

Once a raw signal has been successfully preprocessed, the highly nonlinear scattering models are used to invert the signal and estimate the quantities of interest. As with any measurement, the data is corrupted by several known and unknown sources of noise. Any calculated parameters from the model are at best, an estimate of their true value given the data and the noise. Therefore, these values are to be reported as a most likely or probable value and an uncertainty. The uncertainty corresponds to a range of values that contains the most probable value and some confidence percentage on the range provided. Nonlinear least squares regression provides the framework for inverting our signal and calculating estimated parameters and their uncertainty [35].

Even after a successful pre-process and possible smoothing of your data any model, even with already optimized parameters, will deviate from the real signal. Letting the data be $\mathbf{b}$, our model as a function of the quantities of interest be $\hat{\mathbf{b}}\left(\mathbf{x}, \theta\right)$, and the error in the post-processed signal be $\mathbf{e}$, we can write this general relationship as

$$\mathbf{e}(\mathbf{x}, \theta, \mathbf{b}) \equiv \mathbf{b} - \hat{\mathbf{b}}(\mathbf{x}). \tag{3.44}$$

Given $\mathbf{e}, \mathbf{b}, \hat{\mathbf{b}} \in \mathbb{R}^n$, $\mathbf{x} \in \mathbb{R}^p$ with $p \leq n$, the error sum of squares is

$$\hat{S}(\mathbf{x}, \mathbf{b}) \equiv \sum_{i=1}^{n} [b_i - \hat{b}_i(x)]^2 = \sum_{i=1}^{n} [e_i(\mathbf{x}, \mathbf{b})]^2. \tag{3.45}$$

The least squares estimate , $\hat{\mathbf{x}}$, of the true quantities of interest $\mathbf{x}^*$, is one that minimizes $\hat{S}(\mathbf{x}, \mathbf{b})$ with $\mathbf{x}$ over some domain (typically specified by the user) $\mathbb{X}$ [31]. This is the case when the noise is independent and identically distributed (IID), the expected value of the noise is zero, $E[\mathbf{e}(\mathbf{x}, \mathbf{b})] = \mathbf{0}$ with some variance $\sigma_i^2 \; \forall i \in n$, that $\hat{\mathbf{b}}$ is approximately continuous, and that $\mathbb{X}$ is a bounded subset of $\mathbb{R}^p$ [22]. When these assumptions are true, the least squares estimators below are consistent estimates of the true quantities of interest and the variance in the residuals, viz.

$$\hat{\mathbf{x}} \approx \mathbf{x}^*, \text{ and }, \; s^2 \equiv \hat{S}(\hat{\mathbf{x}})/(n-p) \approx \sigma_{\mathbf{e}}^2. \tag{3.46}$$

The above assumptions hold well for the standard high-fidelity model of an optical process. Physically, there are ranges on each parameter quantity of interest, bounding the subspace of possible values. The models are derived from continuous mathematical formulations of the laws of classical physics, like Maxwell's equations. The data collected is often light sourced from the relevant process of interest; the collection of light on a detector is a random process whose noise approaches IID in the limit of many collection cycles.

Given that the least squares estimator is approximately zero at a local optima, the Jacobian must adhere to

$$\frac{\partial}{\partial \mathbf{x}} \hat{S}(\mathbf{x}, \mathbf{b})|_{\hat{\mathbf{x}}} \approx \mathbf{0}, \tag{3.47}$$

then

$$\left[\frac{\partial}{\partial \mathbf{x}} \hat{S}(\mathbf{x}, \mathbf{b})|_{\hat{\mathbf{x}}} \right] \cdot [\mathbf{e}(\mathbf{x}, \mathbf{b})|_{\hat{\mathbf{x}}}] \approx \mathbf{0}. \tag{3.48}$$

For nonlinear $\hat{\mathbf{b}}(\mathbf{x})$, iterative methods are required to solve Equation 3.48 , see Chapter 2 of [22] for details . In our case, this is done using the least squares method in Python.

In order to approximate the covariance matrix for the parameters of interest, moments of the residuals are required in the case of nonlinear models where the variance is affected by the local curvature of the model with respect to the parameters of interest; see Chapters 4 and 5 for the details [22]. Approximating the Hessian of $\hat{S}(\mathbf{x}, \mathbf{b})$ with the square of it's Jacobian,

$$\mathbb{H} \approx \left[[\frac{\partial}{\partial \mathbf{x}} \hat{S}(\mathbf{x}, \mathbf{b})]^T \cdot [\frac{\partial}{\partial \mathbf{x}} \hat{S}(\mathbf{x}, \mathbf{b})] \right]^{-1}, \tag{3.49}$$

the estimate of the covariance matrix is

$$\mathbb{C} \approx \frac{\mathbb{H} \cdot \hat{S}(\mathbf{x}, \mathbf{b})}{(n-p)}. \tag{3.50}$$

The variance in the j^{th} element of $\hat{\mathbf{x}}$ are the $(j^{\text{th}}, j^{\text{th}})$, or diagonal elements of $\mathbb{C}$. Using Equation 3.48 to solve for the least squares estimate for the parameters of interest and Equation 3.50 for their variance, a 95% confidence interval on the quantity of interest can be expressed as

$$\hat{\mathbf{x}} \pm 2.0 \sqrt{\text{diag}\,(\mathbb{C})}. \tag{3.51}$$

The framework in this section can be used to estimate the quantities of interest array and the covariance matrix for uncertainty quantification and correlations between the variables.

The extent to which this method and a Bayesian probability model agree is unclear. Section 3.7 outlines a Bayesian inference model that pedagogically accounts for relevant sources of uncertainty that are difficult to include in the least squares framework. The uncertainty profiles produced are then explored and discussed to determine if and when a full Bayesian probability model may be required.

3.7 Bayesian Inference and Model Selection

3.7.1 Background and Bayes' Equation

Bayesian inference is the process of updating a prior probability distribution given an observation [63].In this text, "distribution" is used loosely to refer to both probability density and mass functions (PDFs and PMFs). Often in optical experiments, the measurement models are high-fidelity, dependent on many parameters, and a single optical setup comprises multiple diagnostics that provide partial information about the QoI. In the context of parameter estimation and UQ, an uncertainty model is developed based on prior information about the QoI and then updated subject to the measurement data. The resultant "posterior" information may be employed as prior information in subsequent inferences and refined in light of new data. This approach can be useful in a staged inference problem, where QoI from an earlier inference are nuisance parameters in a subsequent inference; this is the case for Bayesian inference applied to LRS-calibrated LTS data. Bayesian inference has been extensively leveraged for UQ by the fusion community [23]. However, LTS for EP applications entails unique considerations compared to fusion applications due to their distinctive pre-processing requirements and model equations. For instance, advances in detection, dispersion, and filtering technology have enabled the use of a single intensified-spectrograph system, which have sufficient spectral range and resolution to determine the QoI [162]. This section describes a Bayesian framework for evaluating LRS-calibrated LTS measurements of EP-relevant plasmas.

The QoI, measured signals, physical parameters, and models are cast as random variables that are characterized by probability distributions. These distributions describe one's knowledge of the parameters – narrow distributions indicate a high degree of confidence while wide distributions signify uncertainty. The posterior distribution, $\mathbb{P}(\mathbf{x}, \boldsymbol{\theta}|\mathbf{b})$ [163], conveys one's knowledge of the QoI following a measurement. There are several distributions of interest in our framework. The likelihood, which is the PDF that determines how

likely a given data $\mathbf{b}$ was produced by a set of QoI and nuisance parameters. The prior PDF, or simply prior, $\mathbb{P}(\mathbf{x}, \boldsymbol{\theta})$, is the joint-PDF of the QoI and nuisance parameters based on any information about these variables that is independent of the measurement. Prior information may include physical limits, results from previous experiments, and so on. The posterior is the joint distribution of the QoI and nuisance parameters, conditioned on the observed data through the likelihood.

The posterior is a comprehensive Bayesian solution to an inverse problem since it carries all the measured and prior information about the QoI and nuisance parameters. The prior and likelihood are constructed to include as much information about the system and measurement scenario as is practical. The posterior, $\mathbb{P}(\mathbf{x}, \boldsymbol{\theta}|\mathbf{b})$, likelihood, $\mathbb{P}(\mathbf{b}|\mathbf{x}, \boldsymbol{\theta})$, prior, $\mathbb{P}(\mathbf{x}, \boldsymbol{\theta})$, and evidence, $\mathbb{P}(\mathbf{b})$, are related by Bayes' equation:

$$\mathbb{P}(\mathbf{x}, \boldsymbol{\theta}|\mathbf{b}) = \frac{\mathbb{P}(\mathbf{b}|\mathbf{x}, \boldsymbol{\theta})\, \mathbb{P}(\mathbf{x}, \boldsymbol{\theta})}{\mathbb{P}(\mathbf{b})}. \tag{3.52}$$

The evidence itself, a.k.a. the marginal likelihood, is the marginal joint distribution,

$$\mathbb{P}(\mathbf{b}) = \iint \mathbb{P}(\mathbf{b}|\mathbf{x}, \boldsymbol{\theta})\, \mathbb{P}(\mathbf{x}, \boldsymbol{\theta})\, \mathrm{d}\boldsymbol{\theta}\, \mathrm{d}\mathbf{x}. \tag{3.53}$$

The posterior is summarized using point estimates, like the maximum a posteriori (MAP) estimate of the QoI, $\mathbf{x}_{\mathrm{MAP}}$. The MAP point estimate is the estimate that maximizes the nuisance parameter marginalized posterior,

$$\mathbb{P}(\mathbf{x}|\mathbf{b}) = \iint \mathbb{P}(\mathbf{x}, \boldsymbol{\theta}|\mathbf{b})\, \mathrm{d}\boldsymbol{\theta}. \tag{3.54}$$

Point estimates are not sufficient for UQ, which requires at least the spread of the posterior about the MAP to convey an estimate of uncertainty.

3.7.2 Likelihood and Prior PDFs

A measurement model that is a function of the QoI, $\hat{\mathbf{b}}(\mathbf{x}, \boldsymbol{\theta})$, is the basis for determining the QoI in any optical experiment. In this case, the model corresponds to either the Raman or Thomson model from Section 3.4. These models are close approximations to the real physical process being observed, but discrepancies arise due to noise and other imperfections in the system. The likelihood function quantifies the chance that the data, $\mathbf{b}$, could have been observed given a hypothetical set of QoI and nuisance parameters, $\mathbf{x}$ and $\boldsymbol{\theta}$. This probability corresponds to the distribution of errors,

$$\mathbf{e}\left(\mathbf{x}, \boldsymbol{\theta}, \mathbf{b}\right) \equiv \mathbf{b} - \hat{\mathbf{b}}\left(\mathbf{x}, \boldsymbol{\theta}\right), \tag{3.55}$$

where $\mathbf{x}$ and $\boldsymbol{\theta}$ are ideal parameters for a set of data.

In this work, the data are a spectrum, assumed to have been preprocessed (binned, etc.) ahead of being passed to the framework. See Chapter 2 of Ref. [140] for a detailed explanation of preprocessing of raw LTS and LRS signals. The starting point for inversion is a spectrum that is background- and reflection-corrected by subtracting the plasma emission spectrum and the background reflection spectrum from a raw LTS spectrum. Common sources of noise – like thermal noise in detection systems, read noise on the face of a solid-state detector, and many others – can be approximated as Gaussian; see Refs. [163, 167] for details. Moreover, macroscopic representations of measurement noise correspond to the macro-scale averaging of many noise-creating processes and, as such, adhere to the central limit theorem [163].

Therefore, we choose to cast the likelihood function in this work as a Gaussian likelihood, given by

$$\mathbb{P}(\mathbf{b}|\mathbf{x}, \boldsymbol{\theta}) = \det(2\pi\boldsymbol{\Gamma}_{\mathrm{e}})^{-1/2} \exp\left(-\frac{1}{2}\mathbf{e}^{\top}\boldsymbol{\Gamma}_{\mathrm{e}}^{-1}\mathbf{e}\right), \tag{3.56}$$

with $\boldsymbol{\Gamma}_{\mathrm{e}} \in \mathbf{R}^{d_{\mathrm{b}} \times d_{\mathrm{b}}}$ being the error covariance matrix. The size of the data, d_{b} – in this case

the number of points making up a spectrum – is on the order of the number of pixels in a row on the spectrograph detector (usually in the thousands). Assuming that the errors are independent and identically distributed, with variance σ_{e}^2, then $\mathbf{\Gamma}_{\mathrm{e}} = \sigma_{\mathrm{e}}^2\mathbf{I}$ and the likelihood simplifies to

$$\mathbb{P}(\mathbf{b}|\mathbf{x},\boldsymbol{\theta}) = \left(2\pi\sigma_{\mathrm{e}}^2\right)^{-d_{\mathrm{b}}/2}\exp\left(-\frac{\mathbf{e}^{\top}\mathbf{e}}{2\sigma_{\mathrm{e}}^2}\right). \tag{3.57}$$

The prior PDF incorporates information about the QoI and nuisance parameters that is independent of the data. Any prior information that can be explicitly encoded in a probability distribution can be included. This information may include physical bounds, dynamical relations, previous estimates of the QoI, etc. We assume that our prior information about the QoI is uncorrelated and Gaussian, in which case

$$\mathbb{P}(\mathbf{x}) = \prod_{i=1}^{d_{\mathrm{x}}}\frac{1}{\sqrt{2\pi\sigma_{\mathrm{x},i}^2}}\exp\left[-\frac{(x_i-\mu_{\mathrm{x},i})^2}{2\sigma_{\mathrm{x},i}}\right], \tag{3.58}$$

where

$$\mu_{\mathrm{x},i} = \min(x_i) + \frac{\max(x_i)-\min(x_i)}{2} \tag{3.59}$$

is the center of the physically plausible range of values for x_i and

$$\sigma_{\mathrm{x},i} = \frac{1}{3}\left[\max\left(x_i\right) - \min\left(x_i\right)\right] \tag{3.60}$$

ensures that 99.7% of the PDF occupies this range. The same procedure is used to define $\mathbb{P}(\boldsymbol{\theta})$, and since the QoI and nuisance parameters are independent, we set $\mathbb{P}(\mathbf{x},\boldsymbol{\theta})$ to $\mathbb{P}(\mathbf{x})\,\mathbb{P}(\boldsymbol{\theta})$. The variables d_{x} and $d_{\boldsymbol{\theta}}$ represent the length of the QoI and nuisance parameter vectors, respectively.

3.7.3 Sampling from and Approximating the Posterior PDF

The posterior PDF is a high-dimensional function that is not generally available in closed form. We consider two methods for accessing the posterior for UQ and model selec-

tion: sampling and Laplace's approximation. Given the dimension of the data, d_{b}, a log-scale posterior density will be used for sampling to avoid issues with arithmetic and machine rounding of small probabilities. Substituting Eqs. Equation 3.58 and Equation 3.57 into Equation 3.52 and grouping terms yields the negative-log posterior,

$$-\ln[\mathbb{P}(\mathbf{x},\boldsymbol{\theta}|\mathbf{b})] = \frac{\mathbf{e}^{\top}\mathbf{e}}{2\sigma_{\mathrm{e}}^2} + \sum_{i=1}^{d_{\mathrm{x}}} \frac{\left(x_i - \mu_{\mathrm{x},i}\right)^2}{2\sigma_{\mathrm{x},i}^2} + \sum_{i=1}^{d_{\boldsymbol{\theta}}} \frac{\left(\theta_i - \mu_{\boldsymbol{\theta},i}\right)^2}{2\sigma_{\boldsymbol{\theta},i}^2} + Z, \tag{3.61}$$

where Z is a constant that does not affect the topology of the distribution.

Markov chain Monte Carlo (MCMC) refers to a class of methods that can be used to sample a posterior PDF. As the number of samples becomes large, the density of samples becomes proportional to the target distribution. There are several MCMC algorithms available for sampling the posterior, including Gibbs, slice, and Metropolis–Hastings sampling. The Metropolis–Hastings algorithm generates steps with components along each dimension of $\mathbf{x}$ and $\boldsymbol{\theta}$ at once, as opposed to Gibbs and slice sampling, which generate sequential samples along individual dimensions of the distribution. To allow for flexibility in the model input vectors, Metropolis–Hastings sampling was chosen. The Markov chain is initiated at the least-squares estimate of the QoI to minimize the "burn-in" time. For the LRS inference, in the case of the pressure, which was measured, its mean and variance is set by the data. The remaining prior widths are set by choosing physically sensible minimum and maximum ranges for the parameters. Then, the posteriors for the relevant parameters of the LRS inference are used to construct the priors for those variables in the LRS inference. The rest of the priors are constructed in the same way as above. MCMC chains in this work are run until the cumulative mean trace and correlation signals are determined to be approximately stationary.

It is often convenient to invoke an approximate form of the posterior which bears the name of Laplace: Assuming the posterior is smooth, strongly-peaked, and unimodal, it may be modeled using a Gaussian PDF that is centered at the global maximum and fit to the lo-

cal curvature at that point [163]. The maximum is found by an optimization algorithm, and the Jacobian at that point is squared to approximate the Hessian and thereby estimate the inverse covariance matrix. The utility and validity of this model of $\mathbb{P}(\mathbf{b}|\mathbf{x}, \boldsymbol{\theta})$ for a sequential inference, such as LRS-calibrated LTS, is not known a priori. In addition, the effect of the accuracy of prior information on the ability to distinguish between candidate submodels is also unclear at this stage. These questions are explored in Section 3.8 and Subsection 3.9.2.

3.7.4 Bayesian Model Selection

Up until now, our discussion of Bayesian inference has assumed a fixed model of the target process, and thus a constant set of QoI. Many models are implicated in any estimation of the QoI, including the measurement model, physics models (like the submodels in Section 3.4), error distributions, priors, hyperpriors, etc., and we do not always know the best models to use, a priori. Bayesian model selection enables the comparison of models with incommensurate QoI. In this section, we are particularly interested in the application of model selection to plasma submodels to deduce the presence of non-equilibrium behavior and ensure robust estimation of the unknown parameters.

To start, it should be noted that any inference is implicitly conditional on the model. We make this dependence explicit and express an update using the ith model, M_i,

$$\mathbb{P}(\mathbf{x}, \boldsymbol{\theta}|\mathbf{b}, M_i) = \frac{\mathbb{P}(\mathbf{b}|\mathbf{x}, \boldsymbol{\theta}, M_i)\,\mathbb{P}(\mathbf{x}, \boldsymbol{\theta}|M_i)}{\mathbb{P}(\mathbf{b}|M_{\mathrm{i}})}. \tag{3.62}$$

We can compute the so-called model-posterior PDF for M_i using Bayes' equation,

$$\mathbb{P}(M_i|\mathbf{b}) = \frac{\mathbb{P}(\mathbf{b}|M_i)\,\mathbb{P}(M_i)}{\mathbb{P}(\mathbf{b})}. \tag{3.63}$$

The "model likelihood", $\mathbb{P}(\mathbf{b}|M_i)$, indicates the degree to which a model and one's prior assumptions are consistent with the measurement vector, $\mathbf{b}$. Therefore, the ratio of model

likelihoods for candidate models M_i and M_j can be used to assess their relative plausibility:

$$B_{i,j} \equiv \frac{\mathbb{P}(M_i|\mathbf{b})}{\mathbb{P}(M_j|\mathbf{b})} = \frac{\mathbb{P}(\mathbf{b}|M_i)\,\mathbb{P}(M_i)}{\mathbb{P}(\mathbf{b}|M_j)\,\mathbb{P}(M_j)}, \tag{3.64}$$

where $B_{i,j}$ is the so-called Bayes factor. Bayes factors greater than one imply that the data in $\mathbf{b}$ are more consistent with model i than model j; vice versa for $B_{i,j} < 1$; and one is indifferent to M_i and M_j when $B_{i,j}$ is equal to unity.

Assigning a prior distribution to a *model* requires comprehensive knowledge of the model space, which is rarely available. Absent specific information, we assume that all our submodels are equally plausible: $\mathbb{P}(M_i) \approx \mathbb{P}(M_j)$ for all i and j. This assumption is used in conjunction with Equation 3.62 to calculate the Bayes' factor,

$$B_{i,j} \approx \frac{\mathbb{P}(\mathbf{b}|M_i)}{\mathbb{P}(\mathbf{b}|M_j)} = \frac{\iint \mathbb{P}(\mathbf{b}|\mathbf{x},\boldsymbol{\theta},M_i)\,\mathbb{P}(\mathbf{x},\boldsymbol{\theta},M_i)\;\mathrm{d}\mathbf{x}\,\mathrm{d}\boldsymbol{\theta}}{\iint \mathbb{P}(\mathbf{b}|\mathbf{x},\boldsymbol{\theta},M_j)\,\mathbb{P}(\mathbf{x},\boldsymbol{\theta},M_j)\;\mathrm{d}\mathbf{x}\,\mathrm{d}\boldsymbol{\theta}}. \tag{3.65}$$

Equation 3.65 may be approximated via the Monte Carlo method:

$$B_{i,j} \approx \frac{N_j}{N_i} \frac{\sum_{k=1}^{N_i} \left(2\pi\sigma_{\mathrm{e},i}^2\right)^{-d_\mathrm{b}/2} \exp\!\left(-\frac{\mathbf{e}_i^\top \mathbf{e}_i}{2\sigma_{\mathrm{e},i}^2}\right)}{\sum_{k=1}^{N_j} \left(2\pi\sigma_{\mathrm{e},j}^2\right)^{-d_\mathrm{b}/2} \exp\!\left(-\frac{\mathbf{e}_j^\top \mathbf{e}_j}{2\sigma_{\mathrm{e},j}^2}\right)}. \tag{3.66}$$

In this expression, N_i and N_j are the number of samples drawn from $\mathbb{P}(\mathbf{x},\boldsymbol{\theta}|M_i)$ and $\mathbb{P}(\mathbf{x},\boldsymbol{\theta}|M_j)$, respectively, which are used to evaluate the numerator and denominator, in turn. The error variances, $\sigma_{\mathrm{e},i}^2$ and $\sigma_{\mathrm{e},j}^2$, may be model-specific, in principle, but we use a single variance for all our plasma submodels.

We take the logarithm of Equation 3.66 to provide numerical stability. Our results are presented in terms of $\log(B_{i,j})$ such that positive values indicate stronger support for model M_i than M_j, negative values suggest the opposite, and zero indicates indifference.

Monte Carlo estimation of the log-evidence is effective when the prior PDF plays a large role in an inference. However, when the prior is very diffuse compared to the likelihood, this technique leads to an excessive number of samples in low-density regions of the model

evidence, which poses a large computational cost. Efficient estimation of the log-evidence is an active area of research; see Refs. [54, 119, 148] for alternative methods to estimate this quantity.

3.8 Distinguishing Velocity Distribution Functions with Bayesian Model Selection

3.8.1 Synthetic Data, Priors, and Test Matrix

As stated above, we put independent Gaussian distributions on all our QoI and nuisance parameters. In the general case, a combination of priors, and specifically a log-uniform prior for the electron number density, may be preferred, as was recommended in Ref. [154]. Additionally, it is assumed that an LRS Bayesian inference or least-squares inversion has been used to provide the mean and width of the priors for η and $\lambda_{\rm i}$, which are nuisance variables in the LTS inversion. Table 3.6 outlines the $3\sigma_{{\rm x},i}$ ranges for the prior PDFs. These values were pulled, stretched and rounded from a previous least-squares signal inversion of collected LTS data, as representative of an acceptable approximation to the posterior or 'true' prior.

Table 3.6: Description of the $3\sigma_{{\rm x},i}$ ranges for the submodel parameters used in the synthetic LTS prior distributions.

Parameter	**Minimum**	**Maximum**
$\gamma_{\rm MD}$	0.25	0.75
$T_{\rm e}$	2	3
$T_{\rm e}^{\rm M}$	2	3
$T_{\rm e}^{\rm D}$	1	2
$n_{\rm e}$	1×10^{18}	5×10^{18}
$v_{\rm d}$	-50	50
η	0.160	0.190
$\lambda_{\rm i}$	531.9	532.1

In order to explore the effects of SNR and prior uncertainty on the "distinguishability" of candidate submodels, synthetic data are generated at several SNRs and degrees of prior "misinformation". We define the SNR as the ratio of the generated data's signal power to

the noise power,

$$\mathrm{SNR} \equiv \frac{\mathrm{E}\left[\max\left(\hat{\mathbf{b}}\right)^2\right]}{\mathrm{E}\left[d_{\mathrm{b}}^{-1}\left(\hat{\mathbf{b}}-\widetilde{\mathbf{b}}\right)^2\right]}, \tag{3.67}$$

where $\mathrm{E}(\cdot)$ is the expectation operator. Using this formula, we generate synthetic data with a prescribed SNR by setting the variance to

$$\sigma_{\mathrm{noise}}^2 = \frac{\mathrm{mean}\left[\max(\mathbf{b})^2\right]}{\mathrm{SNR}}. \tag{3.68}$$

For ground truth values of $\mathbf{x}$ and $\boldsymbol{\theta}$, the simulated measurements are given by

$$\widetilde{\mathbf{b}} = \hat{\mathbf{b}}(\mathbf{x}, \boldsymbol{\theta}) + \mathbf{e}_{\mathrm{synth}}, \tag{3.69}$$

where $\mathbf{e}_{\mathrm{synth}}$ is an independent and identically-distributed random variable with zero mean and variance $\sigma_{\mathrm{noise}}^2$.

We characterize the performance of Bayesian model selection as a function of the accuracy and precision of the prior. To do this, the prior PDFs can be widened and offset as a function of a percentage of the original range and mean:

$$\mu_{\mathrm{x},i}^{\mathrm{shift}} = \mu_{\mathrm{x},i}\left(1 + \frac{\kappa_i^{\mathrm{shift}}}{100}\right) \tag{3.70}$$

and

$$\sigma_{\mathrm{x},i}^{\mathrm{stretch}} = \mu_{\mathrm{x},i}^{\mathrm{shift}} \pm \frac{\mathrm{range}(x_i)}{2}\left(1 + \frac{\kappa_i^{\mathrm{stretch}}}{100}\right), \tag{3.71}$$

where $\kappa_i^{\mathrm{shift}}$ and $\kappa_i^{\mathrm{stretch}} \in [-100, 100]$. These parameters allow independent stretching and shifting of the prior PDF within a $\pm 3\sigma_{\mathrm{x},i}$ range with respect to the original, data-generating prior's $\pm 3\sigma_{\mathrm{x},i}$ range.

The cases presented in Secs. Subsection 3.8.2–Subsection 3.8.4 were generated in the following way. First, for a given combination of $\kappa_{\mathrm{x},i}^{\mathrm{shift}}$ and $\kappa_{\mathrm{x},i}^{\mathrm{stretch}}$, baseline values of $\mathbf{x}$ and

$\boldsymbol{\theta}$ were drawn from $\mathbb{P}(\mathbf{x}, \boldsymbol{\theta})$ according to Table 3.6. These were used to generate a synthetic signal, $\hat{\mathbf{b}}(\mathbf{x}, \boldsymbol{\theta})$, using M_1 and M_2 from Table 3.3. Models M_1 and M_2 were chosen for this comparison because they are parameterized with the same parameter vector $\mathbf{x}^{\mathrm{T}}$. Then, at each of the 1150 SNR values between 1 and 100, the data was perturbed according to Equation 3.69. The value of $\ln(B_{2,1})$ was calculated at each SNR two times, each using 500 samples from the perturbed prior. Similarly, to explore the ability to detect deviations from the submodels, model M_3 (a binary Maxwellian–Druyvesteyn plasma) was used to generate the data at a given value of γ_{MD}, according to the process outlined above. In these cases, 25 values of γ_{MD} between 0 and 1 were used, with 25 values of SNR between 1 and 100.

3.8.2 Effects of Prior Uncertainty

To understand the effect of uncertainty in the prior (i.e., based on its width) on one's ability to distinguish candidate submodels, $\ln(B_{2,1})$ is calculated using priors at varying levels of width misinformation, with $\kappa_{\mathrm{x},i}^{\mathrm{stretch}} \in \{0, 100, 300\}$ for all x_i.

The results are presented in Figure 3.4. We expect data generated with M_1 to produce $\ln(B_{2,1}) < 0$ and data generated with M_2 to produce $\ln(B_{2,1}) > 0$. Additionally, we expect the magnitude of $\ln(B_{2,1})$ to decrease with decreasing SNR. At each SNR, a line of best fit was computed by averaging the two values of $\ln(B_{2,1})$ at each SNR and then fitting a line. This is shown in Figure 3.4. In Figure 3.4, Figure 3.6, and Figure 3.8, all purple data points and the best fit line being positive, and all blue points and the best fit line being negative, indicate that, in all cases, the correct model was inferred.

In the base case (a), in which the generating distribution functions are used as the priors (i.e., there is no prior misinformation), the data demonstrates that the proposed method can distinguish between candidate submodels over the entire range of SNRs from 1 to 100. Furthermore, there is strong support for the correct model when the SNR ≥ 5. In cases (b) and (c), where there is prior misinformation in the form of a stretched PDF, the ability to

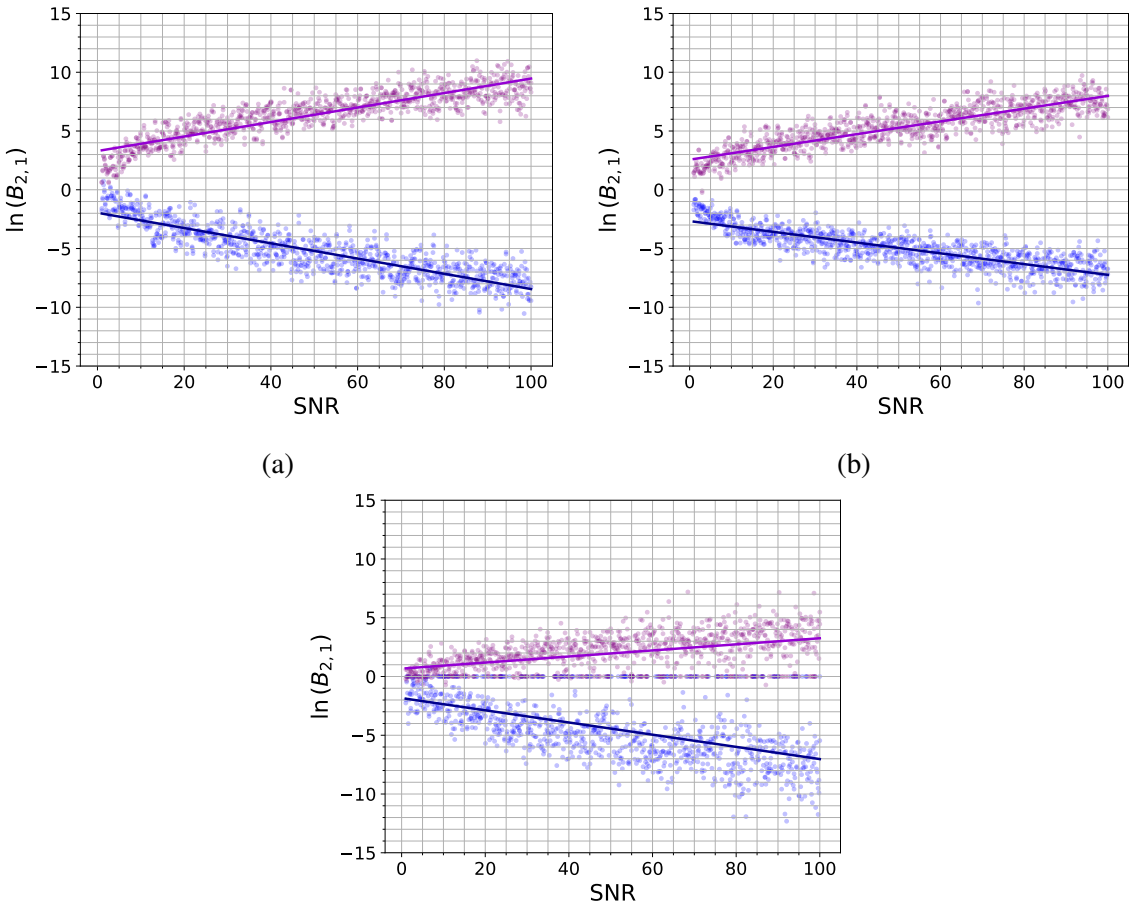

(a) (b)

(c)

Figure 3.4: $\ln(B_{2,1})$ versus SNR over priors with increasing misinformation: (a) $\kappa_{\mathrm{x},i}^{\mathrm{stretch}}$ = 0, (b) $\kappa_{\mathrm{x},i}^{\mathrm{stretch}}$ = 100, and (c) $\kappa_{\mathrm{x},i}^{\mathrm{stretch}}$ = 300. Synthetic data generated from model M1 is in blue, and synthetic data generated from model M2 is in purple. Dots indicate the calculated value of $\ln(B_{i,j})$, and lines indicate a line of best fit. $|\ln(B_{i,j})|$ substantially greater than zero indicates that the Bayesian framework is able to correctly identify the right model.

distinguish between the correct model is decreased compared to (a); case (c) occasionally returns indistinguishable values of $\ln(B_{2,1})$, which were automatically set to 0 in the data processing code.

Figure 3.5 explores the ability to detect deviations from each submodel using the binary model M_3. Similar to the pure-Maxwellian and pure-Druyvesteyn cases, support for the model drops with decreasing SNR. However, the ability to distinguish between the "degree of Maxwellianization" is maintained over the SNR range considered. This indicates that the Bayesian model selection framework is able to correctly distinguish between the

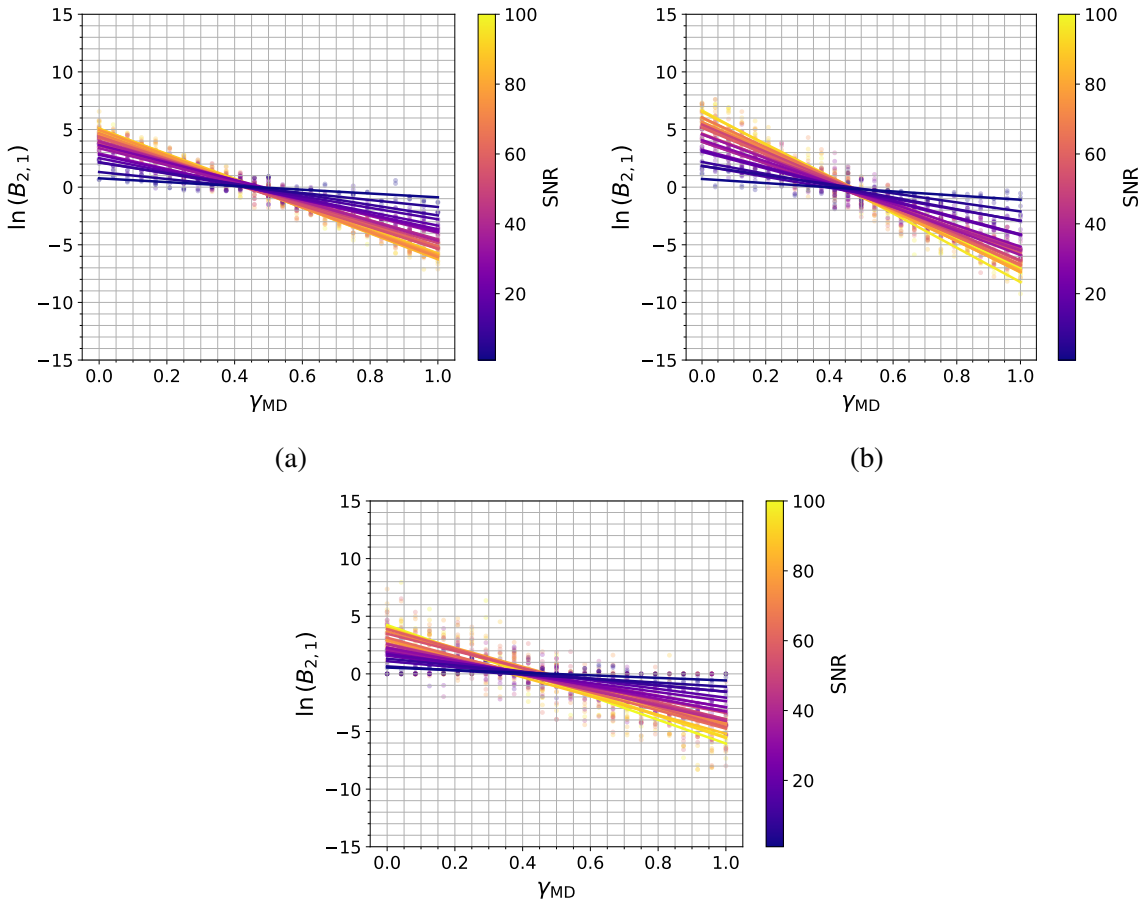

Figure 3.5: $\ln(B_{2,1})$ versus γ_{MD} at varying SNR levels over decreasingly certain priors for model M_3: (a) $\kappa_{\mathrm{x},i}^{\mathrm{stretch}} = 0$, (b) $\kappa_{\mathrm{x},i}^{\mathrm{stretch}} = 100$, and (c) $\kappa_{\mathrm{x},i}^{\mathrm{stretch}} = 300$. Dots indicate the calculated value of $\ln(B_{i,j})$, and lines indicate a line of best fit. γ_{MD} characterizes how "Maxwellian" the plasma is.

candidate submodels and can distinguish between interpolated submodel candidates accurately in accordance with the interpolation parameter γ_{MD} over decreasingly informative priors. However, the slope of the $\ln(B_{2,1})$ versus γ_{MD} decreases in magnitude with increasing prior widths (cases (b) and (c)), indicating that the models are harder to distinguish with wider priors.

3.8.3 Effects of Prior Inaccuracy

We wish to understand the effect of the accuracy of the mean of a prior PDF on the ability to distinguish candidate submodels as a function of SNR. To do this, $\ln(B_{2,1})$ is calculated using priors at varying levels of prior mean misinformation, with $\kappa_{\mathrm{x},i}^{\mathrm{shift}} \in \{1, 20, 30\}$ for all x_i except λ_{i}. The incident wavelength was fixed during this test, as the signal inversion is extremely sensitive to the center wavelength. Additionally, any shift past a percentage of 30 on any of the other variables led to uncomputable submodels, with the data processing code returning $\ln(B_{2,1})$ = 0 overall SNR values. The results are presented in Figure 3.6.

As opposed to the uniform stretching of the prior information, Figure 3.6 indicates that shifting the prior mean by as little as 1% leads to a rapid drop in support for the correct model, which is shown by the spread of the raw values of $\ln(B_{2,1})$. This is true even at moderately-high SNRs, above around 50, and gets progressively worse at larger shifts in the prior means from the true prior. Even small shifts in the prior mean with respect to the true value lead to persistent effects on the residuals that skew $\ln(B_{2,1})$, leading to the stark contrast between Figure 3.6 and Figure 3.4. This sensitivity to prior inaccuracy can be indicative of a very strong prior distribution compared to the information in the data. In such cases, it is often desirable to collect higher SNR data and use wider prior distributions, especially when considering extensions to higher-order mixtures of distribution functions.

Accurate discernment of the degree of Maxwellianization is evident at small prior information shifts from Figure 3.7. However, again, at large shifts from the true mean, the ability to discern the degree of Maxwellianization (γ_{MD}) is lost, even at high SNR.

The data above assumes perfect information about the laser intensity, λ_{i}. However, the same trends are also observed when the mean of λ_{i} is subjected to shifts of $\kappa_{\lambda_{\mathrm{i}}}^{\mathrm{shift}} \in \{0.01, .5\}$, indicating the sensitivity of the model selection on a very accurate estimate of the center wavelength. This means that when the laser wavelength is included as an unknown parameter, even sub-percentage errors in the estimates of the center wavelength lead to the complete loss of model distinguishability.

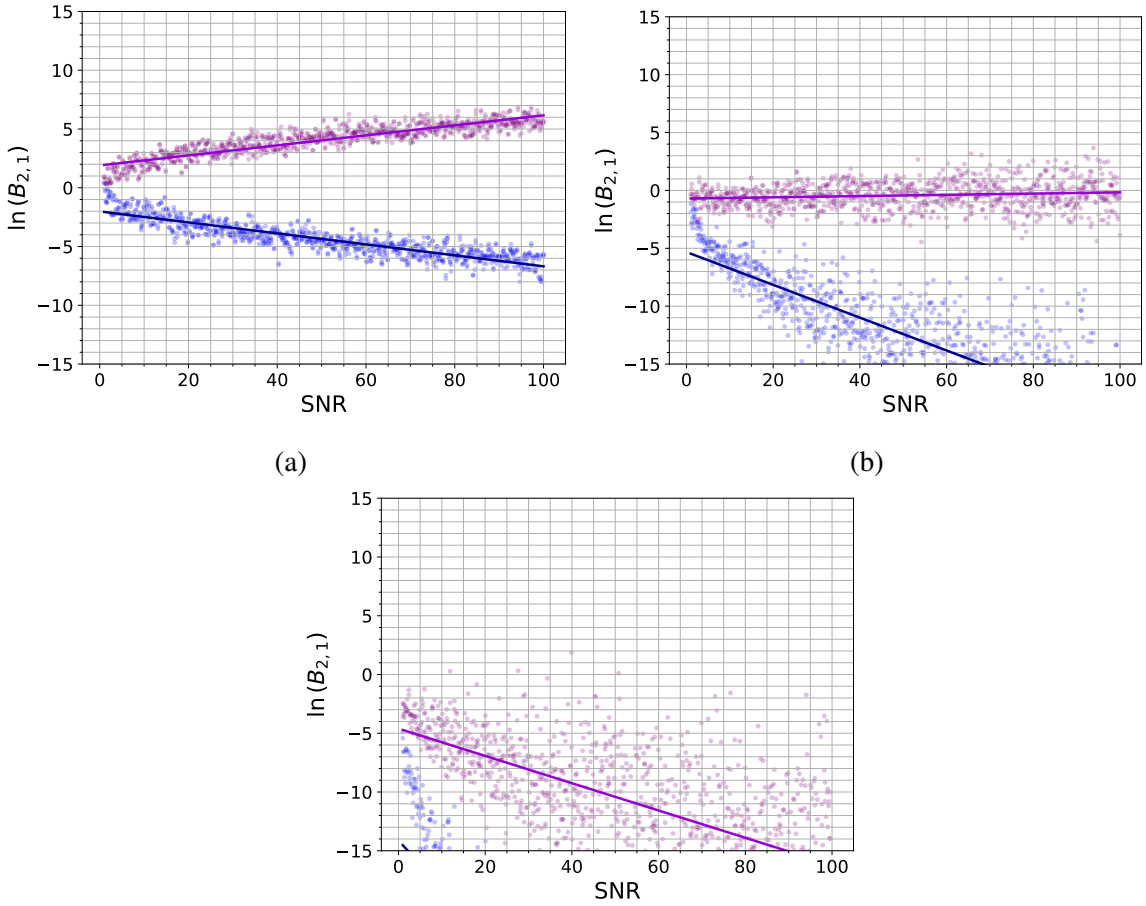

(a) (b)

(c)

Figure 3.6: $\ln(B_{2,1})$ versus SNR for decreasingly accurate priors: (a) $\kappa_{\mathrm{x},i}^{\mathrm{shift}}$ = 1, (b) $\kappa_{\mathrm{x},i}^{\mathrm{shift}}$ = 20, and (c) $\kappa_{\mathrm{x},i}^{\mathrm{shift}}$ = 30. Synthetic data generated from model M1 is in blue, and synthetic data generated from model M2 is in purple. Dots indicate the calculated value of $\ln(B_{i,j})$, and lines indicate a line of best fit. $|\ln(B_{i,j})|$ substantially greater than zero indicates that the Bayesian framework is able to correctly identify the right model.

3.8.4 Interactions of Inaccuracy and Uncertainty

To understand the effect of simultaneously inaccurate and uncertain prior PDFs on the ability to distinguish between candidate submodels, $\ln(B_{2,1})$ is calculated using priors at varying levels of prior mean and width misinformation, with $\kappa_{\mathrm{x},i}^{\mathrm{stretch}} \in \{10, 25, 100\}$ and $\kappa_{\mathrm{x},i}^{\mathrm{shift}} \in \{2, 5, 20\}$ for all x_i except for λ_{i}. λ_{i} was fixed during this test for the reason presented above. The results are shown in Figure 3.8.

Overall, the ability to accurately distinguish between candidate submodels is preserved

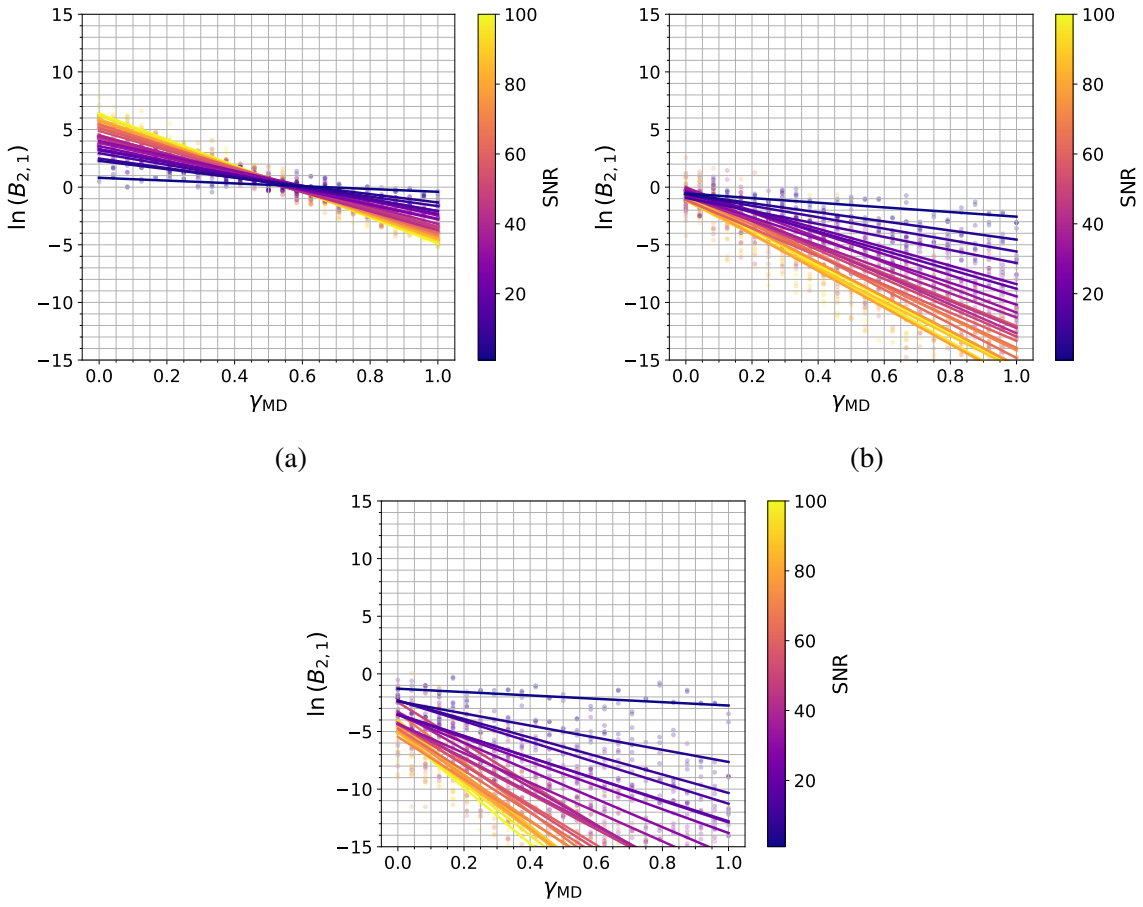

Figure 3.7: $\ln(B_{2,1})$ versus γ_{MD} at varying SNR levels over decreasingly informative priors with Model M_3: (a) $\kappa_{\mathrm{x},i}^{\mathrm{shift}} = 1$, (b) $\kappa_{\mathrm{x},i}^{\mathrm{shift}} = 20$, and (c) $\kappa_{\mathrm{x},i}^{\mathrm{shift}} = 30$. Dots indicate the calculated value of $\ln(B_{i,j})$, and lines indicate a line of best fit. γ_{MD} characterizes how "Maxwellian" the plasma is.

over SNRs greater than five, getting worse as the priors diverge from the true priors. However, there is an artificially inflated and artificially deflated support for the Maxwellian and Druyvesteyn models, respectively, as the priors diverge from the true priors, indicating that poorer initial construction of the information in the priors results in an incorrect preference for a Maxwellian submodel. These trends are mirrored in Figure 3.9, indicating that the ability to discern small deviations from Maxwellian or Druyvesteyn submodels is lost even at values of $\gamma_{\mathrm{MD}} = 0$, with an inflated preference for the Maxwellian submodel. In short, even for small deviations from a Druyvesteyn submodel, incorrect priors may artificially

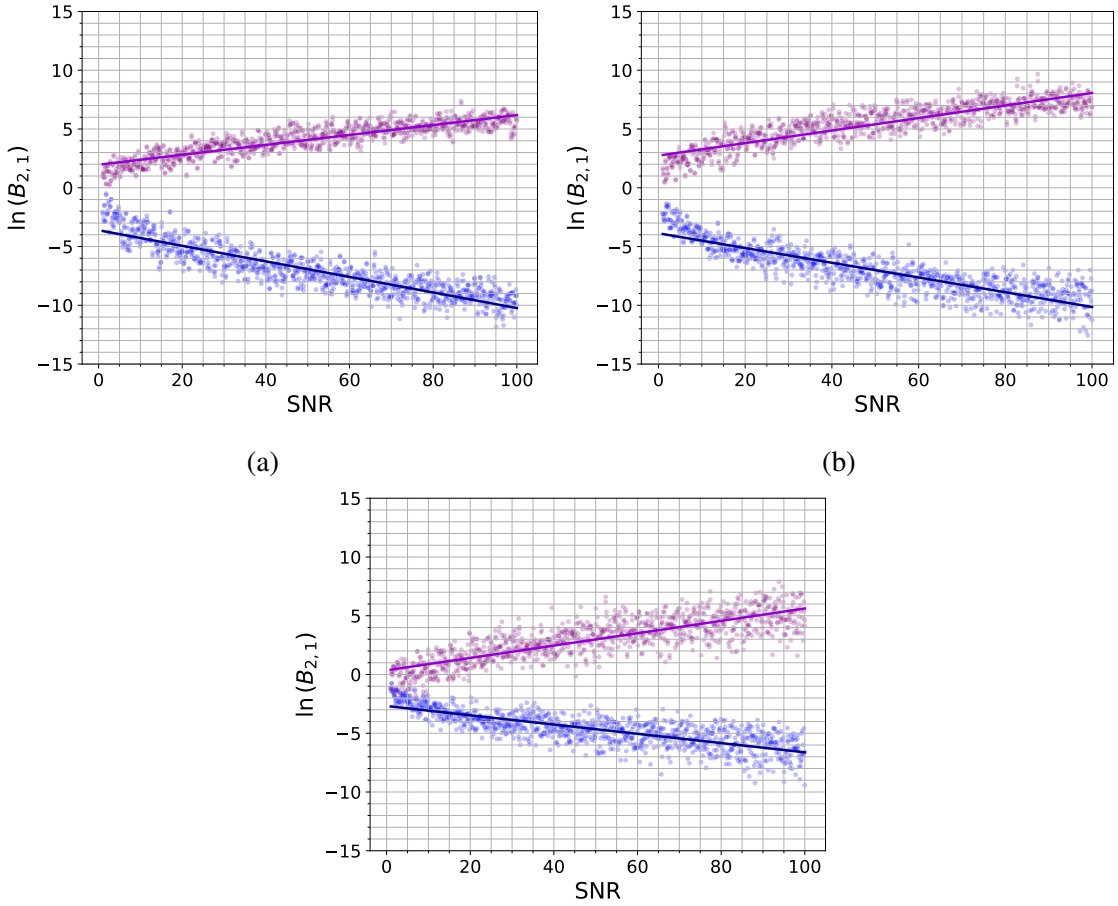

(a) (b)

(c)

Figure 3.8: $\ln(B_{2,1})$ versus SNR over decreasingly informative priors: (a) $(\kappa_{\mathrm{x},i}^{\mathrm{stretch}},\ \kappa_{\mathrm{x},i}^{\mathrm{shift}}) = (10,\ 2)$, (b) $(\kappa_{\mathrm{x},i}^{\mathrm{stretch}},\ \kappa_{\mathrm{x},i}^{\mathrm{shift}}) = (25,\ 5)$, and (c) $(\kappa_{\mathrm{x},i}^{\mathrm{stretch}},\ \kappa_{\mathrm{x},i}^{\mathrm{shift}}) = (100,\ 20)$. Synthetic data generated from model M1 is in blue, and synthetic data generated from model M2 is in purple. Dots indicate the calculated value of $\ln(B_{i,j})$, and lines indicate a line of best fit. $|\ln(B_{i,j})|$ substantially greater than zero indicates that the Bayesian framework is able to correctly identify the right model.

prefer a Maxwellian submodel, even if they are wide enough to include the true mean.

The cases presented in Secs. Subsection 3.8.3, Subsection 3.8.2, and Subsection 3.8.4 indicate the necessity of well-constructed priors. However, the uncertainty bounds and correlations provided by a least-squares inference need to be validated by comparing the posterior generated using the Laplace approximation to the posterior PDF using MCMC sampling. This is explored in Subsection 3.9.2. Additionally, the artificial preference of a Maxwellian submodel, even when the candidate submodels being compared are parame-

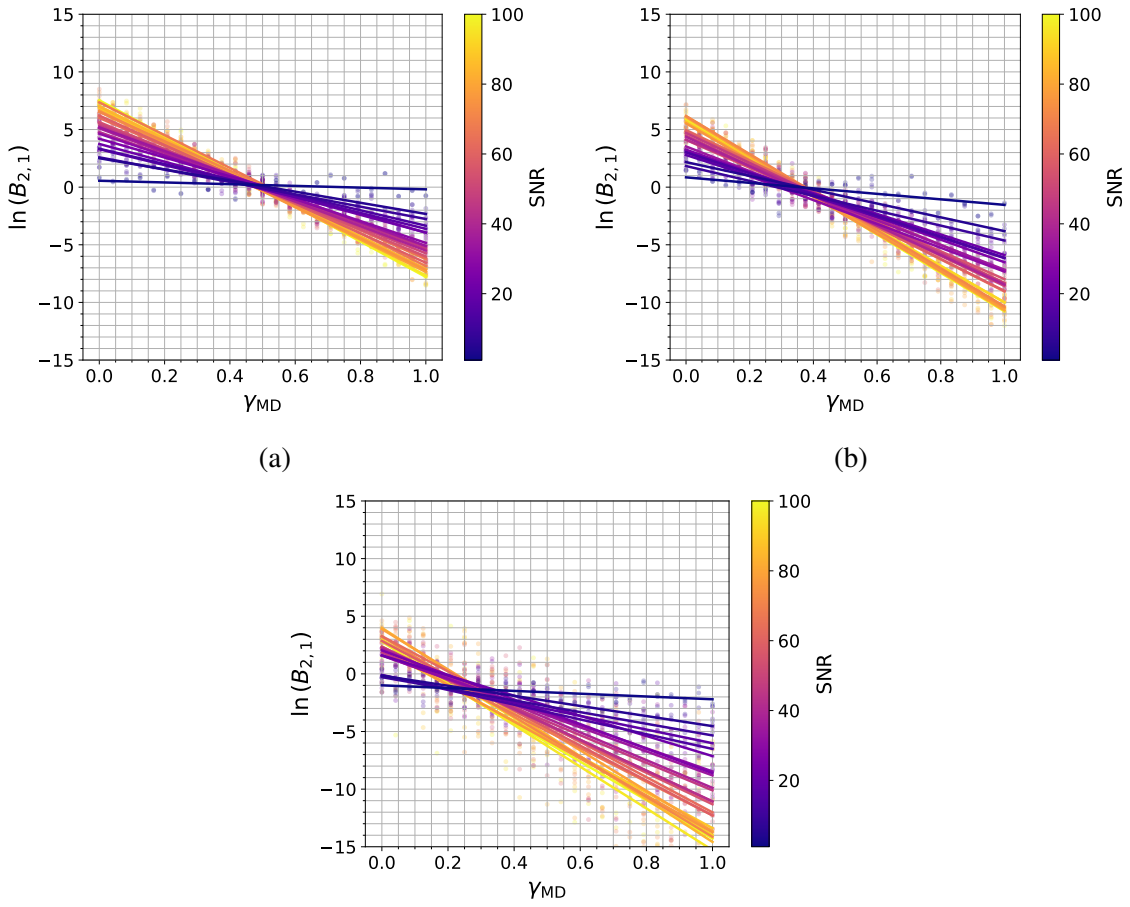

Figure 3.9: $\ln(B_{2,1})$ versus γ_{MD} at varying SNR levels over decreasingly informative priors: (a) $(\kappa_{\mathrm{x},i}^{\mathrm{stretch}},\ \kappa_{\mathrm{x},i}^{\mathrm{shift}}) = (10,\ 2)$, (b) $(\kappa_{\mathrm{x},i}^{\mathrm{stretch}},\ \kappa_{\mathrm{x},i}^{\mathrm{shift}}) = (25,\ 5)$, and (c) $(\kappa_{\mathrm{x},i}^{\mathrm{stretch}},\ \kappa_{\mathrm{x},i}^{\mathrm{shift}}) = (100,\ 20)$. Dots indicate the calculated value of $\ln(B_{i,j})$, and lines indicate a line of best fit. γ_{MD} characterizes how "Maxwellian" the plasma is.

terized with the same $\mathbf{x}$, brings into question how the fidelity of the model, or models with increased parameter spaces, affects the selection of the model. This question is explored in Subsection 3.8.5

3.8.5 Transdimensional Model Selection

To understand the effect of model fidelity on the ability to distinguish between candidate submodels as a function of SNR, data are generated using models M_1, M_2, M_3, and M_4 according to the parameters in Table 3.6. Then, the values of $\ln(B_{2,1})$, $\ln(B_{3,1})$, and $\ln(B_{4,1})$

are calculated twice using 1,000 samples drawn from the actual data generating (true) priors at 1,000 SNRs between 1 and 100.

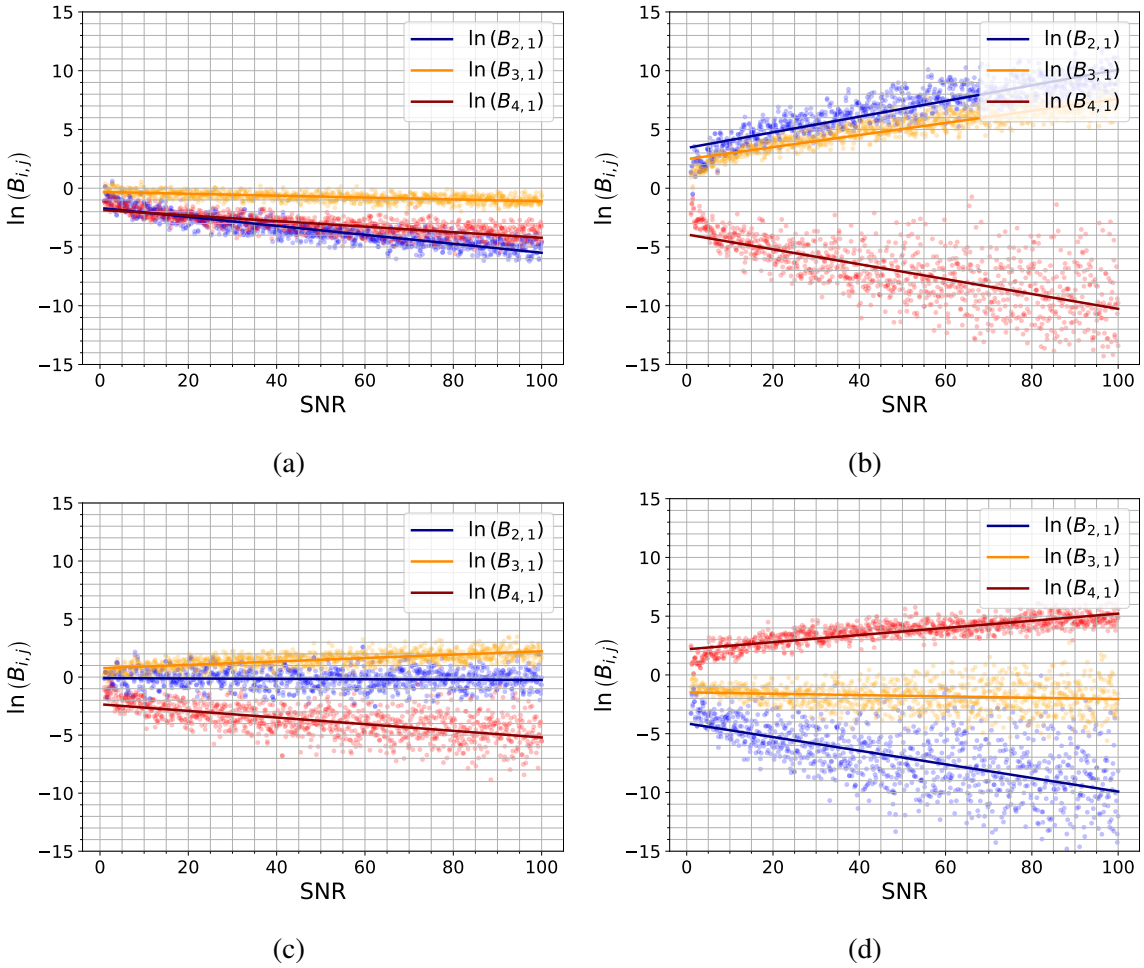

Figure 3.10: $\ln(B_{i,j})$ versus SNR over several data generation cases; (a) data generated with M_1, (b) data generated with M_2, (c) data generated with M_3, and (d) data generated with M_4. $\ln(B_{2,1})$ (blue), $\ln(B_{3,1})$ (orange), $\ln(B_{4,1})$ (red). Dots indicate the calculated value of $\ln(B_{i,j})$, and lines indicate a line of best fit.

The results are given in Figure 3.10. In case (a), with data generated via M_1, the $\ln(B_{i,j})$ indicate that, in the case where the true data are Maxwellian, regardless of which model is being compared to the Maxwellian model, the model selection framework is able to discern the correct model.

In case (b), with data generated with M_2, $\ln(B_{2,1}) > \ln(B_{3,1}) > \ln(B_{4,1})$, with the spread of $\ln(B_{2,1})$ and $\ln(B_{3,1})$ both being less than $\ln(B_{4,1})$. This indicates that the model

selection framework was able to correctly distinguish between the models. This is due to the fact that $\ln(B_{3,1})$ was a single temperature, multi-model distribution. Values of γ_{MD} near zero would effectively create the same distribution as model M_2, leading to a higher preference than model M_4 because the temperatures were not allowed to overlap in the data-generating priors.

In case (c), with data generated with M_3, $\ln(B_{3,1}) > \ln(B_{2,1}) > \ln(B_{4,1})$ also indicates the ability to correctly determine the model, as well as the preference for M_1 over the higher parameter space M_4. This is likely due to the non-overlapping temperatures for M_4 making it impossible to generate an equivalent single temperature distribution.

Finally, in case (d), with data generated with M_4, $\ln(B_{4,1}) > \ln(B_{3,1}) > \ln(B_{2,1})$. Again, the ability to discern the correct model is clear. The order of preference is also expected. That is, because M_1 and M_2 are single temperature and density fraction models, they are not able to properly fit the intermediate shapes created by the superposition of EVDFs with multiple temperatures and number density fractions.

Cases (a)–(d) indicate that the assumption of equally probable priors on the models, $\mathbb{P}(M_i) \approx \mathbb{P}(M_j)$ used in deriving Equation 3.66 is valid over the fidelity of the models evaluated, as compared to the Maxwellian submodel. Additionally, increasing model fidelity does result in a preference for the correct submodel that best describes the data, validating the model selection framework.

3.9 Application of Bayesian LTS Methods to ns-Pulsed Plasmas

We now demonstrate the Bayesian LTS model selection and signal inversion process using experimental data. An LRS-calibrated LTS system was developed for an optically-accessible, stainless-steel, pressure-controlled vacuum cell that was designed to generate pulsed and steady-state DC discharge plasmas. However, at high steady-state bias voltages, arcing events prevent the collection of spectra due to plasma instability; the ns-pulsed plasma was chosen for study here.

3.9.1 Experimental Setup

This section provides a brief description of the system outlined in Chapter 4. The plasma was generated by kV-level biases between a set of stainless steel electrodes with 24-mm diameter, 26.53-mm spacing. The electrodes were floating with respect to the stainless-steel body of the vacuum cell, which was tied to the electrical ground. Power feedthroughs isolated the discharge electrodes from the vacuum test cell, ensuring that their base configuration was floating with respect to the vacuum cell and, therefore, with respect to the electrical ground. The voltage pulse width was 200 ns, with a 100 Hz frequency. A sample discharge image and a setup schematic are given in Figure 3.11 (a).

Thomson and Raman scattering were stimulated by the second harmonic output of a pulsed Nd:YAG laser (Quantel Q-Smart 850, 200 mJ/pulse). The interrogation was steered, shaped, polarization-aligned, and focused into the test section using a series of mirrors, lenses, half-wave plates, and polarizing beamsplitter cubes, then transmitted to the plasma through Brewster windows on the vacuum cell. The scattered light was collected, relayed, and imaged onto the spectrometer using achromatic optics. A diagram of the detection system optical setup is presented in Figure 3.11(b). The system detection solid angle, $\Delta\Omega$, was optimized by maximizing the collection angle of the first collection lens while using the two volume Bragg-grating notch filters (BNFs) as marginal- and chief-ray-limiting apertures. Two BNFs (Optigrate BNF-532-OD4) were used to filter the centerline laser Rayleigh scattering and reflections to maximize the usable length along the interrogation beam waist, see Reference [162] for details. LRS and LTS signals were detected by an intensified camera (Princeton Instruments PM4-1024i-HB-FG-18-P46, 15-ns gate, 3000 shots) coupled to a spectrometer (Princeton Instruments Isoplane 320A, 2400 l/mm grating). A delay generator (Berkeley Nucleonics BNC-577) controlled the relative timing of the detector gate delay with respect to the laser Q-switch to maximize the signal collected on the detector. The delay generator also controlled the relative timing of the laser and ns-pulsed power supply trigger, thus allowing measurements at different times in the pulsed

plasma cycle. Descriptions of previous iterations of the plasma and LTS facilities at Georgia Tech and Texas A&M University can be found in Bak *et al.* [162]. A diagram of the detection system optical setup is presented in Figure 3.11. Please see Reference [175] for a detailed description of the LTS and plasma cell used in this work.

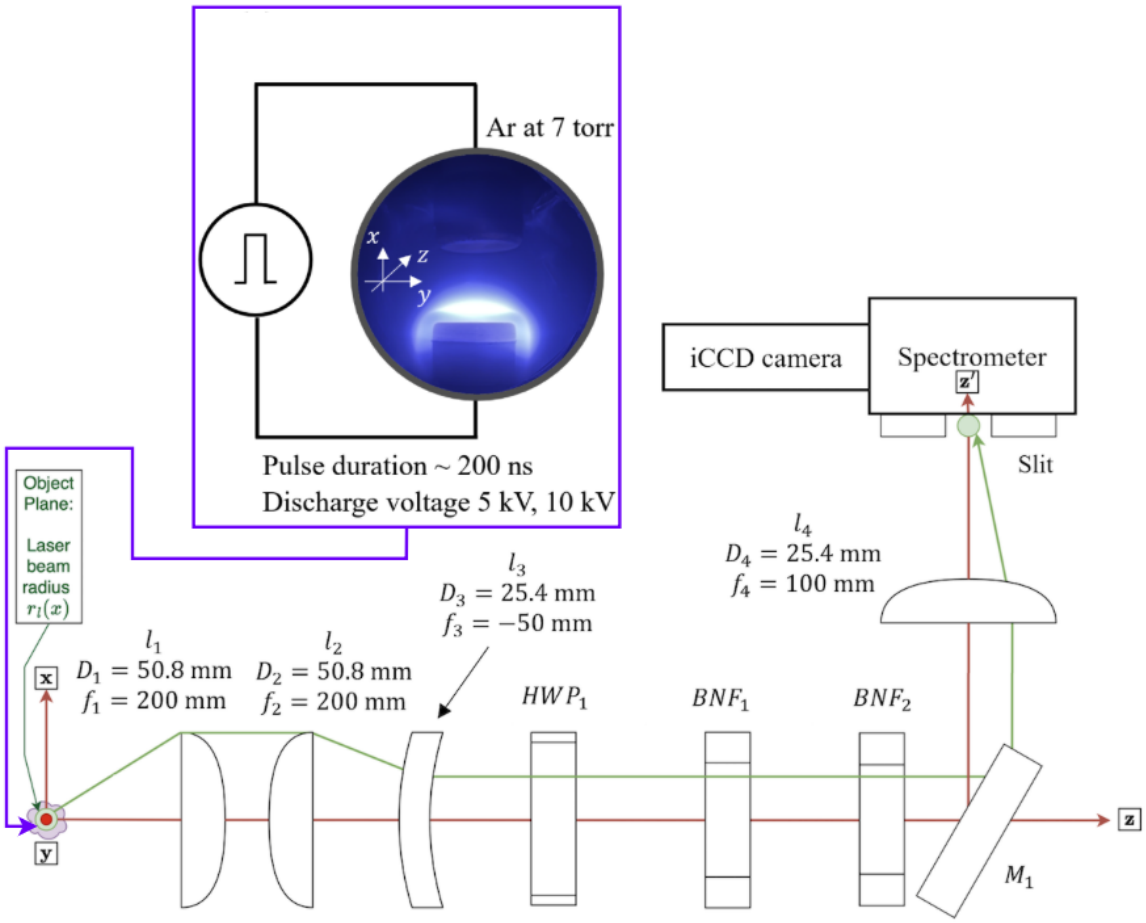

Figure 3.11: A nanosecond pulsed discharge setup and a sample discharge image as well as the diagram of the collection system optical setup . The interrogation laser beam propagates in the x direction, is polarized in the y direction, and the scattering is collected in the z direction. M, l, HWP and BNF are acronyms for mirrors, lenses, half wave plates, and Bragg notch filters, respectively.

LRS was collected at N_2 neutral background pressures of 10, 7, and 4 Torr. Then, a background spectrum, B_r, was taken at the 0.8 Torr base pressure of the system. The subtraction of these two signals left the pure Raman spectrum to be analyzed. For the LTS measurements, plasma was generated at 7 Torr Ar neutral background pressure with two

discharge voltages, 5 and 10 kV. At each LTS condition, measurements were obtained with the plasma on, laser on; plasma off, laser off, and plasma off, laser on. These signals were appropriately subtracted, following Ref. [140], to yield the LTS spectrum to be analyzed.

3.9.2 Bayesian Inference and Model Selection

In order to compare the Laplace approximation described in Subsection 3.7.3 to that of a full MCMC-sampled Bayesian inference, the nonlinear least square method was used to determine the relevant QoI and their variance. The parameter vectors used were

$$\mathbf{x}_{\mathrm{LS}}^{\mathrm{R}} = [T_{\mathrm{g}}, \tau, \eta, \lambda_{\mathrm{i}}], \tag{3.72}$$

and

$$\mathbf{x}_{\mathrm{LS}}^{\mathrm{T}} = [T_{\mathrm{e}}, n_{\mathrm{e}}, v_{\mathrm{d}}] \tag{3.73}$$

for the least-squares optimization. Variables that have the same effect on the inference of interest – like p_{g} and η on the Raman inference, or η and n_{e}, or v_{d} and λ_{i} on the Thomson inference– are not easily decoupled and their uncertainty is not included using the standard least-squares residuals methods. At each target Raman pressure, the expected value and variance of p_{g} was estimated using the mean and square of the standard deviation of the pressure trace. Then, a scaled and shifted Gaussian was fit to the B_{r} signal to provide initial estimates of τ and λ_{i}. The initial estimate of the gas temperature, T_{g}, was chosen to be 295.15 K. The temperature bounds were chosen to be ± 10 %, and the other variables in the LRS LS vector were allowed to range $\pm 100\%$.

The least-squares method was used to determine $\mathbf{x}_{\mathrm{LS}}^{\mathrm{R}}$ and its variance, $\delta\mathbf{x}_{\mathrm{LS}}^{\mathrm{R}}$, in accordance with a 95% confidence interval procedure [22], after approximating the least-squares covariance matrix. The least-squares covariance matrix, $\mathbf{\Gamma}_{\mathrm{LS}}$, is approximated using the

Jacobian, $\mathbf{J}$, from the least-squares algorithm in the Python package,

$$\mathbf{\Gamma}_{\mathrm{LS}} \approx \frac{\left(\mathbf{J}^{\top}\mathbf{J}\right)^{-1}\mathrm{diag}(\mathbf{e})^{2}}{N_{\lambda} - \mathrm{length}(\mathbf{x}_{\mathrm{LS}})}, \tag{3.74}$$

where $\mathbf{A}^2 = \mathbf{AA}$. This same method is used to quantify the uncertainty in the LTS case. Two fitted spectra are presented in Figure 3.12.

In order to calculate $\mathbf{x}_{\mathrm{LS}}^{\mathrm{T}}$, λ_{i} and η are assumed to be constant at their optimal value for reasons stated previously, and their uncertainty is not propagated forward. This leads to a possible solution for each individually collected Raman spectrum, although in the ideal case, they should all produce the same value of λ_{i} and η. There can be a small to possibly large variation in these parameters, specifically η, which can produce very different results in the inversion of the Thomson signal for n_{e} and v_{d}. Ignoring the uncertainty in η and comparing it to Bayesian inference will provide insight into when it is necessary to propagate the uncertainty in η forward and when it is appropriate to simply use the uncertainty from the least-squares residuals.

The value of the relevant LS-LRS inference parameters η and λ_{i} where each $\mathbf{x}_{\mathrm{LS}}^{\mathrm{R}}$ evaluated is shown in Figure 3.13. The source of the 10% variation in the mean values of η in Figure 3.13 can be attributed to several factors. The vacuum cell pumpdown compression is expected to be μm order. The laser itself has an energy stability of 4% and pointing stability of at most μrad. The combination of which could possibly lead to micro movements of the beam height and lateral location in the test section compounding into the observed 10% variation in η.

Generally, uncertainty in λ_{i} is due to relative misalignment of the image of the laser beam on the detector relative to the calibrated center wavelength pixel on the detector. This is why λ_{i} is included as a QoI. When the system has tight alignment, random fluctuations in the calculated values between Raman signals are expected, but like in our case, the fluctuations will be much less than 1%. Additionally, micro-movements of the beam

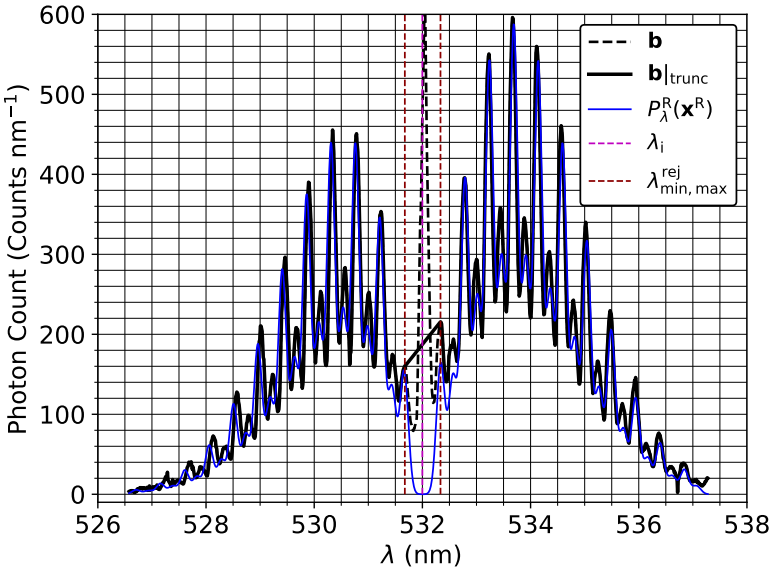

(a)

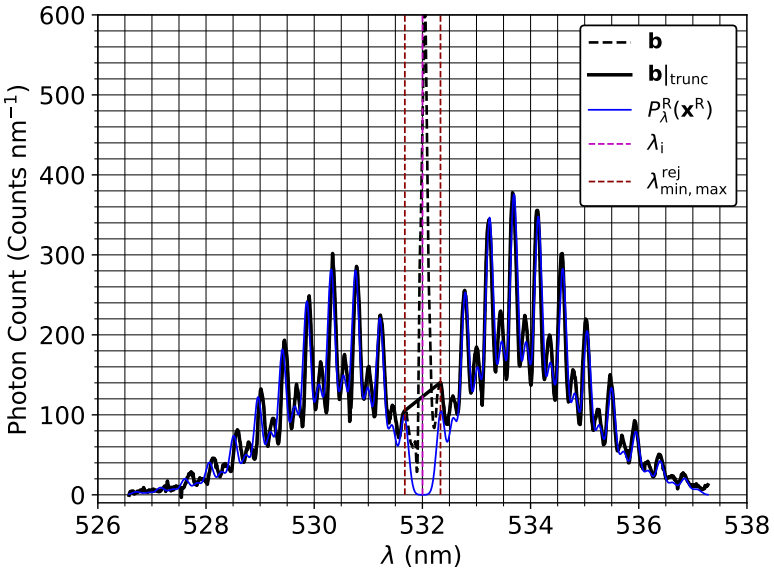

(b)

Figure 3.12: Raman least-squares fit at two background pressures; (a) p_{g} = 10 Torr, and (b) p_{g} = 7 Torr. The data and rejected data lines are presented in black and black-dashed. The estimated center wavelength is presented with a purple-dashed line, and the rejected data region is presented with red-dashed lines.

perpendicular to the spectrometer slit would introduce small changes in the calculated λ_{i} from the LRS inversion. This can be eliminated by assuming that λ_{i} is 532 nm. That assumption may allow for better relative bulk velocity measurements but will likely result

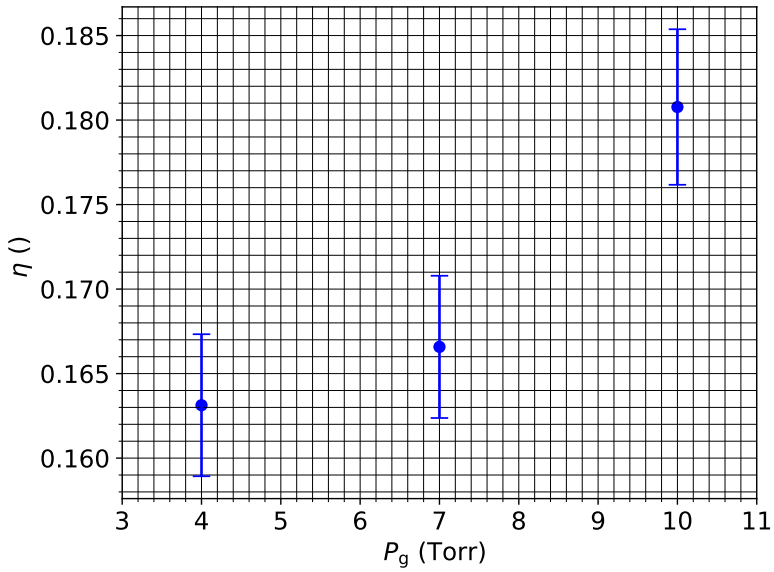

(a)

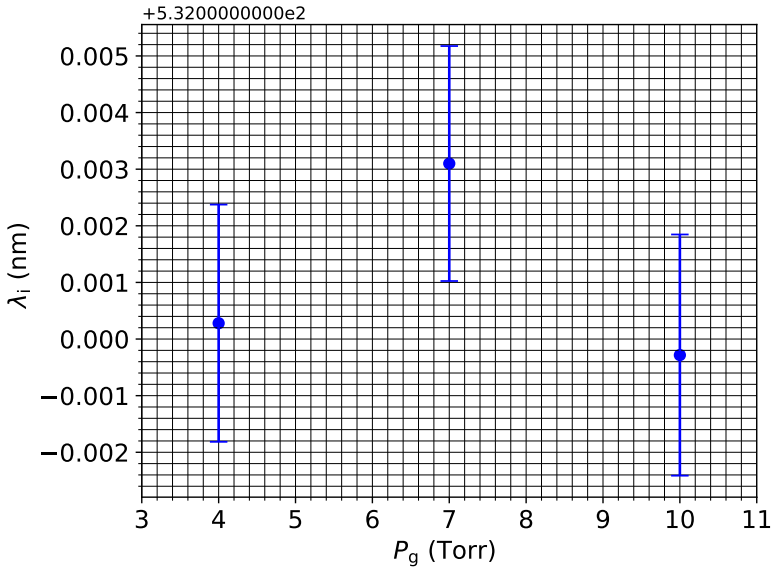

(b)

Figure 3.13: Raman least-squares inferred parameters versus p_g ; (a) η, and (b) λ_i.

in less accurate FWHM, neutral gas temperature, and calibration constant measurements when misalignment is prevalent.

At each value of η and λ_i from the LS-LRS, the bounds used for the LS-LTS inversion were T_{e_o} = 10 eV, n_{e_o} = 1×10^{20} m^{-3}, and v_d = 0 km s^{-1}, all bounded by $\pm 100\%$. The collected Thomson spectra are presented in Figure 3.14. The QoI calculated from each of

the 7 Torr Raman conditions is presented in Figure 3.15.

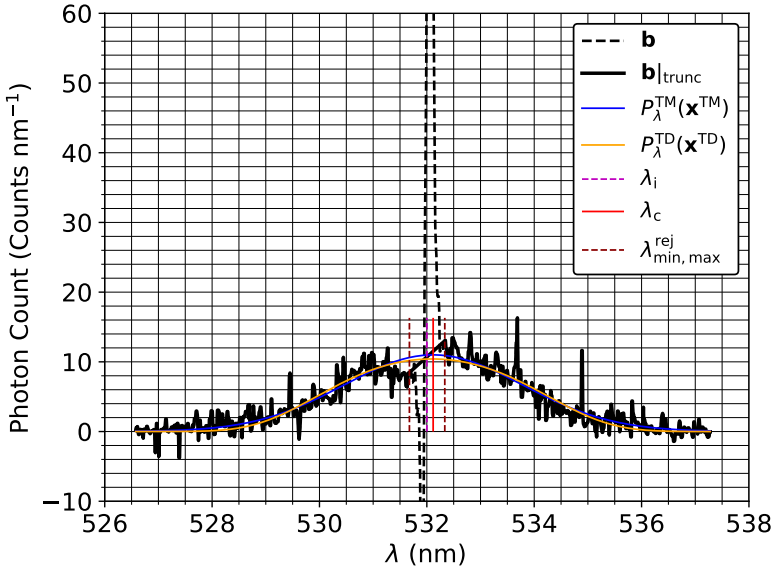

(a)

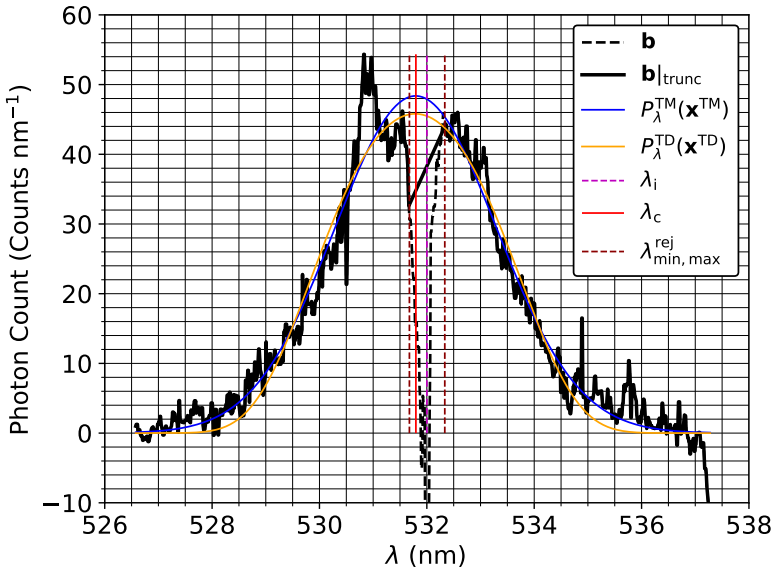

(b)

Figure 3.14: Thomson least-squares fit at two discharge voltages; (a) V_{D} = 5 kV and (b) V_{D} = 10 kV. The data and rejected data lines are presented in black and black-dashed. The estimated center wavelength is presented with a purple-dashed line, and the rejected data region is presented with red-dashed lines. The SNR estimates using the Maxwellian and Druyvesteyn submodels are 4 and 5 in (a) and 15 and 14 in (b), respectively.

The uncertainty in the calculated LRS parameters that are nuisance parameters in the

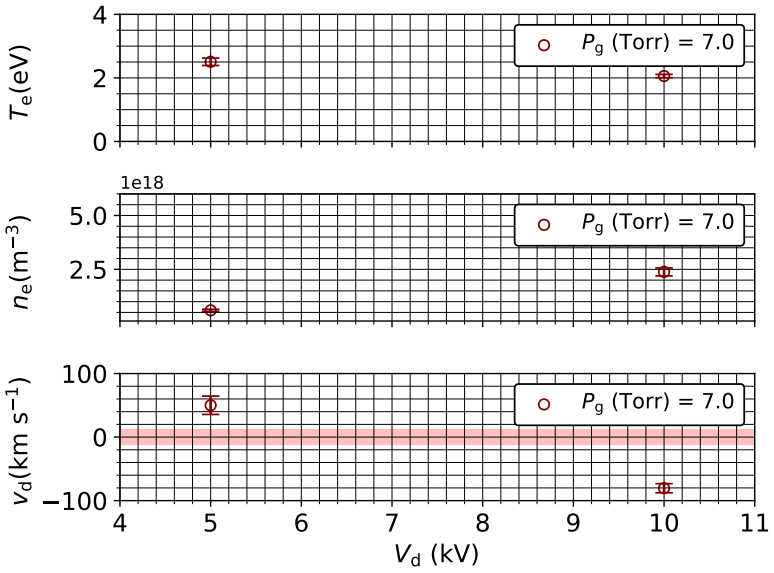

(a)

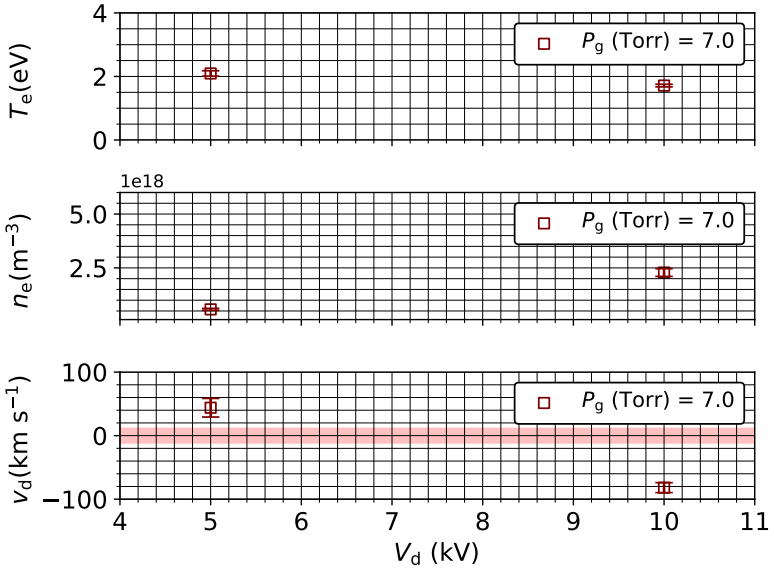

(b)

Figure 3.15: Individual elements of the Thomson QoI $\mathbf{x}_{\mathrm{LS}}^{\mathrm{T}}$ versus V_{D}. The Maxwellian submodel inversion is shown in (a) with a circle marker, and the Druyvesteyn submodel in (b) with a square marker.

LS-LTS inference at a given pressure has no effect on the electron parameters because there was no way of incorporating that information using the LS residuals method directly without additional uncertainty propagation. However, the predicted electron number density

shows a large dependence on the predicted optical efficiency constant η across pressures at each given LS-LRS condition. Additionally, the predicted value and uncertainty are highly dependent on the model chosen to invert the signal of interest. This likely is due to the inability of the LS residuals method to robustly include information like the LRS uncertainty profile into the LTS analysis. This further motivates our more robust Bayesian method for including the relevant uncertainty profile from the LRS inference into that Thomson signal inversion.

Hence, the Bayesian inference framework was implemented for the LTS submodels M_1 and M_2. The general methodology follows that outlined in Section 3.7. The Bayesian inference model parameter vectors are taken as the same vectors presented in Section 3.4. The priors are described in Table 3.7, and the results are presented below. These ranges set the $3\sigma_{\mathrm{x},i}$ values for the Gaussian prior PDFs described in Eqs. Equation 3.58, Equation 3.59, and Equation 3.60.

Table 3.7: Description of the $3\sigma_{\mathrm{x},i}$ ranges for the LRS case at 7 Torr.

Parameter	**Minimum**	**Maximum**
p_{g}	$0.99 * p_{\mathrm{g_o}}$	$1.01 * p_{\mathrm{g_o}}$
T_{g}	250	350
τ	0	0.5
η	0	1
λ_{i}	531	533

A one million-element long Markov chain was constructed using a custom Metropolis–Hastings algorithm implemented in Python. This system was was used to sample the log posterior for the 7 Torr Raman scattering spectrum. The chain was started at the LS-MAP estimate to reduce burn-in time. The marginal and joint posterior distribution functions are presented in Figure 3.17.

The prior was sampled as a set of independent Gaussian distributions, shown in Figure 3.16 in orange. The least squares posterior was constructed as follows; given that the pressure, p_{g}, was not included in the least squares inference, the prior was sampled. For

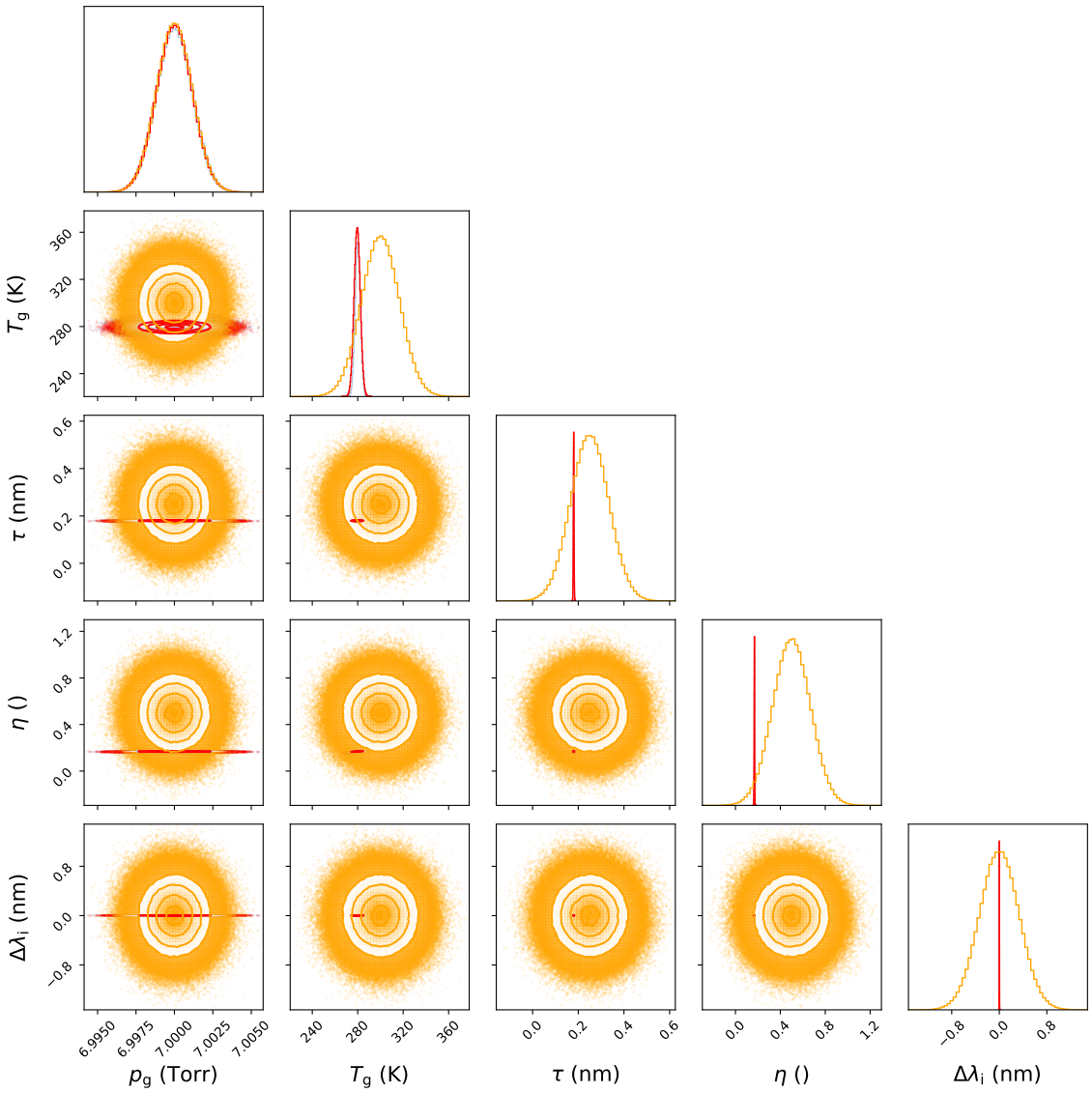

Figure 3.16: LRS marginal and joint posterior distribution functions for all LRS model inputs along with the prior and least squares posterior estimates. Samples from the prior are in orange, and the Bayesian and LS posteriors in steel blue and red.

the rest of the variables included in $\mathbf{x}_{\mathrm{LS}}^{\mathrm{R}}$, the least squares MAP estimate and the covariance matrix were used to sample from a multivariate Gaussian distribution; this is shown in Figure 3.17 in red. The Markov chain samples are shown in steel blue.

Across all cases except for the neutral gas pressure, the width of the priors is larger than that of the posterior estimates. Additionally, the priors used for Bayesian inference covered a wider range than those for the least square case. However, least-squares posterior esti-

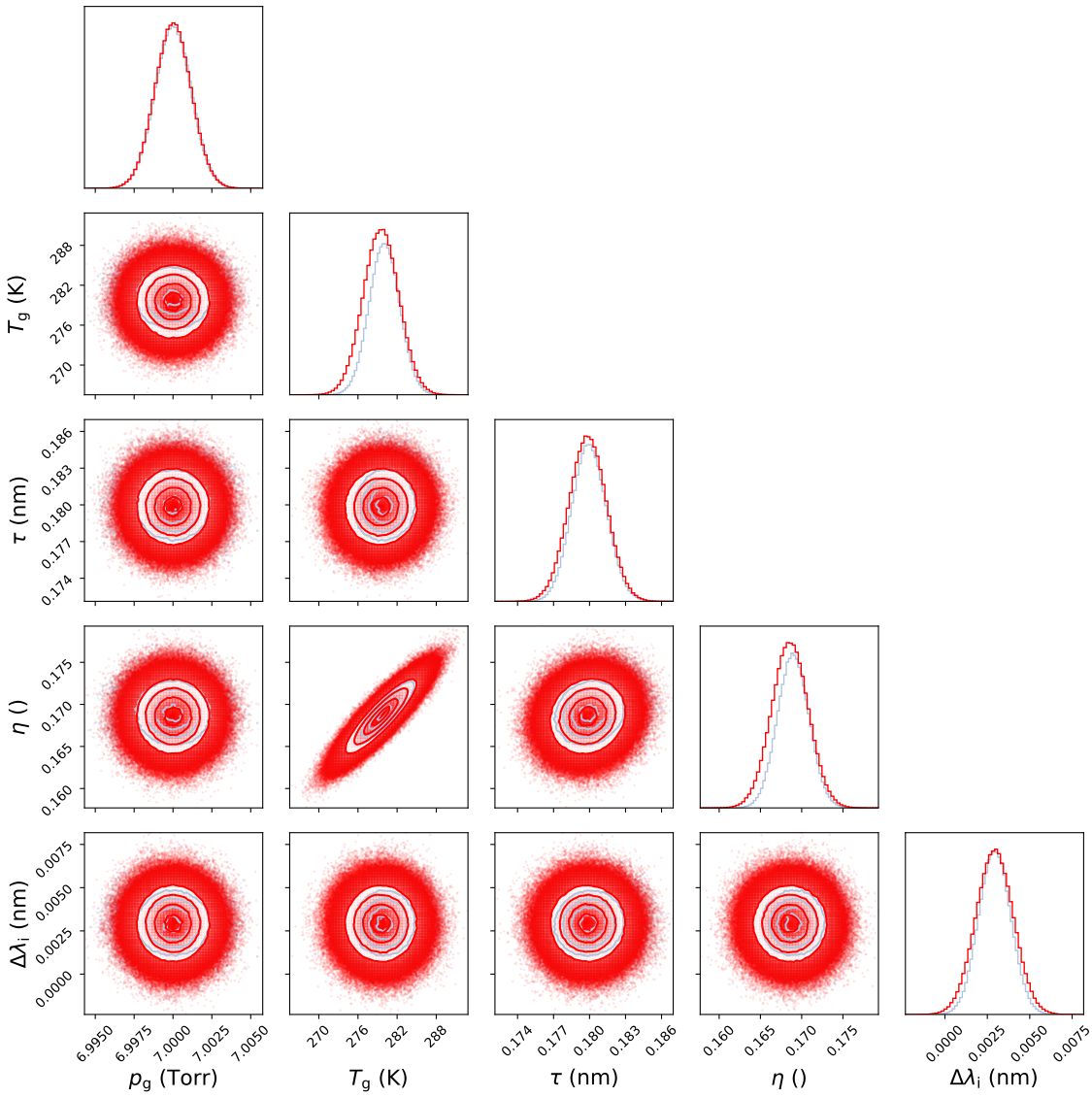

Figure 3.17: LRS marginal and joint posterior distribution functions for all LRS model inputs along with the prior and least squares posterior estimates. The Bayesian and LS posteriors are presented in steel blue and red.

mates for the LRS case are consistent with Bayesian inference estimate. The case presented here covers the most conservative estimate of the priors, i.e, the case where the priors were the widest. This shows that even for generally uninformed priors the least squares provides comparable uncertainty and parameter correlations.

Similarly, in the Thomson case, for both models M_1 and M_2, a one million element length Markov chain was sampled. The priors for the nuisance parameters of the LS in-

Table 3.8: Description of the $3\sigma_{\mathrm{x},i}$ ranges for the LTS case at 7 Torr neutral background pressure 10 kV.

Parameter	**Minimum**	**Maximum**
$T_{\mathrm{e}}^{\mathrm{M}}$	0	100
$T_{\mathrm{e}}^{\mathrm{D}}$	0	100
n_{e}	1×10^{16}	5×10^{20}
v_{d}	-1000	1000

ference were set from the posterior of the LRS inference. The priors for the LS QoI are described in Table 3.8, and the results are presented below.

Figure 3.18 shows marginal and joint posterior PDFs for both the Druvesteyn and Maxwellian models, with the Maxwellian model in blue and the Druyvesteyn model in orange, their LS posterior estimates in purple and red, and their prior estimates in green. Figure 3.19 shows the same without the prior distribution. Again, the MAP estimates and uncertainty bounds seem to be in agreement, showing the utility and necessity as shown in the last section for accurate prior information. The joint posteriors show divergence in the correlations between variables. This is due to the addition of the nuisance parameter uncertainties in the probability model that were not available with simple least squares inversion. This indicates that the propagation of uncertainty, even for staged inferences like the one presented here, in which there is an LRS inference informing the nuisance parameters of the LTS inference, is very sensitive to the nuisance parameters of each previous inference.

As the width of the nuisance parameter priors increase, the more divergence between the MAP estimate and the most probable value from the Bayesian inference was observed. When the width of the prior for η in the LS inference was artificially increased by more than 15% the width of the posterior of the electron number density was observed to extend past 10% compared to the base case. This indicates that for low SNR LRS measurements, or cases like the one presented here where relatively high uncertainty between estimates of η are present, the LS estimated error bars are not representative of the true uncertainty and that propagation of the uncertainty on η or Bayesian inference is required.

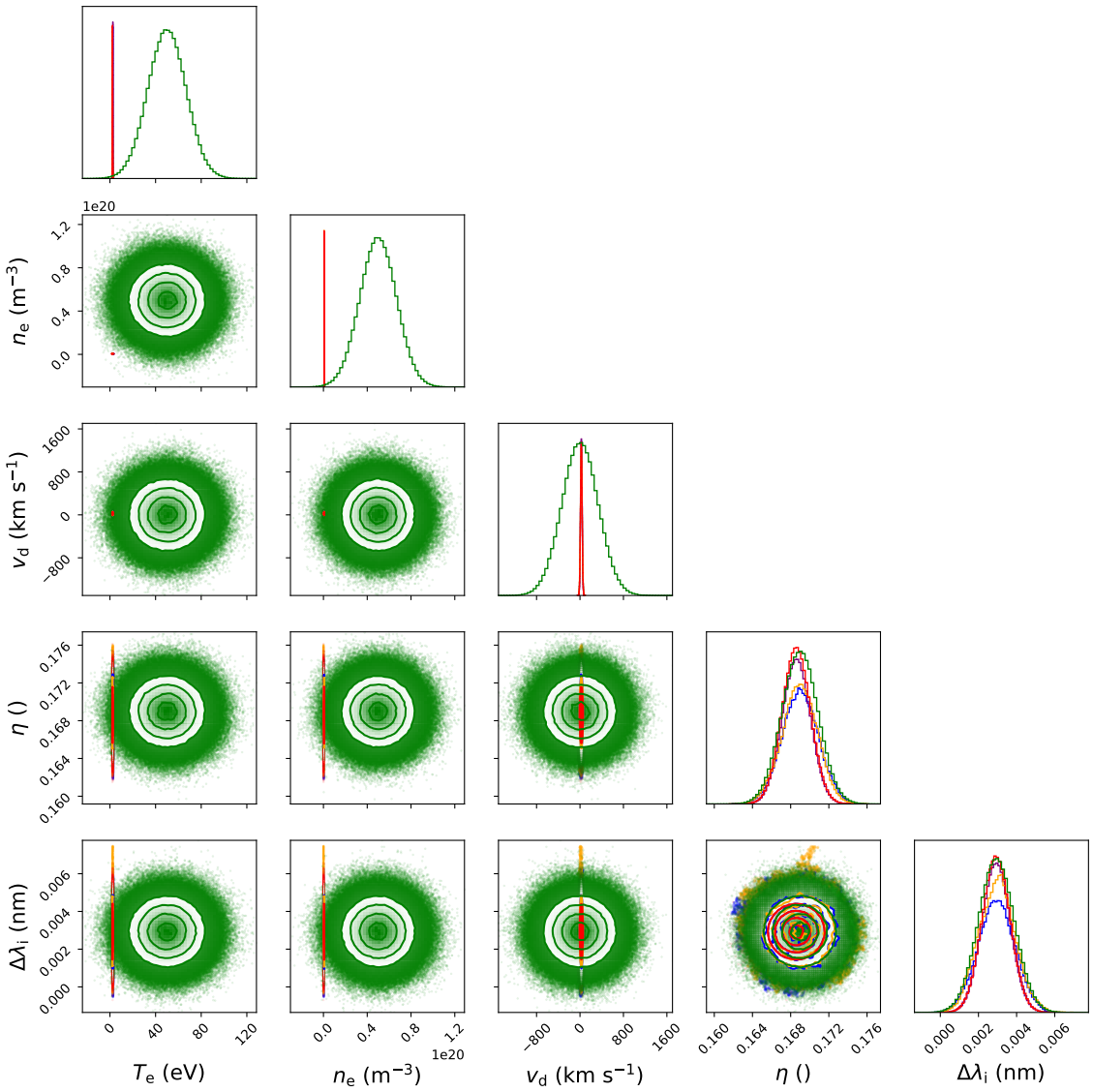

Figure 3.18: LTS marginal and joint posterior distribution functions for all LTS model inputs along with the prior and least squares posterior estimates. Samples from the prior are in green, the Bayesian posteriors for the Maxwellian and Druyvesteyn submodels in blue and orange, respectively as well as the posterior estimates of the LS inference in purple and red, respectively.

The consistency in predicting a lowermost probable electron number density and electron temperature in the Druyvesteyn cases with similar uncertainty profiles and with all other most probable QoI having almost identical predictions indicates the importance of selecting the best model. Selecting the best model based on the available information and fidelity of the inferences is important as the predicted electron temperatures and densities

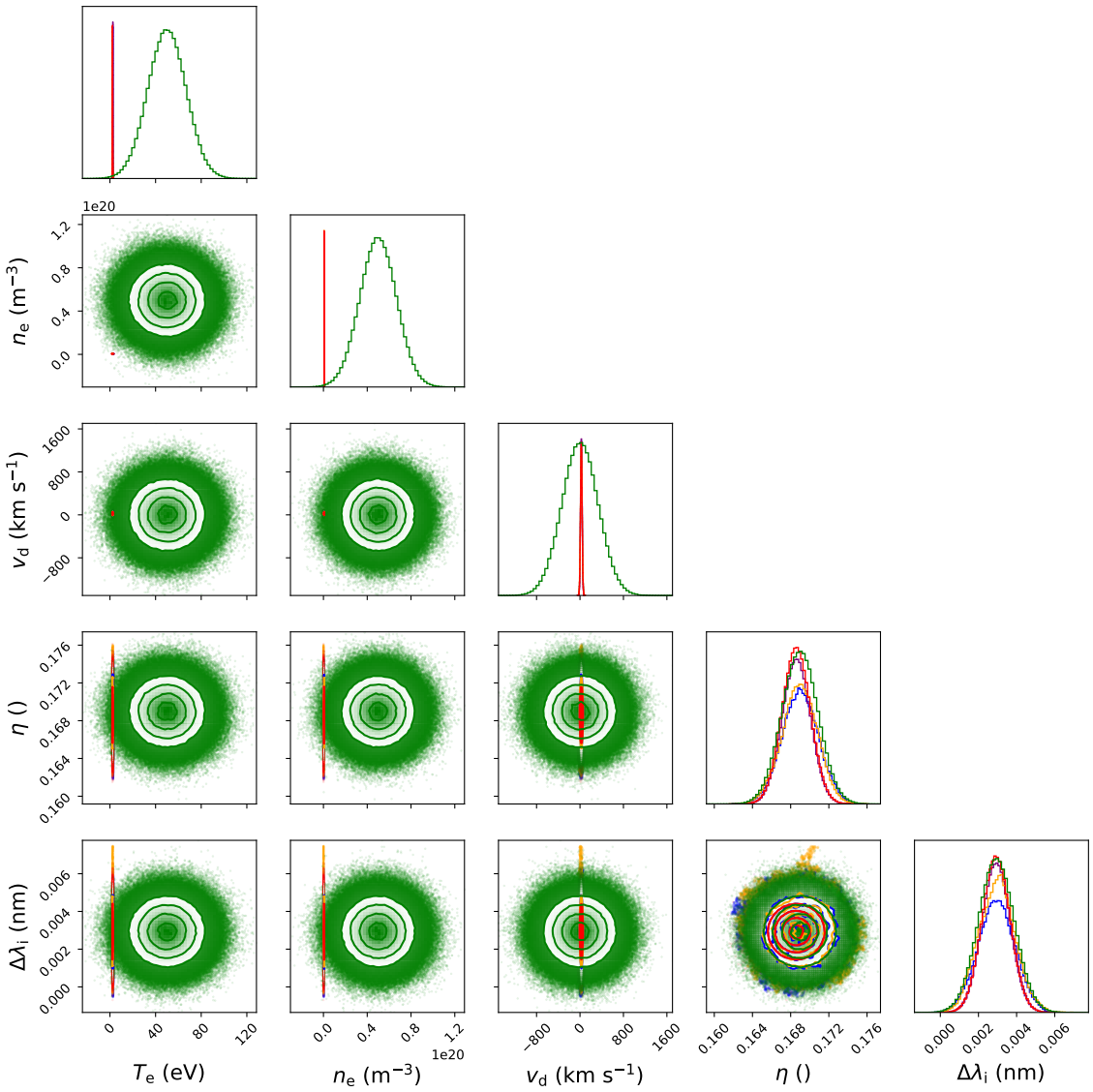

Figure 3.19: LTS marginal and joint posterior distribution functions for all LTS model inputs along with the prior and least squares posterior estimates. The Bayesian posteriors for the Maxwellian and Druyvesteyn submodels are in blue and orange, respectively as well as the posterior estimates of the LS inference in purple and red, respectively.

can vary up to 10 and 15 percent, respectively.

The $\ln(B_{2,1})$ were calculated using 250,000 samples and were approximately 0 in both cases. This is due to the fact that, as stated in the previous section, inaccurate priors lead to indistinguishably of the models. Calculating the values $\ln(B_{2,1})$ using 250,000 samples and drawing from a uniform prior that was constructed using the minimum and maximum

values across both Maxwellian and Druyvesteyn posteriors were calculated to be -1.07 and -35.76 for the 5 and 10 kV cases, respectively. This is consistent with the SNR difference evident in the spectra presented in Figure 3.14. This indicates good support and is distinguishable between models in the high SNR case (10 kV), in which the supported model can be taken as ground truth. In the low SNR case, it may be necessary to deploy several other candidate submodels, or bring in additional prior information from other experiments in order to justify the unequal a priori probability of the submodels, $\mathbb{P}(M_i) \neq \mathbb{P}(M_j)$, providing additional support of one candidate submodel over the other.

3.10 Summary

This chapter outlined the physics, model equations, and signal inversion techniques that are used to invert raw LRS and LTS spectra. The effects of the accuracy and uncertainty of prior information, the signal SNR, and the model fidelity on model selection in LTS experiments was explored by implementing a generalized LTS model that, in the limits of $\gamma_{\mathrm{MD}} \in [0, 1]$ and a single electron temperature, collapses into a Maxwellian–Druyvesteyn EVDF-based spectrum.

It was determined that, below SNRs of 5, $\ln(B_{i,j})$ cannot discriminate between candidate submodels, regardless of γ_{MD}, the model fidelity, or the accuracy of prior information. Additionally, the Bayesian framework demonstrates that at LTS signal SNRs above 10, the Laplace approximation is valid for LRS-calibrated LTS experiments and a least squares inversion is a sufficient description of the uncertainty. However, in cases where the LRS SNR is low, the LTS inference would be further compromised by nuisance parameters from the LRS inference, and a full Bayesian inference or some other form of uncertainty propagation may be required. This validates the widespread use of LS inferences for the determination of the MAP and uncertainty bounds on the QoI, and in cases where the SNR is high, the lengthy implementation of such Bayesian methods is unnecessary. However, in the cases where variable correlations are necessary, the addition of a single nuisance variable has

small but noticeable effect on the predicted correlations for the LTS QoI. Therefore, in cases where the variable correlations are critical; for example, for closure validation in EP-related LTS experiments, full Bayesian inferences may be required depending on the signal SNR.

CHAPTER 4
DISCHARGE VOLTAGE EFFECTS ON THE SPATIAL DISTRIBUTION OF THE ELECTRON NUMBER DENSITY AND TEMPERATURE IN A NS-PULSED PLASMA; DETECTION LIMIT ESTIMATES AND SPATIAL RESOLUTION INVESTIGATIONS

It is necessary to empirically determine the practical number density detection limits of the notional LTS setup constructed with a given interrogation laser, spectrometer, and detector, assuming a maximum collection period per spectrum of no more than 10 minutes. This 10-minute limit is set by the fact that, in the general case, four separate raw LTS spectra are required to produce an invertible LTS signal, making the total time per point of interest up to 40 minutes assuming a 10 Hz interrogation beam laser. To achieve this, a benchtop vacuum cell with floating electrodes, biased with a ns-pulsed power supply capable of generating a pulsed DC discharge plasma, was constructed. A free space collection and detection LTS system was implemented around this discharge cell and used to quantify the notional detection limit. The work is summarized in [175]. This system was used to perform the studies in [170, 171].

4.1 Experimental Layout

This section details the tabletop vacuum cell and LTS systems that were constructed in order to generate a plasma with sufficient number density for study, and then generate LRS and LTS in order to measure the relevant plasma properties.

4.1.1 Vacuum Test Cell and Electrodes

A custom vacuum test cell was constructed from off-the-shelf and custom CF and KF equipment from Kurt J. Lesker. Isometric and front views of the cell are shown in Fig-

ure 4.1.

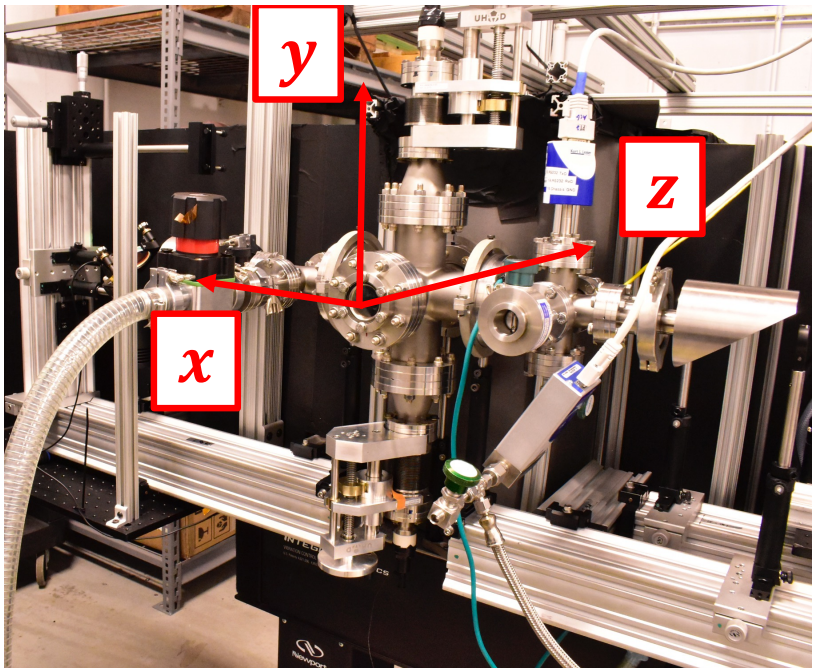

(a) Isometric view of the plasma cell.

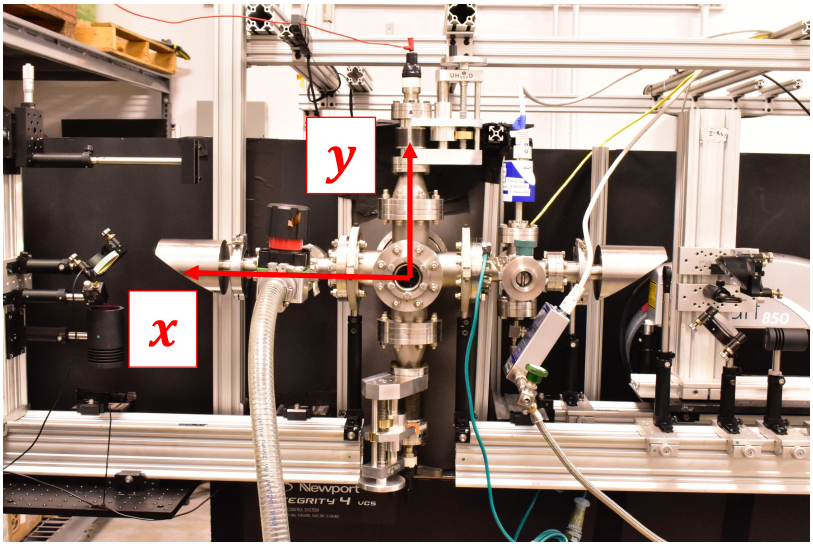

(b) Front view of the plasma cell.

Figure 4.1: Isometric and front views of the plasma cell.

The main body of the cell is stainless steel a C6-045 4.5" CF 6-way cross tube which houses the plasma-generating electrodes. In the positive and negative y directions, two CRN450X275 4.5" to 2.75" CF conical reducing nipples are used to interface the main body of the cell to two LSM38-50-H-ES bellows flanged linear translation feedthroughs.

The bellows flanged linear feedthroughs have 50 mm of total travel and are laser etched every 1 mm. These translation feedthroughs allow for relative movement of the electrodes with respect to the body of the cell. The main power feedthroughs are EFT0313753 2.75" CF flanged, 3/4" diameter isolated (from the vacuum cell body) copper feedthroughs. Being too short to reach the test section, they were extended via 8966K11 3/4" copper rods from McMaster-Carr and interfaced via 1/4-28 threaded copper rods. The electrodes were 1/2" thick, 24 mm diameter stainless steel discs. In order to shield the copper from the plasma, the 3/4" copper rods were centered down the barrel of the vacuum test cell along the $\mathbf{y}$ and $-\mathbf{y}$ directions and then lined with a 3/4" ID alumina tubes. The electrodes are pictures in Figure 4.2. This lining served two purposes. First, in a steady state discharge configuration (i.e., not pulsed), at the estimated densities and temperatures, the copper was expected to and observed to vaporize when in when the plasma was ignited. In order to avoid vaporization during steady state, non-pulsed operation, the electrodes were made of stainless steel. Secondly, this reduced the electrical line of sight from the floating electrodes to the grounded vacuum cell walls.

Baffles are placed in the $\mathbf{x}$ direction on either side of the test section to reduce reflections from the 'wings' of the cell, to be detailed shortly. Without baffles, the stray light in the test section is increased from reflections from the wings of the cell – this has a significant impact on the signal-to-noise ratio (SNR) and number density detection limits in the cell. The baffles were machined in order to be press fit in the cavity of the 6-way cross tube. Baffles with several IDs from 1 to 20 mm were constructed. The correctly sized baffles, being the ones that barely clip the edge of the beam at their given location, were placed in situ during alignment to minimize stray light. These baffles also acted as the targets that defined the optical axis in the $\mathbf{x}$ direction.

In the $-\mathbf{z}$ direction, one RF450X275 zero-length 4.5" to 2.75" reducing flange is used to interface a VPZL-275 high transmissibility viewport on the back of the cell for visual access to the test section during alignment. In the $\mathbf{z}$ direction, a VPZL-450 high transmissibility

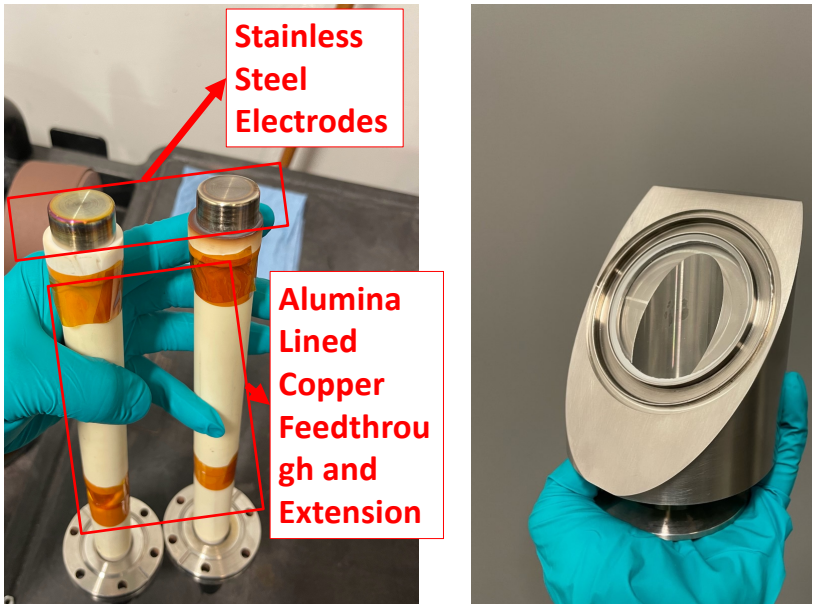

Figure 4.2: Vacuum cell electrodes and brewster window.

4.5" CF viewport provides optical access for the detection optics to the test section. To

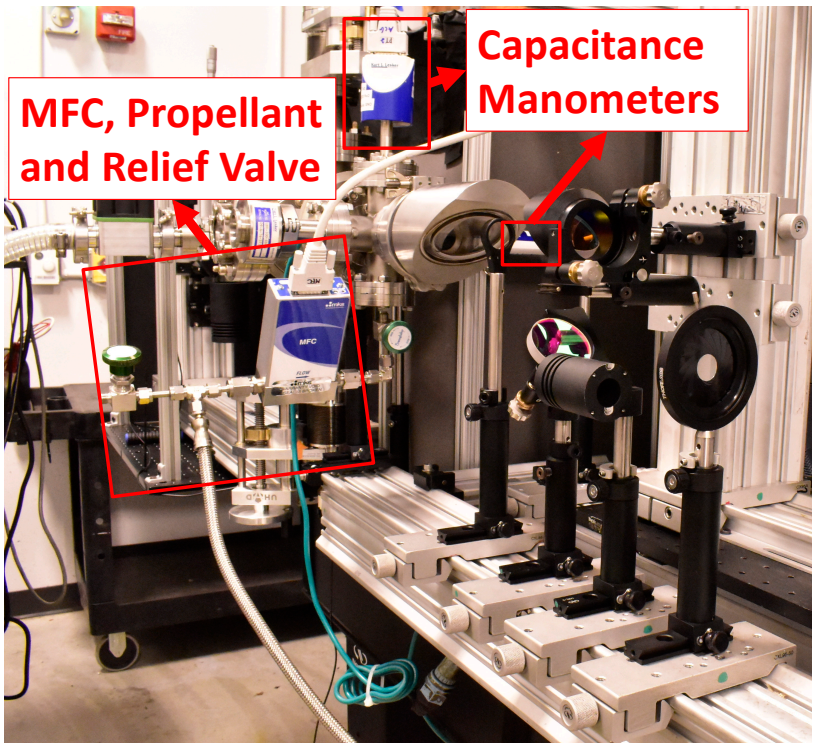

Figure 4.3: Vacuum cell pressure control section.

the right, in the $-$x direction, a C6-0275 2.75" CF 6-way cross tube houses the pressure

measurement and mass flow devices. This interfaces to the core of the cell via another zero-length 4.5" to 2.75" reducing flange. Two capacitance manometers (CMs) , one XCG-BT-FB-1 with a range of 1000 to 1 Torr and one ACG-HT-2-1 with a 10 Torr to 1 mTorr range were used to measure the pressure in the vacuum cell over the desired range of 760 Torr to 100 mTorr for the collection of LTS and LRS spectra. A single analog MKS GE50A013502RMV020 mass flow controller (MFC), with a maximum flow rate of 500 sccm was used as the neutral gas input to the system. This MFC is designed to take an optional input signal and the desired setpoint signal and use internal PID control logic to output the requisite flow to maintain the desired pressure setpoint. The CMs and the MFC were tied to a NI-USB-6211 that was controlled via a custom LabView VI. The VI read the CMs voltages, chose the appropriate signal given the range of the CMs, and then output that signal to the MFC in order to control the pressure in the cell. To complete the $-\mathbf{x}$ portion of the vacuum cell, a F0275XQF50 2.75" CF to KF50 reducing nipple interfaced the 2.75" CF cross tube to a custom Torr Scientific NSQ1462-25 KF50 Brewster window . The pair of custom Brewster windows used on the cell were designed with a 25 mm clear aperture and are pictures in Figure 4.2. Figure 4.3 pictures the pressure control wing.

To the left, in the $\mathbf{x}$ direction, a C-0275 2.75" CF cross tube interfaces to the main body of the cell via another zero length 4.5" to 2.75" reducing flange. Similar to the right wing, the 4-way cross in the $\mathbf{x}$ direction interfaces to the second Brewster window via another 2.75" to KF50 reducing nipple. A F0275XQF25 2.75" CF to KF50 adapter interfaces a C33355000 KF25 diaphragm valve to the cell. This valve seals the cell from the Alcatel Adixen 2010SD rotary vane vacuum pump and also acts as a variable conductance valve to modulate the pumping speed. The pump and valve are connected via a 1" ID, 6' long PVC tube that interfaces to the pump and valve via PVC to KF25 adapters. At the pumps working pressure of 2.1×10^{-3} mbar, its throughput is rated as 2.97 l/s or 178×10^{-3} ccm. Conductance loss calculations modeling the length from the pump to the test section as a 1" ID, 7' long pipe estimated the test section pumping throughput to be 154×10^{-3} ccm.

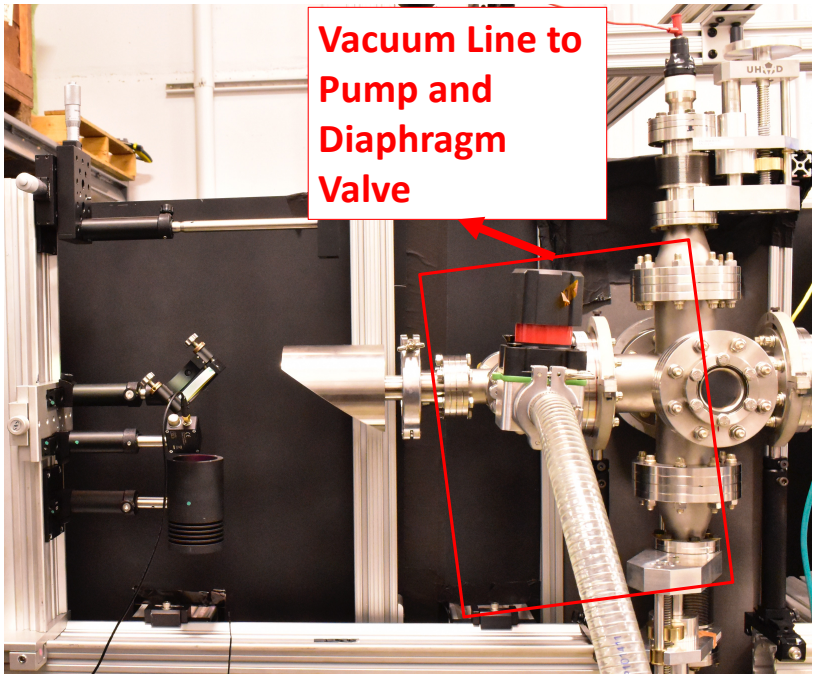

Figure 4.4: Vacuum cell vacuum pulling section.

A throughput of up to 100×10^{-3} ccm for pressures at 100 Torr for N_2 was necessary to maintain the pressure during the detection system calibrations via Raman scattering. This would have required an impractically sized MFC and flow rates into the cell. Instead, the diaphragm valve is used to decrease the conductance by restricting the orifice size of the pump at the cell. In this way, the desired pressures can be reached by first backfilling the cell with the MFC open and the diaphragm valve closed, then actuate the valve in order to re-establish pumping and allow for fine control of the pressure via the pressure control loop. Figure 4.4 depicts the vacuum pulling and pressure control wings of the vacuum cell. After the cell was placed, the interrogation beam and collection systems were put into place and aligned.

4.1.2 Cell Electrical Configuration

The body of the vacuum cell described in Subsection 4.1.1 was tied electrically to the surface of the optical table, both of which were intentionally tied to the ground via a ground bar installed in the facility. As discussed in Subsection 4.1.1, the power feedthroughs isolated

the discharge electrodes from the vacuum test cell, ensuring that their base configuration was floating with respect to the vacuum cell. Therefore, the tying of the vacuum cell and table to the ground resulted in the base configuration of the electrodes in the cell as floating with respect to the facility ground. The air side of the power feedthroughs were tapped with a 3.5-mm hole in order to couple to the high-voltage, 22-AWG Cicoil wires from the power supply that were terminated at 4 mm banana plugs to facilitate troubleshooting and switching between power supplies for pulsed and steady-sate operation. A TE Connectivity TE2500B1R0J 1-Ohm, 2500-W resistor was placed in series between the vacuum cell anode and the power supply anode terminal. This resistor was chosen due to it's high power rating. The voltage across the electrodes was driven by a 10 kHz maximum repetition rate, NSP-120-20F Eagle Harbor floating, ns-pulsed power supply. The electrical configuration of the vacuum test cell and electrodes is diagrammed in Figure 4.5.

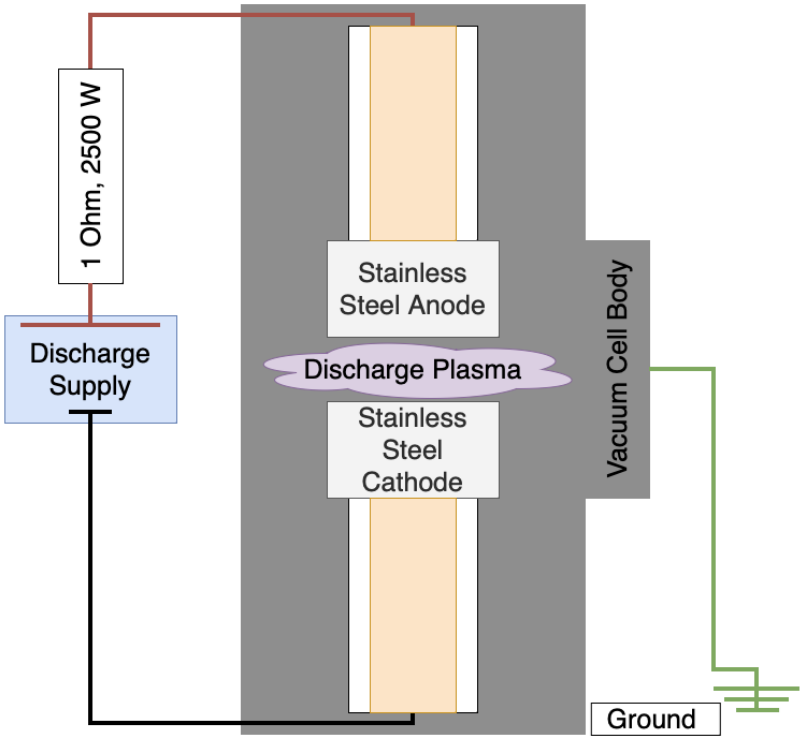

Figure 4.5: Vacuum cell electrical configuration.

A Berkeley Nucleonics BNC-577-8C model delay generator was used as the master

clock for the synchronization of timing events in the system. It controlled the internal timing of the Quantel Q-Smart 850 laser Q-switch with respect to the lamp to ensure the maximum rated energy per pulse was extracted from the laser. First, the laser was tuned via its internal tuning to ensure maximum energy per pulse extraction at the rated factory settings and internal timing. Then, the laser was switched to external timing and the Q-switch delay was adjusted until the maximum laser energy was extracted once again. A Princeton Instruments PM4-1024i-HB-FG-18-P46 detector was coupled to an Isoplane 320A spectrometer to form the system's spectrograph. Additionally, the delay generator controlled the timing of the detector gate delay and the ns-pulsed power supply trigger, both with respect to the laser Q-switch. This was done for two reasons. Firstly, the relative timing with respect to the Q-switch of the gate delay ensured full control in order to maximize the signal collected by coinciding the gate delay with respect to the laser signal monitored near the test cell on an oscilloscope to maximize signal collected. Secondly, controlling both signals with respect to the Q-switch signal allowed for accurate relative timing between the start of the gate opening and the start of the plasma pulse, giving ns-resolution on the placement of the collection of LTS along the plasma pulse. The plasma pulse current was monitored using a CP030 current clamp on an HDO404A WavePro oscilloscope. The oscilloscope was triggered using the Q-switch signal. Given that the highest possible frequency in the system is 10 kHz, dictated by the ns-pulsed power supply, the base period for the delay generator, T_{o} , was set to 10 kHz and the timing was synchronized around this in order to have the possibility of driving the pulser to its maximum frequency without needing to reconfigure the timing. This configuration required operating the laser-timig-based signals (lamp, Q-switch, and detector gate signals), that were at 10 Hz in a duty cycle configuration in order to achieve a relative 10 Hz timing frequency for the laser-based signals. All command signals to the detector, as well as the pulsed plasma driving signal, were controlled relative to the laser Q-switch signal. The relative timing parameters are given in Table 4.1.

In Table 4.1, $\Delta t_{\mathrm{QL}}, \Delta t_{\mathrm{GQ}}, \Delta t_{V_{\mathrm{D}}\mathrm{Q}}$ are the delays for the Q-switch relative to the lamp,

Table 4.1: System timing configuration.

Device	Sync	On/Off	Pulse Width (μs)	Delay (μs)
Lamp	T_{o}	1/999	100 μs	0
$\mathrm{Q_{sw}}$	A/Lamp	1/999	100 μs	Δt_{QL}
Gate	C/$\mathrm{Q_{sw}}$	1/999	10 μs	Δt_{GQ}
Pulser	C/$\mathrm{Q_{sw}}$	$V_{\mathrm{D}}^{\mathrm{on}}/V_{\mathrm{D}}^{\mathrm{off}}$	$\Delta t_{V_{\mathrm{D}}}$	Δt_{PQ}

the detector gate relative to the Q-switch, and the pulser with respect to the Q-switch and are set in situ to achieve the desired relative timing. The lamp to Q-switch delay is set to optimize the laser energy and is experiment-independent, and the gate delay is set to straddle the laser pulse in order to capture and maximize the signal, the gate width is set in the detector software. After the lamp to Q-switch delay is set to maximize laser output power, the laser pulse signal, as measured on an oscilloscope, happens some time later, usually a few hundred microseconds. The gate to Q-switch delay is optimized in order to straddle the laser pulse signal on the oscilloscope with the gate output signal from the detector. These delays were determined to be Δt_{QL} = 287 μs and Δt_{GQ} = 689 ns, respectively. The pulser to Q-switch delay, the pulse on and off duty cycle, and the pulse width are all set to drive the NSP-120-20F supply and are experiment specific and to be described in the specific experimental configuration.

4.1.3 Interrogation Optical Beam System

Given the shear size of the vacuum cell, and in anticipation of other plasma cells and sources to be deployed on the LTS rig, a construction rail system using XT95 and XT95SP class 95 mm construction rails from Thorlabs of various lengths was used to suspend the cell off of the INT4-46-12-A 4' x 6' Newport optical table.

First, a set of construction rails were coupled to each other and to the table using XT95P13 construction rail mounting elements from Thorlabs. These allowed for a rigid system of construction rails that was suspended slightly off of the table with the capabil-

ity of supporting several hundreds of lbs reliably. In order to integrate the compact laser chosen for this setup, a Quantel Q-Smart 850, a MB1224 1' x 2' optical breadboard was coupled to the rail system. On this breadboard, two flat rails were placed to support rail carriers holding the interrogation beam optics as well a vertically placed XT95 rail for height adjustment of the beam through the optical axis defined by the $\mathbf{x}$ axis of the vacuum cell. The vacuum cell was placed as at the intersection of the two legs of the construction rail system. This can be seen in Figure 4.1 and depicted in the optical diagram of the system, as well as in Figure 4.7.

Table 4.2: Master optical diagram for the system.

Element	Aperture Size	Focal length	Part	Sourced
Laser	-	-	Q-Smart 850	Quantel
$I - M_i$	50.8 mm	-	RX-532-45-UF-2038	Lattice Electro Optics
$I - BD_i$	20.0 mm	-	ABD0975NP	Kentek
$I - PM_1$	20.0 mm	-	UP19K-15S-H5-D0	Gentec
$I - i_i$	Variable	-	ID50	Thorlabs
$I - HWP_i$	20.0 mm	-	CW0-532-02-08-R10	Lattice Electro Optics
$I - PBS_1$	25.4 mm	-	PBH-532-10	Lattice Electro Optics
$I - l_1$	25.4 mm	-50 mm	UF-PC-25.4-50-532	Lattice Electro Optics
$I - l_2$	25.4 mm	100 mm	UF-PX-25.4-100-532	Lattice Electro Optics
$I - l_3$	25.4 mm	400 mm	UF-PX-25.4-400-532	Lattice Electro Optics

Table 4.3: Interrogation beam optical parameters.

Table 4.2 is the system's master optical diagram, outlining the interrogation beam path and collection beam path, with the part numbers in Table 4.3. As stated above, for ease of alignment and relative height, construction rails were used throughout the entire optical table to raise the height of all of the elements, including the laser. This was to prevent any swaying of the aligned optics due to long optical posts and possible vibrations from the placement of the vacuum pump. Most of the optics were coupled to the optical rails, both flat and cube, via Newport CXL95 class 95 mm rail carriers upon which Newport MRL class dovetail rails were placed, allowing for full movement of any optical element along

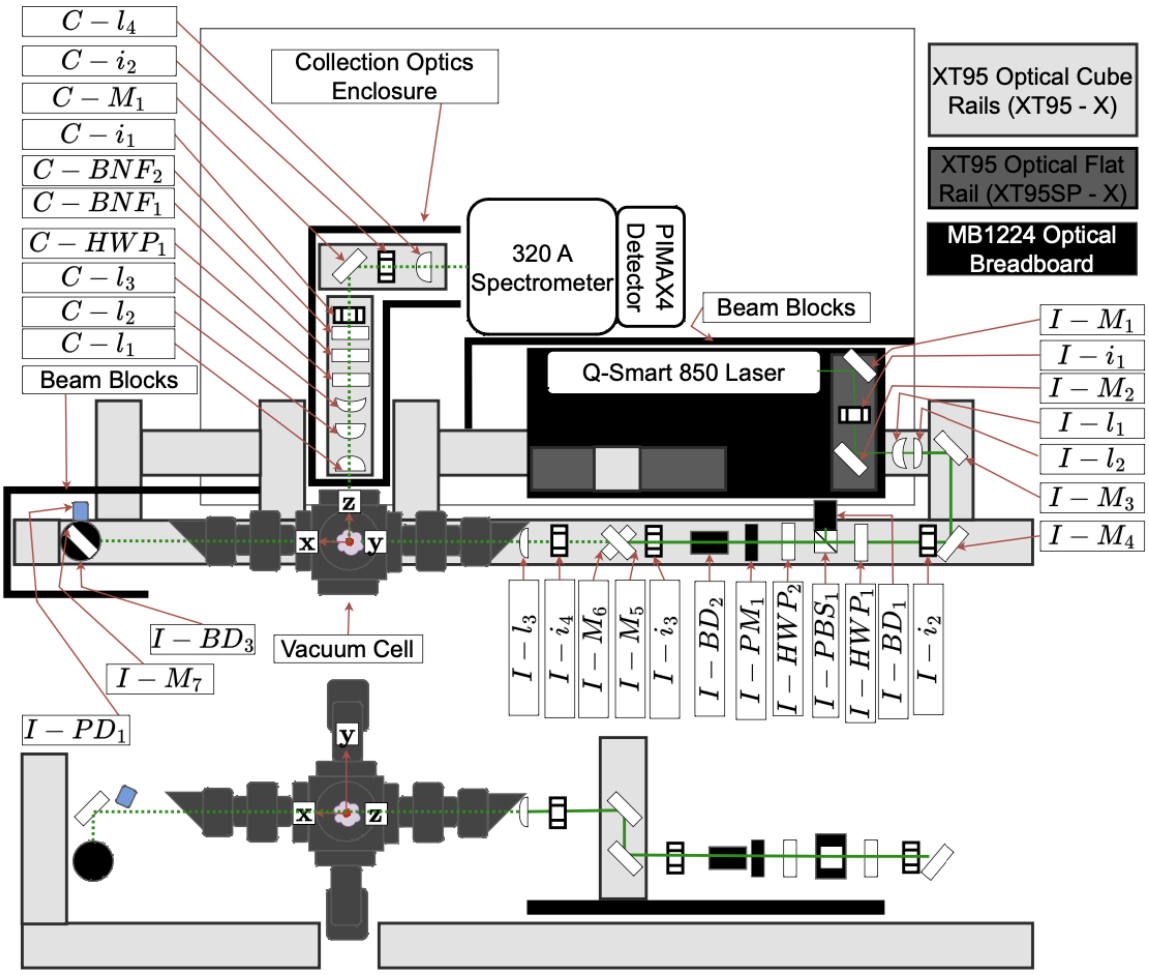

the optical axis and perpendicular to it. The optics were coupled to the rail carriers and dovetails via Newport MCF class dovetail rail carriers, Newport VPH class optical post holders, and 1/2" Thorlabs TRX class optical posts. The optics themselves were placed in various types of holders to couple to the posts. All mirrors were placed into Newport Ultima class kinematic mirror mounts. Any exceptions to this will be detailed below. The 10 Hz, 532 nm wavelength laser beam exits the laser aperture and $I - M_1$ steers the laser beam onto the first XT95 flat rail, aligned along that rail using $I - i_1$, constituting the first leg of the optical beam interrogation axis, pictured in Figure 4.6. The laser beam was turned on at an alignment-appropriate power, and $I - i_1$ was height aligned with respect to the laser beam aperture. This set the height for the entire first 3 legs of the interrogation beam optical axis. $I - i_1$ was not placed on dovetails but rather had its post holder directly

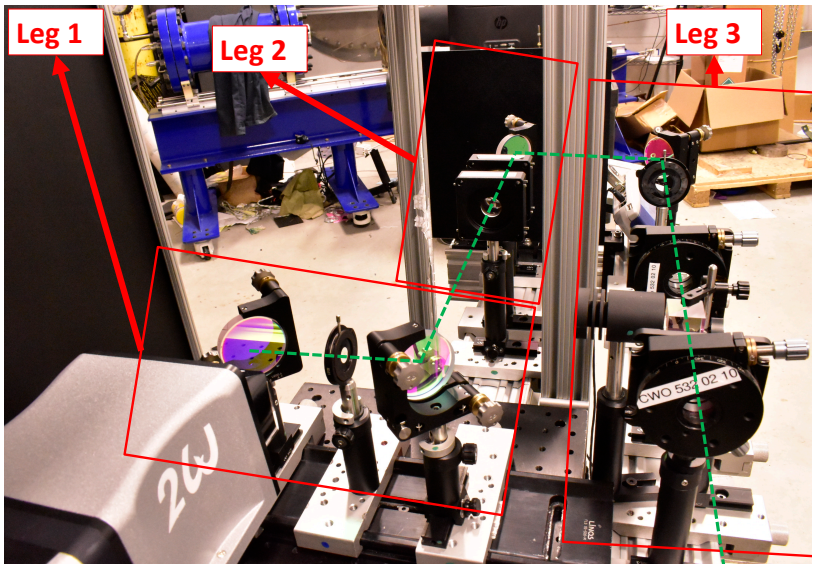

Figure 4.6: First and second legs of the interrogation beam optical system.

screwed into a hole on the 95 mm rail carrier that was along the center line of the first flat rail. With $I - i_1$ aligned, it was used as the target along the first leg to align mirrors $I - M_1$ and $I - M_2$ along the center line of the first optical rail. Each mirror was aligned iteratively until the laser beam was aligned with respect to the target, ensuring it was going straight down the center line of the first flat rail, and height and laterally aligned until the beam was hitting the center of the mirrors as well. With $I - M_2$ aligned, it was moved out of the way. Under the assumption that the beam was aligned correctly with respect to the first target, a second target $I - i_2$ was placed on the main leg of the optical axis as the beam was allowed to cross over it from the first flat rail. Then, this target was height aligned with respect to the second target. This was necessary because the first target was on a flat rail that was itself sitting on a breadboard coupled to the larger cube rails using am XT95P13, so their heights were not consistent. These targets reconciled the heights, ensuring that the beam was maintained at the same height throughout the first three legs of the optical axis. Once this was done, $I - M_2$ was placed and steered the beam along the second leg of the optical axis and $I - i_2$ was used to align the beam at the same height as the first leg along the center-line of the optical rail.

The second leg of the optical axis, pictured in Figure 4.6, expanded the beam via a 2-1 beam expander with $I - l_1$ and $I - l_2$. With the beam aligned down the leg, $I - l_1$ was placed, the target behind it, and then it was laterally and height adjusted until the beam hit the center of the target clear aperture. This same method was applied to $I - l_2$. Then, the relative distance was adjusted until the near and far field beam diameter did not change, ensuring collimation after the beam expander. $I - M_3$ and $I - M_4$ steered the beam on the main leg of the interrogation beam optical axis with the beam expanded to $d_2 = 2d_1$ with some unknown approximately linear polarization. This is to reduce the likelihood of damaging the interrogation optics, the beam expansion reduces the laser energy per area; although high-energy optics were used throughout the interrogation beam path.

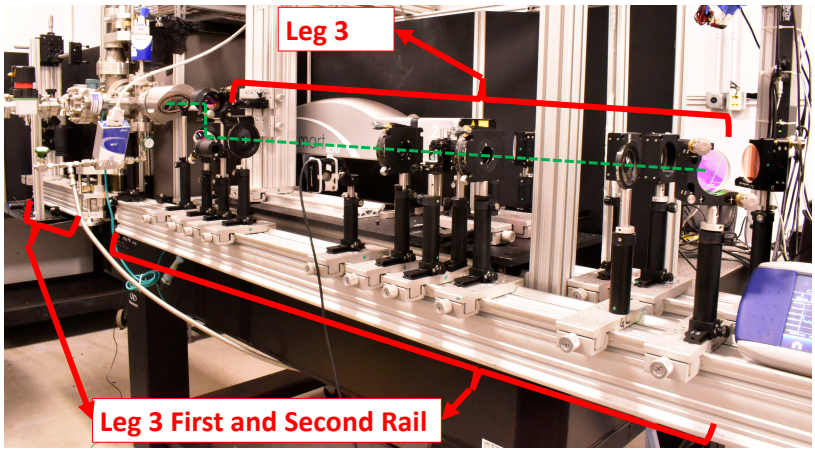

Figure 4.7: Third leg of the interrogation beam optical system.

The third leg of the interrogation beam optical system is pictured in Figure 4.7. First, $I - i_2$ is removed from the second leg of the optical axes and then used as the main target along the third leg. $I - M_3$ and $I - M_4$ and $I - i_2$ are used to iteratively align the beam along the centerline of the third leg of the optical axis and height and laterally align the mirrors until the beam is hitting the center of the open aperture of $I - i_2$ and mirrors $I - M_3$ and $I - M_4$. Then, with the beam aligned, $I - i_3$ is aligned with respect to $I - i_2$, providing a second main leg iris for ease of alignment. With this alignment having been performed, the second XT95 rail that holds the optical cell in place with aligned with respect to the first

by moving $I - i_3$ onto this rail and adjusting its position until the beam was straight along this rail. This ensured that both rails were self-consistently aligned so that the center-line of one rail coincided with the center-line of the other, these rails being shown Figure 4.7. The rest of the optical were pass-through in general and were aligned such that the already aligned beam was hitting them in the center and not being clipped by any of the holders. Then, $I - i_3$ was placed back onto the main leg rail and the interrogation beam optics were aligned.

A polarization-dependent power modulator is constructed with $I - HWP_1$, $I - PBS_1$ and $I - BD1$. This was necessary to maintain the nominal operational mode of the laser at it's optimal Q-switch delay and provide the flexibility for external modulation of the power. The orientation of $I - BD1$ was chosen such that the reflected portion was $\mathbf{S}$ polarized, which ended up being $\mathbf{z}$ polarized. However, in the cell, $\mathbf{y}$ polarization was required. $I - HWP_2$ was used to tune the polarization along the desired axis in the cell. The polarization is optimized by collecting Rayleigh scattering signal. The depolararization effect of the LRS signal makes it ill suited for optimizing the polarization. Both HWPs were placed on Newport 481-A-S fine rotation stages that allowed for fine polarization and power control into the cell. The beam energy was measured after HWP_2, with $I - PM_1$ (Gentece UP19K-15S-H5-D0) which is placed on a flip mount in order to be easily moved out of the beam path. The power was always measured after the second HWP because there is a non-negligible power loss across the polarization-dependent power modulator and the second HWP, of about 5%. Then, $I - BD_2$ is also placed on a flip mount, blocking the beam before continuing down the optical beam path. This constituted the main set of optics that steer and shape the beam along the laser aperture height aligned first 3 legs of the interrogation optical beam path.

$I - M_5$ and $I - M_6$ steer the beam up to the optical axis defined by the center of the cell. This was an iterative process. First, $I - M_5$ was placed on a 45-degree mount (PS-45-ULT), and an irs was used to align it vertically to ensure an approximately 90-degree turn.

In the same fashion, its height and lateral location were aligned to ensure the beam hit the center of the mirror. $I - M_6$ was placed at an arbitrary height along the vertically placed XT95 rail using its rail carrier but was aligned so that the beam hit the mirrors center and made an approximately 90-degree turn. The cell itself was straddled along the two final rails and set on rail carriers. This allowed for height, angle, and lateral adjustment of the cell along the pre-aligned optical rails. The cell itself was placed at an arbitrary height, and using a digital level was ensured to be ≤ 0.1 degrees in pitch and yaw angles to ensure it was straight. Then, using iris $I - i_3$, the beam was clipped until it was an appropriate size and then baffles were placed in the cavity of the cell to act as alignment targets. First, $I - i_4$ was placed as close as possible to the cell with the beam passing through the crooked cell. The iris was height aligned along the height of the baffles, coinciding with the center-line of the cell that defined the in-cell optical axis.

Then, this iris was used to align the beam at this height on the final two optical rails, ensuring that the beam was straight at the height of the optical axis of the center-line of the cell. This was done by adjusting the height of $I - M_6$ and its angle with the kinematic mounts. Then, the cell was aligned such that the straight beam hit the two baffle targets. This process was repeated until there was no error in the height of the beam with respect to the cell. This process ensures that the targets used defined all of the optical axes and were used to monitor alignment day to day. With everything having been self-consistently aligned to be straight, $I - l_3$ was placed and aligned height-wise and laterally until the beam was aligned down the centerline of the cell and iris once again. Its position was adjusted until the focus was in the center of the cell, and the baffles were iteratively decreased in size until the test region cavity was as dark as possible, indicating minimization of stray light. This tedious process ensures that the beam makes only approximately 90-degree turns and that everything is as straight as possible, minimizing effort during re-alignment. Then, $I - M_7$ is placed in order to steer the beam vertically after the cell, minimizing light traveling back into the cell and minimizing stray light, terminating at $I - BD_3$. $I - PD_1$

photo-diode monitors the diffuse light from the beam dump and acts as an indicator of the timing of the laser. The distance to the test cell is less than 1 m, so the expected timing error at the speed of light propagation of about 3 m per ns is ns level error. This is on the order of the jitter of the laser and accounted for with the detector gate width.

Then, the collection optics are aligned with respect to the interrogation beam optical axisa and detailed in Subsection 4.1.4. Finally, with the cell aligned and the optics in place, the rest of the wings of the cell are built around the placed cell. When the Brewster windows are added, there is a slight misalignment of the height of the beam and possibly lateral location of the beam, depending on the care in Brewster window alignment. This is easily remedied by using the kinematic mounts to readjust the beam until the stray light in the cell is minimized and the beam location is restored.

4.1.4 Collection and Detection System

As detailed in Subsection 4.1.3, the interrogation beam is steered and shaped (both physical shape and polarization) in order to travel down the center of the vacuum cell propagating along $\mathbf{x}$, polarized along $\mathbf{y}$. To maximize the scattering signals in this configuration, the detection optics are placed along the $\mathbf{z}$ direction, whose optical access is enabled via windows on the vacuum cell detailed in Subsection 4.1.1. Although, in reality, the configuration of the interrogation and detection branches were set given the geometry of the optical table and the desired orientation of the cell. Then, the polarization is matched. Nonetheless, the mutual perpendicularity was desired regardless of the order in which the setup manifested.

The height of the center of the barrel of the test cell sets the optical axis for the detection system along $\mathbf{z}$. The collection system optics were chosen to maximize the solid angle of collection while allowing for maximum transmissibility through the relevant apertures, which are the laser line filtering elements in our case. The detection system optical diagram and parameters are presented in Figure 4.8 and Table 4.4.

Light is scattered from the laser beam waist intersection with the ensemble of particles

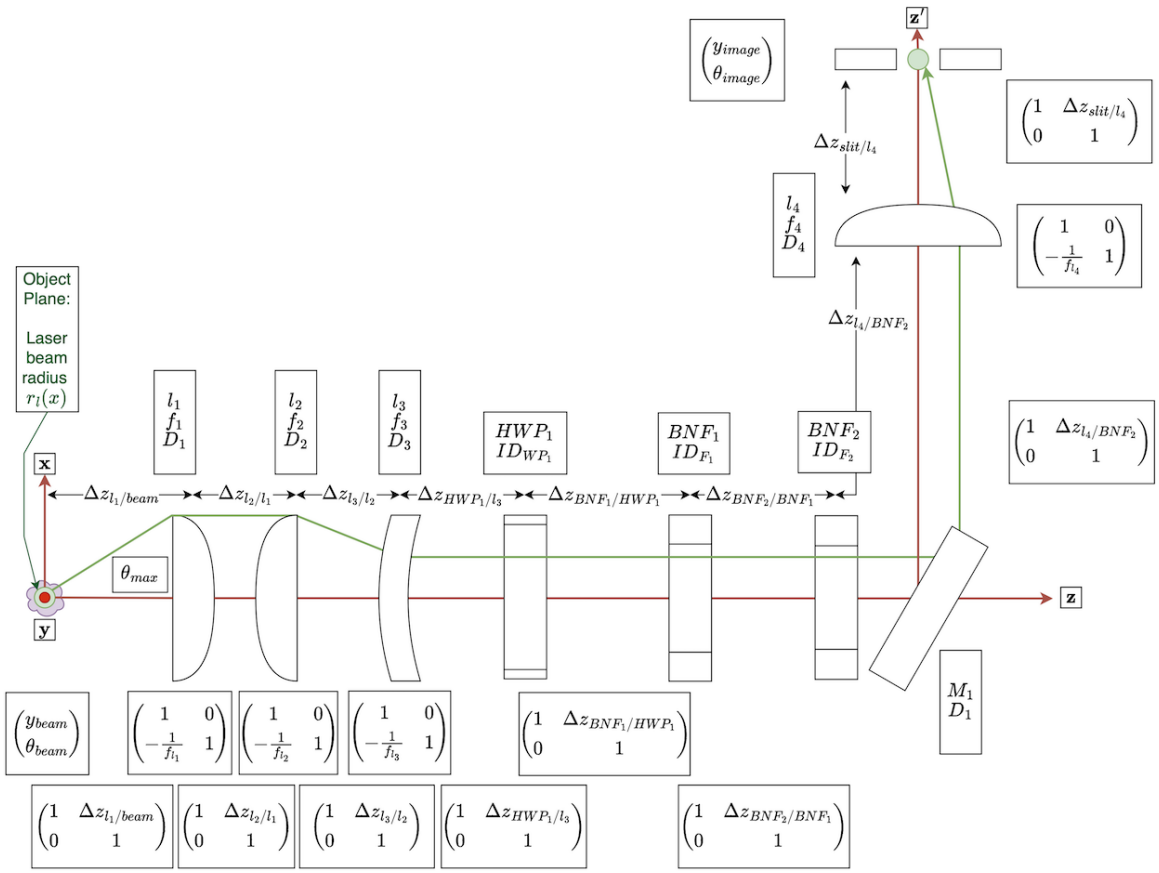

Figure 4.8: Collection system optical diagram.

of interest, represented as the purple cloud in Figure 4.8. In order to maximize the collection of light, large diameter lenses with as short of focal lengths as possible are required. However, the filtering elements are limited in size to 12.5 and 15 mm, respectively. A simple 2 lens collection system will be at odds with the goal of maximizing the collected light and filtering by passing through the clear aperture of the filters. A four-lens collection system whose goal is to collect as much light as possible, and through a series of relays, changes the diameter of the collected light marginal rays in order to pass through the clear aperture of the filters were optimized for this application. There are limits to how much such relays can be exploited; see [162] for details.

The collected light is detected from $C - l_1$ with focal length $C - f_{l_1}$, whose distance from the object plane is set to match the focal length ($\Delta z_{l_1/beam} = C - f_{l_1}$) in order to collimate the light and use the entire detection solid angle of the first collection lens. The

Table 4.4: Detection system optical parameters.

Element	D or ID (mm)	f or Distance (mm)	Part	Sourced
$\Delta z_{l_1/beam}$	-	200	-	-
l_1	50.8	200	ACT508-200-A	Thorlabs
$\Delta z_{l_2/l_1}$	-	25	-	-
l_2	50.8	200	ACT508-200-A	Thorlabs
$\Delta z_{l_3/l_2}$	-	150	-	-
l_3	25.4	-50	ACN254-050-A	Thorlabs
$\Delta z_{HWP_1/l_3}$	-	25	-	-
HWP_1	25.4	25	WPH10E-532	Thorlabs
$\Delta z_{BNF_1/HWP_1}$	-	25	-	-
BNF_1	12.5	-	BNF-532-OD4-15	Optigrate
$\Delta z_{BNF_2/BNF_1}$	-	25	-	-
BNF_2	12.5	-	BNF-532-OD4-15	Optigrate
$\Delta z_{l_4/BNF_2}$	-	75	-	-
l_4	25.4	100	AC508-100-A	Thorlabs
$\Delta z_{slit/l_4}$	-	100	-	-

collected light immediately leaving $C - l_1$ is relayed via $C - l_2$. This would normally create a 1-1 image after $C - l_2$, however, a negative lens $C - l_3$ with focal length is placed at $\Delta z_{l_3/l_2} = C - f_{l_2} + C - f_{l_3}$ in order to collimate the rays immediately leaving l_3. The rays are then passed through $C - HWP_1$, used to match the polarization dependence of the grating inside the spectrometer. The half-wave plate buys an additional 5%-10% in the signal. Immediately after $C - HWP_1$, the collected (and collimated) rays pass through the laser line volume Bragg grating notch filters $C - BNF_1$ and $C - BNF_2$, with clear apertures ID_{BNF_1}, ID_{BNF_2}, and $OD4$ blocking when properly aligned. Our filters were purchased from OptiGrate about three years apart, so $ID_{BNF_1} \leq ID_{BNF_2}$. The sizing of our detection elements used ID_{BNF_1} as the filter size. The laser line-filtered scattered rays are then steered with mirror M_1 through l_4 with f_{l_4}, that is placed a distance of $\Delta z_{sp/l_4} = C - f_{l_4}$ from the slit plane. This creates the sharpest image of the test section on the slit of the spectrometer at the slit plane. The slit plane is comprised of two slits; the slit is built into the spectrometer $slit_1$ and a secondary slit, $slit_2$ that is placed perpendicular

to the first slit. The entire spectrometer is turned 90 degrees such that $slit_1$ is parallel to the propagation of the beam path along $\mathbf{x}$, making $slit_2$ parallel to $\mathbf{y}$. As previously stated, the collection solid angle and magnification / spatial resolution of the measurement are set by the collection optics in the case of a free space optical system. The general form of the detection system in Figure 4.8 was used along with the equations in Section 3.3 to size the optics in Table 4.4. The calculations are summarized and presented below.

In order to use the entire maximized solid angle (via large lenses and shortened focal lengths), the limiting aperture of the detection system must be the collection lens, $C - l_1$, while ensuring that all of the rays pass through the clear aperture of $C - BNF_1$. To do this, the marginal ray (Equation 3.35) at the aperture of the filter must be less than or equal to half of the clear aperture of the filter. With the marginal ray as,

$$r^m(z_{beam}) = [r_{beam}, \theta_{max}]^T = [r_{beam}, tan^{-1}(\frac{D_{l_1}}{2f_{l_1}})]^T, \tag{4.1}$$

and using Equation 3.34, we can express our first condition as

$$r(z_{BNF_1}) = O^{beam}_{BNF_1} r^m(z_{beam}) \leq [ID_{F_1}/2.0, 0]^T, \tag{4.2}$$

with

$$O^{beam}_{BNF_1} = O_{fs}(\Delta z_{BNF_1/l_3}) O_l(f_{l_3}) O_{fs}(\Delta z_{l_3/l_2}) O_l(f_{l_2}) O_{fs}(\Delta z_{l_2/l_1}) O_l(f_{l_1}) O_{fs}(\Delta z_{l_1/beam}). \tag{4.3}$$

In order to maintain good spatial and spectral resolution while maintaining the maximum collection area possible (ideally the entire diameter of the beam), for a beam that is notionally $\leq$ 100 μm in diameter, we need to ensure that the magnification through our optical system is no more than M=2. Therefore, the ratio of the beam image ray height at the slit plane to the beam height at the object plane can be more than 2. To do this, the ray at the

slit plane must be solved for. Propagating forward from the filter plane using Equation 4.2, as

$$r(z_{slit}) = O_{slit}^{BNF_1} r(z_{BNF_1}), \tag{4.4}$$

with

$$O_{slit}^{BNF_1} = O_{fs}(\Delta z_{slit/l_4}) O_l(f_{l_4}) O_{fs}(\Delta z_{l_4/BNF_1}) O_{BNF_1}^{beam} \tag{4.5}$$

Additionally, we can define one from the object plane to the filter plane, which is any plane after l_3,as

$$O_{fp}^{op} = O_l(f_{l_3}) O_{fs}(\Delta z_{l_3/l_2}) O_l(f_{l_2}) O_{fs}(\Delta z_{l_2/l_1}) O_l(f_{l_1}) O_{fs}(\Delta z_{l_1/op}). \tag{4.6}$$

The height of the marginal ray at the filter plane is then given by the following product

$$O_{fp}^{op} r^m(0). \tag{4.7}$$

The minimum focal length is set by the vacuum test cell to f=200 mm, and the maximum lens diameter that led to a reasonable amount of light collected without increasing stray light collection, as well as achromatic off the shelf, was set to D_l = 50.8 mm and formed the basis for the optimized diameters and focal lengths in Table 4.4. These parameters yield a magnification of M= 2 and an optimized solid angle of $\Delta\Omega$ = .05 sr, and a marginal ray height of $r(z_{BNF_1})$ = 6.16 mm, just under the 6.25 mm required to pass through the smaller of the filters unclipped.

Finally, as stated, the spectrograph is comprised of a Princeton Instruments ISOPLANE-320A spectrometer and PM4-1024i-HB-FG-18-P46 PIMAX4. The spectrometer was ordered with a ARC-SP-ES motorized slit, a SLIT SHUTTER-ISOPLANE320 slit shutter and a 3-grating turret, which housed approximately 532 nm optimized I3-120-500-P 1200,

I3-180-500-P 1800, and I3-240-HVIS-P 2400 l/mm gratings to allow for multiple electron temperature range measurements.

4.2 Effects of Pressure, Voltage, and Phase Delay On Plasma Discharge Properties

In order to explore the parameter space of electron properties for an electrode diameter of D_{e} = 24 mm, with electrode spacing Δy_{e} = 26.5 mm. The electrode extenders were machined such that at an electrode linear stage and anode linear stage engraving of 25 mm and 25 mm, the electrodes were spaced 26 mm apart and centered around the center axis of the vacuum cell. Once they were machined, a telescoping bore gauge was used to measure the actual separation of 26.5 mm. The distance of the beam is always tracked with respect to the cathode, $\Delta y_{\mathrm{b/c}}$. Additionally, to minimize data acquisition time, the background spectra for subtraction were collected at a single condition per LTS experiment. This is equivalent to assuming that the emissions, background, and reflections and Rayleigh scatter were uniform across the spatial extent between the electrodes. This assumption was a good one, except in a few cases to be discussed.

The neutral background pressures were $P_{\mathrm{g}} \in$ [2,12] Torr and floating discharge voltages in $V_{\mathrm{D}} \in$ [8,20] kV. The parameter space required exploration in order to determine the highest number density points available for a spatial survey between the electrodes in the plasma. The plasma pulse width $\Delta t_{V_{\mathrm{D}}}$ was set to 240 ns, the maximum available on the pulsed power supply, and the effective frequency $f_{V_{\mathrm{D}}}$ was set to 100 Hz. This set $[V_{\mathrm{D}}^{\mathrm{on}}, V_{\mathrm{D}}^{\mathrm{off}}]$ to [1,99] and $\Delta t_{V_{\mathrm{D}}}$ = 240 ns in Table 4.1. The detection system parameters for all subsequent tests are presented in Table 4.5

Table 4.5: Detection system collection parameters.

E_{i} (mJ)	grating (mm^{-1})	w_{slit_1} µm	w_{slit_2} mm	Δt_{gate} (ns)	gain ()	shots ()
200	2400	150	5	8	100	3,000

The relative timing of the laser beam pulse rising edge (bs) was varied with respect to the rising edge of the plasma pulse start (ps) was varied via a variation in the pulser voltage trigger with respect to the Q-switch ($\Delta t_{V_{\mathrm{D}}\mathrm{Q}}$). During the pressure sweeps, this was set arbitrarily at 10 Torr at a discharge voltage of 20 kV until a sufficient amount of LTS was detected for analysis. Then, the pressure was varied at this delay condition. At this condition, $\Delta t_{\mathrm{bs/ps}}$ was 230 ns corresponding to a $\Delta t_{V_{\mathrm{D}}\mathrm{Q}}$ of 140 ns. The relative delay was measured using cursors on the oscilloscope with an uncertainty of 1 ns. After this, all delays were calculated using the above relative delay conversion factor. The test matrix for the pressure sweeps is presented in Table 4.6. The results are shown in Figure 4.9

Table 4.6: Pressure sweep test matrix.

P_{g} (Torr)	V_{D} (kV)	$\Delta t_{\mathrm{bs/ps}}$ (ns)	$\Delta y_{\mathrm{b/c}}$ (mm)
2 to 12	20	230	13.25

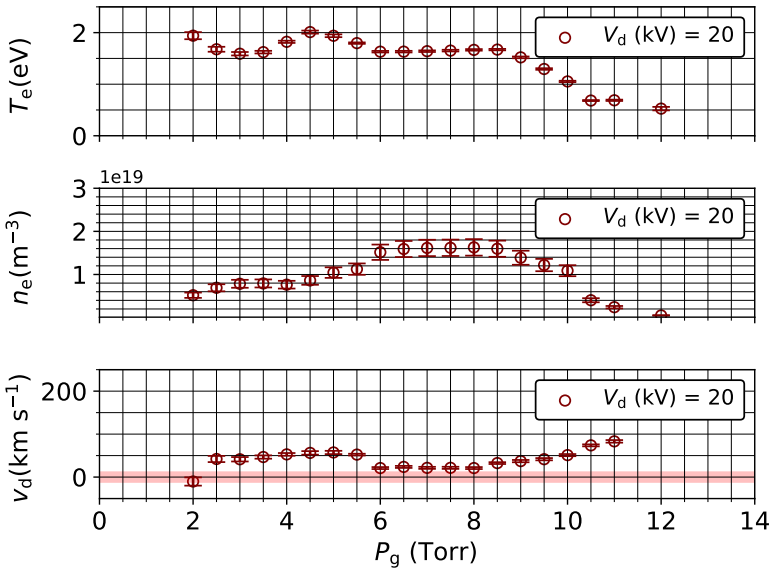

Figure 4.9: Spatial variation in electron properties versus pressure.

The results are shown in Figure 4.9. The electron property dependence on pressure was assumed to be similar across all temporal points along the laser pulse. The working

pressure was chosen to be 6 Torr, representing the beginning of the low slope linear region between 6 and 8.5 Torr.

With a working pressure of 6 Torr being chosen, a phase-resolved sweep of the laser beam pulse start with respect to the plasma current pulse start was performed to determine the region where the plasma properties were expected to have minimal variation. The test matrix for the phase delay sweep is presented in Table 4.7. The results are shown in Figure 4.10. The leading edge dynamics show very abrupt changes in the electron properties as

Table 4.7: Phase delay sweep test matrix.

P_g (Torr)	V_D (kV)	$\Delta t_{bs/ps}$ (ns)	$\Delta y_{b/c}$ (mm)
6	20	30 to 490	13.25

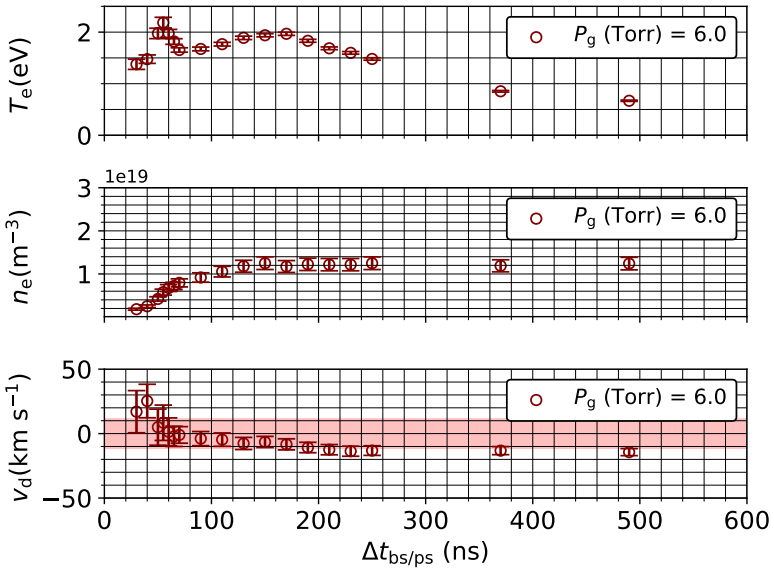

Figure 4.10: Variation in electron properties versus phase delay.

the plasma develops, followed by two regions of relatively gentle changes in the properties with phase delay. A phase delay of $\Delta t_{bs/ps}$ of 150 ns was chosen as the region with approximately constant electron density and temperature averaged between the desired time, the previous time point, and the following time point. The existence of plasma after the

240 ns width of the commanded pulse is expected and is consistent with the pulsed plasma work using the same pulsed power supply in [132, 145, 149]. The falling edge leads and can take hundreds of ns to die down. This interesting for several reasons. Firstly, it is often assumed that the peak current corresponds to the peak electron number density; however, the phase resolution along the centerline of the electrodes in this study indicates that the maximum number density points along the plasma current pulse starts toward the steady-state portion near the falling edge and continue until the applied discharge voltage has died off, with the electron temperature more closely following the voltage than the electron number density. This may indicate that for a given maximum discharge voltage and pulse width, the plasma dynamics are such that during the leading edge of the applied voltage, the steady state structures that are associated with DC discharges, i.e., the electron and ion-rich sheath and presheaths, may not be fully formed to shield the bulk plasma from the biased electrode boundary conditions and instead the energy associated with the applied electric field is going directly to ionization. After the steady state portion, in this diagram, after about 150 ns, the sheath spatial structures are expected to be fully formed, shielding the plasma from the biased electrodes and absorbing the necessary potential changes from the plasma potential to the respective electrode bias with respect to the plasma potential. A leading-edge spatially resolved investigation was conducted in order to investigate the temporal evolution of the spatial distribution of the electron properties. The test matrix is presented in Table 4.8 The results for the 40-ns to 70-ns delay cases are presented in Figures 4.11 to 4.14. There are several noteworthy items. Firstly, the 30 ns condition was approaching the SNR detection limits overall spatial points. Given this, the least squares

Table 4.8: Leading edge phase delay test matrix.

P_{g} (Torr)	V_{D} (kV)	$\Delta t_{\mathrm{bs/ps}}$ (ns)	$\Delta y_{\mathrm{b/c}}$ (mm)
6	20	40 to 70	3.25 to 23.25

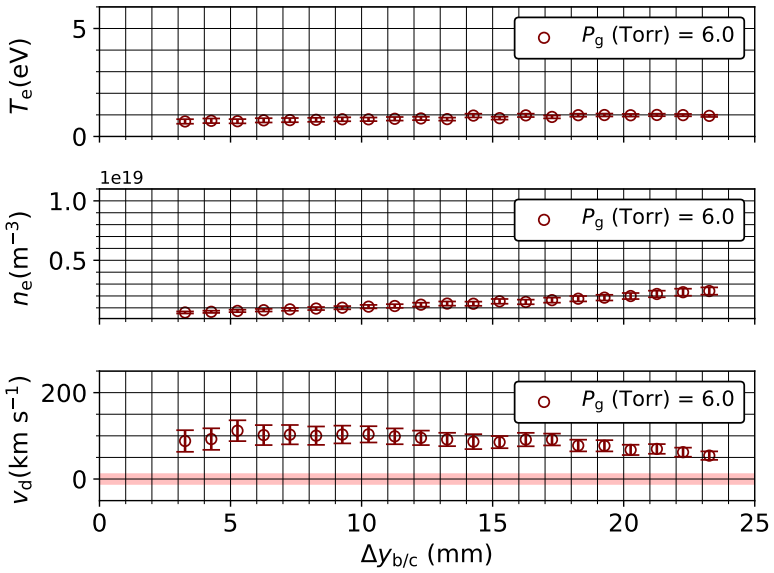

Figure 4.11: Spatially resolved electron properties at a 40-ns delay with respect to the leading edge of the plasma pulse.

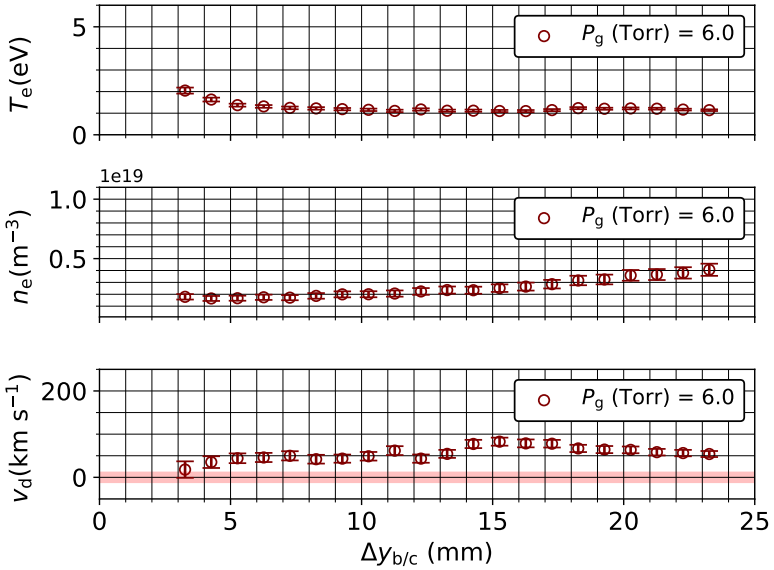

Figure 4.12: Spatially resolved electron properties at a 50-ns delay with respect to the leading edge of the plasma pulse.

uncertainty analysis was not able to be performed due to an uninvertable matrix operation necessary to estimate the covariance matrix, this is why these data are not presented. However, the minimum estimated number density during this experiment was 5.3×10^{17} m^{-3}. Secondly, the 70-ns condition was taken one day apart from the rest of these conditions.

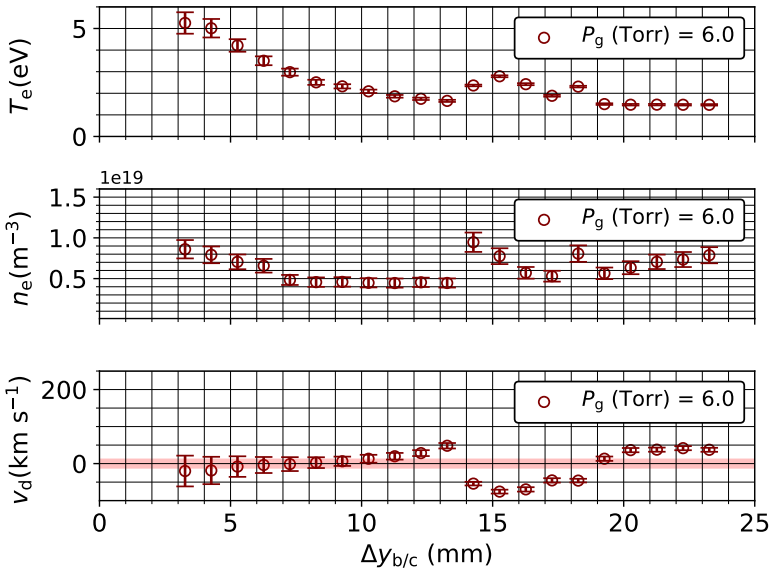

Figure 4.13: Spatially resolved electron properties at a 60-ns delay with respect to the leading edge of the plasma pulse.

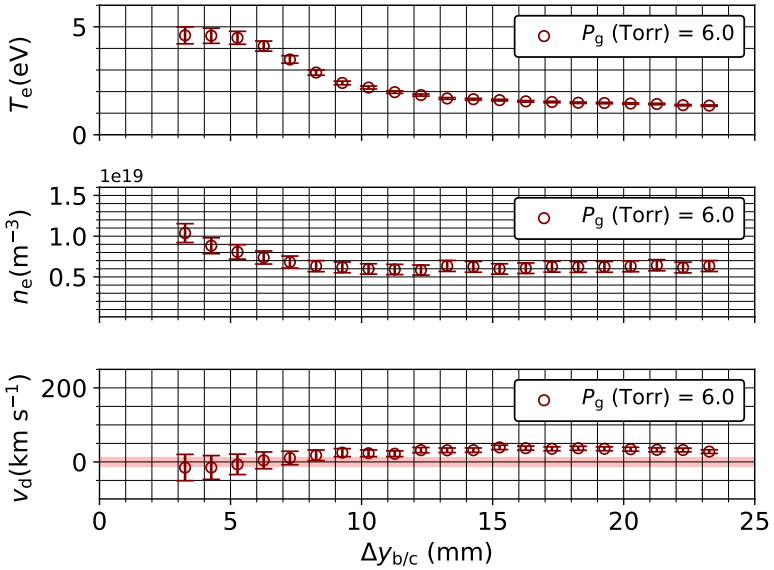

Figure 4.14: Spatially resolved electron properties at a 70-ns delay with respect to the leading edge of the plasma pulse.

Thirdly, one would expect that as the number density increases past the projected detection limit, the uncertainty would decrease. However, the charts present the opposite trend. These are artificially inflated due to the fact that the emissions are uniform spatially, but not uniform temporally across the pulse, with leading edge emissions being stronger than

the steady state and falling edge emissions. This was confirmed after the test from observations at several points along the leading edge. However, the emission data was not saved. As suggested by the phase delayed sweep, the non-monotonic variation in the centerline plasma properties was indicative of a rapidly evolving plasma. During the rising edge of the plasma pulse, the spatial structures are evolving rapidly as can be seen by the charts presented in Figures 4.11 to 4.14. Therefore, later in the pulse, during the crest or falling edge with the slow tail off in the voltage where the plasma parameters are varying more gently is the target temporal section to be studied.

Finally, voltage sweeps taken with electrode accidentally set to a spacing of Δy_{e} = 32.5 mm at two different delays along the pulse showed a linear increase of the electron temperature from 1.2 eV to 1.7 eV, about a 50% change, and a number density change from $0.5 \times 10^{18}\ \mathrm{m}^{-3}$ to about $2.5 \times 10^{18}\ \mathrm{m}^{-3}$, a 500% change. In both cases, the trends showed a monotonic increase in both the electron number density and temperature. It is assumed that these trends hold at the desired electrode spacing, indicating that the 20 kV condition would always lead to the highest number density compared to the lower voltage setpoints.

As stated at the beginning of this chapter, one of the goals of this experiment was to quantify the notional number density limit for the given set of capital pieces of equipment. The experiment yielded a minimum number density of $5.3 \times 10^{17}\ \mathrm{m}^{-3}$ at 3,000 accumulations and 100% gain on the detector. 3,000 accumulations at 10 Hz is approximately 5 minutes of collection time for a spectrum. Accumulating to 6,000 shots would lead to a projected number density limit of ap proximately $2 \times 10^{17}\ \mathrm{m}^{-3}$. A re-esimation of this density detection limit and a system improvements to further decrease the detection limits are outlined in Section 4.3.

4.3 External Discharge Voltage Boundary Condition Effect on the Spatially Resolved Electron Temperature and Density Profiles

4.3.1 Spatial Resolution and Discharge Study Test Matrix

In order to spatially resolve the electron properties between the electrodes, their electrode spacing was held constant while the electrodes themselves were actuated in the $\pm\mathbf{y}$ direction with respect to the laser beam, effectively moving the plasma with respect to the laser beam allowing for probing of the plasma properties axially between the electrodes. As stated previously, the electrodes were spaced at 26.5 mm at linear actuator engraving markings of 25 mm and 25 mm, respectively, each etched with 1 mm marks from 1 to 50 mm. Therefore, at the 25 mm mark, the beam was 13.25 mm away from each respective electrode. All that was required was incremental movements in 1 mm steps towards each respective electrode for spatial resolution. In theory, the plasma could have been moved such that the electrodes were just 1 μm away from the laser beam. However, strong reflections and stray light from the cell prohibited this as the center line light began to saturate the detector at less than 3.25 mm away from each respective electrode. Additionally, at a distance of less than 1.525 mm, the electrode (being 24 mm diameter) would block the solid angle of collection from the lenses, requiring spatially resolved Raman calibration. The test matrix for the experiments is presented in Table 4.9, with the collection parameters outlined in Table 4.5.

Table 4.9: Spatially resolved voltage sweep test matrix.

P_{g} (Torr)	V_{D} (kV)	$\Delta t_{\mathrm{bs/ps}}$ (ns)	$\Delta y_{\mathrm{b/c}}$ (mm)
6	8 to 20	150	3.25 to 23.25

4.3.2 Confirmation of Statistical Stationality of the Plasma Pulse

Early in the benchmarking of the tabletop system, 300 oscilloscope traces were taken per condition and overlaid to confirm the statistical stationality of the plasma pulse. These scans were taken at the start of the plasma pulse acquisition over a period of less than five minutes. These scans are not presented here. Having confirmed the statistical stationality of the plasma current pulse gave confidence that, over the collection period of a spatially resolved dataset at about 2 hours for 24 points given that 3,000 shots takes five minutes at 10 Hz.

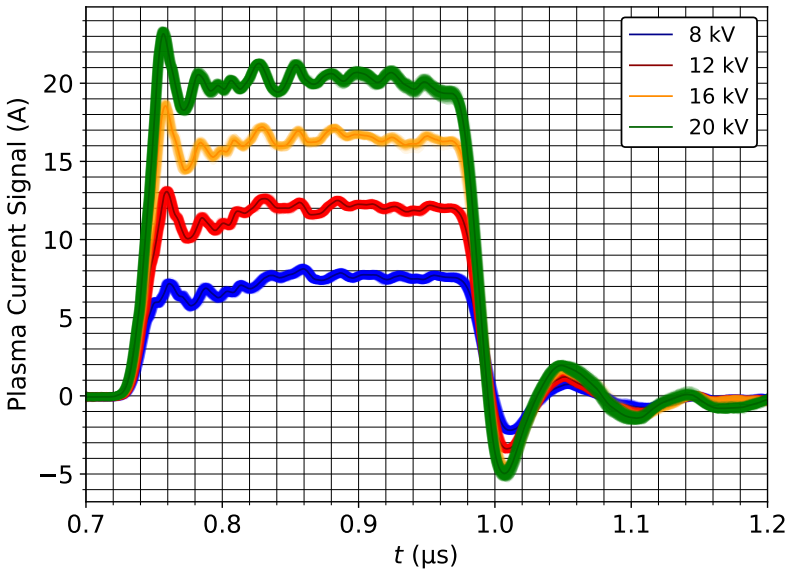

Figure 4.15: Individual and averaged discharge current signals at several discharge voltages. Individual oscilloscopelines are plotted with thin soft colored lines, and the average oscilloscopesignal is plotted with a dark colored line. The 8, 12, and 20 kV cases used 100 oscilloscope traces, the 16 kV case used 21 oscilloscope traces.

Instead, 50 oscilloscope signals were taken at the start of the spatially resolved dataset, at $\Delta y_{\mathrm{b/c}} = 3.25$ mm, and then again at $\Delta y_{\mathrm{b/c}} = 23.25$ mm, almost two hours later to confirm statistical stationality of the plasma signal. Additionally, as a backup, at each spatial point, a single oscilloscope signal was taken. In the 16-kV case, an error in data acquisition made the signals unusable. Instead, the 21 usable backup signals were used. These signals

are overlaid in Figure 4.15, with the individual signals in transparent thin-lined colors, and the averaged signal over in dark colors. The peak currents for the four cases were 23.2,18.5,13.1, and 8.1 A, respectively. The maximum value of the average percentage difference between the individual scans and the average scan over all 4 voltage conditions is less than 0.5%, indicating that over the two-hour collection period of each spatially resolved dataset, the plasma pulse can be considered statistically stationary.

4.3.3 Results, Spatial Resolution Limitations and System Improvements

The resulting spatially resolved electron property distributions are presented in Figures 4.16 to 4.19. Further analysis of this data with sheath models is summarized in [175].

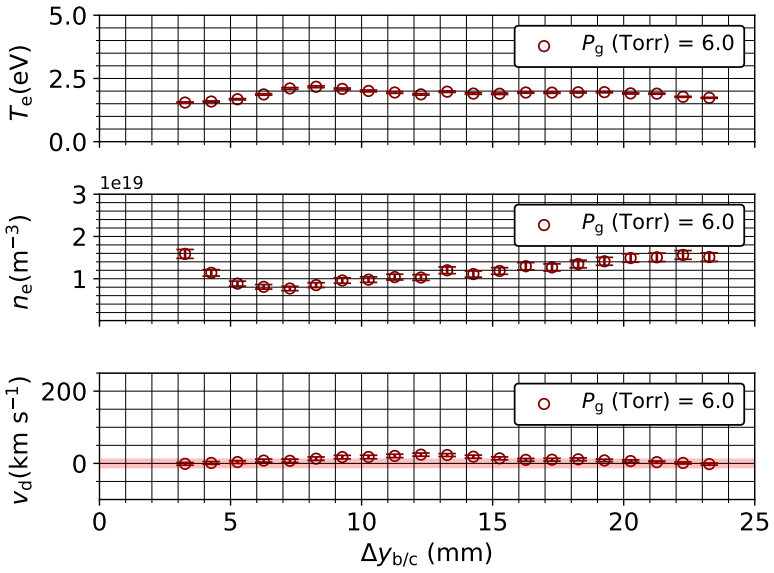

Figure 4.16: Spatially resolved electron properties at discharge voltage of 20 kV.

Changes of electron density of 50% in a distance of 1 mm, and gradients in the electron density approaching the cathode, suggest that the measurement volume resolution approaching the electrodes, to within a distance of less than 5 mm, must be finer than 1 mm. The measurement volume step must be finer in order to resolve gradients in electron properties accurately. Finer movement of the interrogation volume can be achieved through a relationship between a turn of the worm gear driving the linear actuators and the engravings

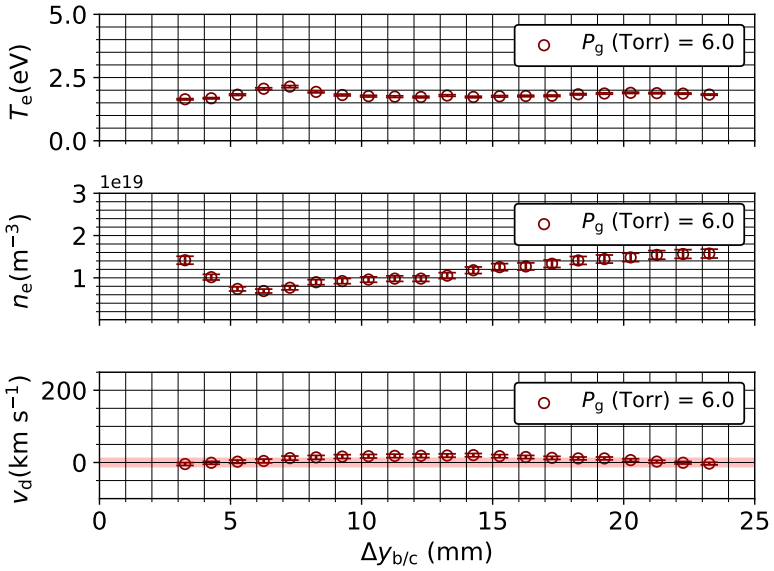

Figure 4.17: Spatially resolved electron properties at discharge voltage of 16 kV.

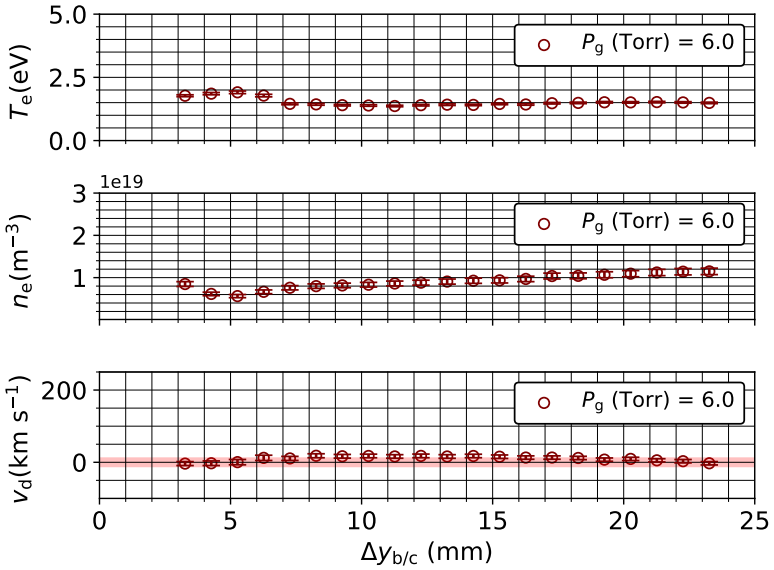

Figure 4.18: Spatially resolved electron properties at discharge voltage of 12 kV.

on the linear actuator. This is a planned system improvement.

The minimum probing distance of 3.25 mm, which was limited by reflection saturation at the center wavelength and solid angle sub-tension as the electrodes are approached, must be addressed in order to decrease the detection limit. This can be resolved by changing the third lens in the collection optical train to a positive focal length lens and placing a slit at

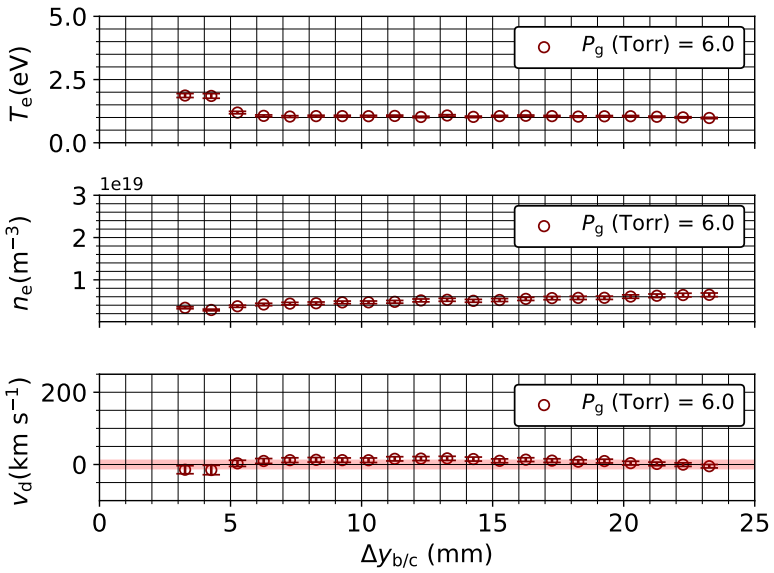

Figure 4.19: Spatially resolved electron properties at discharge voltage of 8 kV.

the focal point between the second and third lenses to minimize reflection propagation. Additionally, averaging several frames that are on-ccd accumulated after saturation limits the maximum number of accumulations can help to improve SNR ratio. The sub-tension of the collection solid angle as the electrodes protrude into the solid angle cone can be accounted for by collecting spatially resolved LRS close to the electrodes. Additionally, the discharge condition trade space must be explored to generate a larger sheath and presheath at the cathode. Decreasing the neutral pressure will increase the presheath thickness. An electron density 5×10^{16} m^{-3} and temperature of 5-10 eV will create a thicker sheath. However, the role of discharge voltage is unclear because of the discrepancy between collisional and collisionless sheath theory.

Finally, the system detection limit must be improved. This can be done by making two simple changes to the system. First, taking advantage of hardware binning over the vertical pixels illuminated by the beam image will increase SNR ratio by decreasing read noise. Second, expanding the beam waist diameter via a change in the focal length will allow the full laser energy to be leveraged from the laser. In the current configuration, at a projected peak signal to mean noise ratio of 1, the detection limit is 2×10^{17} m^{-3}. These changes will

likely decrease the detection limit to below 5×10^{16} m^{-3}.

4.3.4 Summary

A pressure-controlled discharge plasma cell capable of generating pulsed plasmas with number densities of approximately 1×10^{17} to 1×10^{19} m^{-3} was developed. A laser Thomson scattering system was developed around this cell in order to study the spatial variation in electron properties perpendicular to the plasma bounding electrodes, in particular in the near cathode region, which is of interest due to the cathode sheath and presheath potential drop. The measurement volume step of 1 mm between the electrodes and a minimum electrode probing distance of 3.6 mm proved to be enough to resolve gradients in the electron properties between the bulk plasma and the cathode negative glow region. These represent some of the first laser Thomson scattering measurements with resolution perpendicular to the plasma bounding electrodes in such a glow-like discharge. However, the relatively high bulk plasma density leads to an expected combined sheath and presheath length of less than the minimum probing point, according to [175] and therefore the properties in this region remain unresolved. Small modifications of the cell to decrease the number density detection limit and increasing the resolution in the movement of the interrogation volume are necessary to explore the sheath and presheath regions for model validation.

CHAPTER 5
LARGE VACUUM TEST FACILITY THOMSON SCATTERING MEASUREMENTS IN THE KRYPTON PLUME OF A LANTHANUM HEXABORIDE HOLLOW CATHODE

5.1 Introduction

This chapter presents the implementation of a large vacuum test facility laser Thomson scattering system for use on live EP devices, like hollow cathodes and HETs, with a minimum number density that does not exceed $1\times10^{17}\mathrm{m}^{-3}$. The system is adapted to the facility from the work in Chapter 4. The data is presented and the number density limit is confirmed. This work is summarized in [176].

5.2 Experimental Setup

5.2.1 Vacuum Test Facility

This experiment was conducted in Vacuum Test Facility 2 (VTF-2) at the Georgia Tech High Power Electric Propulsion Laboratory (HPEPL). VTF-2 is a 4.9 m diameter and 9.2 m long stainless-steel chamber. Medium vacuum is achieved via one Leybold SV630 841 m^3/hr rotary-vane pump to 7 Torr, after which a rough vacuum pressure of 30 mTorr via one Leybold RA5001 6456 m^3/hr blower. High vacuum is achieved via ten PHPK CVI TM1200i cryopumps that line the facility. Each of the 10 pumps operates by cooling a cryosail to an average temperature of 13 K by an external closed-loop helium cryostat system. This effectively pumps the atoms in the chamber by absorbing the ones that strike the cryosails. Each cryosail requires radiation shielding that is provided by individual liquid Nitrogen shrouds that are all connected in parallel to a recirculating liquid Nitrogen system that liquefies the gaseous nitrogen via two Stirling Cryogenics SPC-4 cryogenerators [48].

This system provides a combined xenon pumping speed of 350,000 l/s and achieves an ultimate base pressure of 1.9×10^{-9} Torr - N_2.

The pressure in the facility from an atmospheric pressure of approximately 760 Torr to a medium vacuum of 1 Torr was monitored via a 1000 to 1 Torr range Kurt J Lesker XCG-BT-FB-1 capacitance manometer mounted on a flange on the periphery of the chamber. A capacitance manometer was chosen for its accuracy of $\pm0.5\%$ and the fact that no gas specific corrections are needed for the pressure. The gauge was calibrated per factory specifications and then a linear correction was applied to account for the non-ideal orientation of the gauge. Accurate pressure readings from 760 Torr to 1 Torr that represent the pressure as close to the laser beam scattering section are critical for accurate absolute number density calibration of a laser Thomson scattering system via Rayleigh or Raman scattering as they are both linearly dependent on the pressure. A stand-alone experiment verifying that the pressure when the gauge is mounted on a flange as opposed to being directly in the test section was performed. The divergence was less than 1%.

At high vacuum, the pressure at 0.5 m radially from the test section and at the periphery of the facility were monitored via two Agilent Bayard-Alpert 571 hot-filament ionization gauges. The operational pressures during the experiments presented are the average of the two internal and periphery pressures, corrected to kryton via Equation 5.1,

$$p_{\text{operational}-\text{corrected}} = \frac{1}{c_{\text{corr}}}\left(p_{\text{operational}} - p_{\text{base}}\right) + p_{\text{base}}, \tag{5.1}$$

with c_{corr} being equal to 1.96 and 2.87 for krypton and xenon, respectively [1]. At steady state, the base pressure in the facility was 2.55×10^{-7} Torr $-$ N_2. During the experiment, the corrected operational pressure was 1.33×10^{-6} Torr $-$ Kr

Mass flow was provided by a system mounted externally to the facility. Two MKS GE40A mass flow controllers (MFCs), connected upstream to a propellant bottle set to 20 psi were used to provide mass flow to the internal devices. The MFCs have full-scale

ranges of 100 and 50 sccm on xenon, respectively. The internal MKS software was used to switch the working propellant to krypton, after which the full-scale for the controllers were 200 and 750 sccm, respectively. The flow controllers were zeroed via the internal software procedure. Then, the controllers were calibrated at the test section inside of VTF-2 using a DryCal 800-10 volumetric flow rate meter system to create a linear fit between the desired flow rate and the actual measured flow rate in the test section after the meters of propellant lines between the external MFCs and the test section. 5 points were averaged at every desired flow rate. Mass flows reported are the corrected flowrates.

5.2.2 Cathode Discharge, Cathode Discharge Mounting and Relative Movement

The test article in this experiment was a 60 A Lanthanum hexaboride (LaB_6) hollow cathode whose design heritage stems from the HERMeS and H6 HETs hollow cathodes, designed for use in the H9 [104] and extrapolation into the X3 nested HET [72], referred to going forward as the H9 cathode. Over the last decade, the need for high-current hollow cathodes capable of operating from 10 to 350 A of discharge current have been developed to meet the need for higher power HETs for high thrust and longer lifetime missions [84, 102]. The target discharge current for this experiment was 25 A. An external stainless-steel cylindrical anode of length L_{anode} = 211.1 mm and diameter D_{anode} = 301.6 mm was placed 152.4 mm away from the H9 keeper face and used to close the discharge circuit. The anode and cathode keeper were aligned coaxially. Figure 5.1 shows the discharge circuit and the mounting of the discharge circuit in the facility.

In order to spatially resolve the electron properties in the near keeper plume of the H9 cathode, relative movement between the cathode plume and the interrogation beam scattering volume was required. This was accomplished by mounting the cathode discharge assembly on Parker 4062000XR motion stages. The motion stages were configured in an $\mathbf{x}_{\text{chamber}} - \mathbf{y}_{\text{chamber}}$ configuration, with $\mathbf{z}_{\text{chamber}}$ oriented according to the right hand rule. Figure 5.2 shows the orientation of the motion stages, their positive travel direction,

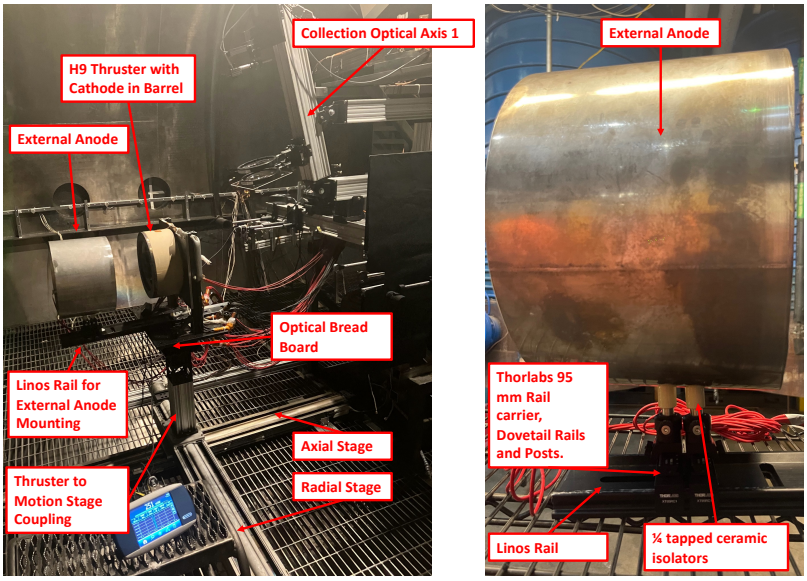

Figure 5.1: Cathode discharge mounted to the axial and radial stages inside of VTF-2.

and the chamber axis definitions, as well as the interrogation, collection, and detection optical axes to be described in Subsection 5.2.3. Figure 5.1 shows the cathode, HET, and external anode mounted on the motion stages. They were coupled via a custom stainless-steel coupler designed to interface with a Thorlabs breadboard coupler. Thorlabs XT95 class 95 mm rails were coupled on one side to the custom stage and then to a lab jack for discharge circuit height alignment relative to the interrogation beam. This jack was then coupled to a breadboard that was the base for the mounting of the discharge assembly. The anode was placed with a black one-sided 95 mm rail and rail carrier assembly. This choice was two-fold; firstly, the rail allowed for easy alignment perpendicular to and along the axis coincident with the center axis of the cathode. Secondly, it was black to help minimize reflections from the surface of the rail from entering the collection optical axis and leading to stray light that would make optical alignment difficult.

5.2.3 Internal and External Interrogation Beam Optical Systems and their Alignment

Figure 5.2 outlines the notional relative positions between the VTF-2 facility and the capital components for this experiment. The dashed line in green represents the desired optical

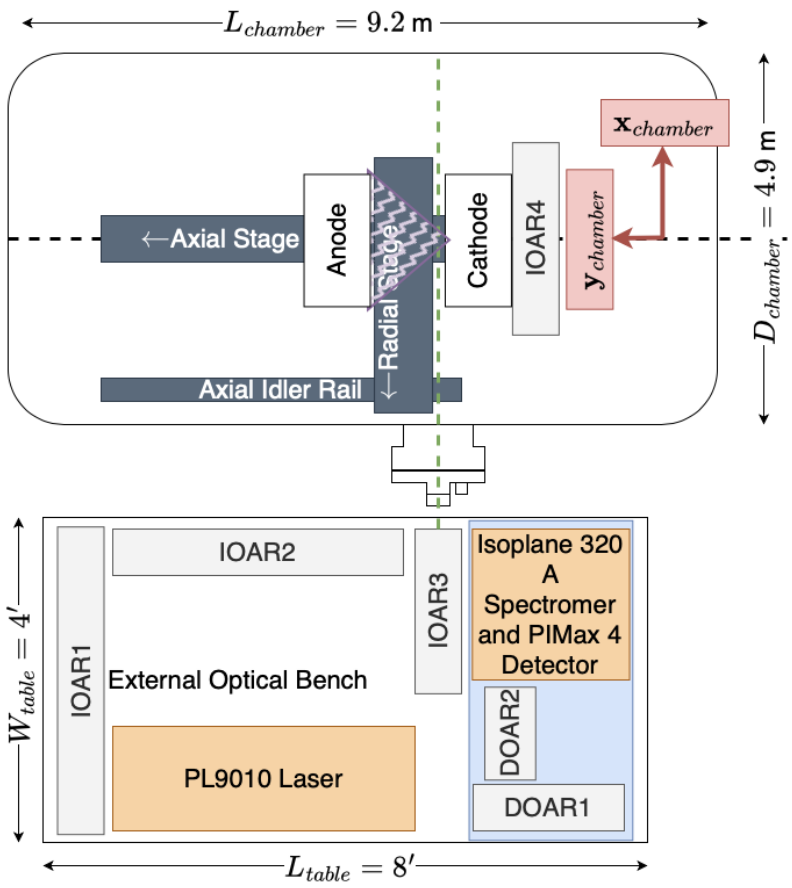

Figure 5.2: Notional diagram of the relative location of the external optical system with respect to the vacuum test facility. IOAR and DOAR area acronyms for interrogation optical axis rails and detection optical axis rails respectively

axis for the interrogation beam. This dashed line is notionally coincident with the center-line of the two flanges depicted in the figure on either side of the facility radially, parallel to $\mathbf{x}_{\text{chamber}}$, and coincident with the chamber midplane. The structures inside of the chamber, including the thrust stand, are designed to facilitate coaxiality of HETs and other plasma sources with the axial center-line of the chamber parallel to $\mathbf{y}_{\text{chamber}}$.

The interrogation laser beam system is diagrammed in Figure 5.3. It begins external to VTF-2, on an 8 " thick 8’ x 4 ’ Newport RS2000 optical table placed on four Newport S-2000A-428 automatic leveling, vibration isolating legs. Although the vibration stabilizing legs were initially used to ’float’ the table, during fine alignment, it was determined that the day-to-day change in the alignment or the risk of accidental perturbation of the table

by a human and the effect on the alignment in the interrogation section was too large. Throughout these experiments, the automatic leveling capabilities of the stabilizing legs were not used. Instead, the table was leveled manually. The surface of the table was 36 " from the ground, and the relative distance from the surface of the optical table to the center plane of VTF-2 is 76". On top of this optical table, an injection seeded amplitude DLS Powerlite 9010 Nd:YAG laser frequency doubled using a 2nd harmonic generator type II crystal provided a 9 mm diameter beam with a laser pulse width between 5 and 8 ns. The laser energy, at 532 nm wavelength output, was measured at 1.15 J/pulse after installation. The laser beam is steered externally along three legs.

The first two legs are aligned on two one-sided XT95SP class 95 mm rails parallel to the surface of the optical table, while the third provides the periscope distance vertically from the surface of the table parallel to $\mathbf{z}_{\mathrm{chamber}}$ to bring the beam to the height of the chamber midplane. Interrogation beam optical axis 1 (IOA1) is aligned along a rail using four self-consistently aligned irises, $I - i_1$ to $I - i_4$, to pre-define an optical axis parallel to the surface of the optical rails and aligned laterally with the center of the rails, along which the laser beam was then aligned. Then, the rest of the optics on IOAR1 and IOAR2 were placed sequentially. When all optics were placed, they were adjusted perpendicular to the optical axis to ensure that the beam was passing through the centers of the irises and coincident with the pre-defined optical axis. First, a 2-1 beam expander was placed using $I - l_1$ and $I - l_2$. The relative position of $I - l_1$ and $I - l_2$ was changed with a micrometer stage until the beam was approximately collimated. Table 5.1 outlines the optical components used.

Then, a polarization-dependent beam energy splitter was constructed using half wave plate $I - HWP_1$ and polarizing beamsplitter cube $I - PBS_1$. This was necessary to maintain the nominal operational mode of the laser at it's optimal Q-switch delay and provide the flexibility for external modulation of the power. Immediately after $I - HWP_1$ is a power meter, $I - PM_1$, placed on a flip mount for easy flipping into the optical beam path for laser energy measurement. After this alignment procedure, irises $I - i_1$ and $I - i_2$

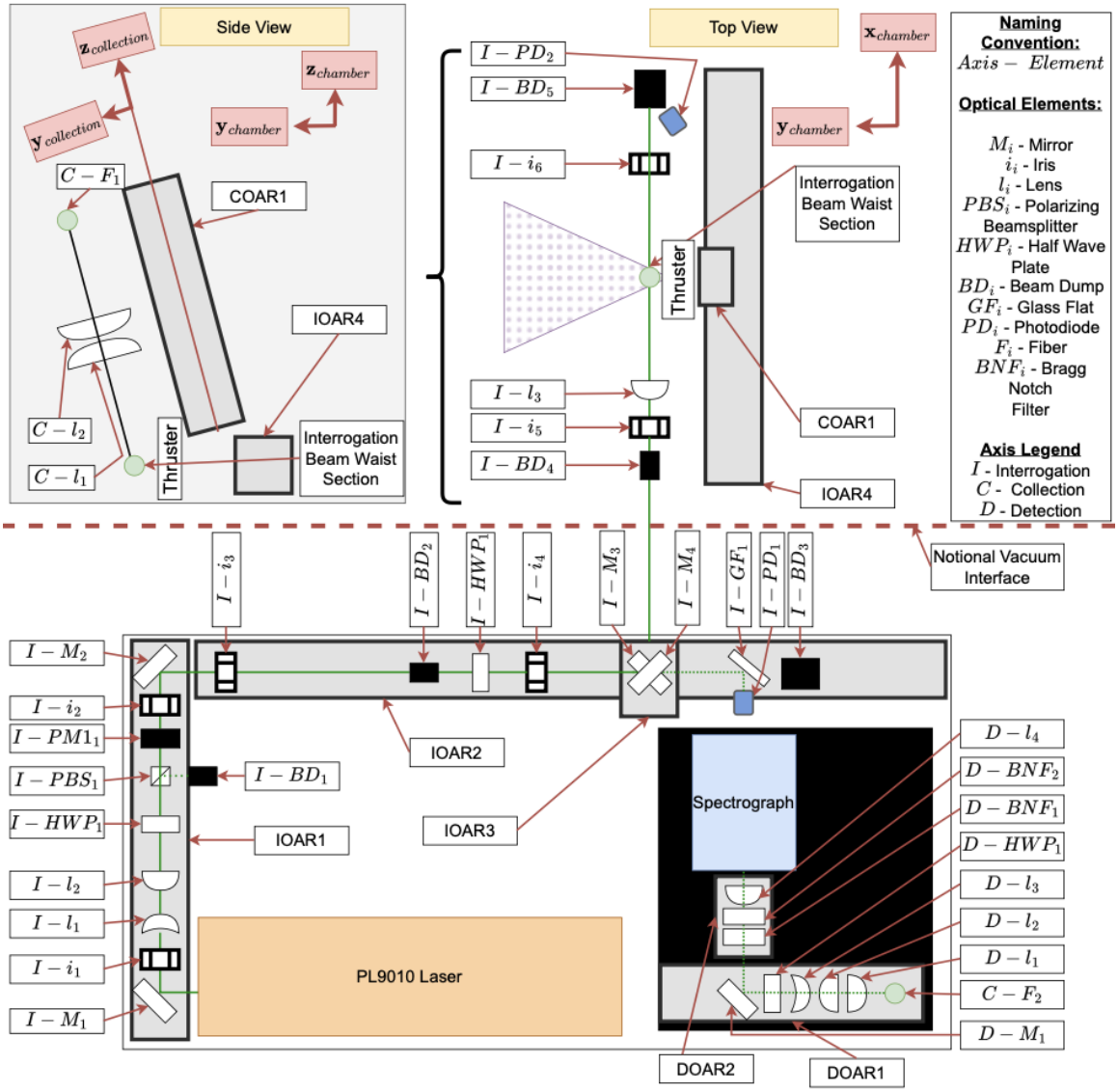

Figure 5.3: Master optical diagram for the interrogation, collection and detection systems. The vacuum interface is represented as the large thick red dashed line.

were placed as far apart as possible on IOAR1. Then, $I-M_2$, $I-BD_3$ as well as $I-i_3$ and $I-i_4$ were placed to align the optical axis defined by the irises along IOAR2. This ensured that the laser beam was coincident with the optical axis defined by the irises along both legs that were parallel to the surface of the table. After this was completed, the laser output energy was controlled using the internal software of the laser and stepped up in 100 mJ/pulse increments while correcting the alignment through $I-i_1$ to $I-i_4$ using $I-M_1$ and the terminal mirror inside of the laser head, which could be called $I-M_0$. This ensured

Table 5.1: Interrogation beam optical parameters.

Element	**Aperture Size**	**Focal length**	**Part**	**Sourced**
Laser	-	-	DLS Powerlite 9010	Amplitud/Continuum
$I-M_i$	50.8 mm	-	RX-532-45-UF-2038	Lattice Electro Optics
$I-BD_i$	20.0 mm	-	ABD0975NP	Kentek
$I-PM_1$	20.0 mm	-	UP52N-50S-QED-D0	Gentec
$I-i_i$	Variable	-	ID50	Thorlabs
$I-HWP_i$	20.0 mm	-	CW0-532-02-08-R10	Lattice Electro Optics
$I-PBS_1$	25.4 mm	-	PBH-532-10	Lattice Electro Optics
$I-l_1$	25.4 mm	-50 mm	UF-PC-25.4-50-532	Lattice Electro Optics
$I-l_2$	25.4 mm	100 mm	UF-PX-25.4-100-532	Lattice Electro Optics
$I-l_3$	25.4 mm	400 mm	UF-PX-25.4-400-532	Lattice Electro Optics

that as the thermal state of the internal optics changed and shifted the alignment, it was corrected. Finally, the laser was allowed to fire for one-half hour until it was determined that the laser's internal thermal state was constant, and a final adjustment to the alignment was made to ensure the beam was coincident with $I-i_1$ to $I-i_4$. Then, $I-HWP_1$ was adjusted until the output leaving the polarization-dependent energy splitter was 50 mJ/pulse. In this way, the energy was always controlled externally to the laser, providing the most repeatable and consistent alignment. With the major alignment task complete, $I-HWP_2$ and $I-BD_2$ were placed in the same fashion, adjusting their degrees of freedom perpendicular to the optical axis until their apertures were coincident with the laser beam. $I-HWP_2$ is critical as it controls the polarization inside of the chamber in the collection volume. The polarization is optimized by collecting Rayleigh scattering signal. The depolararization effect of the LRS signal makes it ill suited for optimizing the polarization. For monitoring of jitter and timing, an uncoated glass flat $I-GF_1$ was used to direct a small portion of the beam energy onto $I-PD_1$ that was monitored on an oscilloscope. This concluded the alignment of the laser beam and optics along IOAR1 and IOAR2 parallel to the surface of the optical table. Figure 5.3 shows the maser optical diagram for the system.

Before entering the chamber, along IOAR3, two mirrors $I - M_3$ and $I - M_4$ create a polarization rotating periscope to bring the laser beam up to the height of the center axis of VTF-2 along IOAR3, which was 2 m in length. IOAR3 was supported by an auxiliary set of four sides rails for structural support. IOAR 3 was aligned along the direction parallel to $\mathbf{y}_{\mathrm{chamber}}$ such that the center of IOAR3 was within $\pm$ 25 mm of the centerline of the dashed axis in Figure 5.2. Mirror $I - M_3$ was on a micrometer translation stage along IOAR2, and $I - M_4$ was on a micrometer translation stage along IOAR3. The beam was then able to pass through into the facility along the center axis defined by the dash in Figure 5.2. A custom Torr Scientific NSQ1462-25 KF-flanged Brewster window was placed on the flange that was coaxial with this dashed axis in order to minimize reflections for safety. Additionally, along the entire interrogation optical axis, boxes were constructed using matte-painted aluminum to minimize the likelihood of specular and diffuse reflections from being visible even when the system was in operation.

After the beam passed through the vacuum interface, it was aligned along the final interrogation beam optical axis, IOAR4, which is fixed inside the vacuum facility on a A Thorlabs MB2436 24"x36" breadboard that sits atop a custom structure that is clamped to the thrust stand. This custom steel structure is bolted to the thrust stand using two axial members and one lateral member and was designed for quick deployment on to and off of the thrust stand for experiments while also being very rigid.

IOAR4 is a 1.5 m long four-sided rail that was placed hanging off of the breadboard. With the output of the laser to the facility at 50 mJ/pulse, iris $I-i_5$ and $I-i_6$ were iteratively aligned along IOAR4 to maximize the perpendicular distance from IOAR4 and ensure that the beam passing through the Brewster window was not clipped. This maximized perpendicular distance from IOAR4 ensures that when the plasma source is as close to IOAR4 as possible, the beam is as far away from the face of the source as possible, allowing for more probing space in front of the source. With this axis defined by $I - i_5$ and $I - i_6$, $I - BD_4$ was the first item placed on IOAR4 on a flip mount in order to stop the beam at the begin-

ning of IOAR4 when necessary. Then, $I - BD_5$ and $I - PD_2$ were placed in order to stop the beam at the far end of IOAR4 to avoid reflections inside the chamber and be able to monitor the laser pulse inside the chamber. Once this was complete, $I - l_2$ adjusted outside of the facility on it's micrometer stage until the beam was collimated along the entire length of the interrogation optical axis terminating inside of the facility. This required slight adjustments of mirrors $I - M_0$ to $I - M_4$ to maintain alignment along the optical axes defined by $I - i_1$ to $I - i_6$. However, this is critical as the path length from $I - l_2$ is meters, and collimation up to the final focusing lens $I - l_3$ is critical for a small diffraction-limited spot size in the test region. Finally, $I - l_3$ was placed and aligned on IOAR4, and the focus was roughly aligned to the center of IOAR4 before being fine-aligned later using a micrometer stage. Figure 5.4 shows the internal interrogation optical axis used in this experiment.

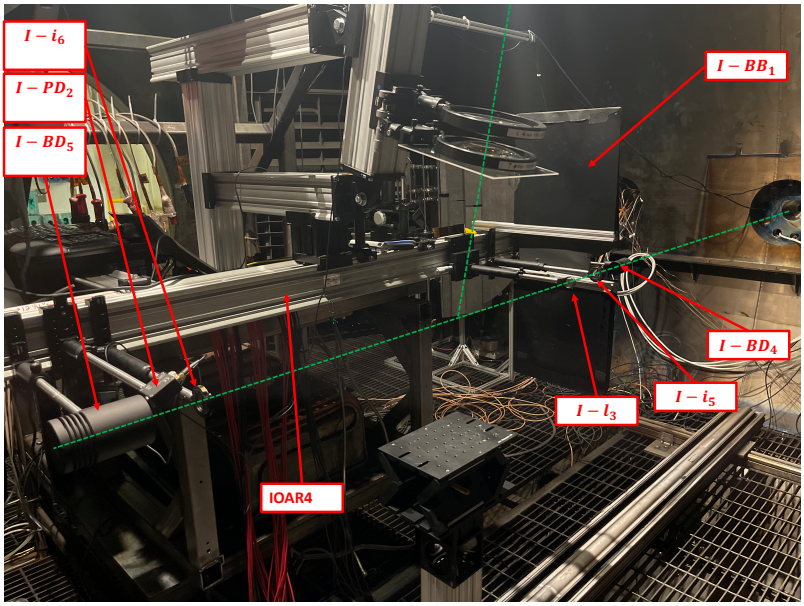

Figure 5.4: A photo of the internal optical rail structure that supports the last leg of the interrogation optical axis and the collection optical axis. The internal interrogation optical axis and the collection optical axis are shown in green.

Figure 5.5 shows an earlier iteration of IOAR4 without the beam blocking, photodiode, and smaller beam dump, with the focused beam. Several degrees of freedom have been mentioned when aligning an optic along and perpendicular to a pre-defined optical

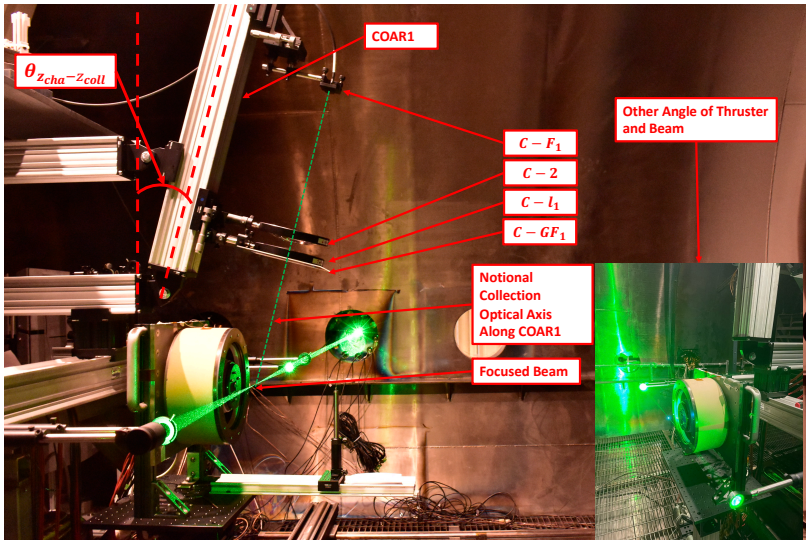

Figure 5.5: A previous iteration of the internal rail structure with the HET in place during alignment. The focus of the interrogation beam is clearly visible. The collection optical axis and its intersection with the focus of the beam is shown in green. A second view is presented in the bottom right before the collection optics were added and before the collection optical rail was placed at the necessary angle with respect to the chamber axes.

axis parallel to the surface of an optical rail. The critical piece for the alignment of the interrogation and collection branches is the necessary degrees of freedom parallel to and perpendicular to the desired optical axis. The optical rails define an approximately straight surface along which, with the help of optical rail carriers, an optical axis can be defined at some height using the perpendicular degree of freedom defined by the optical post and post holder. The center aperture of a master iris allows for this axis to be defined, and then once it is defined, other apertures can be aligned with respect to this to allow for multiple targets to facilitate aligning optics (lenses, etc.) by having multiple targets. Additionally, the fixed position of the irises allows for monitoring of alignment during operation and from day to day, allowing small adjustments to be made for realignment. Aligning in this way ensures that things are going straight and that turns are made at 95 degrees, minimizing losses of laser energy into the facility. Additionally, the targets on the rail structure inside the facility allow for alignment of the interrogation beam to be corrected as the chamber compresses during pumpdown operations. This will be discussed in a later subsection. In

short, great care was taken in providing the requisite degrees of freedom, and in some cases micrometer resolution in said degrees of freedom, to control the location of the beam inside of the facility from outside with the external interrogation beam system, as well as control its shape and polarization. This is critical to maximizing LTS generation. Additionally, the internal interrogation beam optical structure allows for the minimization of the focal length of $I - l_3$. For the same incident beam diameter and divergence angle, a smaller focal length lens reduces the expected beam waist size and length. This increases spatial resolution along and perpendicular to the beam propagation direction, but limits the maximum incident laser energy as was the case in this experiment due to the high fluence. Subsection Subsection 5.2.4 discusses how this scattered light is collected, relayed, and detected.

5.2.4 Internal and External Light Collection and Detection Systems and Their Alignment

Similar to the external and internal interrogation beam optical system, the light collection and light detection systems have internal and external sections. The design goals were simple for the collection and detection systems. The first was simply to maximize the collection numerical aperture while maintaining spatial resolution to less than 2 mm x 2 mm. The second was to be able to adjust the alignment of the collection system from outside of the facility ahead of the expected relative movement of the external interrogation beam system from the internal interrogation beam system as the facility compressed. Finally, the ability to get within $\approx$1-2 mm from the face of the plasma source without blocking the collection solid angle.

Given the size of the facility, the need for a fiber bundle was always expected to relay the light from the internal collection system to the external detection and filtering system. For the sake of bookkeeping, in Figure 5.3, the fiber faces, $C - F_i$ referred to as part of the collection system. Two custom 5 m long Thorlabs FG200LEA- FBUNDLE fiber bundles that were ordered. The bundle was a linear array of 200-μm diameter fibers on one end

and fanned out into individual fibers for feeding through the facility. Both the common linear end and the individual fanned fibers were SMA-ended. The fibers were fed through the facility wall with a custom SQS Fiber Optics HEM048727 4.5" CF flange. The fiber feedthrough and Brewster window are shown in Figure 5.6.

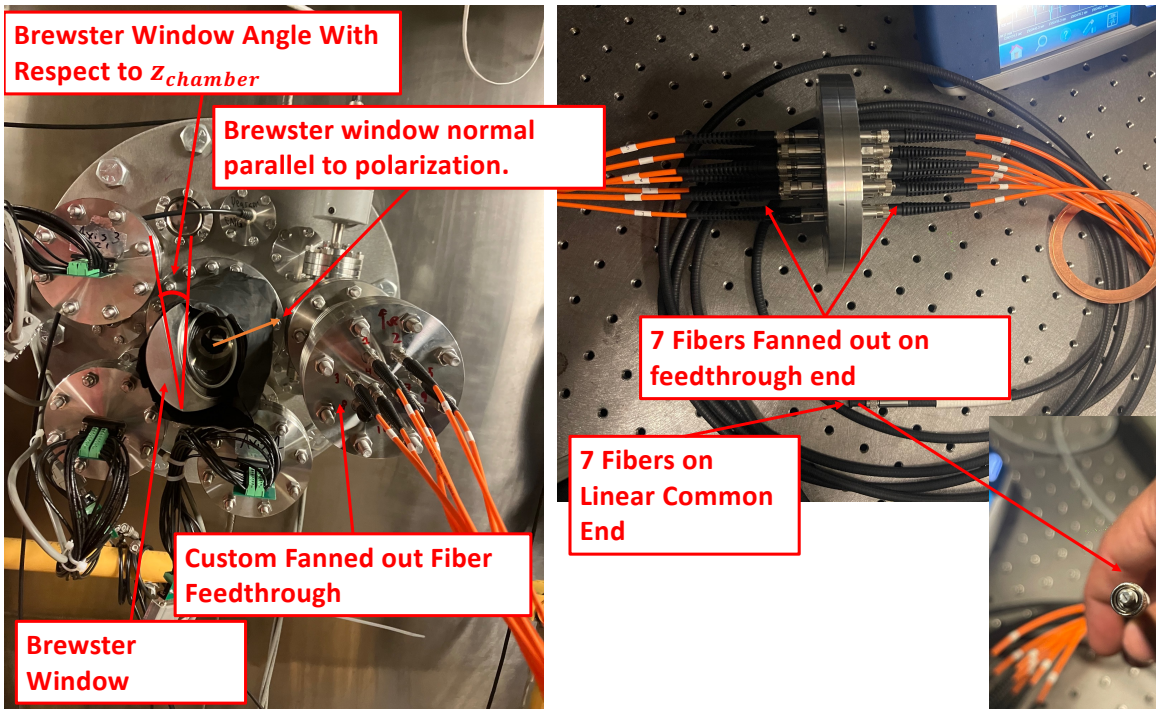

Figure 5.6: Brewster window and fiber flange feedthrough.

On the air side, the second fan bundle was used to relay the light output to the detection system as a linear array. At the time of ordering these pieces of equipment, the goal was to minimize custom parts and maximize off-the-shelf or easily accessible parts. However, a more convenient solution with possibly higher throughput may be a custom fiber feedthrough that is a single fiber bundle with a flange sealed around it. The 200 μm fiber arrays were chosen because they provided good spatial resolution, in theory down to 200 μm $\times$ μm, while having a high numerical aperture of NA = 0.22. A bundle of linearly arranged fibers was chosen because it provided the most light collection along the beam propagation direction without sacrificing spatial resolution in the perpendicular directions. This fiber also ended up being advantageous for alignment as individual fibers could be

'turned off' by disconnecting at the flange.

Of course, a higher NA fiber could have been used. However, this would have presented other challenges. Firstly, matching a higher NA would have required larger diameter lenses, to be discussed shortly. Second and more importantly, from experience, we expected that the image of the linear array of fibers through the external detection system was going to need to be magnified to maximize light throughput and minimize losses due to clipping through the Bragg notch filters (BNF). Expecting a magnification of 2 of the linear array image on the slit plane, any fiber diameter over 200 μm would have led to slit plane image sizes of greater than 400 μm. This was expected to be problematic because increasing the size of the object image on the slit plane requires increasing the size of the slit to capture that light. This decreases spectral resolution, making it slightly more challenging to get a good Raman calibration. Additionally, the size of the image of the rejection ring on the image of the object that you are trying to spectrally filter is dependent, among other things, on the magnification of the optical system [162]. If the rejection ring image is not properly sized relative to the object image, then the slit or another physical block must be placed on the un-filtered portions of the image in order to not saturate your detector when signal-to-noise averaging over many shots to build an image/spectrum.

With the 200 μm, NA = 0.22 fibers sized, the largest diameter shortest focal length lenses were desired. This was limited by the ability to find quality large-diameter lenses and off-the-shelf optical mounts for the lenses for this first iteration. For this reason, Lattice Electro Optics B-PX-150-350-532 150 mm diameter 350 mm focal length lenses were chosen with QiOptiq G036084000 150 mm diameter lens mounts. This was sized using,

$$\mathrm{NA} = n \sin\left(\theta_{\mathrm{lens}}\right), \tag{5.2}$$

with,

$$\theta_{\mathrm{lens}} = \tan\left(\frac{D_{\mathrm{lens}}/2}{f_{\mathrm{lens}}}\right)^{-1}. \tag{5.3}$$

The light collected by the collection lens relay system is all coupled into the fiber. The NA of the lenses was .2095, slightly smaller than the numerical aperture of the fibers. Geometry would suggest that there is about a 10 % loss in the light collection power due to this slightly smaller effective NA of the lenses. Therefore, the first NA limiting element in the system is the NA of the collection lens relay system. However, these were the shortest lead time lenses available at the time of purchase from a trusted vendor, with a NA that approximately matched the NA of the fibers. Two of these lenses were used in order to create a 1 - 1 image of the linear array of fibers onto the interrogation laser beam plane. An AR-coated 200 mm x 200 mm x 2 mm piece of glass was placed ahead of the first collecting lens in order to protect the lenses from deposits from the thruster and cathode as well as allow for ease of cleaning without needing to completely realign the collection optical system. In order to adjust alignment externally to account for the movement of the interrogation beam relative to the collection optics, the mount that housed the linear array of fibers was mounted on an XYZ-configured set of Thorlabs MTS25/M-Z8 motion stages, coupled to a breadboard and 95 mm rail carrier for coarse alignment along the collection optical axis COAR1. Each individual stage was controlled via a Thorlabs KDC101 Kinesis K-Cube DC Servo Motor Controller, connected to the experiment computer via a KCH301 USB controller hub. The stages inside the facility were connected to the controllers outside of the facility using extension cables and 15-pin vacuum feedthroughs. A rotational fiber mount was used in order to allow for a rotational degree of freedom when aligning the fiber image parallel to the beam at the beam plane.

With the ability to collect as much light as possible through the large NA fiber and lenses, as well as correct for alignment from outside of the facility, the need for mm level interrogation near the cathode face without blocking this solid angle was addressed. Interfering with the solid angle defined by the collection lenses is a function of the relative orientation of the collection cone of the lenses with respect to objects that can cross into this cone. This is inconvenient because if the solid angle is spatially dependent, rotational

Raman calibrations would be required at every spatial point. Secondly, and more importantly, blocking the solid angle would decrease light collection power. In an application such as LTS in low-temperature low-density environments inside a large vacuum test facility, where every photon counts, this is undesirable. Defining $\theta_{\mathbf{z}_{\text{cha}}-\mathbf{z}_{coll}}$ as the angle between $\mathbf{z}_{\text{chamber}}$ and $\mathbf{z}_{\text{collection}}$, a simple rotation of the collection axis by an angle greater than the half angle of the collection lenses ensures that the object of interest could be brought right up to the interrogation beam scattering volume without loss in collection solid angle. In this case, $\theta_{\mathbf{z}_{\text{cha}}-\mathbf{z}_{coll}} = 15°$. This angle is clearly shown in Figure 5.5. The blocked and un-blocked cases are shown notionally in Figure 5.7. In the case where the collection axis is not rotated, the minimum axial distance that can be probed along the thruster center line is $\Delta z_{\text{min}} = r_{\text{thruster}} \tan(\theta_{\text{lens}})$. That distance for the H9 cathode sitting in the barrel of the H9 is approximately 30 mm.

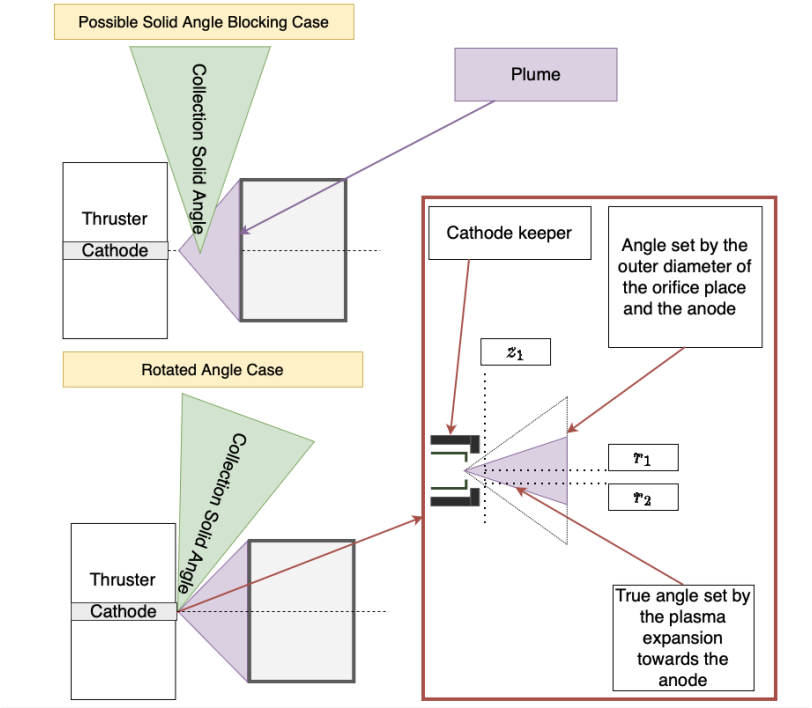

Figure 5.7: Notional diagram of the blocked versus unblocked solid angle cases.

The alignment procedure for the collection branch is similar to that of the interrogation branch. A master iris whose center aperture was about 8.5 " from the surface of its rail

carrier was placed on an optical rail outside of the facility. A pointing laser was used to define this optical axis along the rail, and then a second iris was used so that two targets were available for alignment as references for this optical axis. Then, the collection lenses $C - GF_1$, $C - l_1$ and $C - l_2$ were aligned atop a large rail carrier that had a Newport 426 series micrometer stage on it for fine alignment capabilities along the focusing direction of the lenses, $\mathbf{z}_{\text{collection}}$. This assembly had a dovetail rail and optical post assembly for each of the lenses to adjust their alignment perpendicular to the defined optical axis. Finally, the electric motion stages were manually driven to their half-travel location, then the fiber aperture was manually aligned with the pre-defined optical axis. This location was the 'roughly' aligned location of the mount using the stages and was recorded. This axis is shown in Figure 5.5 by the green line parallel to COAR1. The choice of maximizing the degrees of freedom for the fiber and having it be the only externally controllable optical element on the collection branch was to ensure the best coupling. A pre-defined optical axis along which the collection lenses were aligned ensured that the collection solid angle was maintained and that all that needed to be done to correct this alignment was to move the fiber 'back into' alignment from outside of the facility. With both optical axes, the interrogation and collection, self-consistently aligned, they needed to be intersected to define the interrogation volume and for light to be collected.

The inner chamber optical rail structure facilitated the intersection of the interrogation and collection optical axes. Firstly, the irises and pointing laser used to define the collection optical axes were placed on COAR1 and re-aligned, then the iris closest to the interrogation beam was closed as much as possible to create a fine-pointing laser beam. Then, with the focused beam approximately centered with COAR1 along IOAR1, the entire collection optical axis that was previously set and locked at its desired angle of 15 degrees was translated forward until the collection optical axis, and the interrogation optical axis were coincident. Then, the irises and pointing laser assembly were removed, and a diffuse reflector was placed in the beam path at the focus. Then, the assembly holding $C - GF_1$ and $C - l_1$ was

aligned along $\mathbf{z}_{\text{collection}}$ until this scattered light collected by $C - l_1$ was collimated. Then, $C - l_2$ was placed in its optical mount. After this, the fiber mount was placed at the focus of the scattered light. From the air side, a pointing laser with power below the damage threshold of the fibers was shot through the fiber. Then, in the facility, the interrogation beam focus was aligned with the image of the light coming from the fiber on the interrogation beam plane. This was an iterative process of moving the focus of the interrogation beam as well as making micro changes to the fiber stages, kinematic fiber mount, and fiber rotation until the fibers were aligned parallel to the beam and at the beam focus. With the ability to collect light inside of the facility maximized and relayed to the air side through $C - F_1$, that light at $C - F_2$ needed to be processed, filtered, and then relayed into the spectrograph with the detection system. To facilitate alignment, minimize the possibility of stray light, and take the most advantage of the projected area of the optical table, the entire detection optical system was raised about 1' off of the surface of the optical table. This helped to minimize stray light as the spectrometer was rasied far above the interrogation beam level on the same table.

The spectrograph is comprised of a Princeton Instruments ISOPLANE-320A spectrometer and PM4-1024i-HB-FG-18-P46 PIMAX4. The spectrometer was ordered with a ARC-SP-ES motorized slit, a SLIT SHUTTER-ISOPLANE320 slit shutter, and a three-grating turret, which housed 532 nm optimized I3-120-500-P 1200, I3-180-500-P 1800, and I3-240-HVIS-P 2400 l/mm gratings to allow for multiple electron temperature range measurements. Before the beginning of the experiments, all three gratings were zero-adjusted and wavelength-calibrated using a Princeton INTCAL-WL-CALIB Instruments IntelliCal system. In order to detect the spectrally dispersed light at the detector, the light from the fiber needs to be relayed through the detection optical system. As stated previously, the individual fiber NA = 0.22. However, the f/# of the spectrograph is f/4.6. Given that

$$\text{NA}_{\text{spect}} = n \sin\left(\theta_{\text{spect}}\right) = \frac{1}{2f/\#}, \tag{5.4}$$

The numerical aperture of the fiber and the numerical aperture of the spectrometer do not match. Moreover, in order to maximize the light throughput, the collimated rays passing through the BNF must be less than or equal to the aperture of the BNF. To allow for as much freedom in the light collection, magnification, and collimated ray height through the BNF, a four-lens relay system was used in the detection branch. In order to capture all of the light from the fiber and also leverage all of that light at the spectrometer, the Helmholtz optical invariant had to be respected,

$$y_{\text{fiber}}\theta_{\text{fiber}} = y_{\text{fiber-image}}\theta_{\text{fiber-image}}, \tag{5.5}$$

with $\theta_{\text{fiber-image}} = \theta_{\text{spect}}$. Given this, then

$$M_{\text{detection}} \equiv \frac{y_{\text{fiber-image}}}{y_{\text{fiber}}} \approx 2.02. \tag{5.6}$$

Additionally, the collimated ray height at the BNFs, both of which have the same aperture size in this experiment, must respect

$$y_{\text{BNF}} \leq \frac{ID_{BNF}}{2.0}. \tag{5.7}$$

However, given the size of the filters in this experiment, it was impossible to meet both of the conditions set in Equation 5.7 and Equation 5.6, and there was a non-negligible loss at the filters. Figure 5.8 illustrates the optics used in the relay system and their ideal ray optics matrices used for design and optimization. Table 5.2 outlines the optics used and their relative distances.

The collected light is detected from $D - l_1$ with focal length $D - f_{l_1}$, whose distance from the object plane is set to match the focal length ($\Delta z_{l_1/fiber} = D - f_{l_1}$) in order to collimate the light and use the entire solid angle of the first detection lens. The collected light immediately leaving $D - l_1$ is relayed via $D - l_2$ with $D - f_{l_2}$. This would normally

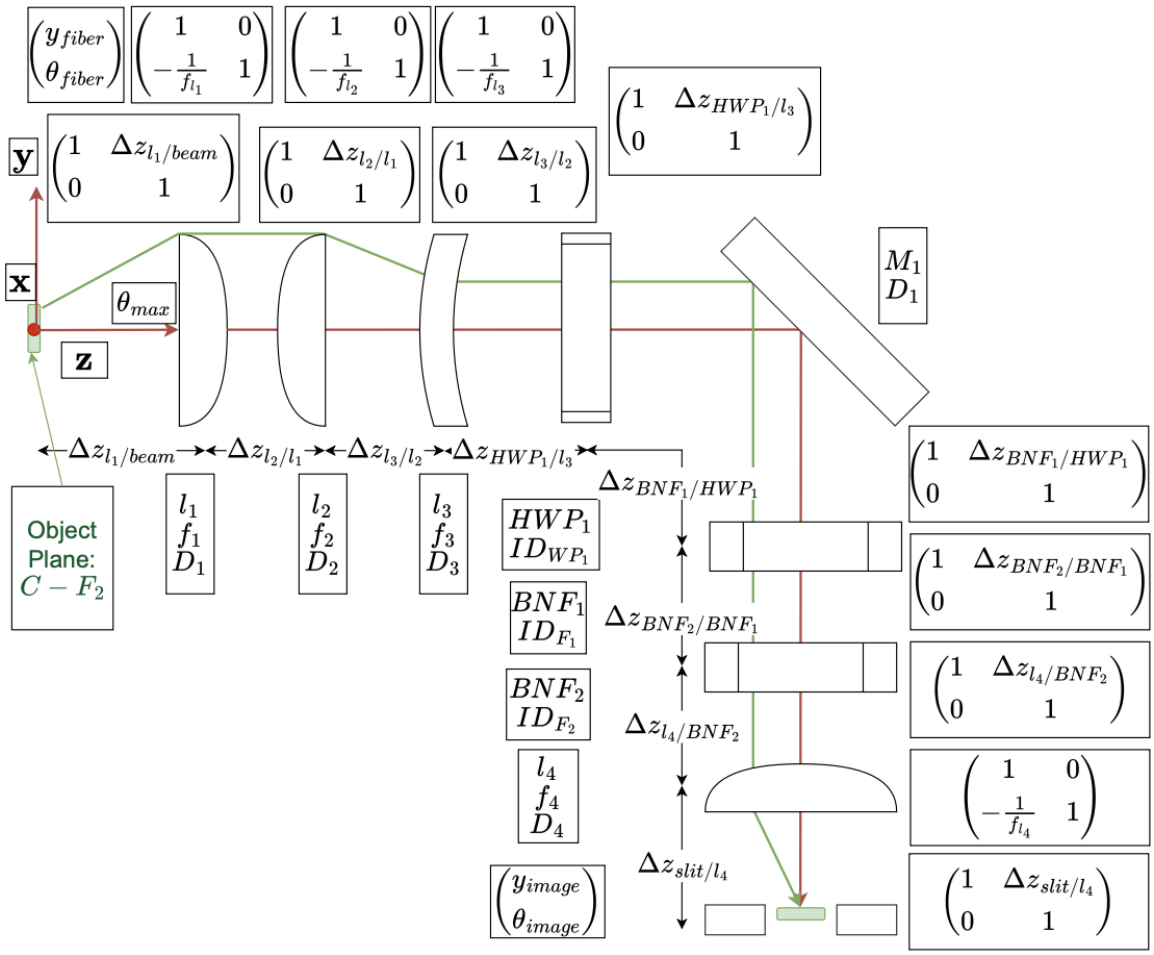

Figure 5.8: Detection system optical diagram.

create a 1-1 image after $D - l_2$, however, a negative lens $D - l_3$ with focal length $D - f_{l_3}$ is placed at $\Delta z_{l_3/l_2} = D - f_{l_2} + D - f_{l_3}$ in order to collimate the rays immediately leaving $D - l_3$. The rays are then passed through $D - HWP_1$, used to match the polarization dependence of the grating inside the spectrometer. The half-wave plate buys an additional 5-10 $\%$ in the signal but must be adjusted between gratings as their polarization dependence may be different. Immediately after $D - HWP_1$, the collected (and collimated) rays pass through mirror $D - M_1$ and then the laser line volume Bragg grating notch filters $D - BNF_1$ and $D - BNF_2$, with clear apertures ID_{BNF_1}=ID_{BNF_2}, and $OD4$ blocking when properly aligned. The laser line-filtered scattered rays are then passed through $D - l_4$ with f_{l_4}, that is placed a distance of $\Delta z_{slit/l_4} = D - f_{l_4}$ from the slit plane. This creates the sharpest image

Table 5.2: Detection system optical parameters.

Element	D or ID (mm)	f or Distance (mm)	Part	Sourced
$\Delta z_{l_1/beam}$	-	100	-	-
l_1	50.8	100	ACT508-100-A	Thorlabs
$\Delta z_{l_2/l_1}$	-	25	-	-
l_2	50.8	200	ACT508-100-A	Thorlabs
$\Delta z_{l_3/l_2}$	-	150	-	-
l_3	25.4	-50	ACN254-050-A	Thorlabs
$\Delta z_{HWP_1/l_3}$	-	25	-	-
HWP_1	25.4	25	WPH10E-532	Thorlabs
$\Delta z_{BNF_1/HWP_1}$	-	25	-	-
BNF_1	15	-	BNF-532-OD4-125	Optigrate
$\Delta z_{BNF_2/BNF_1}$	-	25	-	-
BNF_2	15	-	BNF-532-OD4-15	Optigrate
$\Delta z_{l_4/BNF_2}$	-	75	-	-
l_4	25.4	100	AC508-100-A	Thorlabs
$\Delta z_{slit/l_4}$	-	100	-	-

of the fiber on the slit of the spectrometer at the slit plane. The slit plane is comprised of two slits; the slit is built into the spectrometer $slit_1$ and a secondary slit, $slit_2$, that is placed perpendicular to the first slit. The linear array of fibers is rotated to be parallel to $slit_1$, $slit_2$ is perpendicular to $slit_1$ and acts as a variable mask in order to block stray light if necessary. As stated earlier, slight losses due to the size of the filter were expected. Given an effective numerical aperture of NA = 0.2095 due to the collection lens inside of the facility, $C - l_1$ and $C - l_2$, and a center fiber size of 200 μm, the ray size at the BNF is $y_{\mathrm{bnf}} = 10.63$ mm. This leads to a loss due to the relative size of the rays as the area of the filter aperture over the area of the circle with a radius of y_{bnf}. The area ratio is 0.634. Therefore, the effective collection NA in this configuration is .133, which leads to a usable collection solid angle of $\Delta\Omega = 0.055$ sr. Similar to the previously described alignments, two flat-sided 95 mm rails were to hold the detection optics. All optics were placed on 95 mm rail carriers and dovetail rail assemblies for alignment of their relative distances along the optical axis and perpendicular to the optical axis. Irises were used to create a pre-defined

optical axis, and then all optics were aligned along DOAR1 and DOAR2 with respect to these irises, diagrammed in Figure 5.3. In order to align their relative distances, a pointing laser was shot through the center fiber on the linear end output into the detection branch. The light emanating from the fiber was then used to place the optics sequentially, ensuring collimation after $D - l_1$, and $D - l_3$. Using the center fiber was critical to create the best image of the fiber array on the slit plane. In order to minimize losses due to vignetting, the optics were placed as close as possible, with particular care taken to minimize the distance $\Delta z_{BNF_1/l_3}$. The detection system imaging the face of the fiber, an almost perfect plane, effectively eliminated stray light from passing through the detection system into the spectrometer from inside of the facility. After a preliminary alignment, a box using T-slotted framing and nylon panels from McMaster-Carr was used to cover all of the detection optics to minimize diffuse and specular reflections from the surroundings from introducing stray light into the optical system.

This system has been designed to capture and use as much light as possible, given the physical constraints of the large VTF. It is unclear in the literature at this time if the coupling out of the fiber systems through the detection optics on comparable systems deployed elsewhere have accounted for the effect of the magnification on the light coupled into the spectrometer. The combination of magnification and image size of the fibers on the slit, the size of the rejection ring from the BNF on the image of the fibers on the slit plane, and the slit opening are crucial to leveraging the light that the system designers have worked to capture.

5.2.5 Fine Temporal, Polarization and Fiber Alignment and Chamber Compression Movement Correction

A Berkeley Nucleonics BNC-577-8C model delay generator was used as the master clock for the synchronization of timing events in the system. It controlled the internal timing of the DLS 9010 Q-switch with respect to the lamp to ensure the maximum rated energy per

pulse was extracted from the laser. Additionally, the delay generator controlled the timing of the detector gate delay with respect to the laser Q-switch. This ensured that even if the laser energy needed to be controlled via the Q-switch for any reason the relative timing was maintained. The gate delay was set to the minimum value in the Princeton Instruments Lightfield software and was controlled externally via the delay generator. The gate width was set in the software to 12 ns. The delay was then scanned until the signal on the detector was maximized and stable over $\pm$ 1 ns, indicating that the laser beam pulse was properly straddled by the detector gate.

With the laser and detector temporally aligned, the polarization of the incident interrogation beam laser with respect to its propagation direction and the collection optical axis must be aligned. Additionally, the fiber must be aligned so as to have maximum coupling. In the case of polarization, in order to maximize the scattering generated, the polarization must be mutually perpendicular to both the incident propagation direction and the collection. Given that $\theta_{\mathbf{z}_{\mathrm{cha}}-\mathbf{z}_{coll}} = 15^{\circ}$, then $\theta_{\mathbf{z}_{\mathrm{cha}}-\mathbf{E}_i} = 105^{\circ}$ or -75°. This was optimized by monitoring the Rayleigh signal in the Lightfield software as $I - HWP_2$ was rotated from outside of the facility while simultaneously rotating the Brewster window in order to minimize reflections. The angle of the Brewster window normal that minimized the reflections was indeed parallel to the predicted polarization angle, indicating that everything was as expected.

In order to minimize the number of degrees of freedom for alignment, instead of moving the fiber and the collection lenses relative to each other and also relative to the interrogation beam, the fibers were the only movable optical element from outside of the facility. Given the diameter of the fibers at 200 μm, and the diameter of the beam expected to be ≈100 μm, the movement of the fibers needed to be in steps on the order of μm. The fiber mount was aligned after the stages were homed to have been aligned with the defined collection optical axis on COAR1. With the ability to collect signals having been described in the previous paragraphs, the signal from the test section was used to optimize the alignment of the fiber.

Each direction had a different level of sensitivity. Because the interrogation beam focus was centered along the collection optical axis using the image of the laser-pointed-illuminated fiber, and because the stages had a maximum of 25 mm of travel, the $\mathbf{x}_{\text{collection}}$ axis did not have a strong sensitivity when the fiber was moved for optimization. This is because the observed beam waist was about 25 mm along the $\mathbf{x}_{\text{collection}}$ direction, and the true beam waist (observed through ionizing the air by increasing the laser energy) was about 5 mm. $\mathbf{z}_{\text{collection}}$ was expected to be sensitive on the order of mm. This was not observed during this iteration of the optical setup. As stated, there is a loss of about 40% at the BNFs. As a result, the system 'appears' to be less sensitive in $\mathbf{z}_{\text{collection}}$ until the edges of the travel of the $\mathbf{z}_{\text{collection}}$ because the rays that would indicate this sensitivity are the ones that are being cut off by the BNFs. The system is extremely sensitive in $\mathbf{y}_{\text{collection}}$. This is the direction that effectively overlaps the fiber image with the interrogation beam. We observed that very slow and μm level movements allow for proper coupling of the fiber image and beam in the $\mathbf{y}_{\text{collection}}$ direction. This is critical, as the signal was observed to increase almost 10-fold when properly coupled compared to when it is improperly coupled. Additionally, to avoid optimizing 'into a reflection' by using Rayleigh scattering, it is advised to optimize using rotational Raman scattering directly as it is not subject to the stray light considerations due to the fact that the fiber on the detection side is an almost perfect plane and as a result, the BNF filters can filter out all of the centerline laser light almost perfectly.

In anticipation of the movement of the chamber, several stand-alone tests were performed. The goal of these tests was to determine the effect pumpdown had on critical elements of the VTF-2 LTS setup. The first test was simply to determine the effect of the roughing system vibrations on the signal collected. The first phase of this was tested by simply acquiring the signal with and without elements of the active roughing system and the isolation stabilizing legs inactive with the chamber at atmospheric pressure. It was determined that any vibrations with these active elements did not induce chamber oscillations that were greater than the difference between the image of the fiber on the interrogation

beam waist. If they did, the signal would have decreased due to the periodic movement of the image of the fiber into and out of the interrogation beam waist. This motivated the decision to continue to operate with the vibration-stabilizing legs inactive.

The second test was to determine if, during pumpdown, there was a relative movement of the interrogation beam with respect to the inner optical rail structure. This would indicate that the facility was compressing, leading to the relative movement of items inside the chamber and the systems outside of the chamber. Additionally, this would indicate the possibility that the beam waist could shift relative to the collection optical axis. To test both of these simultaneously, the apertures $I - i_5$ and $I - i_6$ were closed until the beam was barely clipped. A piece of grid-lined burn paper with a 2 mm x 2 mm grid was placed at the interrogation beam waist to determine the relative movement of the beam waist as compared to the inner optical rail system without any correction. This test was performed from 760 to 10 Torr. The beam movement on the irises was approximately observed to be on the order of less than 5 mm and was not pictured. The movement of the beam waist was less than 2 mm x 2 mm. This can be seen on the left in Figure 5.9. This indicated that there was indeed non-negligible relative movement that needed to be accounted for during pumpdown.

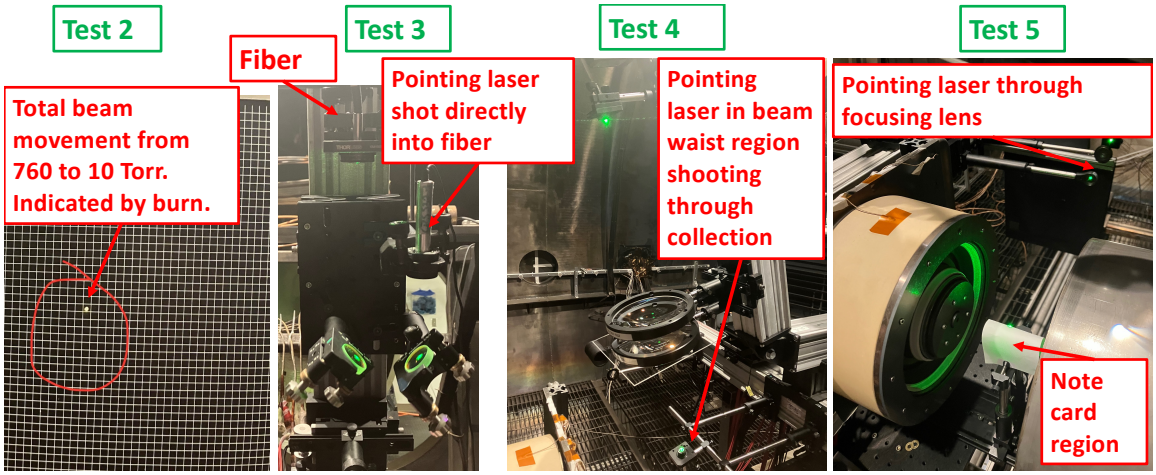

Figure 5.9: Pictures of the internal optical structure movement tests.

The third test was performed in order to determine if the fiber transmission was ad-

versely affected by the pressure in the facility. To do this, a pointing laser was shot directly through the chamber fiber face, and the signal was collected with respect to the background pressure from 760 to 20 Torr. The constant signal strength indicated that the fiber transmission was constant. This is shown in Figure 5.9

A fourth test was used to determine if there was a relative movement of the collection lenses with respect to the fiber or with respect to the interrogation beam optical axis on the rail structure. To test this, a pointing laser was placed in the notional interrogation beam waist position and pointed through the collection lenses inside the chamber, and tested from 760 to 20 Torr. The constant signal strength indicated that there was no relative movement. This is shown in Figure 5.9.

Fifth, to determine if there was any relative movement of the focusing lens on the interrogation optical axis relative to the collection axis, which would move the focus and reduce the scatter generation, a pointing laser was placed on the interrogation optical axis, shot through the focusing lens and aligned so that the beam waist was coincident with the notional interrogation beam waist. Then, a notecard was used to scatter the pointing laser through the collection optical axis. The goal was to observe if the signal collected decreased with pressure, indicating non-negligible movement of the beam waist along the propagation direction. The constant background signal with pressure from 760 to 20 Torr indicated that this was not the case. This test is also shown in Figure 5.9.

A final test was conducted to determine power coupling into the facility. A second power meter was placed inside the facility and was monitored from 760 to 20 Torr. The incident laser energy measured at the first power meter was 30 mJ/pulse. The incident laser energy inside of the facility over the pressure range was 24$\pm$1 mJ/pulse. The constant laser energy inside the facility after the laser beam focus indicated that the energy was properly coupled and not lost inside the facility. The laser energy discrepancy from the first power meter to the second is consistent with two 10 % losses through $I - HWP_2$ and the Brewster window $I - BW_1$.

The tests conducted indicated two very important points. The first is that the relative movement of the beam waist with respect to the collection optical axis is small even if the chamber moves on the order of almost 5 mm. A simple ray tracing software suite will show that translation of the incident rays with respect to the focusing lens should not change the location of the focus but does change the incident angle at the focusing position. This is important because even though the beam incident on the lens is observed to move ≈5 mm, the focus moves < 2 mm perpendicular to the incident laser beam propagation direction. However, given the size of the beam and the fibers, this is non-negligible and must be accounted for. The second point is that the thrust stand optical rail structure is rigid and that the mounting of the optics on this structure ensured no relative movement of anything on the structure.

Given this, the movement of the interrogation beam relative to the inner structure was corrected in the following way. Firstly, before pumpdown, the targets $I - i_5$ and $I - i_6$ were closed so as to barely clip the beam but not cause significant reflections. Then, at every pressure, the alignment was monitored by looking at the position of the beam on the irises. If and when there was movement, the mirror $I - M_3$ was translationally adjusted along $\mathbf{y}_{\text{chamber}}$. Mirror $I - M_4$ did not have to be adjusted translationally, and neither mirror needed to be adjusted in terms of pitch and yaw angles using their kinematic mounts. This means that the thrust stand optical rail structure's relative movement with respect to the exterior was almost entirely translational along $\mathbf{y}_{\text{chamber}}$ due to chamber compression. When the interrogation beam alignment was corrected, the $\mathbf{y}_{\text{collection}}$ translation stage was optimized in order to maximize the signal. This procedure ensured the alignment was always optimized at all pressures. The chamber was observed to compress ≈ 5 mm from 760 to 10 Torr. After this, the chamber movement was negligible with respect to the movement on the iris. However, micrometer-level changes needed to be made using the fiber motion stages.

5.3 Cathode Discharge Test Matrices and Results

As stated previously, rotational Raman scattering is necessary for absolute number density calibration. Several Raman calibration points were taken with air in the facility. The test matrix for the Raman calibration is summarized in Table 5.3 summarizes the target conditions for the experiment. Figures 5.10 and 5.11 present two sample spectra as well as the

Table 5.3: Cathode experiment LRS test matrix.

Species	Pressure
Air	105.0
Air	50.6
Air	26.4
Air	13.0
Air	5.60

center wavelength and system efficiency constants at each pressure that were subsequently used to inform the least squares inversion in the Thomson least squares routine.

There is a somewhat large discrepancy in the calculated calibration constants. This could be due to several factors, including sub-optimal fiber location relative to the beam, although this is unlikely because the fiber location was maximized at each of the conditions. This could have also been due to slightly different local distribution of the Oxygen and Nitrogen fractions in the vicinity of the interrogation volume. Because of this, the parameters used in the LTS spectrum below were the ensemble average over all of the pressures, with $\eta = 0.185 \pm 14.5\%$ and $\lambda_{\mathrm{i}} = 532.07 \pm 0.5\%$. Figures Figure 5.12 and Figure 5.13 show the final configurations of the system at atmosphere and vacuum during operation.

Table 5.4 summarizes the target conditions for the plasma portion of the experiment. The detection system parameters for all subsequent tests are presented in Table 5.5. Figure 5.14 shows a diagram of the radial locations from a top view as well as the relative orientation of the collection-interrogation propagation plane relative to the face of the thruster.

Figure 5.15 presents two sample spectra at the maximum and minimum number density

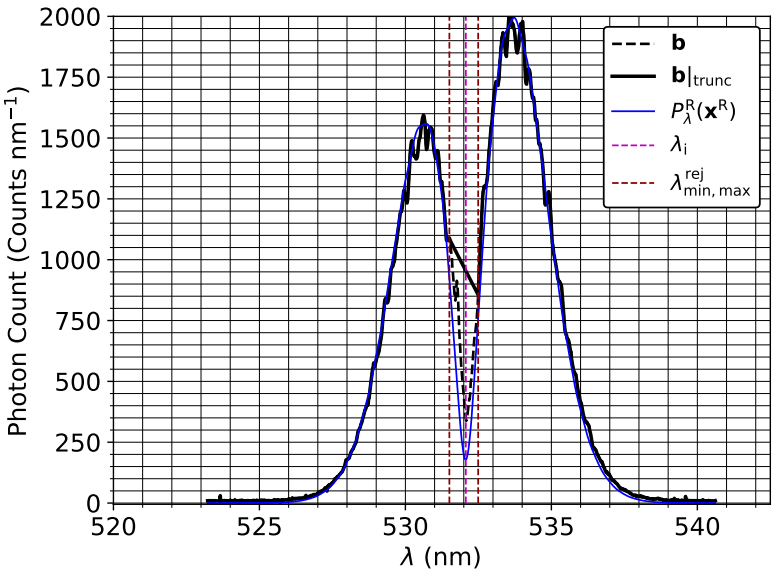

(a)

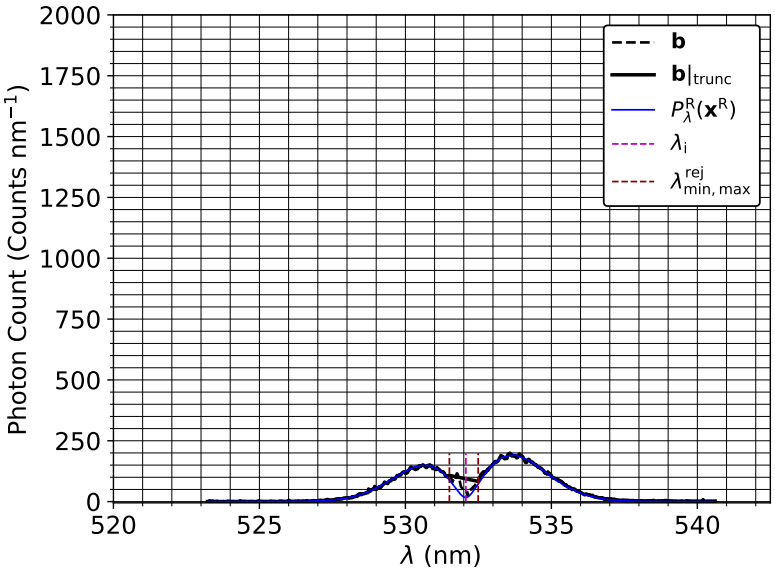

(b)

Figure 5.10: Least squares fitted results for the rotational Raman inversion; (a) and (b) show the raw ($\mathbf{b}$), truncated ($\mathbf{b}|_{\text{trunc}}$) with rejection regions and model spectra ($P_\lambda^{\text{R}}\left(\mathbf{x}_{\text{LS}}^{\text{R}}\right)$) at 105 Torr and 5.6 Torr, respectively.

conditions after background subtraction. as well as the center wavelength and system efficiency constants at each pressure that were subsequently used to inform the least squares inversion in the Thomson least squares routine. Figure 5.16 shows the resulting spatial dis-

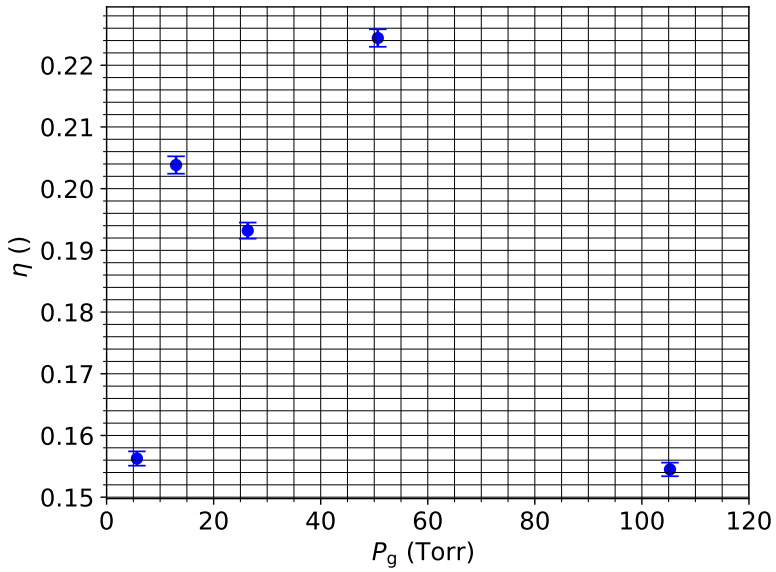

(a)

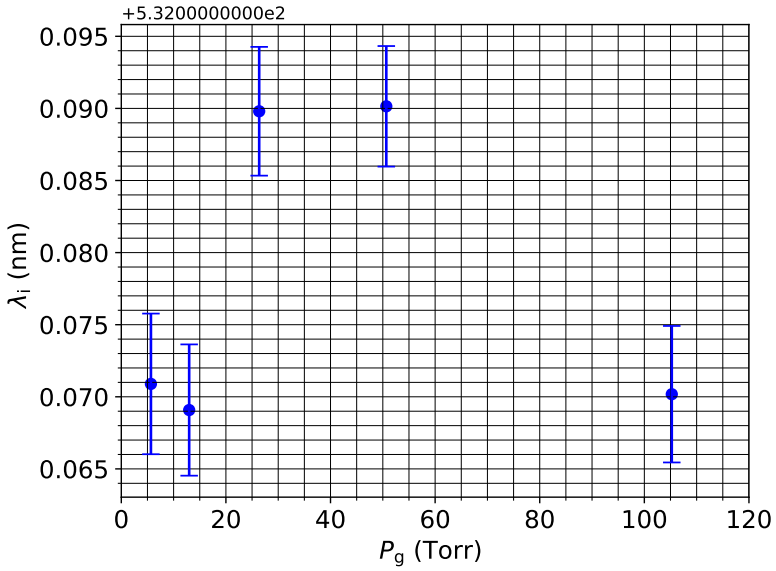

(b)

Figure 5.11: Least squares fitted results for the rotational Raman inversion; (a) shows the system efficiency constant versus background pressure, and (b) estimated center wavelength versus background pressure.

tribution of the parameters of interest processed with Maxwellian and Druyvesteyn velocity distribution functions. Figure 5.17 presents two sample spectra at intermediate conditions representative of SNRs between the minimum and maximum. In these figures, the center

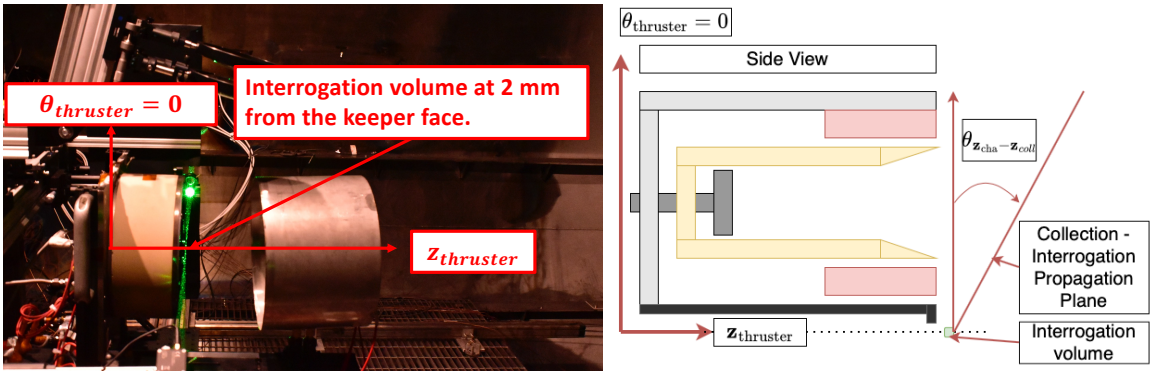

Figure 5.12: Picture of the final configuration of the interrogation and collection system at atmospheric chamber pressure.

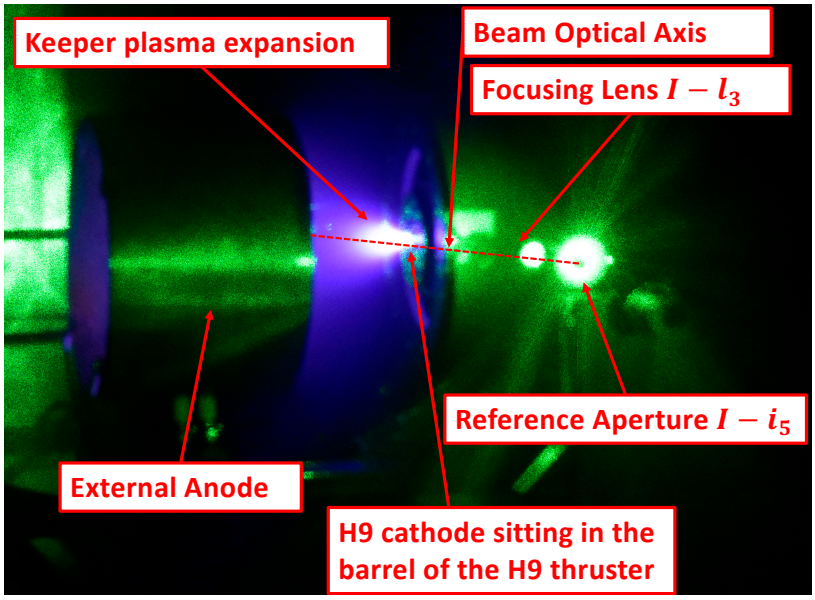

Figure 5.13: Picture of the interrogation system and cathode discharge at vacuum.

Table 5.4: Cathode discharge test matrix.

Species	I_{D} (A)	V_{D} (V)	$\dot{m}_{\text{cathode}}$ (sccm, mg/s)	r_{cathode} (mm)	z_{cathode} (mm)
Kr	25	60	28.725 , 1.79	[0,2]	[2,3,4,5,6,7,8]

wavelength of the spectrum (λ_{c} is distinguished from the incident wavelength calculated from the Raman inversion λ_{i}, showing the ability to distinguish between a spectrum that is shifted from the incident wavelength in order to calculate bulk drift velocity. The incident laser propagation is parallel to $\mathbf{x}_{\text{collection}}$, and the collection axis is $\mathbf{y}_{\text{collection}}$ is shifted

Table 5.5: Detection system collection parameters.

E_i (mJ)	grating (mm^{-1})	w_{slit_1} (μm)	w_{slit_2} (mm)	Δt_gate (ns)	gain ()	shots ()
195	2400	450	5	12	100	3000

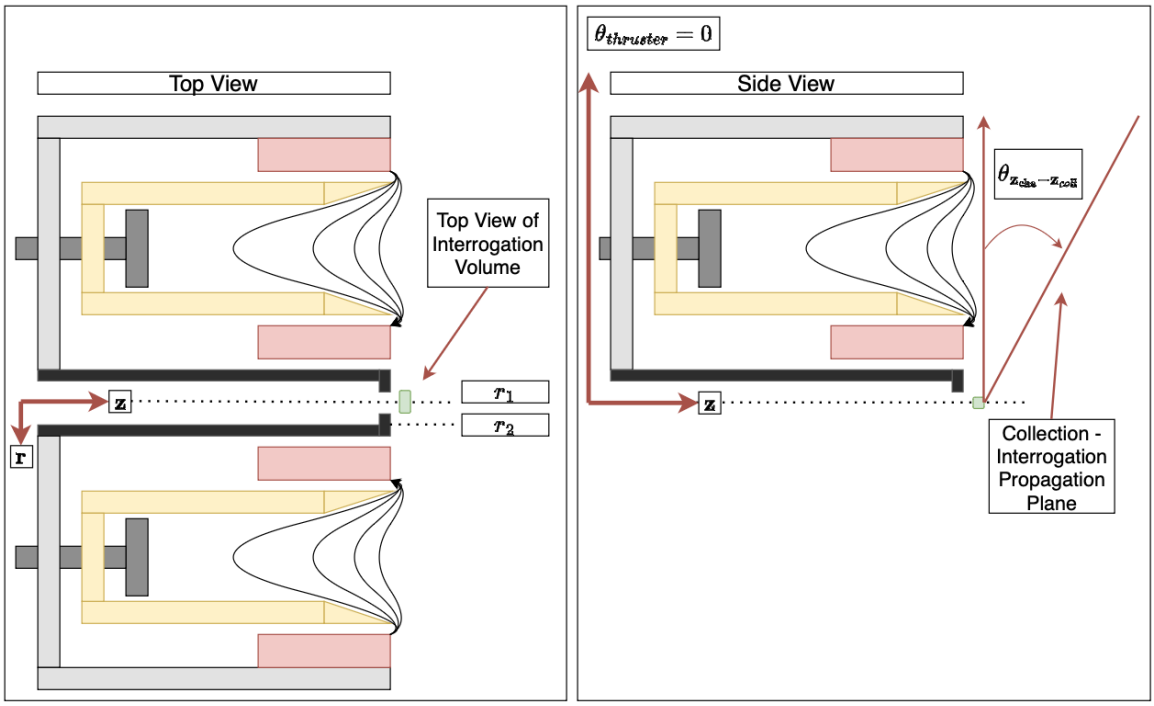

Figure 5.14: Diagram of the radial locations probed relative to the HET from a top and side view.

$\theta_{\mathbf{z}_{\mathrm{cha}}-\mathbf{z}_{coll}} = 15°$ forward with respect to the face of the HET, the drift velocity is pointed $45°$ clockwise from the thruster midplane and $15°$ out from the plane of the thruster face.

5.4 Discussion

5.4.1 Quantitative Comparison with Similar LTS Systems

The inversion and uncertainty based on the signal fits indicate that the system design goals of good signal generation, collection, and throughput were accomplished. The implemented diagnostic acquired signal above the stated detection limit with the least number of accumulations and minimum laser energy compared to similar systems to date [117, 166].

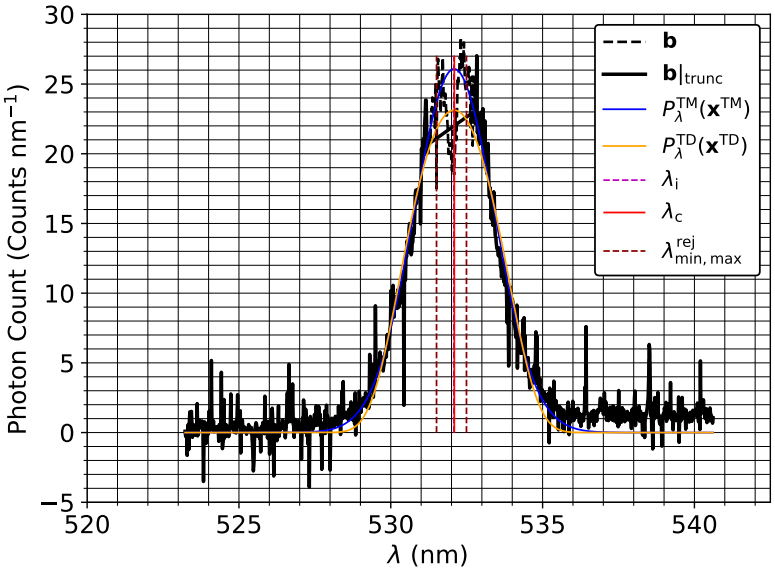

(a)

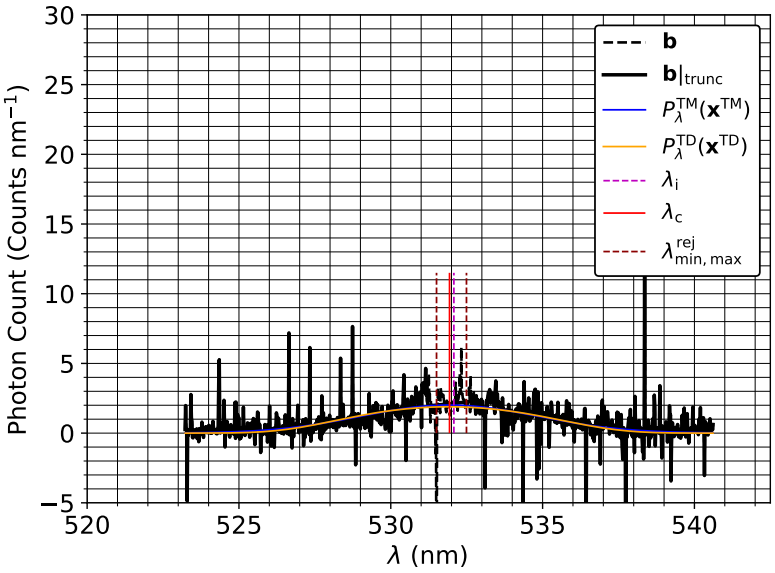

(b)

Figure 5.15: Least squares fitted results for the laser Thomson scattering inversion; (a) and (b) show the raw ($\mathbf{b}$), truncated ($\mathbf{b}|_{\text{trunc}}$) with rejection regions and model spectra for both a Maxwellian ($P_\lambda^{\text{TM}}\left(\mathbf{x}_{\text{LS}}^{\text{TM}}\right)$) and Druyvesteyn spectra distribution function ($P_\lambda^{\text{TD}}\left(\mathbf{x}_{\text{LS}}^{\text{TD}}\right)$). Figures (a) and (b) correspond to absolute number densities of 1.074×10^{18} and 1.85×10^{17} m^{-3} respectively. Figure (a) and (b) were taken along the center line at $z_{\text{beam-cathode}}$ = 2 mm and $z_{\text{beam-cathode}}$ = 8 mm, respectively.

Achieving this SNR and detection limit was in large part due to the minimization of the interrogation focal length. This minimized the beam waist size to match the size of the fiber

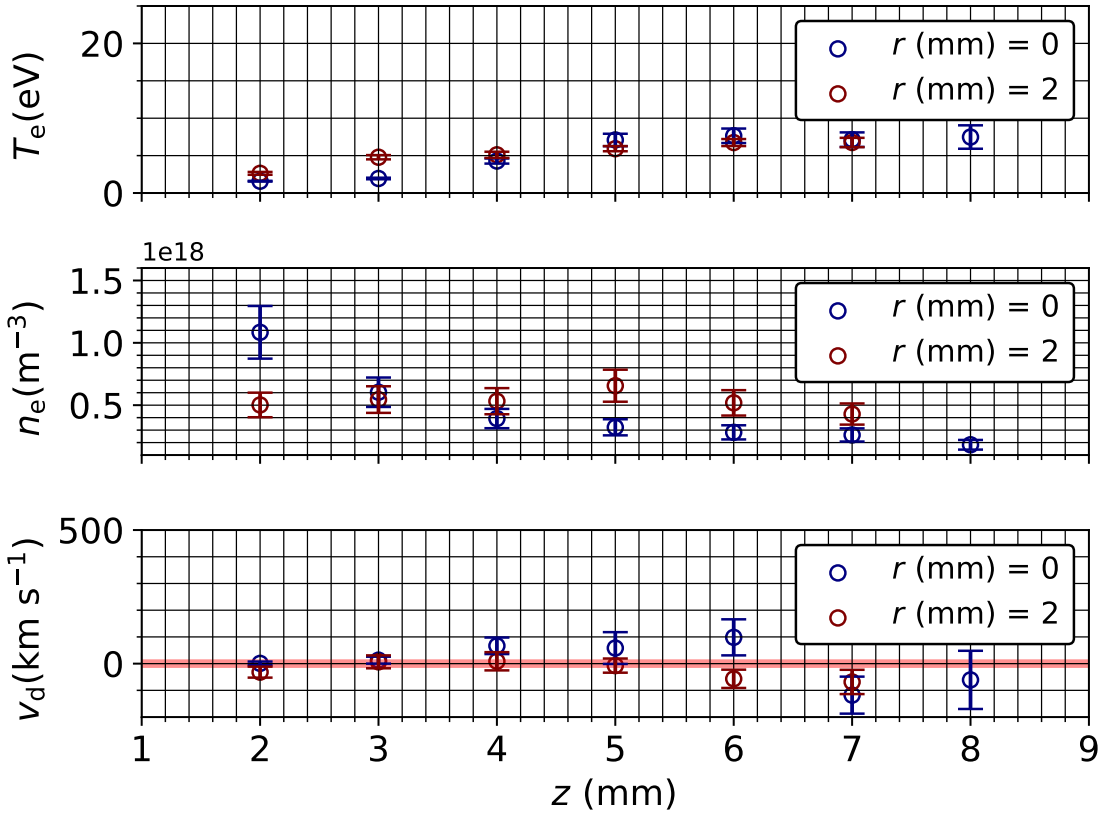

Figure 5.16: Axially resolved electron properties calculated using Maxwellian and Druyvesten spectral distribution functions at two different radii. At a radius of $r_{\mathrm{beam-cathode}}$ = 2 mm, the signal at $z_{\mathrm{beam-cathode}}$ = 8 mm was very low and, as a result, was not included.

image on the interrogation beam plane. Additionally, the two large diameter collection lens system and the four-lens detection optical system both that were designed to maximize light collection and transmission through the system. We can quantitatively compare our system to those found in References [117, 166] through the effective solid angle, detection length, and incident laser energy. Our inner chamber collection system has $E_{\mathrm{i}} L_{\mathrm{det}} \Delta\Omega = 44.1$ mm sr mJ pulse^{-1} at an incident laser energy of 195 mJ/pulse and spatial resolution of 100 µm $\times$ 1.4 mm, given that the beam waist is approx 100 µm. The system has a number density detection limit of 1×10^{17} m^{-3}, maximum expected electron temperature at this limit of 15-20 eV, and minimum drift velocity of 10 kms^{-1}.

Accounting for magnification in Reference [117, 140], the effective $E_{\mathrm{i}} L_{\mathrm{det}} \Delta\Omega$ is 31

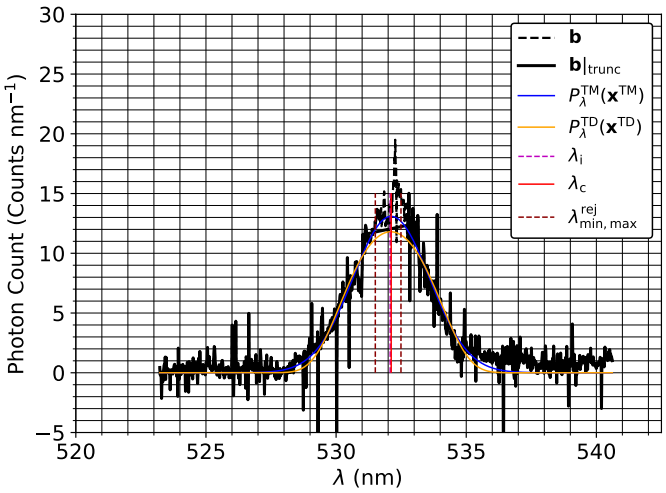

(a)

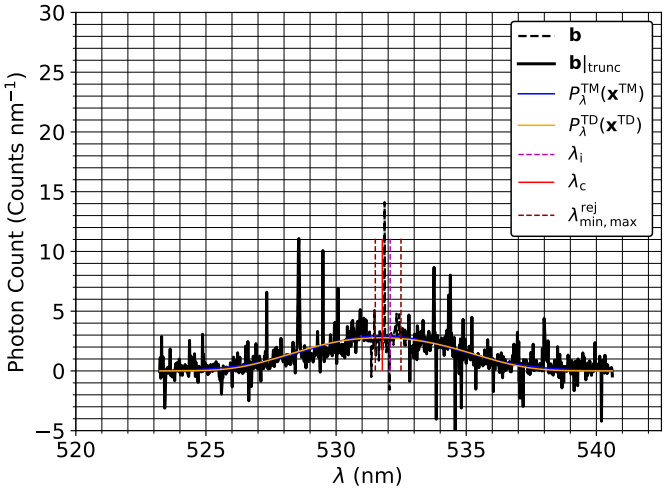

(b)

Figure 5.17: Least squares fitted results for the laser Thomson scattering inversion; (a) and (b) show the raw ($\mathbf{b}$), truncated ($\mathbf{b}|_{\text{trunc}}$) with rejection regions and model spectra for both a Maxwellian ($P_\lambda^{\text{TM}}\left(\mathbf{x}_{\text{LS}}^{\text{TM}}\right)$) and Druyvesteyn spectra distribution function ($P_\lambda^{\text{TD}}\left(\mathbf{x}_{\text{LS}}^{\text{TD}}\right)$). Figures (a) and (b) correspond to absolute number densities of 1.074×10^{18} and 1.85×10^{17} m^{-3} respectively. Figure (a) and (b) were taken along the center line at $z_{\text{beam}-\text{cathode}}$ = 3 mm and $z_{\text{beam}-\text{cathode}}$ = 7 mm, respectively.

mm sr mJ pulse^{-1}, with a spatial resolution of 0.825 μm by 0.495 μm. The authors reported a number density detection limit of 1×10^{16} m^{-3} and maximum detectable temperature at this limit of approximately 50 eV [152], and drift velocity limits of 500 kms^{-1}.

The system in Reference [166] has an effective $E_{\text{i}}L_{\text{det}}\Delta\Omega$ of 40.8 mm sr mJ pulse^{-1}

with a spatial resolution of 200 μm by 200 μm. These calculations do not account for area ratios of collimated rays passing through the filtering elements or conservation of the Helmholtz-Lagrange invariant given the lack of information in Reference [166] necessary to calculate these properties. However, the maximum temperature and minimum drift velocity measured were 12 eV and 600 kms^{-1}. More recent measurements lead to the expected density, temperature and drift velocity limits to be approximately 1×10^{17} m^{-3}, 80 eV, and 5 kms^{-1}. The difference in effective throughput of the systems, the stated detection limits, and the capital spectroscopic equipment (e.g, the spectrometer and detector) highlight the need for standardization of the basic equations and pre/post-processing used across LTS teams against a well documented and known test-set of data.

We expect that future measurements at even more challenging conditions, e.g. at least one order of magnitude lower number densities in the near field plume of HETs, will be possible by increasing the number of laser shots accumulated and incident laser energy, and modifying the beam expansion ratio, the interrogation beam focal length, and changing the acquisition strategy in order to use leverage vertical pixel and horizontal pixel / wavelength binning. Specifically, a reduction in $I - l_1$ to a focal length of 75 mm and increasing $I - l_3$ to a focal length of 600 mm will allow us to increase our incident laser energy to the full output capacity of the laser, 1000 mJ/pulse. Vertical on-detector binning over the entire range of pixels illuminated by the fiber image on the slit plane will reduce read noise by approximately a factor of 10. This will minimize noise on the detector and increase the scattering signal intensity to increase the total SNR and, therefore, decrease the detection limit to an expected 2×10^{16} m^{-3}. Additionally, the radial variations seen in Figure 5.16 necessitate increasing spatial resolution by averaging over fewer fibers with the hardware-based binning. In the current configuration, the spatial resolution can be increased to 200 μm $\times$ 200 μm

5.4.2 Qualitative and Quantitative Comparison of the Electron Property Profiles

Based on the relative size and location of our anode and cathode, the neutral pressure downstream of the cathode exit in our experiment is expected to be 1-2 orders of magnitude lower than those often reported in the literature [38, 60, 127]. This aligns with the 1-2 orders of magnitude lower electron number density presented in Figure 5.16 compared to the these previously reported cathode discharge experiments and simulations[38, 60, 127]. The electron number density decreases by approximately an order of magnitude from 2 mm to 8 mm along the cathode centerline as seen in Figure 5.16. The shape of the centerline axial profile (at $\mathbf{r}_{\mathrm{beam-cathode}} = 0$) is consistent with the previous data[106], showing a sharp drop-off in the electron number density that asymptotically approaches the background electron density. The increasing electron temperature is consistent with LIF, as well as coherent [161] and incoherent LTS [160, 166] measurements that indicate increasing ion temperatures as the plasma expands toward the anode .

The electron temperature and density axial profiles at $\mathbf{r}_{\mathrm{beam-cathode}} = 2$ mm are consistent with a core plume plasma expanding between our cathode and anode, superimposed on a background plasma, with the core plasma bounded by the angle between the cathode orifice plate and the external anode. The plasma expansion is diagrammed in Figure 5.1. The bulk of the plasma is expected to be confined to within this angle. The expanding plasma electrons are thought to be interacting with the background neutrals, which are expected to be of significant density in the region close to the cathode[127], and sustaining a spatially uniform background plasma near the edges of the expanding core plasma between the cathode and the anode. Alternatively, the data could suggest that this region of plasma just outside of the expanding plasma jet is driven by charge exchange due to the approximately constant electron number density up until $z = 5$ mm, which then rapidly decays at a rate consistent with that along the center line. However, this is unlikely since the charge exchange mean free path in a facility of this size is expected to be on the order of meters.

The electron bulk velocity profiles, both along the centerline and at a radius of 2 mm,

indicate acceleration along the positive scattering wave vector up to axial positions of 4-6 mm, followed by deceleration to a negative velocity from 5 to 8 mm. The orientation of the scattering wave vector being almost perpendicular to the cathode axial axis is expected to be the reason for the low drift velocity on the order of tens of kms^{-1}. The bulk drift velocity unit vector and the maximum expansion angle (defined by the relative size and distance of the cathode and anode) are different by thirty degrees. In order for the cathode electrons to make contact with the anode after expanding, they need to accelerate towards the anode, which necessitates a component along the negative scattering wave unit vector. This measured bulk velocity profiles indicate a plasma plume expanding from the plasma orifice in a manner similar to a nozzle, which is then redirected towards the anode through a standing electrostatic potential between the cathode and anode. Full three-component resolution of the plasma bulk velocity with respect to the chamber or thruster basis vectors would require several investigations with an orientation change of the signal collection branch. When applied to the thruster, a simpler option for resolving the bulk velocity components is outlined in Reference [152].

5.5 Summary

A laser Thomson scattering system was implemented in a large-scale vacuum test facility. The diagnostic was used to take axially resolved electron density and temperature measurements of a cathode discharge with an external anode. A mechanical structure inside of the facility allowed for the degrees of freedom necessary to orient the collection and interrogation beam propagation to allow for LTS collection up to the face of the cathode keeper. The internal optical structure also allowed for the placement of the interrogation beam focusing lens inside the facility. This minimized its distance to the thruster, maximizing the collected scatter through the beam waist diameter less than or equal to in size than the image of the fibers on the beam plane. Additionally, the internal single optical degree of freedom through the movement of only the fiber face relative to pre-defined collection op-

tical axes and lenses allowed for easy alignment correction to the true optimum alignment from outside of the facility using a simple set of targets and a single set of motion stages. The mechanical and optical layout described is adaptable to other large VTF facilities. This system allowed for relatively high SNR data to be acquired with minimal laser energy and accumulations, allowing for implementation using smaller, more compact lasers. Methods for maximizing the SNR in this configuration are discussed in the previous section. The data collected provides a path forward for measurements of the electron temperature and density in the near field of high-power HET discharges. The number density and temperature data collected corroborates previous measurements in this region, with the expected rapid decay in number density having been observed. Discrepancies in the magnitude of the electron density have been attributed to the size and placement of the discharge anode. This may be cause for a standardization of the relative position and size of discharge anodes in stand-alone cathode experiments for easier comparison across measurements and measurement comparison to plasma simulations.

CHAPTER 6
LARGE VACUUM TEST FACILITY MEASUREMENTS IN THE NEAR FIELD PLUME OF A HIGH CURRENT DENSITY MAGNETICALLY SHIELDED HALL EFFECT THRUSTER

6.1 Introduction

The previous chapter outlined a preliminary large vacuum test facility implementation of an LTS system that required several modifications for LTS to be collected in the plume of an MS HET. Modifications to the interrogation beam optical axis, incident laser energy, spectral acquisition strategy, thruster azimuthal probing location, and thruster discharge conditions were necessary to achieve LTS measurements in the near field plume of the HET.

6.2 Experimental Setup

6.2.1 Vacuum Test Facility

This experiment was conducted in Vacuum Test Facility 2 (VTF-2) at the Georgia Tech High Power Electric Propulsion Laboratory (HPEPL). VTF-2 is a 4.9 m diameter and 9.2 m long stainless-steel chamber. Medium vacuum is achieved via one Leybold SV630 841 m^3/hr rotary-vane pump to 7 Torr, after which a rough vacuum pressure of 30 mTorr via one 6456 m^3/hr blower (Leybold RA5001). High vacuum is achieved via ten PHPK CVI TM1200i cryopumps that line the facility. Each of the 10 pumps operates by cooling a cryosail to an average temperature of 13 K by an external closed-loop helium cryostat system. This effectively pumps the atoms in the chamber by absorbing the atoms that strike the cryosails. Each cryosail requires radiation shielding that is provided by individual liquid Nitrogen shrouds that are all connected in parallel to a recirculating liquid Nitrogen system

that liquefies the gaseous nitrogen via two Stirling Cryogenics SPC-4 cryogenerators. [48]. This system provides a combined Xe pumping speed of 350,000 l/s and achieves an ultimate base pressure of 1.9 $\times$ 10 $^{-9}$ Torr - N_2.

The pressure in the facility from the atmospheric pressure of 760 Torr to a medium vacuum of 1 Torr was monitored via a 1000 to 1 Torr range Kurt J Lesker XCG-BT-FB-1 capacitance manometer mounted on a flange on the periphery of the chamber. A capacitance manometer was chosen for its accuracy of $\pm 0.5\%$ and the fact that no gas specific corrections are needed for the pressure. Given space limitations and the orientation of the gauge on the chamber, sitting horizontally as opposed to vertically, at atmosphere after calibration, the gauge reading diverged from the local barometric pressure. All pressures were linearly corrected for the local barometric pressure. Accurate pressure readings from 760 Torr to .01 Torr are critical for accurate absolute number density calibration of a laser Thomson scattering system via Rayleigh or Raman scattering as they are both linearly dependent on the pressure. It is not advisable to use thermal pressure gauges for this activity.

At high vacuum, the pressure at 0.5 m radially from the test section and at the periphery of the facility mounted to a flange were monitored via two Agilent Bayard-Alpert 571 hot-filament ionization gauges. The operational pressures during the experiments presented are the average of the two internal and external pressures, corrected to krypton via Equation (Equation 6.1),

$$p_{\mathrm{operational-corrected}} = \frac{1}{c_{\mathrm{corr}}} \left(p_{\mathrm{operational}} - p_{\mathrm{base}} \right) + p_{\mathrm{base}}, \tag{6.1}$$

with c_{corr} being equal to 1.96 krypton [1]. This chapter outlines experiments conducted over several days. The base and corrected operational pressures for krypton for each experiment will be outlined in their respective subsections.

Mass flow was provided by two MKS GE40A mass flow controllers (MFCs) mounted externally to the facility. The MFCs were calibrated in the test section of VTF-2 using a

DryCal 800-10 volumetric flow rate meter system to create a linear fit between the commanded and actual flow rates after using an average of five points. The MFCs have full-scale (FS) ranges of 100 and 50 sccm on xenon, respectively. The internal MKS software was used to switch the working propellant to krypton, after which the full-scale for the controllers were 200 and 750 sccm, respectively. The flow controllers were zeroed at the beginning of each testing day before ignition of the HET cathode and discharge. Mass flows reported are the actual flow rates corrected through the linear fits.

6.2.2 Thruster Discharge and Relative Motion

The test article in this experiment was the H9 [104], a 9 kW class MS HET, hereupon referred to as "the thruster". The thruster is designed to operate with an internal and coaxial 60 A class Lanthanum hexaboride (LaB_6) hollow cathode whose design heritage stems from the HERMeS and H6 HETs hollow cathodes [72]. The H9 cathode is hereupon referred to as "the cathode". The operational envelopes of the H9 at standard current densities on xenon and krypton are outlined in References [97, 104, 150, 155]. The performance of the H9 at high and ultra-high current densities is outlined in References [156, 168].

Initially, the target discharge condition for these experiments was 6 kW with a voltage of 300 V and a current for this experiment was 20 A with the thruster discharge current floating. However, despite several upgrades to the interrogation laser beam system and spectrum acquisition strategies the near field number density was not high enough to collect LTS in the desires regions. Consequently, the discharge condition was modified to 6 kW with a voltage of 150 V and a current of 40 A, well within the high current density regime [156]. The thruster discharge circuit was floating for all experiments. The thruster was operated with standard lab-grade power supplies. Specifically, the cathode keeper, cathode heater, and thruster inner and outer magnetic circuits were operated using TDK-Lambda GEN60-25, GEN600-2.6, GEN80-42, and GEN40-38 power supplies, respectively. This series of power supplies were chosen due to their rated voltage and current accuracies of 1% of the

desired outputs, respectively. The thruster discharge supply was a Magna-Power Electronics TSA800-54 power supply. It was chosen due to its voltage and current output accuracies of $\pm$ .075% of the full scale values, respectively. The cathode keeper, cathode heater, and thruster magnetic circuits were driven and probed using displays on the power supplies, expected to have a relative uncertainty of 1% as stated previously. All supplies were calibrated with respect to a new Fluke 83V model multimeter. The maximum voltage and current divergence found between the displays and the multimeter was also less than 1%.

The thruster discharge supply was isolated from the thruster using a low-pass discharge filter described Section III.B of Reference [76]. The thruster-side of the discharge filter was probed using a Teledyne Lecroy HDO6104 oscilloscope to capture the dynamics of the thruster discharge voltage and current. Discharge current was probed using a Teledyne Lecroy CP150 model current clamp and the discharge and cathode-to-ground voltages were probed using Powertek DP-25 differential voltage probes. In transitioning from the nominal 6 kW condition on krypton with $0.75B_{\mathrm{o}}|_{\mathrm{Xe}}$ to the high current density 40 A 6 kW condition, the magnet circuit currents were adjusted while keeping the inner and outer coil current ratio constant to minimize discharge oscillations per recommendations in Reference [155]. The coil current ratio and the absolute value of the coil currents did not vary between nominal and high current density condition. A point measurement of the magnetic fieldst strength at 2 mm from the thruster discharge exit plane along the channel center line indicated a difference in strength of less than 1%. Therefore, the topology, dictated by the current ratio, and the maximum field strength relative to the nominal condition on xenon, dictated by the point-measured maximum magnetic field strength, were expected to be consistent with what is expected and measured at other facilities. Additionally, the simulations and measurements of the magnetic field topology from collaborators at JPL were shown to diverge by no more than 2% at the inner discharge channel walls, and be almost perfectly aligned in the near field plume region outside of the discharge channel. This gave us confidence that the topology was as expected.

In order to spatially resolve the electron properties in the near field thruster plume, relative movement between the thruster and the interrogation beam scattering volume is necessary. This was accomplished by mounting the thruster on motion stages that allowed for three degree-of-freedom movement with respect to the interrogation beam scattering volume. This assembly is depicted in Figure 6.1

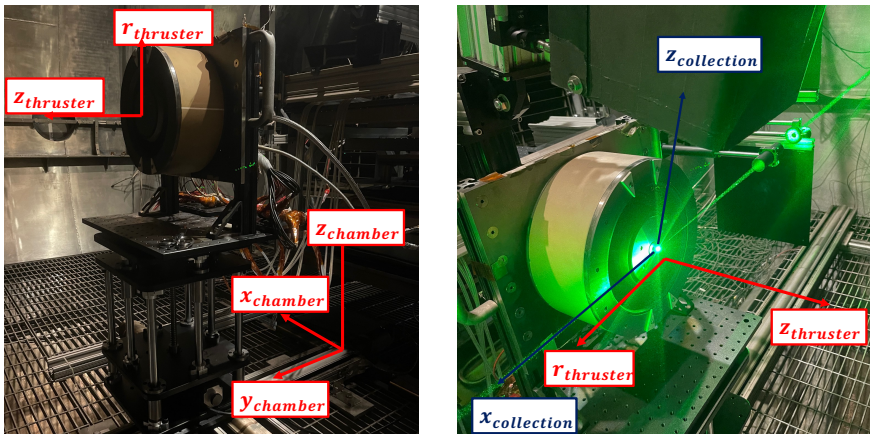

Figure 6.1: Annotated picture with all of the relevant basis vectors.

There are several basis vectors depicted in Figure 6.1. The chamber basis vectors are $\mathbf{x}_{\text{chamber}}, \mathbf{y}_{\text{chamber}}, \mathbf{z}_{\text{chamber}}$. A notional diagram that shows these basis vectors relative to the major components of the experiment are depicted in Figure 6.2.

Figure 6.2 shows the orientation of the motion stages, their positive travel direction, and the chamber axis definitions, as well as the interrogation, collection, and detection optical axes to be described in the next section. The thruster was moved along the chamber basis vectors using Parker 4062000XR planar motion stages and an Optics Focus MOZ-300-150 motorized vertical lift stage. The thruster basis vectors are $\mathbf{x}_{\text{thruster}}, \mathbf{r}_{\text{thruster}}$. The $\mathbf{r}_{\text{thruster}}$ can be rotated 360 degrees about $\mathbf{z}_{\text{thruster}}$, consistent with the cylindrical shape of the device. All probed locations are presented in thruster radius-normalized-coordinates, z/r_{o} and r/r_{o} relative to origin of the thruster, taken to be the thruster centerline and the thruster exit plane. For clarity, the probed points are presented along with the relevant major thruster geometry in the following subsections.

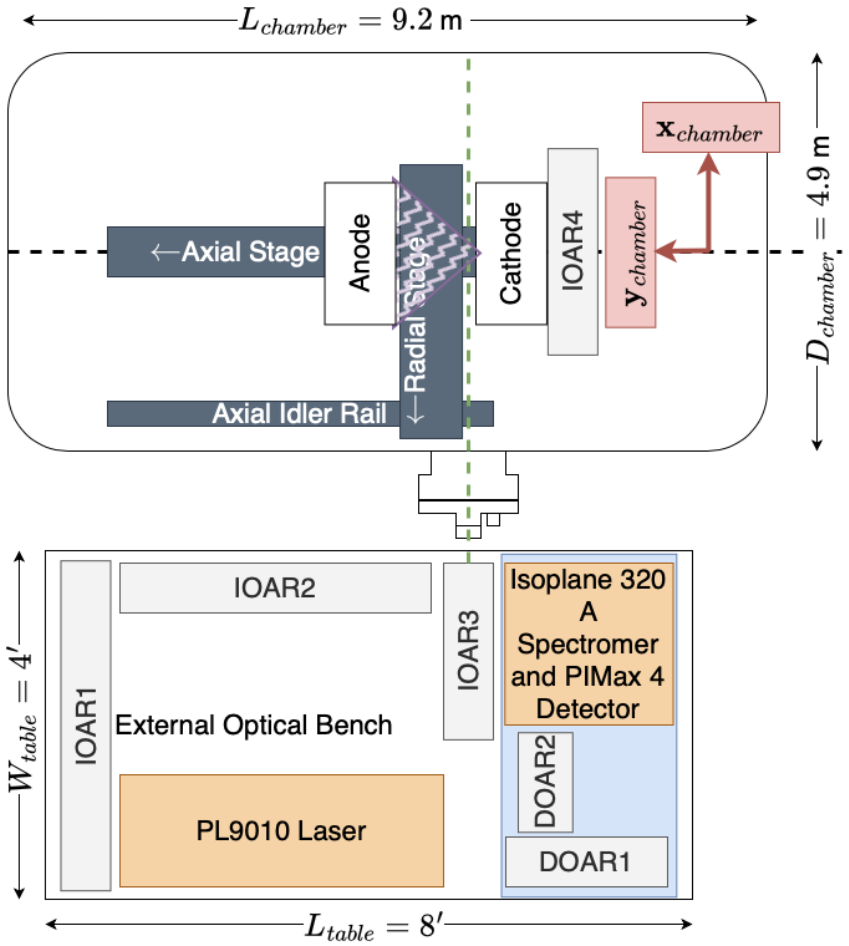

Figure 6.2: Notional diagram of the relative location of the external optical system with respect to the vacuum test facility. IOAR and DOAR area acronyms for interrogation optical axis rail and detection optical axis rail respectively

6.2.3 Interrogation Optical System

The collection and detection systems were thoroughly outlined in the previous chapter. The master optical diagram is presented in Figure 6.3. The irises in the system were used for defining optical axes, aligning, and monitoring alignment throughout the experiment.

The interrogation laser beam system is diagrammed in Figure 5.3. It begins external to VTF-2, on an 8" thick 8' x 4 ' (2.44 m x 1.22 m) optical table (Newport RS2000) placed on four automatic leveling, vibration isolating legs (Newport S-2000A-428). Although the vibration stabilizing legs were initially used to 'float' the table, during fine alignment, it was determined that the day-to-day change in the alignment or the risk of accidental

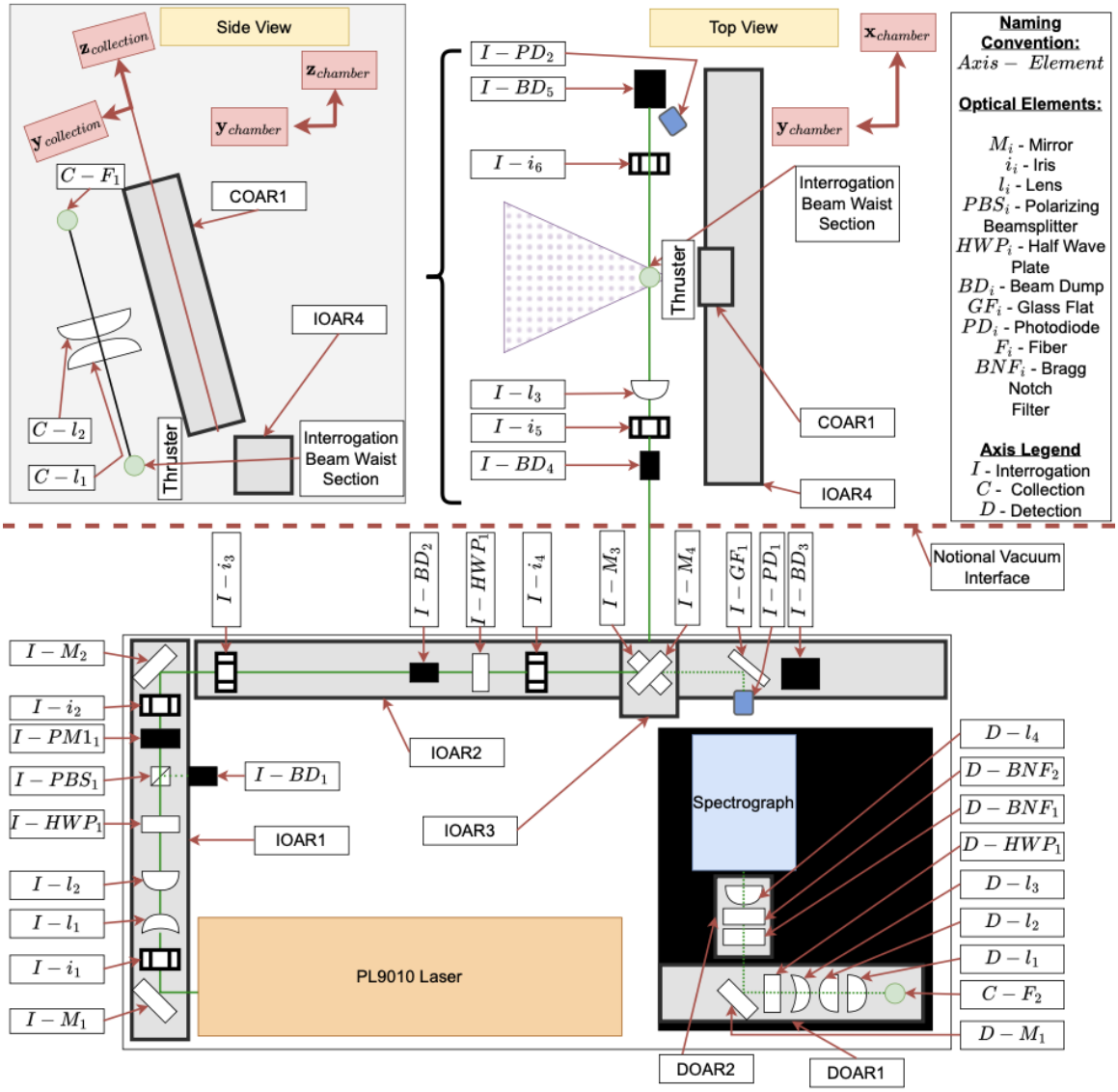

Figure 6.3: Master optical diagram for the interrogation, collection and detection systems. The vacuum interface is represented as the large thick red dashed line.

perturbation of the table by a human and the effect on the alignment in the interrogation section was too large. An injection seeded amplitude DLS Powerlite 9010 Nd:YAG laser frequency doubled using a 2nd harmonic generator type II (2HG-T2) crystal provided a 9 mm diameter beam with a laser pulse width between 5 and 8 ns. The laser energy, at 532 nm wavelength output, was measured at 1.15 J/pulse after installation. The laser beam is steered externally along three legs.

The first two legs are aligned parallel to the surface of the optical table, while the third

provides the periscope distance vertically from the surface of the table parallel to $\mathbf{z}_{\text{chamber}}$ to bring the beam to the height of the center axis of the chamber and coincident with $\mathbf{x}_{\text{chamber}}$. Table 6.1 outlines the optical components used. First, a 1.5-1 beam expander was placed using $I - l_1$ and $I - l_2$. The relative position of $I - l_1$ and $I - l_2$ was controlled with a micrometer stage.

Table 6.1: Interrogation beam optical parameters.

Element	**Aperture Size**	**Focal length**	**Part**	**Sourced**
Laser	-	-	DLS Powerlite 9010	Amplitud/Continuume
$I - M_i$	50.8 mm	-	RX-532-45-UF-2038	Lattice Electro Optics
$I - BD_i$	20.0 mm	-	ABD0975NP	Kentek
$I - PM_1$	20.0 mm	-	UP52N-50S-QED-D0	Gentec
$I - i_i$	Variable	-	ID50	Thorlabs
$I - HWP_i$	20.0 mm	-	CW0-532-02-08-R10	Lattice Electro Optics
$I - PBS_1$	25.4 mm	-	PBH-532-10	Lattice Electro Optics
$I - l_1$	25.4 mm	-50 mm	UF-PC-25.4-50-532	Lattice Electro Optics
$I - l_2$	25.4 mm	75 mm	UF-PX-25.4-100-532	Lattice Electro Optics
$I - l_3$	25.4 mm	600 mm	UF-PX-25.4-400-532	Lattice Electro Optics

Then, a polarization-dependent beam energy splitter was constructed using half wave plate $I - HWP_1$ and polarizing beamsplitter cube $I - PBS_1$. This was necessary to maintain the nominal operational mode of the laser at it's optimal Q-switch delay and provide the flexibility for external modulation of the power. Immediately after the half wave plate is a power meter, $I - PM_1$, placed on a flip mount for easy flipping into the optical beam path for laser energy measurement. $I - HWP_2$ is critical as it controls the polarization inside of the chamber in the collection volume.

Two mirrors $I - M_3$ and $I - M_4$ create a polarization rotating periscope to bring the laser beam up to the height of the center axis of VTF-2. The beam passed through the vacuum interface through a custom Torr Scientific NSQ1462-25 KF-flanged Brewster to maximize energy throughput into the facility and minimize reflections for safety. Mirrors $I - M_3$ and $I - M_4$ were placed on micrometer stages paralell to $\mathbf{y}_{\text{chamber}}$ and $\mathbf{z}_{\text{chamber}}$,

respectively. This allowed for correction of the alignment of the beam with respect to the internal alignment targets when the facility The beam was then able to pass through into the facility along the center axis defined by the dash in Figure 6.2.

A custom steel structure is bolted to the thrust stand using two axial members and one lateral member and was designed for quick deployment on to and off of the thrust stand for experiments while also being very rigid. A Thorlabs MB2436 24"x36" breadboard was coupled to the thrust stand structure and acted as the internal optical breadboard for the internal interrogation and collection systems.

The internal interrogation optical axis is defined by $I - i_5$ and $I - i_6$. The final focusing lens, $I - l_3$, was placed on a micrometer stage for fine alignment of the beam waist with respect to the collection optical axis. $I - BD_5$ stopped the beam after the measurement region, and $I - PD_2$ was pointed at the beam dump to capture specular reflections to monitor timing and jitter. Figure 6.4 shows the internal interrogation optical axis used in this experiment.

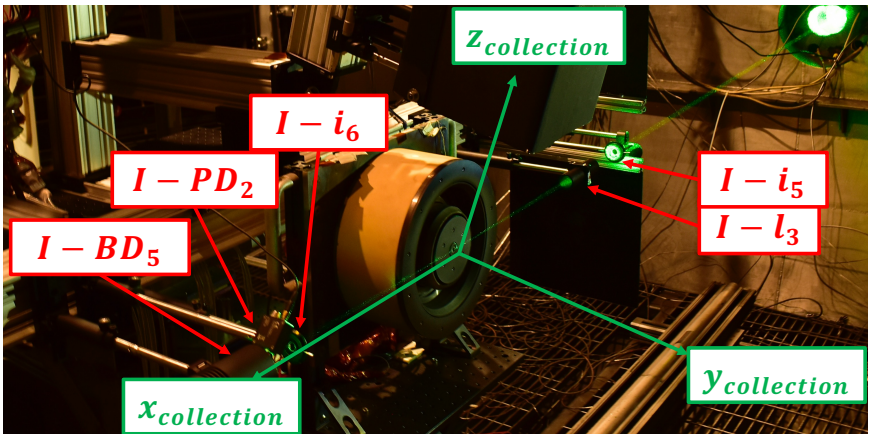

Figure 6.4: A photo of the internal optical rail structure that supports the last leg of the interrogation optical axis and the collection optical axis.

The internal interrogation beam optical structure allows for selection of focal length of $I - l_3$, which serve two purposes. The first purpose is to size the beam waist to be less than or equal to the size of the image of the fibers on the beam plane. This ensures that, for a properly chosen collection numerical aperture, the light collection power is maximized.

If the beam waist is larger than this image, then not all of the light is collected. However, when the beam waist is larger than the image of the fibers, your system is more robust to misalignment of the beam waist and fiber bundle image. The second purpose is to make the beam waist as small as possible without introducing limitations on the incident laser energy due to perturbations to the plasma and perturbations to the neutrals. This ensures that the full capacity of your laser can be leveraged to generate scatter as LTS and LRS are linear in the incident laser energy. This is the reason for subtle changes to $I - l_2$ and $I - l_3$ in this section. The 1-1.5 beam expander and 600 mm focal length of $I - l_3$ allowed the incident laser energy, that was previously limited to approximately 200 mJ/pulse due to ionization of neutrals, to be raised to 1 J/pulse. Additionally, the minimization of the beam waist diameter ensures that the spatial resolution perpendicular to the beam propagation direction is tight. The spatial resolution parallel to the beam propagation direction is controlled by the image of the fiber on the beam plane.

6.2.4 Collection and Detection Optical Systems

Similar to the external and internal interrogation beam optical system, the light collection and light detection systems have internal and external components. The system was designed to maximize the collection solid angle, provide a spatial resolution of less than 1.5 x 2 mm, and facilitate realignment of the collection and interrogation optical axes when misalignment occurred due to facility shifts.

The fiber faces, $C - F_i$ referred to as part of the collection system. Two FG200LEA-FBUNDLE custom fiber bundle were used in the collection system. The bundles were a linear array of seven 200 μm FG200LEA multimode fibers. The bundle was a linear SMA array on one end and fanned out into individual SMA fibers for feeding through the vacuum interface. Both the common linear end and the individual fanned fibers were SMA-ended. The fibers were fed through the facility wall with a custom SQS Fiber Optics HEM048727 4.5" CF flange.

On the air side, the second fan bundle was used to relay the light output to the detection system as a linear array. The 200 μm were chosen to drive the theoretical spatial resolution down to 200 $\mu\mathrm{m} \times \mu\mathrm{m}$, while having a high numerical aperture of NA = 0.22. A bundle of linearly arranged fibers was chosen because it provided the most light collection along the beam propagation direction without sacrificing spatial resolution in the perpendicular directions. The linear array of fibers was mounted on an XYZ-configured set of motion stages constructed using three Thorlabs MTS25/M-Z8. Each individual fiber-stage axis was controlled via a KDC101 Thorlabs Kinesis K-Cube DC Servo Motor Controller.

The NA of the lenses was 0.2095, slightly smaller than the numerical aperture of the fibers. There is about a 10 $\%$ loss in the light collection power due to this slightly smaller effective NA of the lenses. These lenses were used in order to create a 1 - 1 image of the linear array of fibers onto the interrogation laser beam plane. An AR-coated 200 mm x 200 mm x 2 mm piece of glass was placed ahead of the first collecting lens in order to protect the lenses from deposits from the thruster. Additionally, the collection optics were placed in a box for protection from the plasma environment that was expected to be harsher than the one during the stand-alone cathode experiment.

Finally, it was necessary to preserve the collection solid angle, even when the interrogation volume was very close to the thruster so that the thruster does not intersect the collection solid angle, blocking it. Interference with the solid angle subtended by the collection lenses is a function of the relative orientation of the collection cone of the lenses with respect to objects that can cross into this cone. This is inconvenient and limits collection power if solid angle is spatially dependent. In an application such as LTS in low-temperature low-density environments inside a large vacuum test facility this is undesirable. Defining $\theta_{\mathbf{z}_{\mathrm{cha}}-\mathbf{z}_{coll}}$ as the angle between $\mathbf{z}_{\mathrm{chamber}}$ and $\mathbf{z}_{\mathrm{collection}}$, a simple rotation of the collection axis by an angle greater than the half angle of the collection lenses ensures that the object of interest could be brought right up to the interrogation beam scattering volume without loss in collection solid angle. In this case, $\theta_{\mathbf{z}_{\mathrm{cha}}-\mathbf{z}_{coll}} = 15^{\circ}$. Accounting for this

allowed the collection volume to get to within 2 mm of the thruster exit plane.

Although the rotated collection axis with respect to the thruster provides a path to minimization of LRS collection and preservation of the entire solid angle, there are disadvantageous. The rotated collection angle, coupled with the direction of the scattering wave vector, provides measurements of the electron properties that are strictly speaking not aligned with any thruster basis vectors. In order to resolve the axial or radial temperature at all of the desired points would have proven prohibitively time consuming as three measurements of every point at 3 thruster azimuthal slices would have been required to decompose the temperature and electron drift velocity into the thruster frame of reference. Therefore, when electron temperatures are presented in the rest of this section, the lack of decomposition is equivalent to assuming an isotropic temperature at all measured points.

The spectrograph is comprised of a Princeton Instruments ISOPLANE-320A spectrometer and PM4-1024i-HB-FG-18-P46 PIMAX4 The spectrometer was operated with a ARC-SP-ES motorized slit (ARC-SP-ES), a SLIT SHUTTER-ISOPLANE320 slit shutter, and a three-grating turret, which housed a 500 nm optimized I3-120-500-P 1200 l/mm grating that was used for acquisition.

A four-lens relay system was used in the detection branch to capture all of the light from the fiber, relay it without clipping, and at the spectrometer. The optical focal lengths were selected using ray-matrix optics in order to respect the Helmholtz optical invariant. This required a magnification of approximately 2.02. The system used two 25 mm aperture volume Bragg grating notch filters from OptiGrate. Figure 6.5 illustrates the optics used in the relay system and their ideal ray optics matrices used for design and optimization.

Table 6.2 outlines the optics used and their relative distances for maximum light throughput. In order to minimize losses due to vignetting, the optics were placed as close as possible, with particular care taken to minimize the distance $\Delta z_{BNF_1/l_3}$. The detection system imaging the face of the fiber, an almost perfect plane, effectively eliminated 532 nm stray light from passing through the detection system into the spectrometer. After a prelimi-

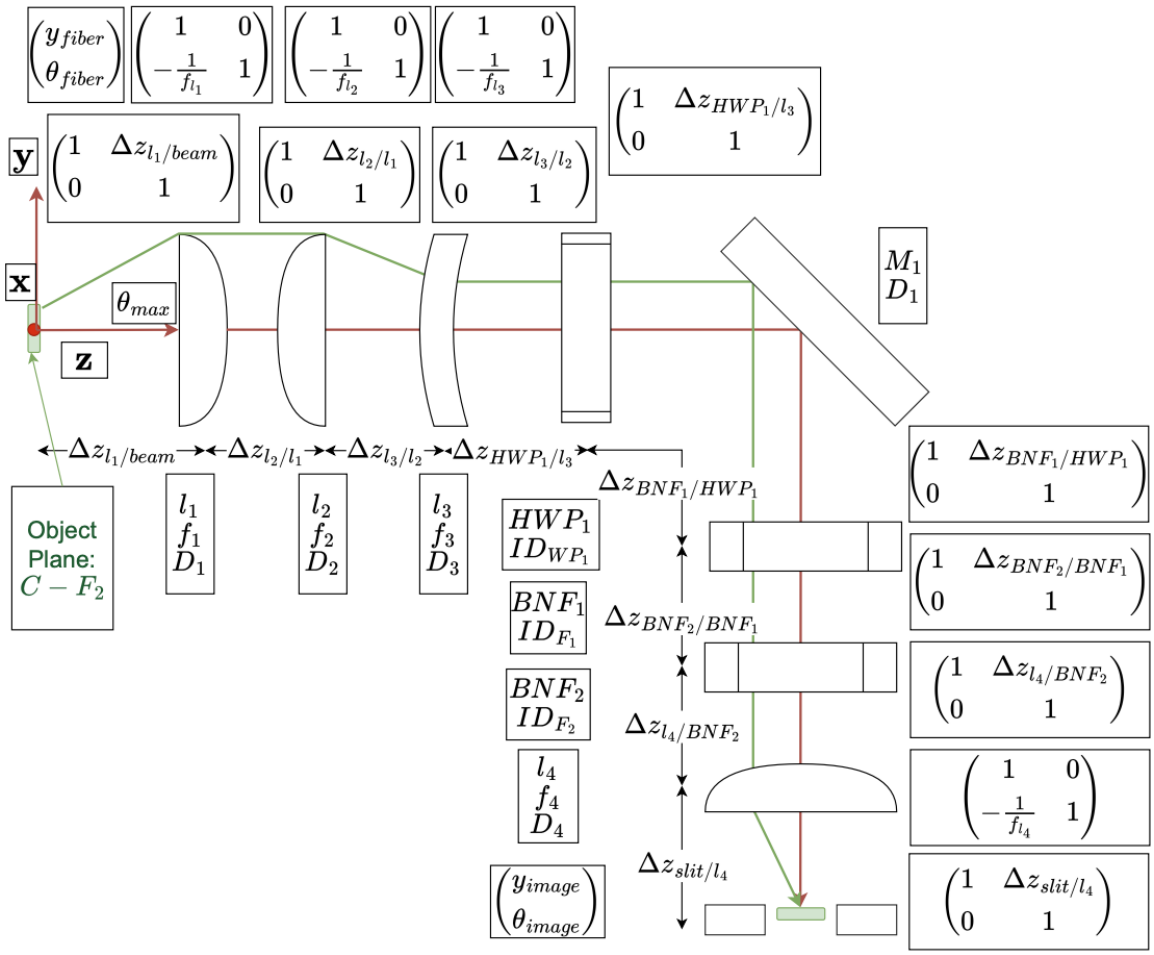

Figure 6.5: Detection system optical diagram.

nary alignment, a box was used to cover all of the detection optics to minimize diffuse and specular reflections from the surroundings from introducing stray light into the optical system.

A Berkeley Nucleonics BNC-577-8C model delay generator was used as the master clock for the synchronization of timing events in the system. It controlled the internal timing of the DLS 9010 (QSW) with respect to the lamp to ensure the maximum rated energy per pulse was extracted from the laser. Additionally, the delay generator controlled the timing of the detector gate delay with respect to the laser QSW. The gate width was set in spectrograph control software to software to 10 ns.

The last chapter discussed several tests that were performed in order to ensure that the

Table 6.2: Detection system optical parameters.

Element	D or ID (mm)	f or Distance (mm)	Part	Sourced
$\Delta z_{l_1/beam}$	-	100	-	-
l_1	50.8	100	ACT508-100-A	Thorlabs
$\Delta z_{l_2/l_1}$	-	25	-	-
l_2	50.8	200	ACT508-100-A	Thorlabs
$\Delta z_{l_3/l_2}$	-	150	-	-
l_3	25.4	-50	ACN254-050-A	Thorlabs
$\Delta z_{HWP_1/l_3}$	-	25	-	-
HWP_1	25.4	25	WPH10E-532	Thorlabs
$\Delta z_{BNF_1/HWP_1}$	-	25	-	-
BNF_1	25	-	BNF-532-OD4-125	Optigrate
$\Delta z_{BNF_2/BNF_1}$	-	25	-	-
BNF_2	25	-	BNF-532-OD4-15	Optigrate
$\Delta z_{l_4/BNF_2}$	-	75	-	-
l_4	25.4	100	AC508-100-A	Thorlabs
$\Delta z_{slit/l_4}$	-	100	-	-

system was only sensitive to the relative movement of the chamber with respect to the outer interrogation system when the facility was pumped to rough and high vacuum. One of the conclusions was that vibrations from the mechanical pump, blower, and compressors driving the radiation shrouds did not affect alignment. This generalizes the system's alignment to being insensitive to noise below 60 Hz when their sources are more than 5 feet away from the optical table. To be discussed later was another source of misalignment that was previously not an issue due to the incident laser energy level. The incident laser energy used in the previous chapter was 200 mJ/pulse. The heating of the interrogation lens did not prove to be an issue that required more than occasional realignment to address. When the incident laser energy was raised above 500 mJ/pulse, the lack of convective cooling of the lens inside of the facility coupled with the fact that in order to collect an emission scan the laser had to be blocked from entering the facility led to thermal cycling of the interrogation lens that required alignment between every point. This point is discussed further in Subsection 6.6.2

6.3 Raman Scattering Calibration, Least Squares and Bayesian Inference Analysis

As stated previously, the thruster discharge condition was modified to a higher current density condition in order to facilitate the collection of LTS over the required spatial locations. However, the SNR is expected to drop below the threshold defined in Chapter 3 for confidently relying on least squares uncertainty profiles as ground truth. Therefore, the data in the subsequent sections are process with the Bayesian inference framework described in Chapter 3. This is under the assumption that the Bayesian inference provides the ground estimates of the quantity of interest and its uncertainty given that the probability model propagates the uncertainty in the nuisance parameters whereas the least squares method does not. The $3\sigma_{\mathrm{x},i}$ ranges used to construct the priors used in the subsequent sections are outlined in Table 6.3 and Table 6.4. In all cases, for the sake of time-efficiency, the length of the Markov chains were limited to 50,000 samples. Additionally, 50,000 samples were used to calculate Bayes' factor, $\ln(B_{2,1})$, as a measure of the support for the Maxwellian versus Druyvesteyn EVDF submodels. The posterior estimates from the LRS inference are used to construct the priors for the nuisance parameters for the LTS inference.

Table 6.3: Description of the $3\sigma_{\mathrm{x},i}$ ranges used for the LRS cases.

Parameter	**Minimum**	**Maximum**
p_{g}	$0.99 * p_{\mathrm{g_o}}$	$1.01 * p_{\mathrm{g_o}}$
T_{g}	200	300
τ	1.0	1.5
η	0	1
λ_{i}	531	533

In all cases, LRS data was collected from air at a barometric pressure corrected value of 5 Torr. LRS was collected with an incident laser energy of 500 mJ/pulse with 50 on-ccd accumulations and an average of 100 frames for a total of 3000 shots. In general, data was acquired in order to maximize on-ccd accumulations. Then averaging over several tens to hundreds of frames once the maximum number of on-ccd accumulations were reached due

Table 6.4: Description of the $3\sigma_{\mathrm{x},i}$ ranges used for the LTS cases.

Parameter	**Minimum**	**Maximum**
$T_{\mathrm{e}}^{\mathrm{M}}$	0	100
$T_{\mathrm{e}}^{\mathrm{D}}$	0	100
$n_{\mathrm{e}}^{\mathrm{M}}$	1.0×10^{16}	1.0×10^{20}
$n_{\mathrm{e}}^{\mathrm{D}}$	1.0×10^{16}	1.0×10^{20}
$v_{\mathrm{d}}^{\mathrm{M}}$	-1000	-1000
$v_{\mathrm{d}}^{\mathrm{D}}$	-1000	-1000

to saturation. This will be specified per LTS experiment. In all cases, on-ccd accumulations were limited by plasma emission lines. Additionally, hardware binning was used over the total region of 300 pixels illuminated by the fiber bundle in the intensity direction in order to minimize read noise and contribute to the maximization of SNR. The spectrometer slit width was opened to 500 μm. A sample spectrum is presented in Figure 6.6. The marginal and joint posteriors are presented in Figure 6.7. The Bayesian posteriors generally exhibit larger FWHMs than that of the least squares posteriors. This is due to the loss of spectral resolution for the chamber implementation of the system. The loss in spectral resolution is evident given that there are no clear spectral lines in Figure 6.6. This leads to less sensitivity in the likelihood PDF about the optimal parameters due to similar values of the square of the residuals near the optimal parameters. The Bayesian and LS posteriors diverge in terms of correlations between the variables, as seen by the agreement in the correlations between τ and T_{g}, but the failure to capture the correlations between P_{g} and η. This is expected as the addition of the uncertainty in P_{g} into the uncertainty model introduces a degree of freedom that can not be captured in the least squares inversion.

6.4 Stray Light Correction

Similar to the non-laser-wavelength stray light present in the spectra presented in Figure 5.6 of Reference [140], interactions between the laser and the graphite thruster and cathode surfaces lead to irrepeatable stray light patterns in the collected data. This fluorescence

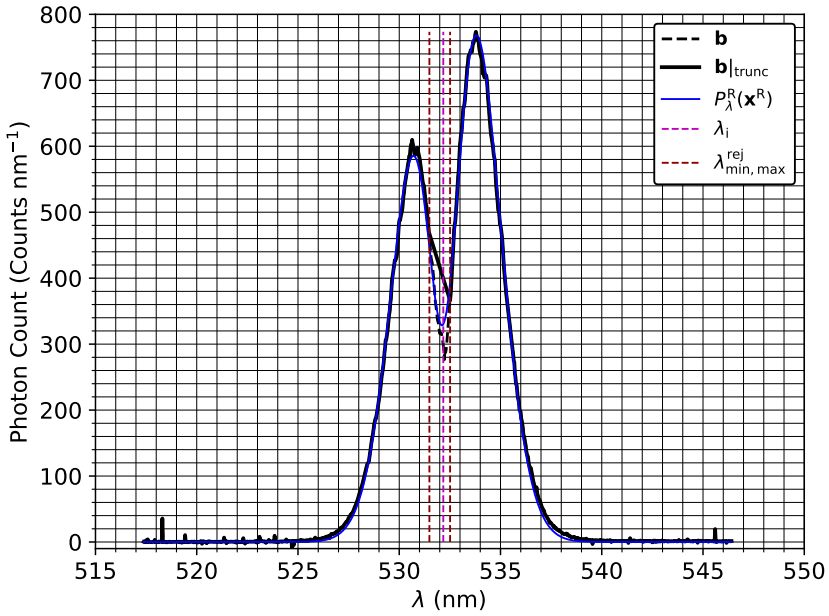

Figure 6.6: Least squares fitted spectrum for the rotational Raman inversion showing the raw and truncated ($\mathbf{b}$ and $\mathbf{b}|_{\text{trunc}}$) spectra with rejection regions and model spectra ($P_\lambda^{\text{R}}\left(\mathbf{x}^{\text{R}}\right)$) at 5.2 Torr.

signal was observed to be spatially dependent, laser energy dependent, and depend on the number of on-ccd accumulations. Whereas the methods in previous chapters allowed for a single set of backgrounds scans to be collected in order to correct the data, background scans were required at all spatial positions. It was determined that a single frame with the same number of on-ccd accumulations was sufficient at each spatial location, dramatically cutting down the time to acquire these background signals. However, the non-repeatability of the stray light required further correction.

The stray light was observed to behave like a piecewise linear function,

$$P_{\text{stray}}(\lambda) = \left\{ \begin{array}{ll} P_{\text{o}}, & \lambda \leq \lambda^* \\ P_{\text{o}} + m\left(\lambda - \lambda^*\right), & \lambda > \lambda^* \end{array} \right\}. \tag{6.2}$$

From Chapter 3, a Thomson spectrum is the result of $A_{\text{T}} - (B_{\text{T}} + (C_{\text{T}} - D_{\text{T}}))$ in accordance with Table 3.5. The correction method first required fitting Equation 6.2 to the $C_{\text{T}} - D_{\text{T}}|_{\text{raw}}$. This line was subtracted to create, $C_{\text{T}} - D_{\text{T}}|_{\text{C1}}$. Then, the region away from

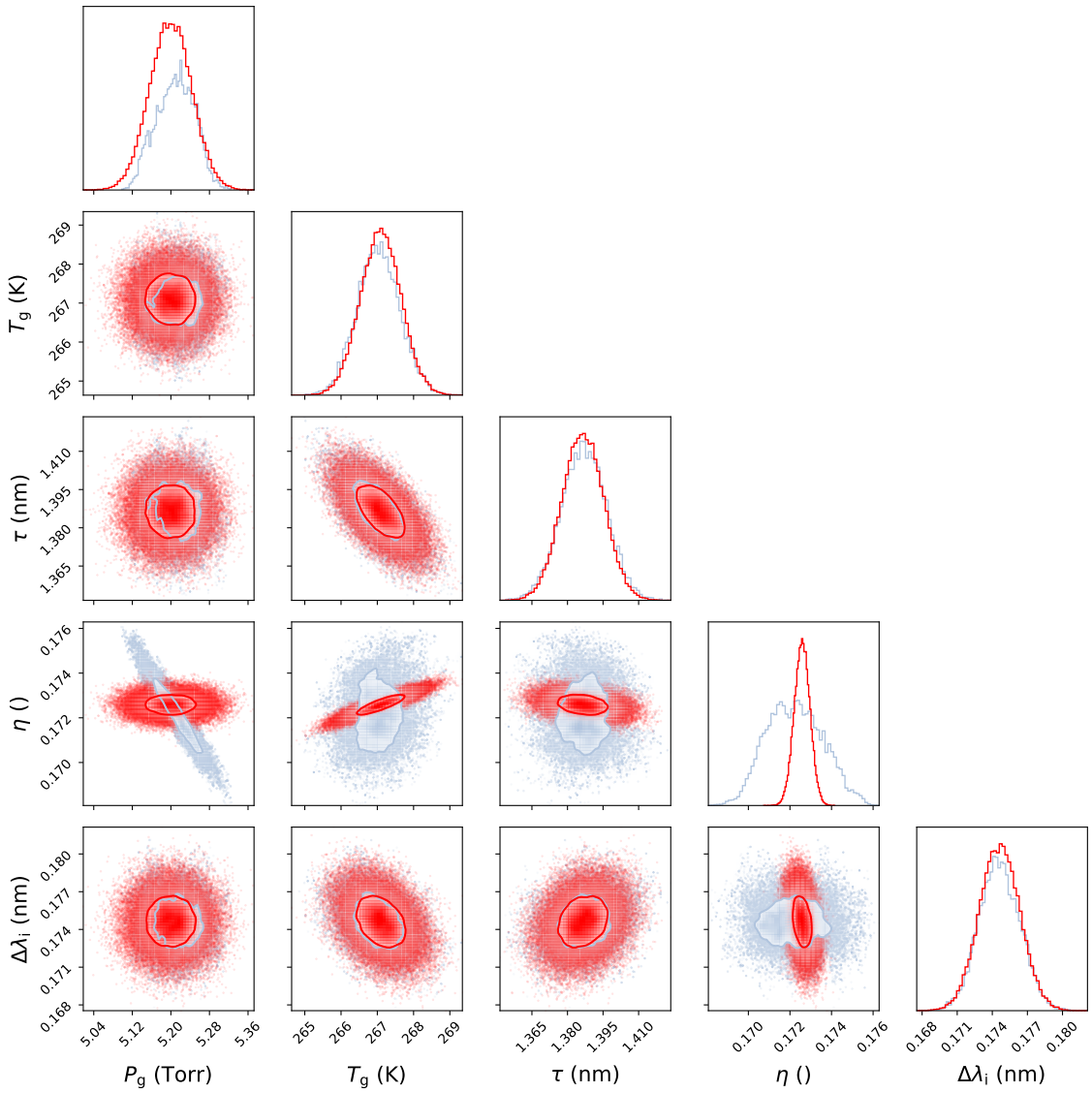

Figure 6.7: LRS marginal and joint posterior distribution functions for all LRS model inputs along with least squares posterior estimates. The Bayesian and LS posterior samples are presented in steel blue and red, respectively. For the sake of clarity, each joint posterior displays a single Mahalanobis contour containing the most probable 11.8% of the distribution.

the center wavelength was set to zero to create $C_{\mathrm{T}} - D_{\mathrm{T}}|_{\mathrm{C2}}$. This correction is shown in Figure 6.8 With $C_{\mathrm{T}} - D_{\mathrm{T}}|_{\mathrm{C2}}$ in hand, it was subtracted from $A_{\mathrm{T}} - B_{\mathrm{T}}|_{\mathrm{raw}}$ to create $A_{\mathrm{T}} - (B_{\mathrm{T}}+(C_{\mathrm{T}}-D_{\mathrm{T}}))|_{\mathrm{raw}}$. Then, Equation 6.2 was fit to the edges of $A_{\mathrm{T}}-(B_{\mathrm{T}}+(C_{\mathrm{T}}-D_{\mathrm{T}}))|_{\mathrm{C1}}$ and subtracted to create $A_{\mathrm{T}} - (B_{\mathrm{T}} + (C_{\mathrm{T}} - D_{\mathrm{T}}))|_{\mathrm{C2}}$. Then, a Gaussian function was fit to $A_{\mathrm{T}} - (B_{\mathrm{T}} + (C_{\mathrm{T}} - D_{\mathrm{T}}))|_{\mathrm{C2}}$ and subtracted from $A_{\mathrm{T}} - (B_{\mathrm{T}} + (C_{\mathrm{T}} - D_{\mathrm{T}}))|_{\mathrm{raw}}$ to create

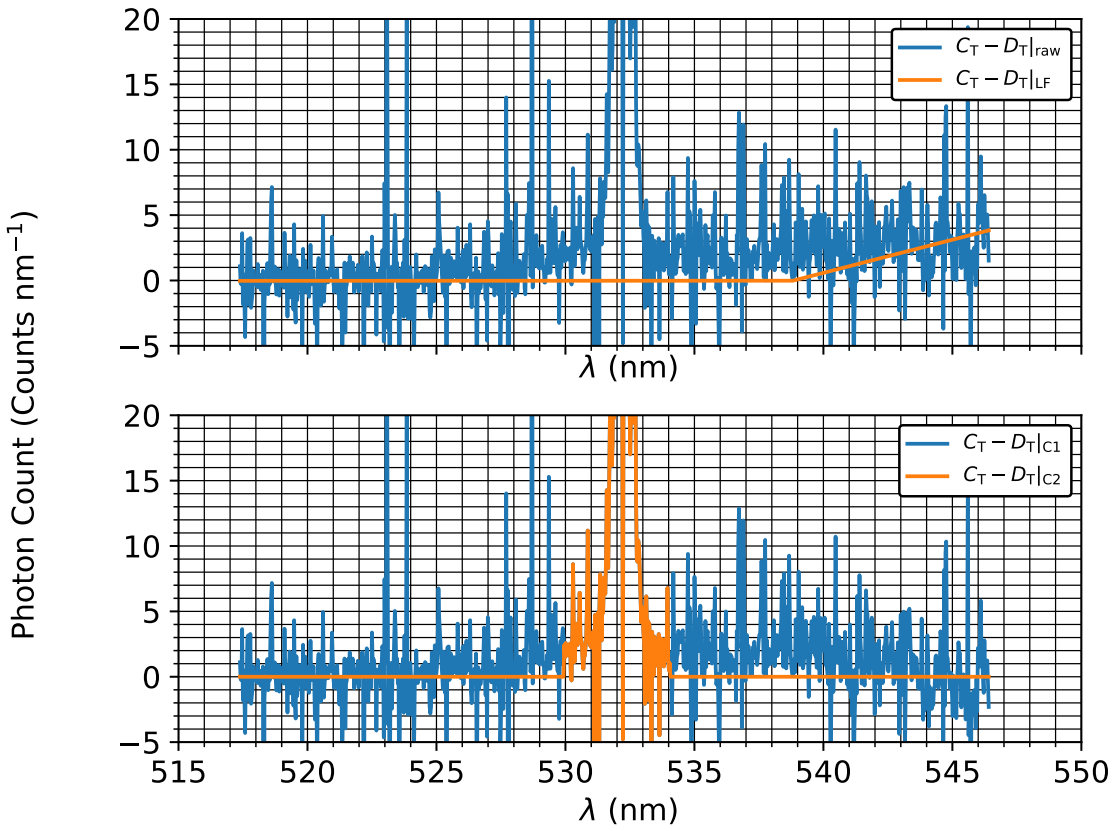

Figure 6.8: Correction of the $C_T - D_T|_{raw}$ spectrum.

$A_T - (B_T + (C_T - D_T))|_{stray}$. Equation 6.2 was then fit to $A_T - (B_T + (C_T - D_T))|_{stray}$ and subtracted from $A_T - (B_T + (C_T - D_T))|_{raw}$ to create $A_T - (B_T + (C_T - D_T))|_{C3}$. A Gaussian function was then fit to $A_T - (B_T + (C_T - D_T))|_{C3}$ and then subtracted from $A_T - (B_T + (C_T - D_T))|_{raw}$. This process was repeated until the parameters of the Gaussian fit converged to less than 1%. The resulting spectrum is taken as $A_T - (B_T + (C_T - D_T))|_{C3raw}$. The rejection region is applied and $A_T - (B_T + (C_T - D_T))|_{C3}$ is taken as the spectrum for LTS calculations. The corrected $A_T - (B_T + (C_T - D_T))$ spectra are presented in Figure 6.9

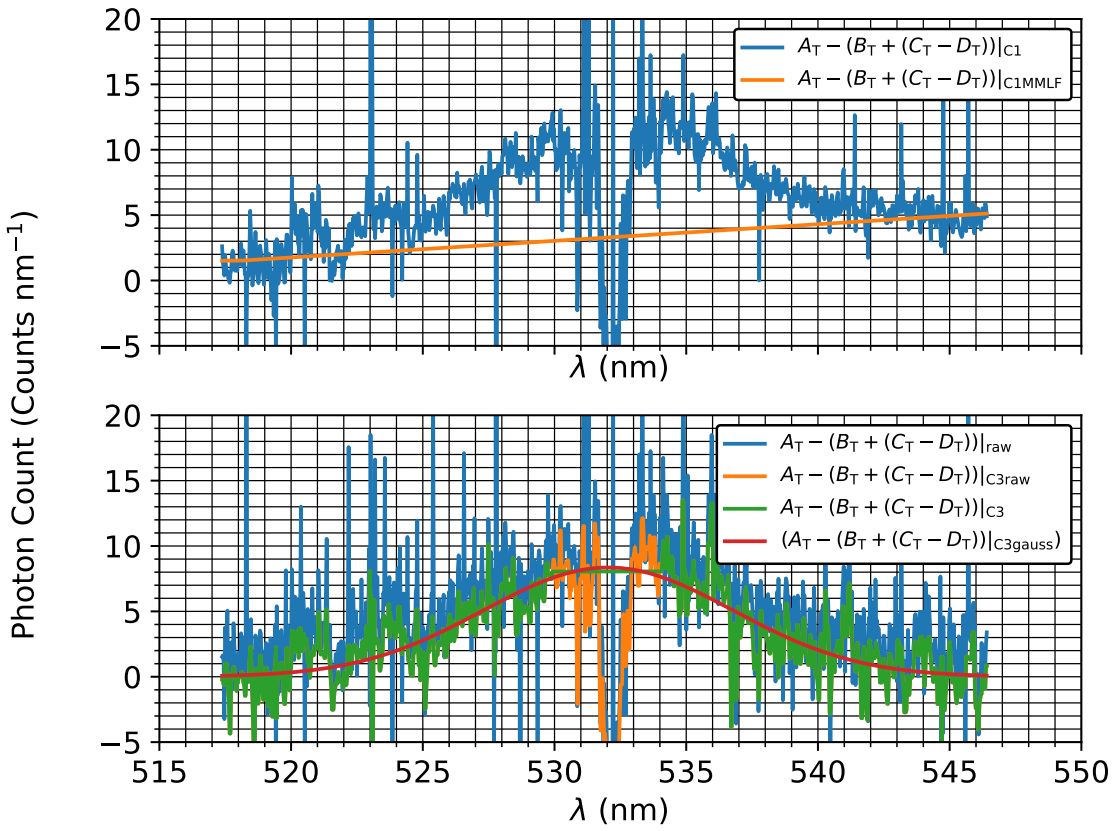

Figure 6.9: Correction of the $A_{\mathrm{T}} - (B_{\mathrm{T}} + (C_{\mathrm{T}} - D_{\mathrm{T}}))$ spectrum.

6.5 Discharge Channel and Cathode Centerline Axial Measurements

6.5.1 Normalized Axial Measurement Locations and Thruster Discharge Telemetry

The measurement locations for this experiment are presented in Figure 6.10. The thruster discharge telemetry is summarized in Figure 6.11 and Figure 6.12. The average facility background pressure during the experiment was 6.66×10^{-6} Torr-Kr $\pm$ 3.6%. The thruster and cathode krypton mass flow rates were 23.87 mg/s and 1.72 mg/s, both with uncertainties of less than 1%. At these flow rates, the thruster discharge voltage and current were 39.83 A $\pm$ 18.9% and 150.83 V $\pm$ 5.8%, respectively. The peak thruster power spectral frequencies were 6.51 kHz $\pm$ 1.76 % and 6.43 kHz $\pm$ 1.91 %, respectively.

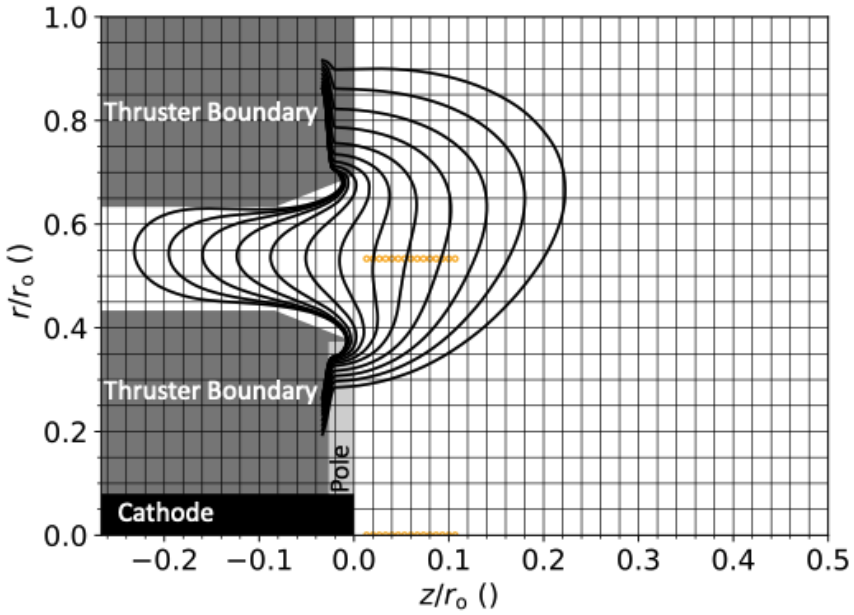

Figure 6.10: Normalized discharge channel and cathode axial measurement locations. The thruster boundaries are represented in grey, the front pole cover in light grey, and the cathode keeper body in black.

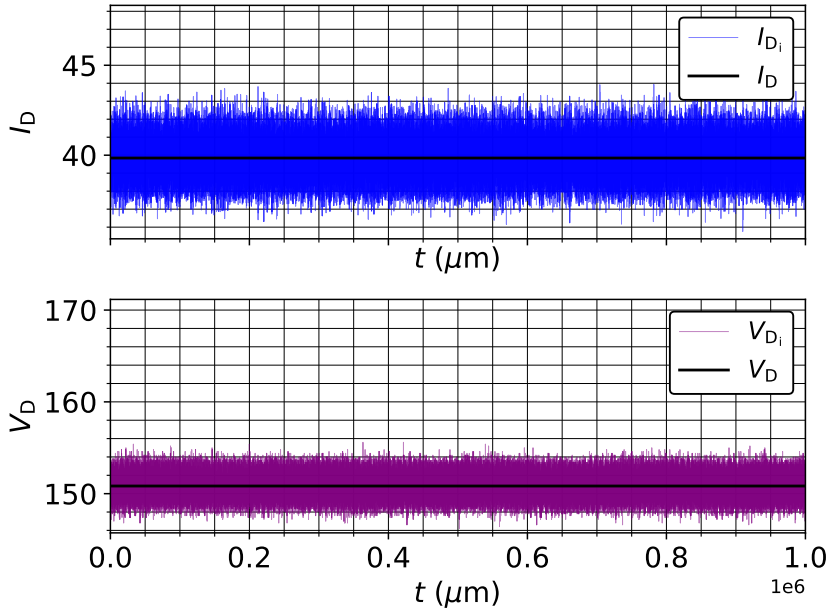

Figure 6.11: Individual and mean thruster discharge telemetry scans for the cathode and channel centerline axial measurements.

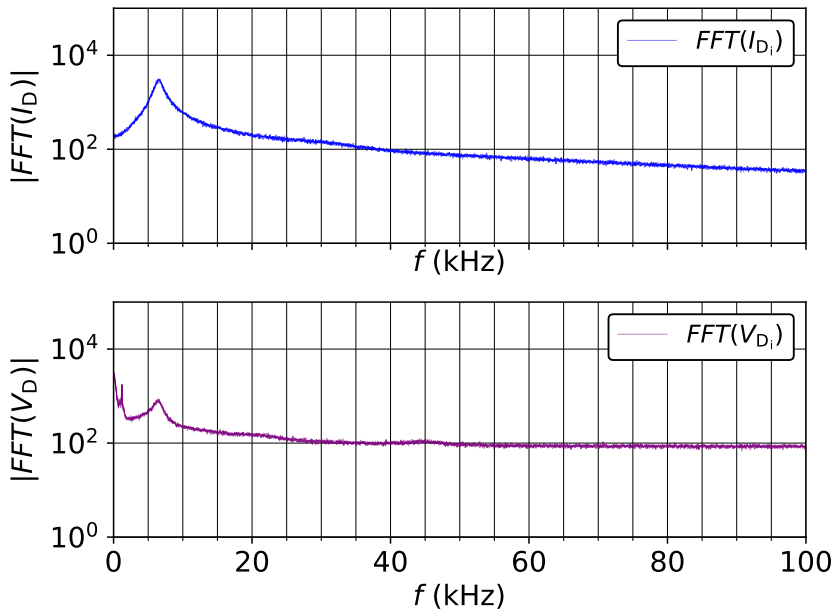

Figure 6.12: Individual thruster discharge telemetry power spectra for the cathode and channel centerline axial measurements.

6.5.2 Spatially-normalized Axial Electron Temperature and Density Profiles

The cathode axial centerline data was collected at an incident laser energy of 1 J/pulse with the number of frames averaged varying from 600 to 30 with a total number of 3000 laser pulses. The normalized cathode centerline axial profile using a Maxwellian submodel is presented in Figure 6.13. The Maxwellian submodel is preferred given the spatially-normalized axial profile of the Bayes' factor presented in Figure 6.14. The models become indistinguishable with axial distance but have strong support for a Maxwellian submodel close to the exit plane of the cathode. The thruster centerline data was collected at the thruster 12 o'clock position azimuthally at an incident laser energy of 1 J/pulse with the 40 frames averaged with each frame having 150 on-ccd accumulations for a total number of 6000 laser pulses. Initially, this was to reduce the emission line strength. The angle of the collection axis with respect to the thruster reduced the plasma line of sight by excluding the cathode plasma and the 6 o'clock channel position plasma. However, the plasma emission strength increased as the axial distance increased and the cathode and 6 o'clock channel

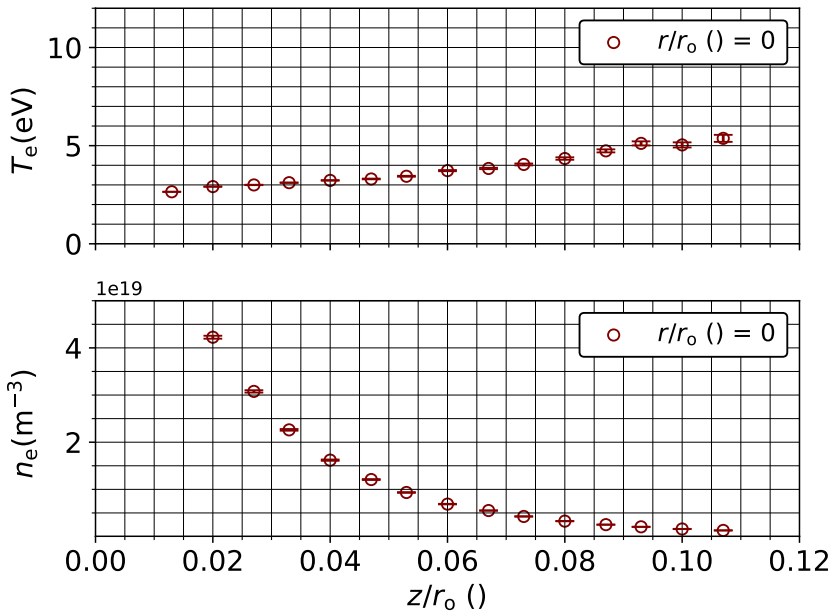

Figure 6.13: Spatially-normalized electron temperature and density profiles at the cathode centerline using a Maxwellian submodel.

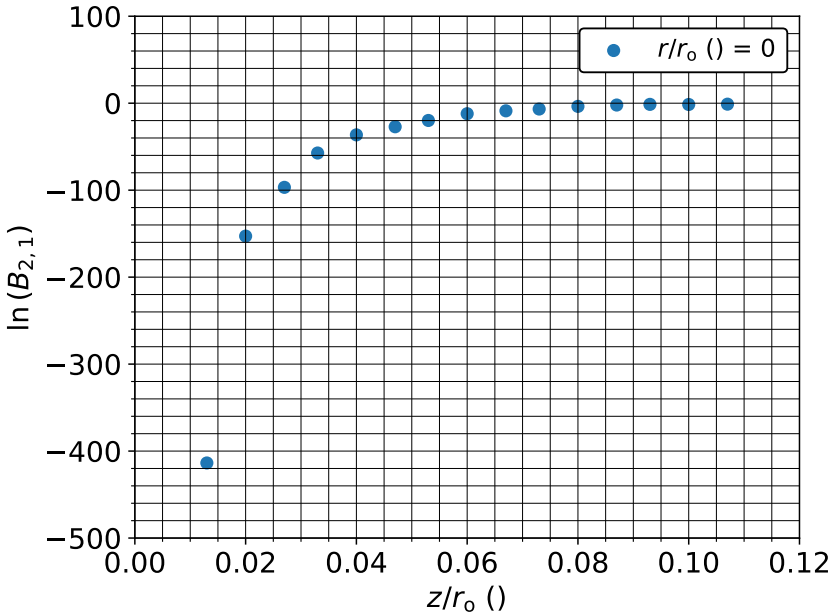

Figure 6.14: Spatially-normalized axial profile of the Bayes' factor for the Maxwellian and Druyvesteyn submodels $\ln(B_{2,1})$.

plasma entered the line of sight. However, this was not the limiting factor in this case. The normalized channel centerline axial profile using a Maxwellian submodel is presented

in Figure 6.15. As opposed to the cathode centerline case, the where was no preference

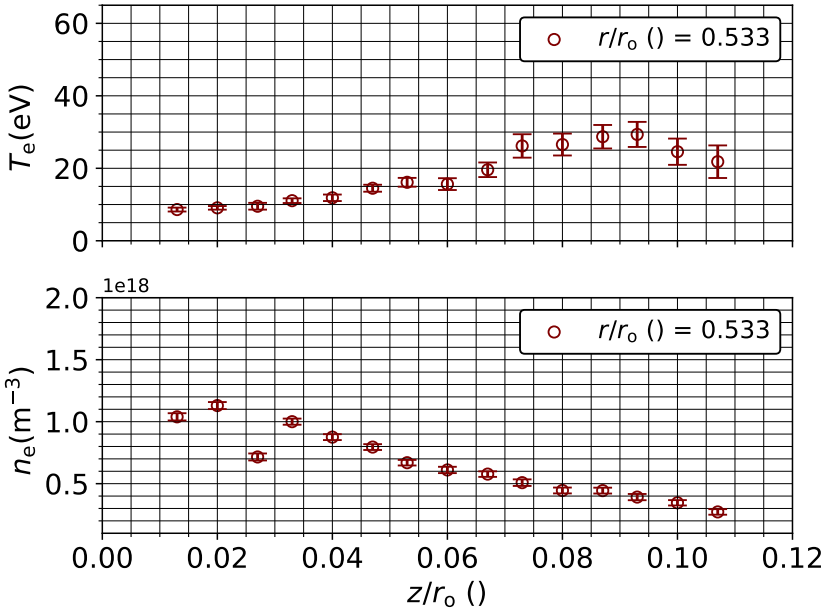

Figure 6.15: Spatially-normalized electron temperature and density profiles at the channel centerline using a Maxwellian submodel.

for a either EVDF along the thruster centerline. The electron number density and along the channel centerline decreases by approximately 85% from the minimum to maximum distance along the channel centerline as opposed to the cathode centerline electron number density that decreases by two orders of magnitude. In both cases, monotonic decreases in the electron number density were expected. The non-monotonic trend in the channel electron number density is attributed to misalignments of the fiber image on the beam plane due to facility movement. The outliers at z/r_o .013 and .039 suffered from misalignment. There is a sparsity of near field probe measurement estimates of electron properties, motivating a comparison of high speed probe measurements and LTS measurements in the near field plume of HETs.

The electron temperature increases by a factor of two along the cathode centerline as opposed to the factor of three increase along the channel centerline, to a maximum of approximately 30 eV at it's peak. This scales to approximately 20% of the discharge volt-

age. High speed probe measurements would lead to an empirical scaling expectation for the maximum electron temperature of 10-15% of the discharge voltage [15, 16, 24, 172]. However, recent and minimally invasive measurements using LTS suggest that this scaling needs to be corrected, as we observed a closer to 20% peak temperature and similar peak temperatures were observed in a similar thruster and low power thruster, both operating at different discharge conditions [140, 152]. Significant divergence between Langmuir probe measurements and LTS was shown in Reference [137] and expected due to the perturbation of the probe to the plasma. However, the near field LTS measurements agree in terms of the peak temperature being approximately 20% of the discharge voltage. Additionally, the maximum temperature along the cathode centerline is two times lower than the minimum temperature along the thruster centerline. This is expected, as the electron temperature close to the exit of the cathode are expected to be far colder than those in the discharge channel.

There are no simulations of this HET at 40 A and 150 V currently available. However, 4.5-kW simulations at 15 A and 300 V can be used for a qualitative comparison. These simulations were expected to have an input anode mass flow rate of approximately 11.8 mg/s [155]. Figure 6.16 and Figure 6.17 present the normalized axial profile of the magnetic field strength along the channel centerline and the normalized electron property profiles along the channel centerline. The 4.5-kW simulations indicate a peak centerline temperature that is about 13% of the discharge voltage. The simulations in Reference [60] show a peak temperature that is approximately 10% of the simulated 300 V at around 30 eV. This is consistent with the measurements from Haas [15] that indicate a peak temperature of approximately 10% of the discharge voltage at 300 V and 5.4 A and 10 A, implying insensitivity of this peak temperature to mass flow rate. Scaling this to our 150 V, 40 A case, a peak temperature of around 15 to 20 was expected. However, we observed a peak temperature of approximately 30 eV. The simulations indicate temperatures that peak before the expected peak in the axial magnetic field, as opposed to our results that indicate a peak

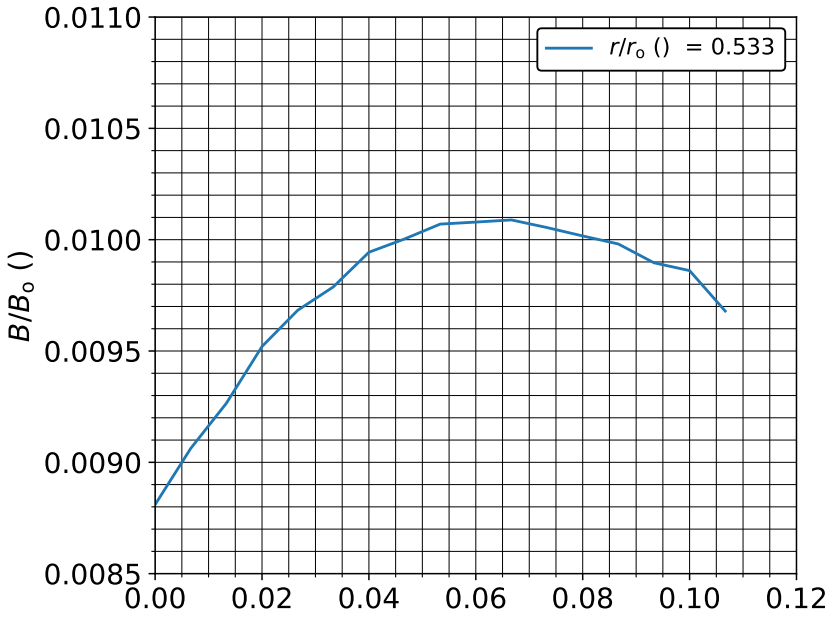

Figure 6.16: Discharge channel centerline normalized magnetic field strength.

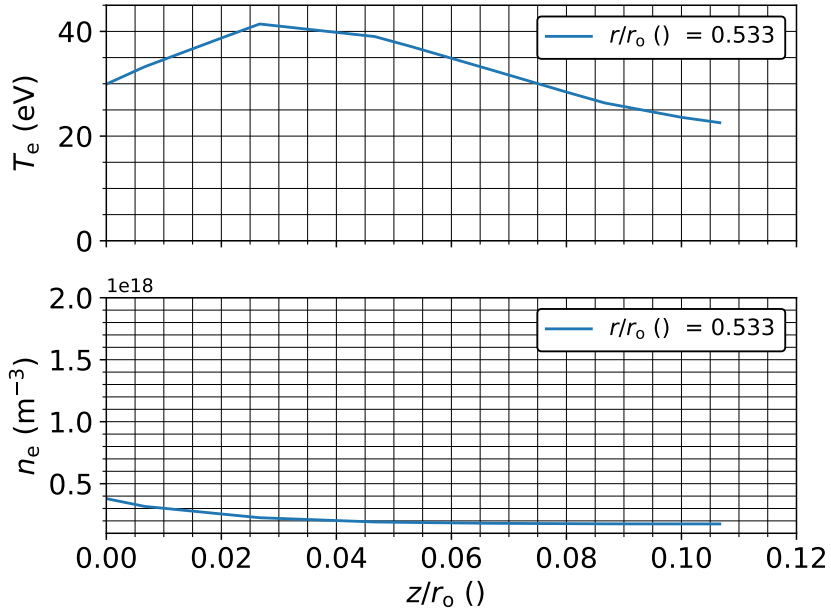

Figure 6.17: Channel centerline electron temperature and density profiles at 300 V and 15 A.

after the peak magnetic field. Previous simulation and experimental efforts indicate that the expected temperature is approximately located at the point of maximum axial electric field strength [92], and is approximately coincident with the axial location of the maxi-

mum magnetic field with temperatures increasing to this point due to Joule heating near the maximum magnetic field [37], and shifted between magnetically shielded and unshielded architectures [152, 157]. The shift in the maximum temperature from the experimentally measured data at 150 V 40 A and the 4.5 kW simulations suggests that at lower voltage, higher current densities the acceleration region is shifted further downstream axially. This agrees with ion velocity distribution function measurements showing the downstream movement of the acceleration region at lower discharge voltages [113]. The location of the peak temperature in [172] being closer to the discharge channel exit plane than our peak temperature is consistent with this as well.

Data taken at several discharge voltages at a normalized axial distance of z/r_{o} = .0133, while maintain constant power of 6 kW can provide insight into the relative peak temperatures and number densities between the 4.5-kW simulation and the 6-kW axial profile. Data was collected at a constant discharge power of 6 kW, with discharge voltages of 300.2 V $\pm$2.5%, 240 V $\pm$2.9%, 201.5 V $\pm$3.3%, 172.5 V $\pm$3.5%, and 148.6 V $\pm$4.7%, respectively. The discharge currents were 20.32 A $\pm$81%, 24.9 A $\pm$42.2%, 29.8 A $\pm$19.6%, 35.1 A $\pm$13%, and 39.7 A $\pm$20%, respectively. The peak thruster power spectral frequencies were 14.3 kHz $\pm$1%, 10.75 kHz $\pm$2.7%, 7.5 kHz $\pm$4.2%, 7.05 kHz $\pm$5.1%, and 6.6 kHz $\pm$2%, respectively. The cathode mass flow rate was held constant at 1.25 mg/s, with anode mass flow rates of 14.5, 5.9, 18.2, 21.4, and 23.8 mg/s, respectively. The flow rate uncertainties were all less than 1%. During these experiments, the chamber operational pressures were 3.96, 4.38, 5.13, 6.00, and 6.85×10^{-6} Torr-Kr, respectively. The electron temperature and density as a function of the notional discharge current are presented in Figure 6.18.

These profiles suggest monotonically decreasing temperatures with decreasing discharge voltages with increasing flow rates. Additionally, they suggest approximately linear increase in the electron density with decreasing voltage and increasing anode mass flow rate. Given that the simulated electron density in the 400 V, 15 A simulations is approximately $4\times10^{17}\mathrm{m}^{-3}$ and the measured electron density at 20 A, 300 V is measured to be

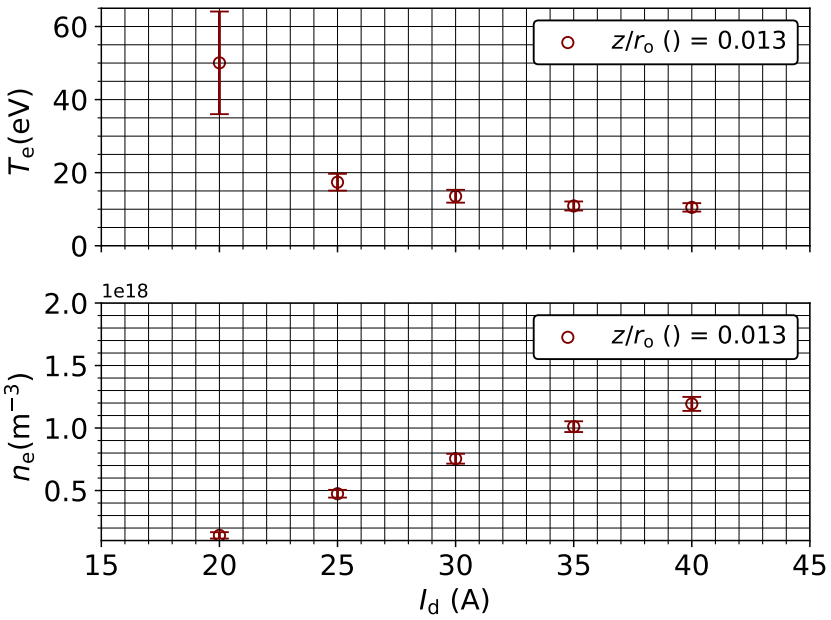

Figure 6.18: Electron temperature and density versus notional discharge current at the channel center line at a normalized axial location of z/r_o = .0133.

less than 1×10^{17}m^{-3} indicate a possible over prediction of the simulated electron density in the 4.5 kW simulation case. The measured electron temperature at 300 V and 20 A at z/r_o = .0133 of approximately 50 eV and the simulated temperature of approximately 37 eV indicates relatively good agreement on the prediction of the temperature. We can assume this given that, at a constant voltage, the temperature can be expected to increase with decreasing mass flow rate. However, it is evident that the divergence in the number density, and specifically the over prediction of the maximum electron number density may provide motivation for a parametric study of the axial profile of the electron temperature and density as a function of discharge voltage and current in order to calibrate the simulations.

6.6 Discharge Channel, Front Pole and Cathode Grid Measurements

6.6.1 Normalized Grid Measurement Locations and Thruster Discharge Telemetry

The measurement locations for these experiments are presented in Figure 6.19. These experiments were carries out over the course of two days; one day dedicated to the near

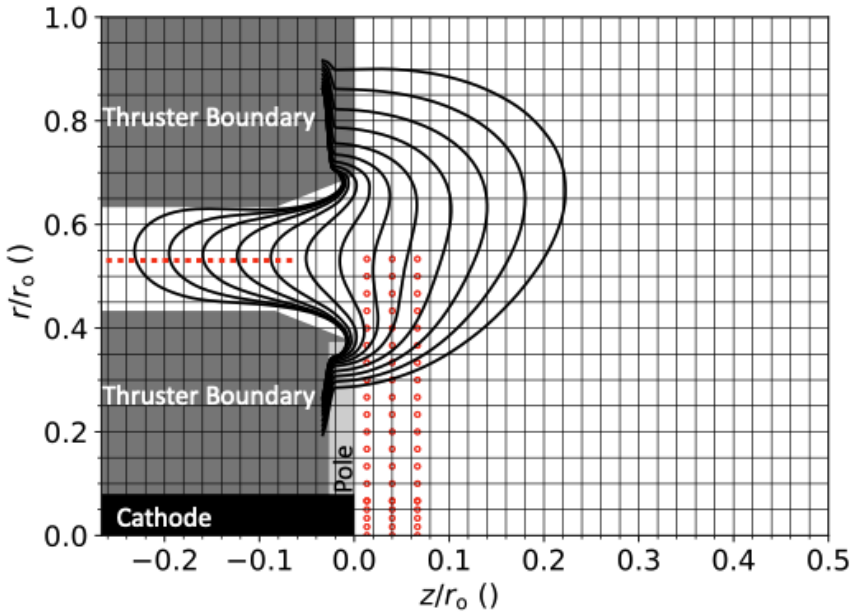

Figure 6.19: Normalized discharge channel, front pole and and cathode grid measurement locations. The thruster boundaries are represented in grey, the front pole cover in light grey, and the cathode keeper body in black.

field cathode grid points, and another dedicated to the thruster and front pole grid points. For the cathode grid, the thruster discharge telemetry is summarized in Figure 6.20 and Figure 6.21. The average facility background pressure during the cathode grid experiment was 7.49×10^{-6} Torr-Kr $\pm$ 1.1%. The thruster and cathode krypton mass flow rates were 24.24 mg/s and 1.78 mg/s, both with uncertainties of less than 1%. At these flow rates, the thruster discharge voltage and current were 39.7 A $\pm$ 16.86% and 150.23 V $\pm$ 4.75%, respectively. The peak thruster power spectral frequencies were 6.41 kHz $\pm$ 1.85 % and 6.33 kHz $\pm$ 1.57 %, respectively.

For the channel and front pole grid, the thruster discharge telemetry is summarized in Figure 6.22 and Figure 6.23. The average facility background pressure during the experiment was 6.85×10^{-6} Torr-Kr $\pm$ 1.4%. The thruster and cathode krypton mass flow rates were 23.94 mg/s and 1.75 mg/s, both with uncertainties of less than 1%. At these flow rates, the thruster discharge voltage and current were 40.5 A $\pm$ 16.6% and 149.7 V $\pm$ 4.12%, respectively. The peak thruster power spectral frequencies were 6.42 kHz $\pm$ 1.76

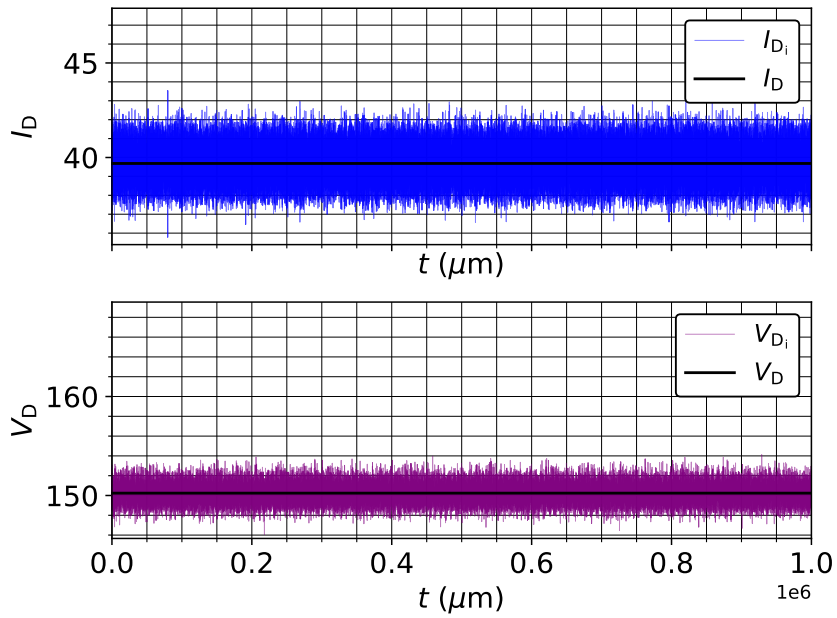

Figure 6.20: Individual and mean thruster discharge telemetry scans for the cathode grid measurements.

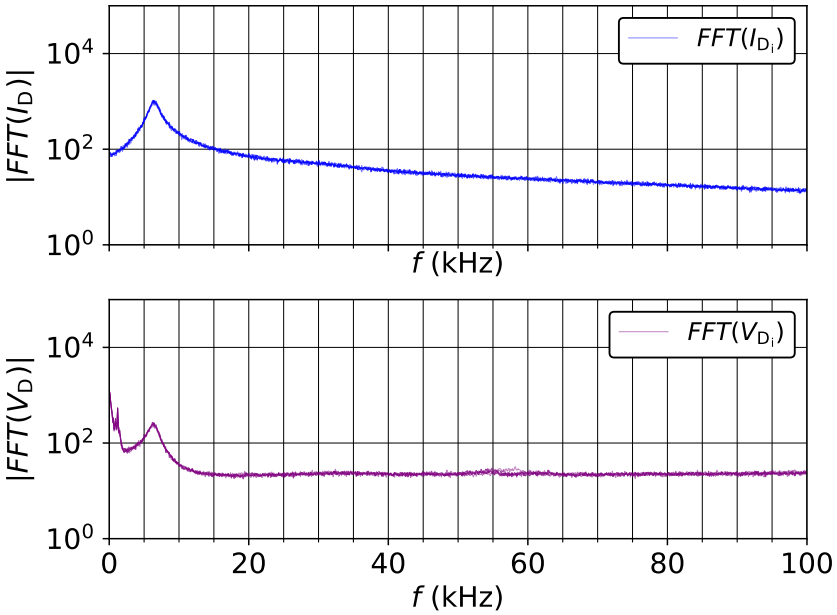

Figure 6.21: Individual thruster discharge telemetry power spectra for the for the cathode grid measurements.

% and 6.33 kHz $\pm$ 1.91 %, respectively.

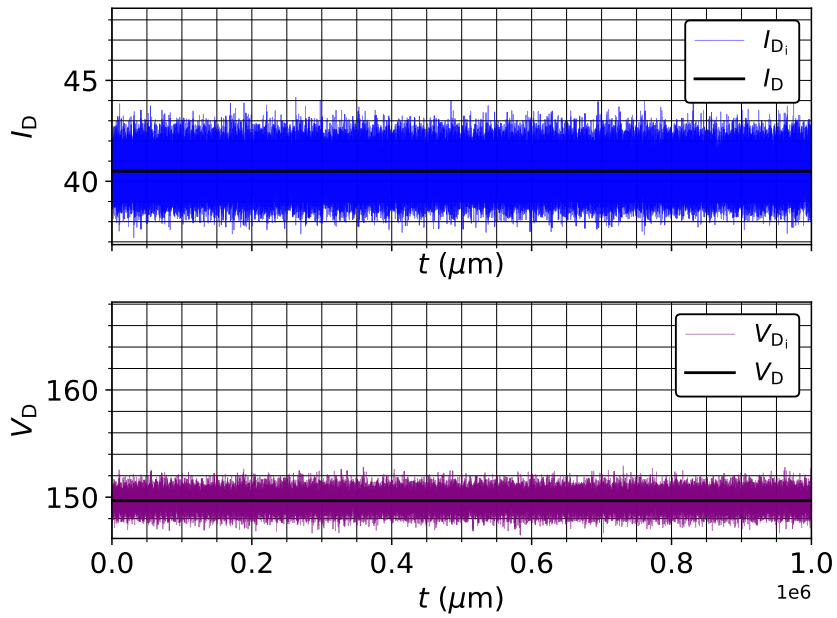

Figure 6.22: Individual and mean thruster discharge telemetry scans for the channel and front pole grid measurements.

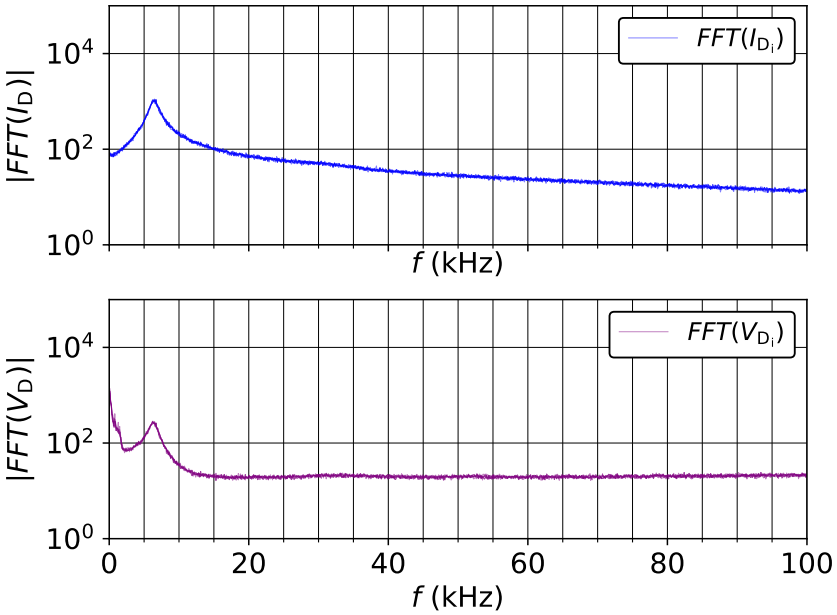

Figure 6.23: Individual and mean thruster discharge telemetry power spectra for the channel and front pole grid measurements.

6.6.2 Spatially-Normalized Discharge Channel, Front Pole and Cathode Grid Electron Properties

The cathode grid data was collected at incident laser energies that varied between of 730 to 760 mJ/pulse with the number of frames averaged varying from 100 to 50 with a total number of 1500 laser pulses. The energy issues were due to laser functionality deterioration due to the total number of shots acquired during the setup and testing of the system. The total number of laser pulses averaged was reduced in order to facilitate a denser grid near the cathode and minimize the time to collection. Periodic realignment of the fiber image with respect to the beam plane allowed for more consistent alignment during the experiment. This was done by returning to the nearest cathode centerline point and realigning the fiber image with respect to the beam. This alignment introduced an average positioning uncertainty of approximately 200 µm. The spatially normalized electron temperature and density profiles for the cathode grid are presented in Figure 6.24. The temperature is observed to

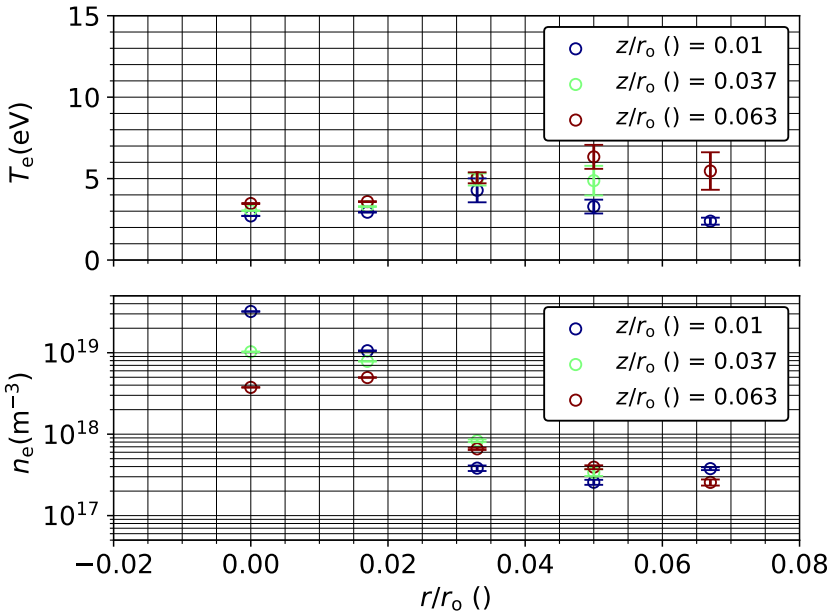

Figure 6.24: Spatially normalized electron temperature and density profiles for the cathode grid.

increase with increasing radius and increasing axial location away from the keeper orifice.

The number density is observed to decrease with increasing radial distance. However, there is a switch in the trend with axial increasing axial distance. In the core plasma in front of the cathode orifice, up to r/r_{o} of approximately .02, the density decreases with increasing axial distance. However, in front of the cathode keeper boundary, the density increases with axial distance. This suggests the existence of a background plasma between the cathode orifice and discharge channel that can create a conductive path for particles to the thruster and cathode surfaces. The inconsistency in the density trend at a r/r_{o} of approximately .065 suggests that misalignment of the fiber image with respect to the beam.

Data collected at the thruster 12 o'clock position leveraging the vertical thruster motion stage was not showing consistent electron number density trends due to misalignment artificially reducing the number density. It was discovered that the thermal state of the lens inside of the chamber at energies above 500 mJ/pulse affected the alignment more frequently than anticipated. Therefore, the thruster 12 o'clock position was abandoned for the thruster 3 o'clock position because the cathode centerline realignment at the thruster 12 o'clock position was was limited by the speed of the vertical motion stage. At the 3 o'clock position, the system could be realigned quickly. For the remainder of the experiments, the system was realigned between every point. The channel and pole grid data was collected at incident laser energies that varied between 620 to 770 mJ/pulse with the number of frames averaged varying from 40 to 10 with a total number of 3,000 laser pulses. This was done to maximize the number of points collected and to minimize the dwell time between realignment of the fiber image. The spatially normalized electron temperature and density profiles for the channel and pole grid are presented in Figure 6.25.

The electron density is observed to decrease monotonically with both distance away from the channel centerline and axial distance. The temperature close to the exit of the discharge channel is observed to remain low and increase towards the channel edge approaching an r/r_{o} of 0.4. At larger axial distance, the temperature is observed to increase and then decrease towards the front pole region from the channel edge. The temperature

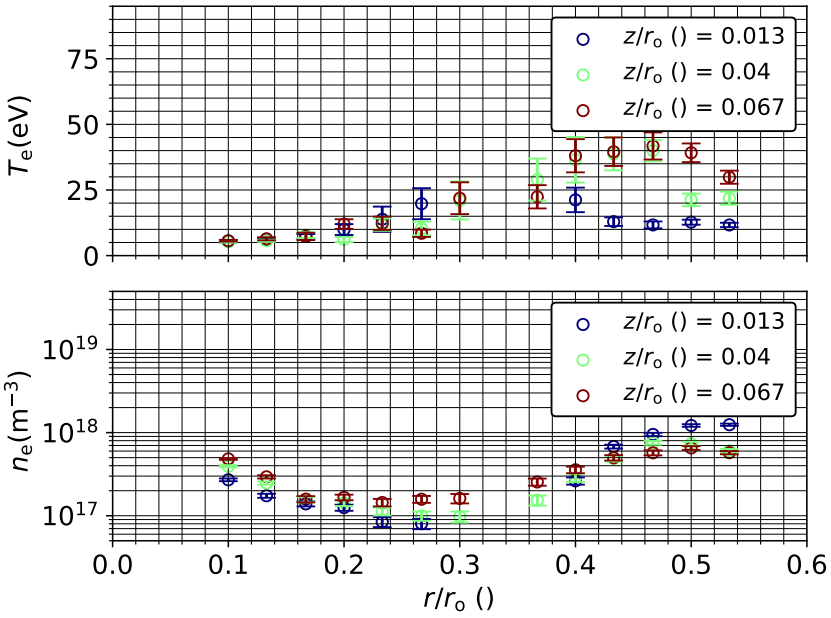

Figure 6.25: Spatially normalized electron temperature and density profiles for the channel and front pole grid.

towards the edge of the channel at distances of r/r_o between 0.36 to 0.5 decreases radially towards the pole, but has less variation axially.

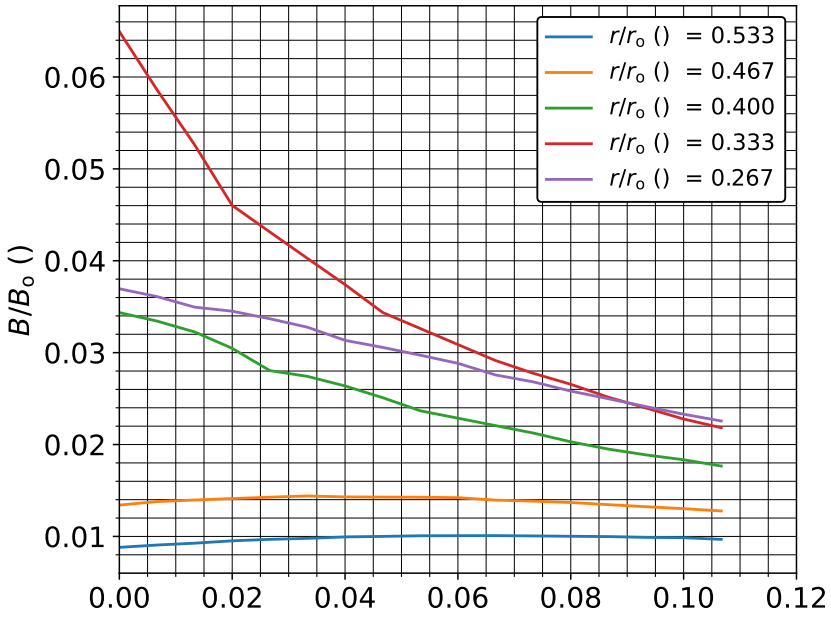

Figure 6.26: Discharge channel centerline normalized magnetic field strength at several radii approaching the front pole region.

Figure 6.26 details the axial profile of the normalized magnetic field strength at several radii. At the discharge channel centerline at a r/r_{o} value of .533, the field strength is about 66% as strong as it is in the front pole region at a r/r_{o} value of .267. The expected increase in magnetic field strength towards the channel edge and into the front pole region suggests a region of highly magnetized electrons in that can quickly thermalize. This is evidenced by the loss in axial sensitivity to to the electron temperature at r/r_{o} values between 0.36 to 0.5.

6.6.3 Discharge Channel and Front Pole Analysis

The electron pressure profiles and a spatial heap map of the channel and front pole grid electron pressure are presented in Figure 6.27 and Figure 6.28.

According to the electron momentum equation, assuming a single ion species denoted by i, and using an isotropic closure for the pressure tensor and a frictional-like collisional model for the viscosity tensor yields

$$m_{\mathrm{e}} n_{\mathrm{e}} [\frac{\partial}{\partial t}(\mathbf{u}_{\mathrm{e}}) + \mathbf{u}_{\mathrm{e}} \cdot \nabla(\mathbf{u}_{\mathrm{e}})] = n_{\mathrm{e}} q_{\mathrm{e}} [\mathbf{E} + \mathbf{u}_{\mathrm{e}} \times \mathbf{B}] - \nabla P_{\mathrm{e}} - \sum_{\mathrm{i}} \nu_{\mathrm{e/i}} m_{\mathrm{e}} m_{\mathrm{e}} (\mathbf{u}_{\mathrm{e}} - \mathbf{u}_{\mathrm{i}}). \quad (6.3)$$

Assuming negligible electron momentum and that the contribution of $\mathbf{u}_{\mathrm{e}} \times \mathbf{B}$ is mostly azimuthal and therefore out of the z, r plane, and rearranging for the electric field vector yields,

$$\mathbf{E} = \frac{1}{n_{\mathrm{e}} q_{\mathrm{e}}} \left[\nabla P_{\mathrm{e}} - \sum_{\mathrm{i}} \nu_{\mathrm{e/i}} m_{\mathrm{e}} m_{\mathrm{e}} (\mathbf{u}_{\mathrm{e}} - \mathbf{u}_{\mathrm{i}}) \right]. \quad (6.4)$$

The inability to accurately model the collisional terms due to anomalous electron mobility in areas of high magnetic field strength, specifically approaching the front pole region, limits our ability to analytically solve for the electric field. However, ignoring collisional term yields

$$\mathbf{E} = \frac{1}{n_{\mathrm{e}} q_{\mathrm{e}}} \nabla P_{\mathrm{e}}. \quad (6.5)$$

In the absence of collisional terms, the trend in the electric field is expected to follow the

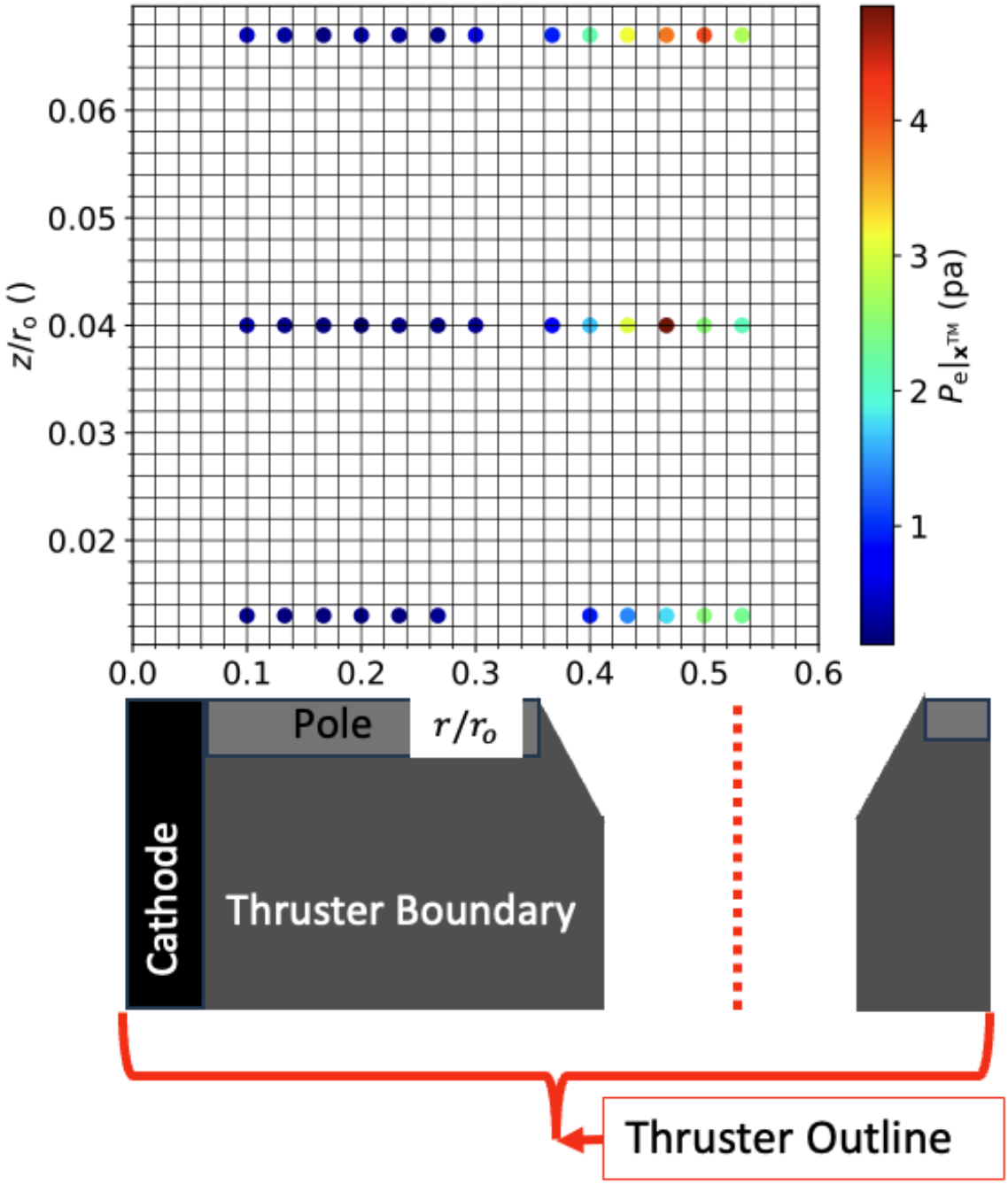

Figure 6.27: Spatial heat map of the channel and front pole grid electron pressure.

trend in the electron pressure. The gradient in electron pressure from the axial centerline at r/r_o of .533 to a minimum between r/r_o of .2 to .3 indicates that accelerated centerline and beam edge ions can be accelerated to the pole given that the acceleration region in this case is located approximately between z/r_o of .08 to .1 according to the axial measurements of

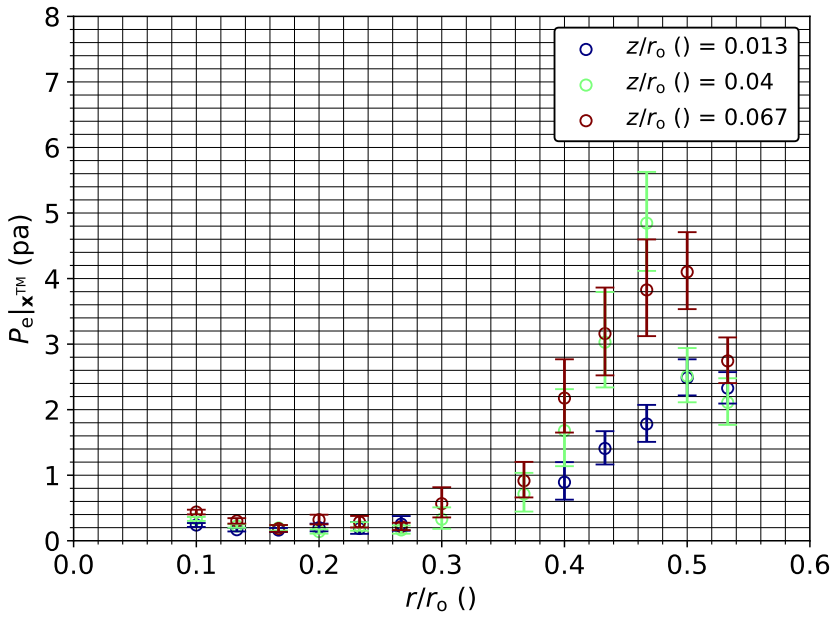

Figure 6.28: Electron pressure profiles in the channel and front pole grid.

the electron temperature and the peak temperatures at this condition [79, 90]. Additionally, the pole region has the lowest electron pressure of the entire region less than z/r_o .08.

6.7 Magnetic Field Line Measurements

6.7.1 Normalized Axial Measurement Locations and Thruster Discharge Telemetry

The measurement locations for this experiment are presented in Figure 6.29. The thruster discharge telemetry is summarized in Figure 6.30 and Figure 6.31. The average facility background pressure during the experiment was 7.05×10^{-6} Torr-Kr $\pm$ 1.76%. The thruster and cathode krypton mass flow rates were 23.5 mg/s and 1.78 mg/s, both with uncertainties of less than 1%. At these flow rates, the thruster discharge voltage and current were 40.23 A $\pm$ 16.4% and 150.79 V $\pm$ 4.2%, respectively. The peak thruster power spectral frequencies were 6.49 kHz $\pm$ 1.68 % and 6.40 kHz $\pm$ 1.76 %, respectively.

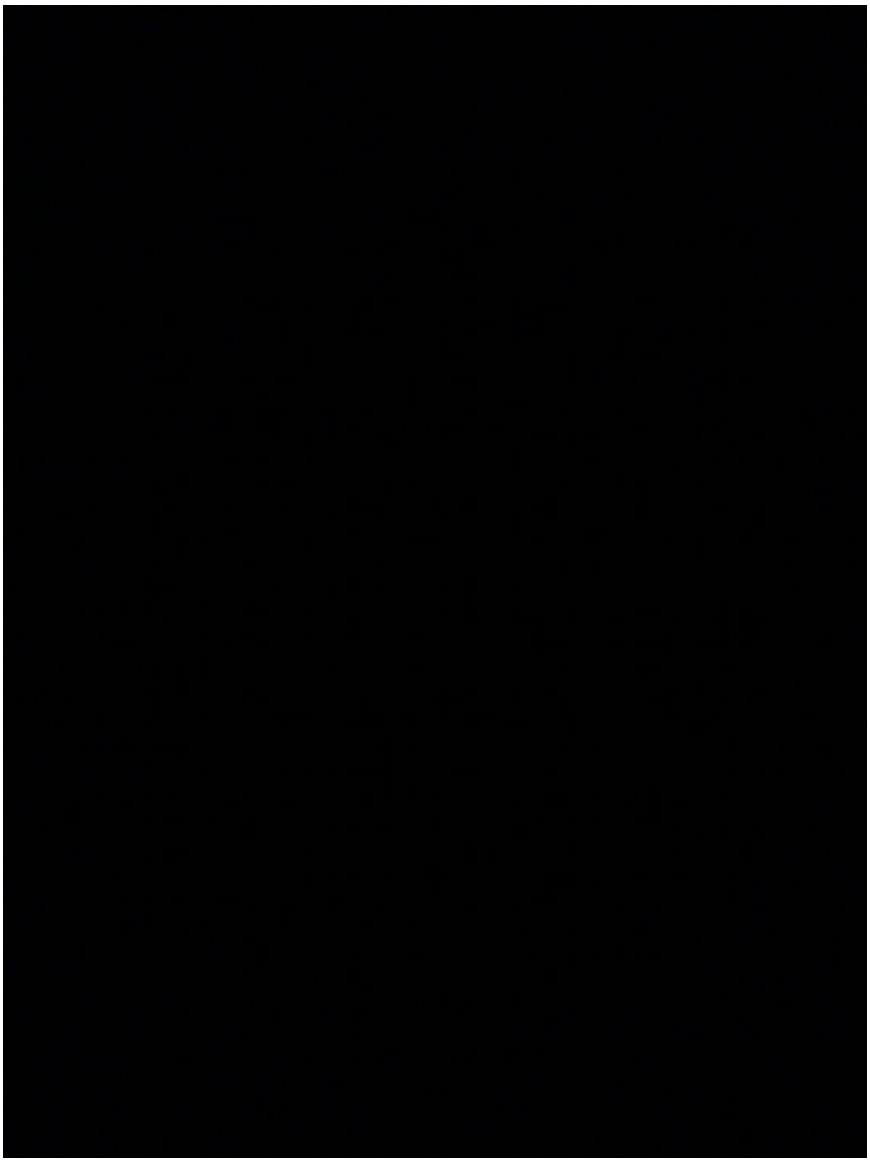

Figure 6.29: Normalized magnetic field line measurement locations in blue. The field lines are numbered one to two from left to right, and the magnetic field line points are numbered one to nine from top to bottom on each respective field line. The thruster boundaries are represented in grey, the front pole cover in light grey, and the cathode keeper body in black.

6.7.2 Electron Temperature and Density Profiles Along Magnetic Field Lines

The electron temperature and density profiles along the first and second magnetic field lines are presented in Figure 6.32.

The electron density along the magnetic field increases as the field line is closer to the discharge channel exit and decreases further away. The electron temperature decreases as

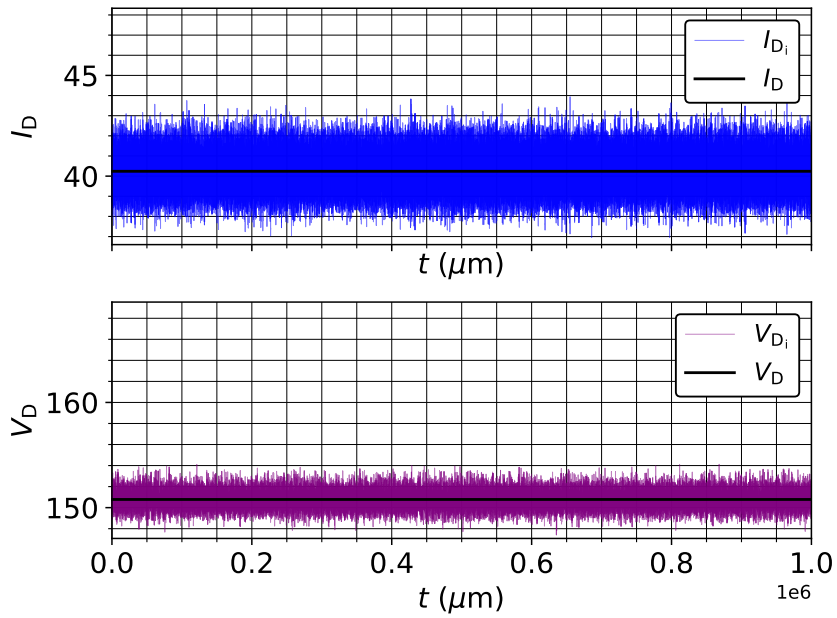

Figure 6.30: Individual and mean thruster discharge telemetry scans.

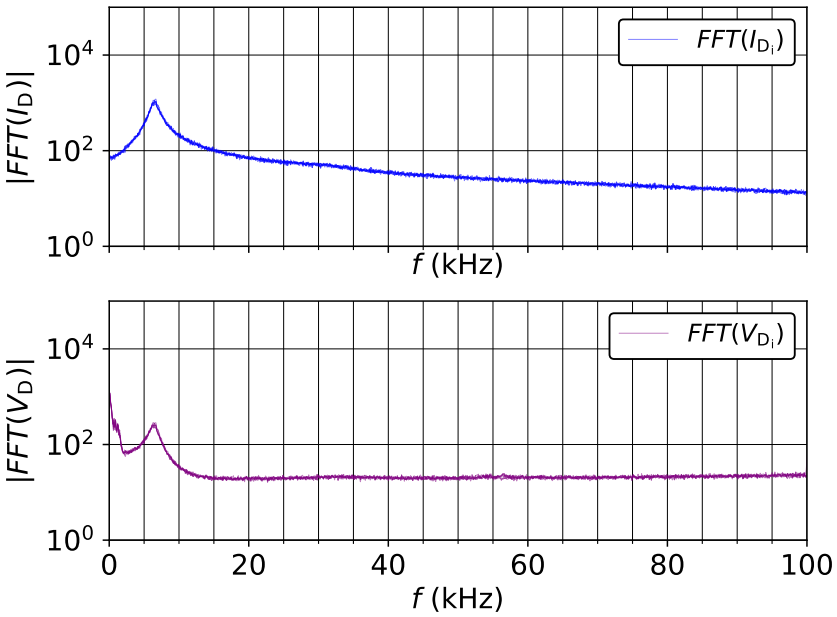

Figure 6.31: Individual thruster discharge telemetry power spectra.

the magnetic field line approaches the discharge channel exit, with higher temperatures being seen towards the inner front pole region as opposed the outer pole region. The sixth point along the second magnetic field line had an artificially low density. This artificially

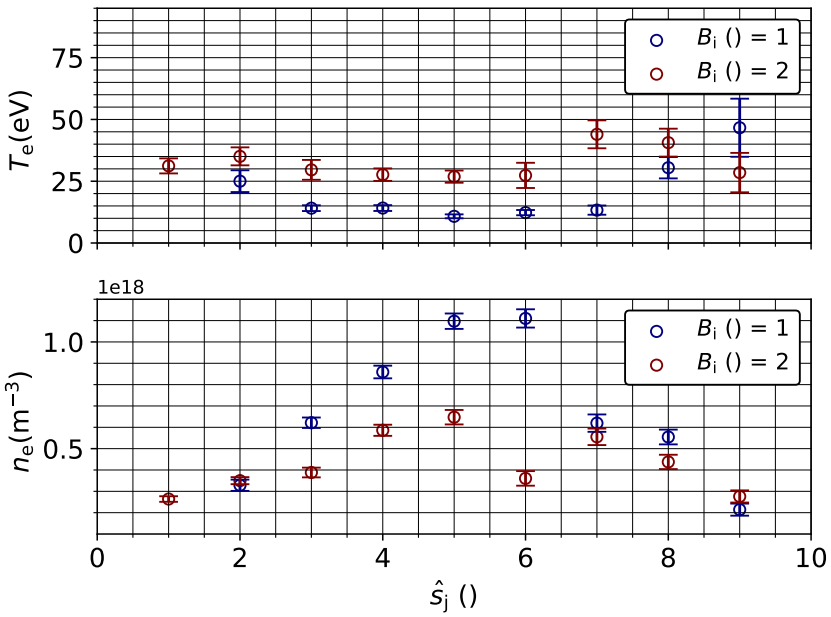

Figure 6.32: Electron temperature and density profiles along the outlined magnetic field lines. The field lines (B_i) are numbered from left to right, and the point along each field line $\hat{s}_j$ are numbered from top to bottom along each field line in Figure 6.29.

low density was due to misalignment during the acquisition of the point even though the system was realigned between acquiring all points. This artificially low density was not observable during the collection of the raw scans. A more robust method for maintaining alignment requires further attention in the next iteration of the system.

6.7.3 Magnetic Field Measurement Analysis

The electron pressure profile the magnetic field lines is presented in Figure 6.33. From the electron momentum equation, in the case of a steady state electrostatic plasma that is collisionless with negligible electron momentum and an isotropic thermalized closure for the pressure tensor, the relationship between the electrostatic potential is given by

$$\nabla\phi = \frac{1}{q_e n_e}\nabla P_e. \tag{6.6}$$

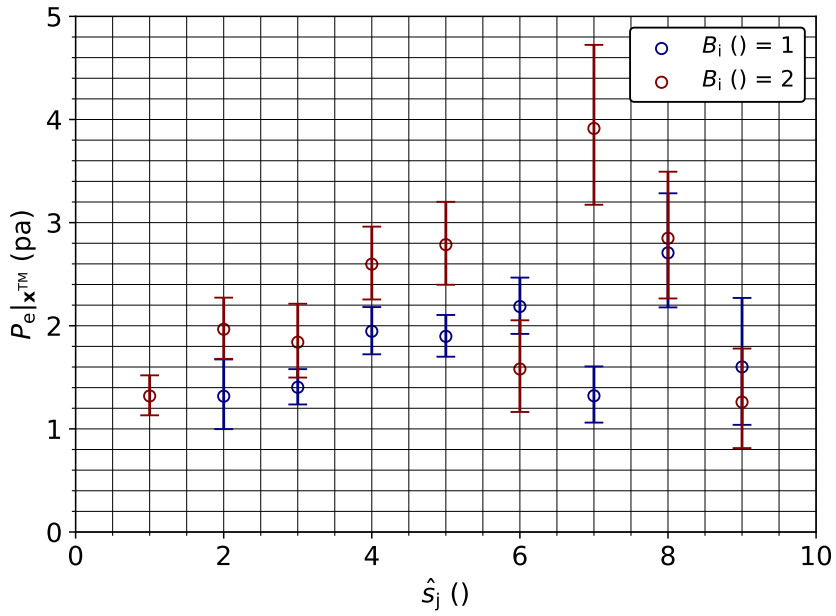

Figure 6.33: Electron pressure along each magnetic field line.

In the case where the temperature along the magnetic field line is constant, the isothermal relationship is recovered [77]. However, the temperature is clearly seen to vary along the magnetic field lines, according to Figure 6.32. This precludes the magnetic field lines from being strictly isothermal and isopotential with respect to the assumptions in the traditional model in [8, 10, 77]. As far back as the work of Morozov in Section 2.2 of [11], the assumption of high mobility along the magnetic field lines has been used to set the along field electron temperaure gradient to zero to recover an isothermal potential. However, the degree to which the gradient of the electron temperature along the magnetic field line can diverge from zero and still be within the limits of validity for an isothermal potential along a magnetic field line has yet to be explored.

Equation 6.6 can admit another solution that is isopotential if the gradient in the electrostatic potential is zero along the magnetic field line. Interpolating between the measured points along the magnetic field line, and calculating the gradient of the electrostatic poten-

tial along each each line according to

$$\frac{d\phi}{d\hat{s}_{\mathrm{j}}} = \frac{1}{q_{\mathrm{e}} n_{\mathrm{e}}} \frac{dP_{\mathrm{e}}}{d\hat{s}_{\mathrm{j}}}. \tag{6.7}$$

yields Figure 6.34.

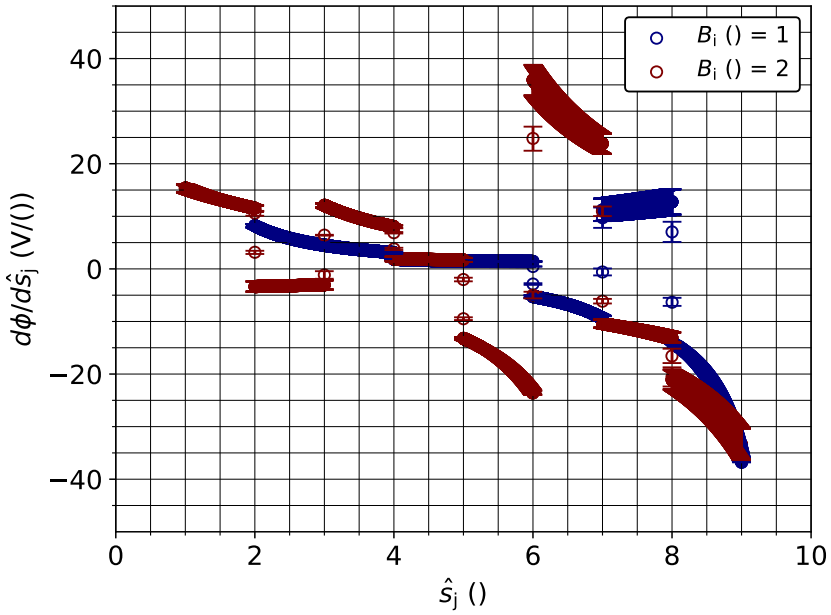

Figure 6.34: Estimated gradient of the electrostatic potential along the each probed magnetic field line.

This non-zero and gradient suggests that the probed field lines cannot be considered isopotential. The gradient in the electrostatic potential in the first field line – in blue – in Figure 6.34 having smaller magnitude between up through point 6 suggests several things. First, because field line 1 is closer to the exit plane and is observed to have a smaller temperature than that of the further field line, that regions where the electron temperature is low like inside of the discharge channel may adhere to the isopotential model or isothermal model more closely than that of the further field lines that approach the acceleration region. It is also observed that the gradient towards and after point 6 on both magnetic field lines increases and converges to similar values. This suggests that as the magnetic field strength increases traversing the channel edge inner pole region, the field lines diverge from the

isothermal and isopotential models more than do towards the channel centerline enar the exit plane.

6.8 Summary

Section 6.2 outlines the experimental setup used to collect the data in this chapter. Modifications to the setup in Chapter 5 were necessary in order to maximize the signal-to-noise ratio and provide the relative movement of the thruster relative to the interrogation beam scattering volume. Section 6.4 outlines the additional preprocessing of the raw signals collected given the broadband linear stray light present from the fluorescence of the surfaces inside of the vacuum chamber during data acquisition that was spatially and collection-acquisition strategy dependent. Section 6.3 outlines the relevant parameters from the Bayesian analysis framework presented in Section 3.7 that was used to process the data in this chapter.

Section 6.5 outlines the axially resolved electron temperature and density measurements along the cathode and discharge channel centerline at 150 V and 40 A discharge. Comparing with a 300 V, 20 A simulation, the comparison suggests that the acceleration zone may be pushed past the peak axial magnetic field point as opposed to before , as indicated by the peak electron temperature in both cases. Additionally, the 300 V, 15 A simulations seem to over predict the number density. Attempts to collect data at 300 V, 15 A yielded no detectable LTS above the detection limit of 1×10^{17} m^{-3}, and attempts to collect data at 300 V and 20 A at the closest probing point yielded a signal that was barely above the detection limit. Data acquired at the closest probed point along the channel centerline as a function of the discharge current keeping the discharge power constant yielded an approximately linear increase in the electron number density with discharge current, and an asymptotically decreasing electron temperature. These datasets and the comparison with the aforementioned simulation highlight the need for a parametric study of the axial profile of the electron temperature and density in order to provide preliminary calibration

data for HET plasma simulations.

Section 6.6 outlines the axially and radially resolved measurements of the electron temperature and density between the cathode centerline and the thruster discharge channel centerline, including the area immediately ahead of the inner front pole cover. Calculations of the electron pressure indicate that it reaches a minimum at the inner front pole. Simplifying assumptions on the electron momentum equation and using the electron pressure gradient indicated by a spatially resolved heat map as a proxy for the gradient in the electrostatic potential. Limitations in calculating the electrostatic potential from the gradient in the electron pressure are due to the inability to account for the collisional terms in the electron momentum equation due to anomalous electron mobility in regions of increasing magnetic field strength towards the inner front pole. However, this proxy indicates that ions can indeed be accelerated towards the pole ahead of the acceleration zone, taken to be the area with the peak electron temperature. This is consistent with LIF ion velocity measurements that indicate that ions from the beam edge and the core beam region that were accelerated in the core beam can be accelerated to the pole.

Section 6.7 outlines electron temperature and density measurements taken along two distinct magnetic field lines. These measurements indicate that the temperature along the magnetic field lines is not constant, suggesting that the isothermal model in the discharge region of magnetically shielded, and specifically high current, HETs may need to be revisited in order to accurately account for the variation in the electron temperature along the field lines. Previous work on the applicability of this model suggested that curvature affects the applicability of the model [64]. The region traversed by the field line, as well as the curvature of the field line, are found to play a role in the deviation from isothermalized magnetic field lines, given that the electron temperature and density are found to vary radially even at constant axial location, and vice versa, as seen in Section 6.6. However, it is possible to maintain a constant potential in accordance with the general assumptions of the isothermal model before the assumption of isothermality is in place. A calculation

of the electrostatic potential gradient in magnetic field line coordinates in one dimension indicates a non-zero gradient in the electrostatic potential. This indicates that, in the probed architecture, the magnetic field lines can not be considered strictly isothermal or isopotential. Additionally, the lines are observed to deviate from the isothermal and isopotential models closer to areas of increased magnetic field strength towards the acceleration region and the channel edge.

CHAPTER 7
CONCLUSIONS, CONTRIBUTIONS, AND FUTURE WORK

7.1 Conclusions and Contributions

The overall goal of this thesis was to probe the electron properties in the near field plume of a MS HET using LTS to provide insight into the plasma structure in the near-field plume of an MS HET. Probing the plasma structure in this region provided insight into the applicability of the isothermal magnetic field line model, and provided a notional description of the electron-property-predicted plasma structure traversing the front pole region from the discharge to cathode centerline. This investigation allowed us to answer the questions presented in Section 1.3. To this end, this thesis provides the following contributions:

1. Implementation of a Bayesian analysis and model selection framework for LRS-calibrated LTS diagnostics.

2. Detailed design and implementation of a discharge plasma cell and LTS system for near plasma boundary and laser plasma and laser neutral interactions.

3. Detailed design and implementation of a large vacuum test facility LTS system for measurements in live EP devices benchmarked on a hollow cathode.

4. Detailed upgrade to the large vacuum test facility LTS system for measurements in the near field discharge of a high current density MS HET. Specifically, axially resolved electron property measurements along the discharge channel centerline, spatially resolved method traversing the front pole region from the channel centerline to the cathode centerline, and measurements along two distinct magnetic field lines.

The first contribution is detailed in Chapter 3 and Reference [174]. The implementation of the Bayesian analysis and model selection framework was used to quantify the SNR lim-

its for accurate model selection between Druyvesteyn and Maxwellian plasma submodels. Additionally, a comparison between the estimated posterior from the Laplace approximation using least-squares inversion and a fully sampled posterior using MCMC shows that, at sufficiently high SNR, the Laplace approximation of the posterior is a conservative estimate. However, at SNRs expected in the plume of HETs, fully sampling the posterior provides the conservative approach to estimating the uncertainty and correlations in the variables of interest. This chapter contributes verifiable model equations and a probability model that can be used in low SNR environments to accurately quantify the uncertainty in LTS quantity of interest measurements.

The second contribution is detailed in Chapter 4. This chapter contributes the sizing and implementation of a stainless-steel vacuum cell for generating steady state and pulsed DC discharge plasmas. Then, the chapter contributes the sizing and implementation of the LTS system that straddles the vacuum cell for plasma property measurements is detailed. This cell was used to quantify a notional detection before attempting the large vacuum test facility implementation, and was used to study the variation in plasma properties between discharge electrodes in a pulsed argon plasma as the plasma boundaries are approached. Analysis is detailed in [175]. This contribution provides a well documented plasma cell and LTS system that can be modified and implemented quickly wherever groups have the desire to study electron properties near and in plasma boundaries like presheaths and sheaths. From Chapter 3 and Chapter 4, implementing and testing the LRS and LTS models and comparing to others in the EP literature, we can conclude that a well-documented reference of the models used in EP-relevant LTS systems based on a common test-set of data will help standardize processing and interpretation across groups.

The third contribution is detailed in Chapter 5. The optical system from the Chapter 4 is modified to straddle the large vacuum test facility VTF-2 facility at Georgia Tech HPEPL. The system is tested by measuring the axial electron property distribution in the near field krypton plume of a lanthanum hexaboride hollow cathode operating with an external anode

along the cathode centerline and one off-centerline radial location. Comparing to similar experiments in the literature, we concluded that the relative position and geometry of the external anode with respect to the cathode requires some standardization across research groups in order to better interpret and compare results.

The final contributions are outlined in Chapter 6. Modifications to the interrogation beam optical axis and the collection acquisition strategy are outlined. This, coupled with Chapter 5 contribute one of the first detailed and, modifiable, and repeatable large vacuum test facility LTS systems in the literature to date. Then, the data acquired along the cathode discharge channel centerline are discussed. We concluded that over prediction of the electron density in lower current density thruster simulations motivate the need for parametric studies of the electron properties along the thruster channel centerline for simulation calibration. Additionally, the location of the peak electron temperature suggests that higher current density conditions may see an axial shift outwards of the acceleration region. This contributes axially resolved electron properties in locations that are important for plasma simulation verification and calibration.

Following that, the spatially and axially resolved data traversing the front pole is discussed. We conclude that this data, to within the limitation of the analysis discussed in the section, agrees with LIF ion velocity measurements indicating that unaccelerated ions from the core channel plasma and beam edges can be accelerated to the pole. This contributes some of the first-ever measurements and analysis traversing regions with a minimally invasive diagnostic that are critical to understanding the life limiting phenomena in MS HETs – pole erosion. This, coupled with the possible acceleration region shifts, may be reason to conclude that higher current density architecture MS HETs may suffer from higher pole erosion rates. However, this will require investigations to confirm.

Finally, measurements along two distinct magnetic field lines indicate that the magnetic field lines in the discharge channel at the probed thruster discharge condition are not strictly isothermal or isopotential. We conclude that these deviations are due to both the concavity

of the magnetic field lines and the relative increase in strength along the magnetic field line. This conclusion motivates the need to revisit models used in these simulations. Additionally, this provides an avenue for basic studies of magnetized plasmas with increasingly complex magnetic field topologies. This contributes the first-ever measurements along two distinct magnetic field lines using LTS.

7.2 Implications and Future Work

7.2.1 Implications

The work in this thesis provided some first-insights into regions that have been difficult to probe with confidence using traditional measurement techniques in the EP community due to advancement in laser-based diagnostics. This provides an avenue for future minimally invasive work that can help contribute to the understanding of the near field plasma environment from the perspective of the electrons. Given that electrons are much more mobile than ions due to their mass difference, it is expected that electrons play a governing role in the plasma dynamics in HETs. Well documented LTS systems, like the ones presented in this work, that are repeatable will allow for measurements, like the ones made in this work to become more common. This will allow for the contribution of data for calibration of simulations and validation of models for unknown terms in physics-based closures in simulations. This will contribute to the predictive design of HETs through simulations that are ever-more reliable given updated understanding of the electron contributions to the plasma. For regions that have phenomena of interest that contribute to the life-limiting factors of HETs, like the front pole region, measurements like the ones made in this thesis will help understand these life limiting mechanisms and predict their long-term effect on HETs more accurately. This will in turn minimize the design and testing efforts for HETs. The work in this thesis provides first steps towards these items. Within the larger world of magnetized plasmas, these minimally invasive measurements will allow for more accurate understanding of fundamental phenomena that plague all magnetized plasmas, from HETs

to Tokamaks. This includes mobility across and along magnetic field lines.

7.2.2 Future Work

LRS calibrated LTS diagnostics have recently been demonstrated across two large vacuum test facilities to provide data that can be used for accurate, minimally invasive estimates of the electron properties in the near field plume of HETs. This work is summarized in this thesis, and other works to include [172, 173] and other studies in progress. The work presented in this thesis, and the SNR limitations given the equipment represent the maximum SNR that can be extracted with the current detector. Future work will include modifications to the scattering geometry from perpendicular to a forward scattering configuration, additional filters, and an upgraded electron multiplying version of the detector used in this work can increase SNR and decrease the detection limit by at least an order of magnitude. This will allow for probing of the HET plume at more nominal conditions. The limitations on the thruster discharge conditions was the SNR required to probe the desired locations.

With respect to this work, a repeat of the axial study presented at the nominal 6 kW, 300 V, 20 A condition would provide insight into the shift in the acceleration region as a function of current density. A parametric study of the axial electron properties at constant power with varying current density and at constant voltage with varying current density will provide the preliminary data necessary to compare measured properties with plasma simulations more accurately. Traversing the magnetic field lines at the nominal HET conditions would determine if the isothermality of the magnetic field line is discharge condition dependent. Traversing the front pole region at different discharge conditions would provide insight into the discharge condition dependence on the acceleration of ions to the pole from the channel core and edge regions.

Beyond, measuring along the magnetic field lines as they approach the highest magnetic field intensity from the channel and from the front pole region may aid in anomalous electron mobility models in this region. Additionally, the affect of electrical boundary

conditions on the studies performed here will provide insight how the relative biasing and conductive pathways of the thruster surfaces affect phenomena of interest like electron mobility and pole erosion.

REFERENCES

[1] S. Dusuhman and J. M. Lafferty, "Scientific Foundations of Vacuum Technique," in vol. 4, John Wiley & Sons, Jan. 1958, ISBN: 0471228036.

[2] C. M. Penney, R. L. St. Peters, and M. Lapp, "Absolute rotational Raman cross sections for N2, O2, and CO2," *Journal of the Optical Society of America (1930)*, vol. 64, no. 5, p. 712, 1974.

[3] W. G. Vincenti, C. H. Kruger, and T. Teichmann, " Introduction to Physical Gas Dynamics," in 10, vol. 19, Krieger Pub Co, Jan. 1975, ISBN: 0882753096.

[4] A. E. Siegman, "Lasers," in 1st ed., vol. 1, University Science Books, Oct. 1986, pp. 858–890, ISBN: 978-0935702118.

[5] H. Amemiya, "Sheath Formation Criterion and Ion Flux for Non-Maxwellian Plasma," *Journal of the Physical Society of Japan*, vol. 66, no. 5, pp. 1335–1338, May 1997.

[6] T. Hori, M. Kogano, M. D. Bowden, K. Uchino, and K. Muraoka, "A study of electron energy distributions in an inductively coupled plasma by laser Thomson scattering," *Journal of Applied Physics*, vol. 83, no. 4, pp. 1909–1916, 1998.

[7] J. D. Jackson, "Classical Electrodynamics," in 3rd ed., Wiley, Aug. 1998, pp. 661–698, ISBN: 9780471309321.

[8] V. Kim, "Main Physical Features and Processes Determining the Performance of Stationary Plasma Thrusters," *Journal of Propulsion and Power*, vol. 14, no. 5, pp. 736–743, 1998.

[9] M. D. Bowden, Y. Goto, T. Hori, K. Uchino, K. Muraoka, and M. Noguchi, "Detection Limit of Laser Thomson Scattering for Low Density Discharge Plasmas," *Japanese Journal of Applied Physics*, vol. 38, no. Part 1, No. 6A, pp. 3723–3730, 1999.

[10] V. V. Zhurin, H. R. Kaufman, and R. S. Robinson, "Physics of closed drift thrusters," *Plasma sources science & technology*, vol. 8, no. 1, R1–R20, 1999.

[11] A. I. Morozov and V. V. Savelyev, "Fundamentals of Stationary Plasma Thruster Theory," in *Reviews of Plasma Physics*, 2000, pp. 203–391, ISBN: 978-1-4615-4309-1.

[12] D. W. Ball, "The Basics of Spectroscopy," in SPIE, Jan. 2001, pp. 91–104, ISBN: 9780819441041.

[13] E. Y. Choueiri, "Fundamental difference between the two Hall thruster variants," *Physics of plasmas*, vol. 8, no. 11, pp. 5025–5033, 2001.

[14] J. M. Haas and A. D. Gallimore, "Internal plasma potential profiles in a laboratory-model Hall thruster," *Physics of Plasmas*, vol. 8, no. 2, 2001.

[15] J. M. Haas, "Low-perturbation Interrogation of the Internal and Near-field Plasma Structure of a Hall Thruster Using a High Speed Probe Positioning System," Ph.D. dissertation, University of Michigan, Ann Arbor, 2001.

[16] J. M. Haas and A. D. Gallimore, "nternal plasma potential profiles in a laboratory-model Hall thruster," *Physics of Plasmas*, vol. 8, no. 2, pp. 652–660, Feb. 2001.

[17] R. B. Miles, W. R. Lempert, and J. N. Forkey, "Laser rayleigh scattering," *Measurement Science and Technology*, vol. 12, no. 5, R33, 2001.

[18] H. Sugai *et al.*, "Electron energy distribution functions and the influence on fluorocarbon plasma chemistry," *Plasma Sources Science and Technology*, vol. 10, no. 2, pp. 378–385, May 2001.

[19] G. J. Hagelaar, J. Bareilles, L. Garrigues, and J. P. Boeuf, "Two-dimensional model of a stationary plasma thruster," *Journal of Applied Physics*, vol. 91, no. 9, 2002.

[20] D. A. Long, "Classical Theory of Rayleigh and Raman Scattering," in *The Raman Effect: A Unified Treatment of the Theory of Raman Scattering by Molecules*, Wiley, 2002, pp. 31–48, ISBN: 978-0-471-49028-9.

[21] Y. Raitses, M. Keidar, D. Staack, and N. J. Fisch, "Effects of segmented electrode in Hall current plasma thrusters," *Journal of Applied Physics*, vol. 92, no. 9, 2002.

[22] G. A. F. Seber and C. J. Wild, "Nonlinear Regression," in 63, vol. 62, Wiley, Feb. 2003, ch. 2, pp. 21–30, ISBN: 9780471725312.

[23] R. Fischer and A. Dinklage, "Integrated data analysis of fusion diagnostics by means of the Bayesian probability theory," *Review of Scientific Instruments*, vol. 75, no. 10, pp. 4237–4239, 2004.

[24] R. R. Hofer, "Development and Characterization of High-Efficiency, High-Specific Impulse Xenon Hall Thrusters," Ph.D. dissertation, University of Michigan, Ann Arbor, 2004.

[25] J. M. Hollas, "Modern Spectroscopy," in 4th ed., Wiley, Jan. 2004, pp. 103–135, ISBN: 978-0470844168.

[26] M. Keidar, A. D. Gallimore, Y. Raitses, and I. D. Boyd, "On the potential distribution in hall thrusters," *Applied Physics Letters*, vol. 85, no. 13, 2004.

[27] H. J. van der Meiden *et al.*, "10 kHz repetitive high-resolution TV Thomson scattering on TEXTOR," *Review of Scientific Instruments*, vol. 75, no. 10, pp. 3849–3851, 2004.

[28] M. J. van de Sande, "Laser scattering on low-temperature plasmas: High resolution and stray light rejection," Ph.D. dissertation, Eindhoven Technical University, 2004.

[29] B. Beal, A. Gallimore, and W. Hargus, "The Effects of Cathode Configuration on Hall Thruster Cluster Plume Properties," in *41st AIAA/ASME/SAE/ASEE Joint Propulsion Conference & Exhibit*, Reston, Virigina: American Institute of Aeronautics and Astronautics, Jul. 2005, ISBN: 978-1-62410-063-5.

[30] D. J. Griffiths, "Introduction to Electrodynamics," in Pearson Prentice Hall, Jan. 2005, ISBN: 978-8178087375.

[31] S. A. Van De Geer, "Estimation," in *Encyclopedia of statistics in behavioral science*, vol. 2, John Wiley & Sons, Ltd Chichester, UK, Jan. 2005, pp. 549–553, ISBN: 978-0-470-86080-9.

[32] P. M. Bellan, "Fundamentals of Plasma Physics," in Cambridge University Press, Jun. 2006, ISBN: 9780511807183.

[33] R. G. Jahn, "Physics of Electric Propulsion," in Dover Publications, May 2006, pp. 1–50, ISBN: 978-0486450407.

[34] B. Pote, V. Hruby, and R. Tedrake, "Performance of a multi-kilowatt non-circular discharge Hall thruster," in *36th AIAA/ASME/SAE/ASEE Joint Propulsion Conference and Exhibit*, 2006, p. 3249.

[35] J. Wolberg, "Data Analysis Using the Method of Least Squares: Extracting the Most Information from Experiments," in Springer, Feb. 2006, ch. 2, pp. 31–71, ISBN: 978-3-540-31720-3.

[36] S. Y.-M. Cheng, "Modeling of Hall thruster lifetime and erosion mechanisms," Ph.D. dissertation, Massachusetts Institute of Technology, 2007.

[37] J. C. Adam *et al.*, "Physics, simulation and diagnostics of Hall effect thrusters," *Plasma Physics and Controlled Fusion*, vol. 50, no. 12, 2008.

[38] D. M. Goebel and I. Katz, *Fundamentals of Electric Propulsion: Ion and Hall Thrusters*. Wiley, 2008.

[39] B. P. LeBlanc, "Thomson scattering density calibration by Rayleigh and rotational Raman scattering on NSTX," *Review of Scientific Instruments*, vol. 79, no. 10, 10E737, 2008.

[40] R. B. Lobbia and A. D. Gallimore, "Two-dimensional time-resolved breathing mode plasma fluctuation variation with Hall thruster discharge settings," in *31st International Electric Propulsion Conference*, Ann Arbor: Electric Rocket Propulsion Society, Sep. 2009.

[41] I. G. Mikellides, I. Katz, R. R. Hofer, and D. M. Goebel, "Hall-Effect Thruster Simulations with 2-D Electron Transport and Hydrodynamic Ions," *University of Michigan, Ann Arbor, MI*, no. c, 2009.

[42] A. V. Nedospasov, "On the estimation by Kadomtsev of coefficients of turbulent transport in magnetized plasma," *Physics of plasmas*, vol. 16, no. 6, p. 60 501, 2009.

[43] K. N. Gabet, N. Jiang, W. R. Lempert, and J. A. Sutton, "Demonstration of high-speed 1D Raman scattering line imaging," *Applied Physics B*, vol. 101, no. 1, pp. 1–5, 2010.

[44] A. Glebov *et al.*, "Novel volume Bragg grating notch filters for ultralow-frequency Raman measurements," *Third EOS Annual Meeting*, 2010.

[45] R. B. Lobbia, "A time-resolved investigation of the Hall thruster breathing mode," Ph.D. dissertation, 2010.

[46] J. B. Boffard, R. O. Jung, C. C. Lin, L. E. Aneskavich, and A. E. Wendt, "Optical diagnostics for characterization of electron energy distributions: argon inductively coupled plasmas," *Plasma Sources Science and Technology*, vol. 20, no. 5, p. 055 006, Oct. 2011.

[47] D. H. Froula, S. H. Glenzer, N. C. Luhmann, and J. Sheffield, "Scattered Power Spectrum," in *Plasma Scattering of Electromagnetic Radiation*, Elsevier, 2011, pp. 31–44.

[48] A. W. Kieckhafer and M. L. R. Walker, "Recirculating Liquid Nitrogen System for Operation of Cryogenic Pumps," in *32nd International Electric Propulsion Conference*, Wiesbaden, Germany: Electric Rocket Propulsion Society, Sep. 2011.

[49] J. M. P. Linares, E. A. D. Carbone, S. Hübner, A. F. H. van Gessel, and J. van der Mullen, "Laser scattering techniques applied to cold atmospheric plasmas: trends and pitfalls," in *15th International Symposium on Laser Aided Plasma Diagnostics (LAPD15), Jeju, Korea*, 2011, G2.

[50] M. Martínez-Sánchez and E. Ahedo, "Magnetic mirror effects on a collisionless plasma in a convergent geometry," *Physics of Plasmas*, vol. 18, no. 3, 2011.

[51] I. G. Mikellides, I. Katz, and R. R. Hofer, "Design of a laboratory hall thruster with magnetically shielded channel walls, phase I: Numerical simulations," in *47th AIAA/ASME/SAE/ASEE Joint Propulsion Conference and Exhibit 2011*, 2011.

[52] I. G. Mikellides, I. Katz, R. R. Hofer, D. M. Goebel, K. De Grys, and A. Mathers, "Magnetic shielding of the channel walls in a Hall plasma accelerator," *Physics of Plasmas*, vol. 18, no. 3, 2011.

[53] E. A. D. Carbone *et al.*, "Discrepancies between different electron temperature methods: probing the electron energy distribution function," in *21st Europhysics Conference on the Atomic and Molecular Physics of Ionized Gases (ESCAMPIG XXI), July 10-14, 2012, Viana do Castelo, Portugal*, 2012, pp. 1–2.

[54] N. Friel and J. Wyse, "Estimating The Evidence – A Review," *Statistica Neerlandica*, vol. 66, no. 3, pp. 288–308, Aug. 2012.

[55] A. L. Glebov, O. Mokhun, A. Rapaport, S. Vergnole, V. Smirnov, and L. B. Glebov, "Volume Bragg gratings as ultra-narrow and multiband optical filters," H. Thienpont, J. Mohr, H. Zappe, and H. Nakajima, Eds., Jun. 2012, p. 84280C.

[56] A. A. Haji Abolhassani and J.-P. Matte, "Multi-temperature representation of electron velocity distribution functions. I. Fits to numerical results," *Physics of Plasmas*, vol. 19, no. 10, p. 102 103, Oct. 2012.

[57] R. R. Hofer, D. M. Goebel, I. G. Mikellides, and I. Katz, "Design of a laboratory Hall thruster with magnetically shielded channel walls, Phase II: Experiments," in *48th AIAA/ASME/SAE/ASEE Joint Propulsion Conference and Exhibit 2012*, 2012.

[58] J. B. Marion and M. A. Heald, "Classical Electromagnetic Radiation," in Dover Publications, Nov. 2012, ch. 10, pp. 335–370, ISBN: 9780486490601.

[59] I. G. Mikellides, I. Katz, R. R. Hofer, and D. M. Goebel, "Design of a laboratory hall thruster with magnetically shielded channel walls, phase III: Comparison of theory with experiment," in *48th AIAA/ASME/SAE/ASEE Joint Propulsion Conference and Exhibit 2012*, 2012.

[60] I. G. Mikellides and I. Katz, "Numerical simulations of Hall-effect plasma accelerators on a magnetic-field-aligned mesh," *Physical Review E - Statistical, Nonlinear, and Soft Matter Physics*, vol. 86, no. 4, 2012.

[61] R. Washeleski, E. Meyer, and L. King, "Laser Thomson Scattering Measurements of Electron Temperature and Density in the Near-Field Plume of a Hall-Effect

Thruster," in *48th AIAA/ASME/SAE/ASEE Joint Propulsion Conference & Exhibit*, 2012, p. 4118.

[62] N. Yamamoto, K. Tomita, K. Sugita, T. Kurita, H. Nakashima, and K. Uchino, "Measurement of xenon plasma properties in an ion thruster using laser Thomson scattering technique," *Review of Scientific Instruments*, vol. 83, no. 7, p. 73 106, 2012.

[63] A. Gelman, J. B. B. Carlin, H. S. S. Stern, and D. B. B. Rubin, "Bayesian Data Analysis," in 3rd ed., Chapman and Hall/CRC, Nov. 2013, ISBN: 978-1439840955.

[64] J. Geng, L. Brieda, L. Rose, and M. Keidar, "On applicability of the "thermalized potential" solver in simulations of the plasma flow in Hall thrusters," *Journal of Applied Physics*, vol. 114, no. 10, 2013.

[65] R. R. Hofer, B. A. Jorns, J. E. Polk, I. G. Mikellides, and J. S. Snyder, "Wear test of a magnetically shielded Hall thruster at 3000 seconds specific impulse," in *33rd International Electric Propulsion Conference*, Washington D.C.: Electric Rocket Propulsion Society, Oct. 2013.

[66] I. G. Mikellides, I. Katz, R. R. Hofer, and D. M. Goebel, "Magnetic shielding of walls from the unmagnetized ion beam in a Hall thruster," *Applied Physics Letters*, vol. 102, no. 2, 2013.

[67] S. Tsikata, C. Honore, and D. Gresillon, "Collective Thomson scattering for studying plasma instabilities in electric thrusters," *Journal of Instrumentation*, vol. 8, no. 10, p. C10012, 2013.

[68] J. Vaudolon, L. Balika, and S. Mazouffre, "Photon counting technique applied to time-resolved laser-induced fluorescence measurements on a stabilized discharge," *Review of Scientific Instruments*, vol. 84, no. 7, p. 73 512, 2013.

[69] R. L. Washeleski, t. E. J. Meyer, and L. B. King, "Application of maximum likelihood methods to laser Thomson scattering measurements of low density plasmas," *Review of Scientific Instruments*, vol. 84, no. 10, p. 105 101, 2013.

[70] N. Wilvert, S. Joshi, and A. Yalin, "Ultraviolet laser plasma preionization and novel thomson scattering method for weakly ionized discharges," in *51st AIAA Aerospace Sciences Meeting including the New Horizons Forum and Aerospace Exposition*, 2013, p. 205.

[71] D. M. Goebel, B. A. Jorns, R. R. Hofer, I. G. Mikellides, and I. Katz, "Pole-piece interactions with the plasma in a magnetically shielded hall thruster," in *50th AIAA/ASME/SAE/ASEE Joint Propulsion Conference 2014*, 2014.

[72] S. J. Hall *et al.*, "Implementation and Initial Validation of a 100-kW Class Nested-channel Hall Thruster," in *50th AIAA/ASME/SAE/ASEE Joint Propulsion Conference*, Reston, Virginia: American Institute of Aeronautics and Astronautics, Jul. 2014.

[73] R. R. Hofer, D. M. Goebel, I. G. Mikellides, and I. Katz, "Magnetic shielding of a laboratory Hall thruster. II. Experiments," *Journal of Applied Physics*, vol. 115, no. 4, 2014.

[74] S. Hübner, J. S. Sousa, V. Puech, G. M. W. Kroesen, and N. Sadeghi, "Electron properties in an atmospheric helium plasma jet determined by Thomson scattering," *Journal of Physics D: Applied Physics*, vol. 47, no. 43, pp. 432 001–1, 2014.

[75] B. A. Jorns and R. R. Hofer, "Plasma oscillations in a 6-kW magnetically shielded Hall thruster," *Physics of plasmas*, vol. 21, no. 5, p. 53 512, 2014.

[76] R. A. Martinez, H. Dao, and M. L. R. Walker, "Power Deposition into the Discharge Channel of a Hall Effect Thruster," *Journal of Propulsion and Power*, vol. 30, no. 1, pp. 209–220, Jan. 2014.

[77] I. G. Mikellides, R. R. Hofer, I. Katz, and D. M. Goebel, "Magnetic shielding of Hall thrusters at high discharge voltages," *Journal of Applied Physics*, vol. 116, no. 5, 2014.

[78] I. G. Mikellides, I. Katz, R. R. Hofer, and D. M. Goebel, "Magnetic shielding of a laboratory Hall thruster. I. Theory and validation," *Journal of Applied Physics*, vol. 115, no. 4, 2014.

[79] I. G. Mikellides and A. L. Ortega, "Assessment of pole erosion in a magnetically shielded hall thruster," in *50th AIAA/ASME/SAE/ASEE Joint Propulsion Conference 2014*, 2014.

[80] F. Brehmer, S. Welzel, B. L. M. Klarenaar, H. J. van der Meiden, M. C. M. van de Sanden, and R. Engeln, "Gas temperature in transient CO ₂ plasma measured by Raman scattering," *Journal of Physics D: Applied Physics*, vol. 48, no. 15, p. 155 201, Apr. 2015.

[81] F. Chen, "Introduction to Plasma Physics and Controlled Fusion," in 3rd ed., Springer Publications, Dec. 2015, ISBN: 978-3-319-22309-4.

[82] A. L. Fabris, C. V. Young, and M. A. Cappelli, "Time-resolved laser-induced fluorescence measurement of ion and neutral dynamics in a Hall thruster during ionization oscillations," *Journal of Applied Physics*, vol. 118, no. 23, p. 233 301, 2015.

[83] C. E. Garner, M. D. Rayman, and J. R. Brophy, "In-flight operation of the Dawn ion propulsion system-arrival at Ceres," in *34th International Electric Propulsion Conference*, vol. 5, Kobe, Japan: Electric Rocket Propulsion Society, Jul. 2015.

[84] D. M. Goebel and J. E. Polk, "Lanthanum hexaboride hollow cathode for the asteroid redirect robotic mission 12.5 kW Hall thruster," in *Joint 30th ISTS, 34th IEPC and 6th NSAT Conf., Hyogo-Kobe, Japan, 4–10 July 2015*, Electric Rocket Propulsion Society, 2015.

[85] B. L. M. Klarenaar, F. Brehmer, S. Welzel, H. J. van der Meiden, M. C. M. van de Sanden, and R. Engeln, "Note: Rotational Raman scattering on CO2 plasma using a volume Bragg grating as a notch filter," *Review of Scientific Instruments*, vol. 86, no. 4, Apr. 2015.

[86] S. J. Langendorf, "Effects of Electron Emission on Plasma Sheaths," Ph.D. dissertation, Georgia Institute of Technology, Atlanta, 2015.

[87] I. G. Mikellides, D. M. Goebel, B. A. Jorns, J. E. Polk, and P. Guerrero, "Numerical simulations of the partially ionized gas in a 100-A LaB6 hollow cathode," *IEEE Transactions on Plasma Science*, vol. 43, no. 1, Jun. 2015.

[88] L. Grimaud, A. Pétin, J. Vaudolon, and S. Mazouffre, "Perturbations induced by electrostatic probe in the discharge of Hall thrusters," *Review of Scientific Instruments*, vol. 87, no. 4, 2016.

[89] W. Huang, H. Kamhawi, and T. Haag, "Plasma Oscillation Characterization of NASA's HERMeS Hall Thruster via High Speed Imaging," in *52nd AIAA/SAE/ASEE Joint Propulsion Conference*, Reston, Virginia: American Institute of Aeronautics and Astronautics, Jul. 2016, ISBN: 978-1-62410-406-0.

[90] B. A. Jorns *et al.*, "Mechanisms for pole piece erosion in a 6-kW magnetically-shielded hall thruster," in *52nd AIAA/SAE/ASEE Joint Propulsion Conference, 2016*, 2016.

[91] S. Mazouffre, "Electric propulsion for satellites and spacecraft: established technologies and novel approaches," *Plasma Sources Science and Technology*, vol. 25, no. 3, p. 33 002, 2016.

[92] I. G. Mikellides, A. L. Ortega, I. Katz, and B. A. Jorns, "Hall2De simulations with a first-principles electron transport model based on the electron cyclotron drift instability," in *52nd AIAA/SAE/ASEE Joint Propulsion Conference, 2016*, 2016.

[93] S. F. Adams, J. A. Miles, and V. I. Demidov, "Non-Maxwellian electron energy distribution function in a pulsed plasma modeled with dual effective temperatures," *Physics of Plasmas*, vol. 24, no. 5, p. 053 508, May 2017.

[94] J. J. Blandino and J. W. Dankanich, "Introduction: Recommended Practices for Performance and Diagnostic Measurement in Electric Propulsion," *Journal of Propulsion and Power*, vol. 33, no. 3, pp. 537–538, May 2017.

[95] J. P. Boeuf, "Tutorial: Physics and modeling of Hall thrusters," *Journal of Applied Physics*, vol. 121, no. 1, 2017.

[96] D. L. Brown, M. L. R. Walker, J. Szabo, W. Huang, and J. E. Foster, "Recommended practice for use of Faraday probes in electric propulsion testing," *Journal of Propulsion and Power*, vol. 33, no. 3, pp. 582–613, 2017.

[97] S. E. Cusson, R. R. Hofer, R. B. Lobbia, B. A. Jorns, and A. D. Gallimore, "Performance of the H9 Magnetically Shielded Hall Thrusters," in *35th International Electric Propulsion Conference, Atlanta, GA*, Electric Rocket Propulsion Society, 2017.

[98] J. W. Dankanich, M. Walker, M. W. Swiatek, and J. T. Yim, "Recommended practice for pressure measurement and calculation of effective pumping speed in electric propulsion testing," *Journal of Propulsion and Power*, vol. 33, no. 3, pp. 668–680, 2017.

[99] C. J. Durot, B. A. Jorns, E. T. Dale, and A. D. Gallimore, "Laser-Induced Fluorescence Measurement of the Anomalous Collision Frequency in a 9-kW Magnetically-Shielded Hall Thruster," in *35th International Electric Propulsion Conference*, Atlanta: Electric Rocket Propulsion Society, Oct. 2017.

[100] A. J. Friss and A. P. Yalin, "Status Update: Cavity-Enhanced Thomson Scattering for Electron Measurements in Electric Propulsion Devices," in *35th International Electric Propulsion Conference, Atlanta, GA*, Electric Rocket Propulsion Society, 2017.

[101] M. P. Georgin, M. Byrne, B. A. Jorns, and A. Gallimore, "Passive high-speed imaging of ion acoustic turbulence in a hollow cathode," in *53rd AIAA/SAE/ASEE Joint Propulsion Conference*, 2017, p. 4973.

[102] D. M. Goebel, G. Becatti, S. Reilly, and K. Tilley, "High current lanthanum hexaboride hollow cathode for 20-200 kW Hall thrusters," in *35th International Electric Propulsion Conference, Atlanta, Georgia*, 2017.

[103] J. T. Gudmundsson and A. Hecimovic, "Foundations of DC plasma sources," *Plasma Sources Science and Technology*, vol. 26, no. 12, p. 123 001, Nov. 2017.

[104] R. R. Hofer, S. E. Cusson, R. B. Lobbia, and A. D. Gallimore, "The H9 Magnetically Shielded Hall Thruster," in *35th International Electric Propulsion Conference, Atlanta, GA*, Electric Rocket Propulsion Society, 2017.

[105] N. John and S. George, "Raman spectroscopy," in *Spectroscopic Methods for Nanomaterials Characterization*, Elsevier, 2017, pp. 95–127.

[106] B. A. Jorns, C. Dodson, D. M. Goebel, and R. Wirz, "Propagation of ion acoustic wave energy in the plume of a high-current LaB6 hollow cathode," *Physical Review E*, vol. 96, no. 2, 2017.

[107] R. B. Lobbia and B. E. Beal, "Recommended practice for use of Langmuir probes in electric propulsion testing," *Journal of Propulsion and Power*, vol. 33, no. 3, pp. 566–581, 2017.

[108] F. L. Pedrotti, L. M. Pedrotti, and L. S. Pedrotti, *Introduction to Optics*. Cambridge University Press, 2017, ISBN: 1108597548.

[109] A. Piel, *Plasma Physics: an Introduction to Laboratory, Space, and Fusion Plasmas*. Springer, 2017, ISBN: 3319634275.

[110] K. A. Polzin *et al.*, "Recommended practice for use of inductive magnetic field probes in electric propulsion testing," *Journal of Propulsion and Power*, vol. 33, no. 3, pp. 659–667, 2017.

[111] J. P. Sheehan, Y. Raitses, N. Hershkowitz, and M. McDonald, "Recommended practice for use of emissive probes in electric propulsion testing," *Journal of Propulsion and Power*, vol. 33, no. 3, pp. 614–637, 2017.

[112] M. N. Shneider, "Ponderomotive perturbations of low density low-temperature plasma under laser Thomson scattering diagnostics," *Physics of plasmas*, vol. 24, no. 10, p. 100 701, 2017.

[113] V. H. Chaplin *et al.*, "Laser-induced fluorescence measurements of acceleration zone scaling in the 12.5 kW HERMeS Hall thruster," *Journal of Applied Physics*, vol. 124, no. 18, 2018.

[114] S. E. Cusson *et al.*, "On channel interactions in nested Hall thrusters," *Journal of Applied Physics*, vol. 123, no. 13, p. 133 303, 2018.

[115] I. Katz, V. H. Chaplin, and A. Lopez Ortega, "Particle-in-cell simulations of Hall thruster acceleration and near plume regions," *Physics of Plasmas*, vol. 25, no. 12, 2018.

[116] B. L. M. Klarenaar *et al.*, "A rotational Raman study under non-thermal conditions in a pulsed CO2 glow discharge," *Plasma Science and Technology*, vol. 27, no. 4, p. 45 009, 2018.

[117] B. Vincent, S. Tsikata, S. Mazouffre, T. Minea, and J. Fils, "A compact new incoherent Thomson scattering diagnostic for low-temperature plasma studies," *Plasma sources science & technology*, vol. 27, no. 5, p. 55 002, 2018.

[118] M. J. Baird, T. V. Kerber, K. M. Lemmer, and W. Huang, "Hall Thruster Plume Measurements of Time Resolved Ion Energy," 2019.

[119] M. A. Chilenski, M. Greenwald, Y. Marzouk, J. E. Rice, and A. E. White, "On the importance of model selection when inferring impurity transport coefficient profiles," *Plasma Physics and Controlled Fusion*, vol. 61, no. 12, p. 125 012, Dec. 2019.

[120] S. Clark *et al.*, "BepiColombo—Solar Electric Propulsion System Test and Qualification Approach," in *36th International Electric Propulsion Conference University of Vienna Austria*, 2019.

[121] S. Cusson, "Impact of Neutral Density on The Operation of High-Power Magnetically shielded Hall Thrusters," Ph.D. dissertation, University of Michigan, Ann Arbor, 2019.

[122] E. T. Dale and B. A. Jorns, "Two-zone Hall thruster breathing mode mechanism, Part I: Theory," in *36th International Electric Propulsion Conference University of Vienna Austria*, 2019.

[123] E. T. Dale and B. A. Jorns, "Two-zone Hall thruster breathing mode mechanism, Part II: Experiment," in *36th International Electric Propulsion Conference University of Vienna Austria*, vol. 352, 2019.

[124] A. J. Friss, "Cavity Enhanced Thomson Scattering for Plasma Diagnostics," Ph.D. dissertation, Colorado State University, 2019.

[125] A. J. Friss, T. Wegner, A. P. Yalin, P. Guerrero, J. E. Polk, and L. K. Johnson, "Fiber Coupled Cavity Enhanced Thomson Scattering Diagnostic for Use in Electric Propulsion Facilities," in *36th International Electric Propulsion Conference University of Vienna Austria*, 2019.

[126] L. Garrigues, G. Sary, B. Vincent, S. Tsikata, and S. Mazouffre, "Numerical modeling and incoherent Thomson scattering measurements of a 5A cathode with LaB 6 emitter," in *36th International Electric Propulsion Conference University of Vienna Austria*, 2019.

[127] S. J. Hall *et al.*, "The effect of anode position on operation of a 25-A class hollow cathode," in *36th International Electric Propulsion Conference University of Vienna Austria*, Electric Rocket Propulsion Society, 2019.

[128] Z. He *et al.*, "Pulse-burst laser-based 10 kHz Thomson scattering measurements," *Plasma Science and Technology*, vol. 21, no. 10, p. 105 603, 2019.

[129] R. Hofer *et al.*, "Completing the development of the 12.5 kW Hall effect rocket with magnetic shielding (HERMeS)," in *36th International Electric Propulsion Conference University of Vienna Austria*, 2019.

[130] I. Khmelevskoi, A. Lovtsov, and D. Tomilin, "Study of two different discharge modes in Hall thruster," in *36th International Electric Propulsion Conference University of Vienna Austria*, 2019.

[131] D. Lev, R. M. Myers, K. M. Lemmer, J. Kolbeck, H. Koizumi, and K. Polzin, "The technological and commercial expansion of electric propulsion," *Acta Astronautica*, vol. 159, pp. 213–227, 2019.

[132] C. Y. Liu, "Investigating physics of nanosecond-pulsed argon plasma discharges for a VLF plasma antenna," Ph.D. dissertation, Georgia Institute of Technology, Atlanta, 2019.

[133] A. Lopez Ortega, I. G. Mikellides, M. J. Sekerak, and B. A. Jorns, "Plasma simulations in 2-D (r-z) geometry for the assessment of pole erosion in a magnetically shielded Hall thruster," *Journal of Applied Physics*, vol. 125, no. 3, 2019.

[134] I. G. Mikellides and A. L. Ortega, "Challenges in the development and verification of first-principles models in Hall-effect thruster simulations that are based on anomalous resistivity and generalized Ohm's law," *Plasma Sources Science and Technology*, vol. 28, no. 1, p. 14 003, 2019.

[135] M. R. Nakles and T. S. Matlock, "Hall thruster near-field plume characterization through optical emission spectroscopy," in *36th International Electric Propulsion Conference University of Vienna Austria*, 2019.

[136] D. Y. Oh *et al.*, "Development of the psyche mission for NASA's discovery program," 2019.

[137] P. J. Ryan, J. W. Bradley, and M. D. Bowden, "Comparison of Langmuir probe and laser Thomson scattering for plasma density and electron temperature measurements in HiPIMS plasma," *Physics of Plasmas*, vol. 26, no. 4, Apr. 2019.

[138] S. Tsikata and K. Hara, "Plasma instabilities in cross-field configuration: an analysis of the relevance of different modes for electron transport," in *36th International Electric Propulsion Conference University of Vienna Austria*, 2019.

[139] S. Tsikata, B. Vincent, T. Minea, A. Revel, and C. Ballage, "Time-resolved electron properties of a HiPIMS argon discharge via incoherent Thomson scattering," *Plasma Sources Science and Technology*, vol. 28, no. 3, p. 3, 2019.

[140] B. Vincent, "Incoherent Thomson scattering investigations in Hall thruster, planar magnetron and ECR ion source plasmas," Ph.D. dissertation, ICARE - Institut de Combustion, Aérothermique, Réactivité et Environnement, Orleans, 2019.

[141] B. Vincent, S. Tsikata, S. Mazouffre, and C. Boniface, "Thomson scattering investigations of a low-power Hall thruster in standard and magnetically-shielded configurations," in *36th International Electric Propulsion Conference University of Vienna Austria*, 2019.

[142] N. P. Brown, "Development and Evaluation of Terahertz Time-Domain Spectroscopy for Electric Propulsion Plasma Diagnostics," Ph.D. dissertation, 2020.

[143] V. H. Chaplin *et al.*, "Time-resolved ion velocity measurements in a high-power Hall thruster using laser-induced fluorescence with transfer function averaging," *Applied Physics Letters*, vol. 116, no. 23, p. 234 107, 2020.

[144] X. Duan, D. Guo, M. Cheng, X. Yang, and N. Guo, "Measurements of channel erosion of Hall thrusters by laser-induced fluorescence," *Journal of Applied Physics*, vol. 128, no. 18, 2020.

[145] C. Y. Liu, M. B. Cohen, and M. L. R. Walker, "Time-Resolved Measurements of Plasma Parameters for Nanosecond-Pulsed Argon Plasmas," *IEEE Transactions on Plasma Science*, vol. 48, no. 4, pp. 1060–1075, Apr. 2020.

[146] A. R. Mansour, C. L. Osgood, R. Sahu, and K. Hara, "Development of a one-dimensional full-fluid moment model for hall effect thrusters," in *AIAA Propulsion and Energy 2020 Forum*, 2020.

[147] A. L. Ortega, I. G. Mikellides, V. H. Chaplin, W. Huang, and J. D. Frieman, "Anomalous ion heating and pole erosion in the 12.5-kw hall effect rocket with magnetic shielding (hermes)," in *AIAA Propulsion and Energy 2020 Forum*, 2020.

[148] F. Sciortino *et al.*, "Inference of experimental radial impurity transport on Alcator C-Mod: Bayesian parameter estimation and model selection," *Nuclear Fusion*, vol. 60, no. 12, p. 126 014, Dec. 2020.

[149] P. J. Singletary, M. B. Cohen, M. L. R. Walker, C. Y. Liu, and C. Y. Chan, "Optical Analysis of Nanosecond-Lifetime Plasma Parameters," *IEEE Transactions on Plasma Science*, vol. 48, no. 1, pp. 179–188, Jan. 2020.

[150] L. L. Su, A. R. Vazsonyi, and B. Jorns, "Performance of a 9-kW Magnetically-Shielded Hall Thruster with Krypton," in *AIAA Propulsion and Energy 2020 Forum*, Reston, Virginia: American Institute of Aeronautics and Astronautics, Aug. 2020, ISBN: 978-1-62410-602-6.

[151] A. Thompson, "SpaceX Launches 60 Starlink Satellites, Nails Rocket Landing in Record-Breaking Flight," *Space.com*, vol. 7, Jan. 2020.

[152] B. Vincent, S. Tsikata, and S. Mazouffre, "Incoherent Thomson scattering measurements of electron properties in a conventional and magnetically-shielded Hall thruster," *Plasma sources science & technology*, vol. 29, no. 3, p. 35 015, 2020.

[153] Y. Wu, A. Starikovskiy, B. Leonov, C. Limbach, and R. Miles, "Time-resolved Electron Temperature and Electron Density Measurements in Nanosecond Pulse Discharges in O2-Ar and CO2-Ar Mixtures," in *AIAA Scitech 2020 Forum*, 2020.

[154] N. P. Brown, S. J. Grauer, J. A. Deibel, M. L. R. Walker, and A. M. Steinberg, "Bayesian framework for THz-TDS plasma diagnostics," *Optics Express*, vol. 29, no. 4, pp. 4887–4901, 2021.

[155] L. L. Su and B. A. Jorns, "Performance comparison of a 9-kW magnetically shielded Hall thruster operating on xenon and krypton," *Journal of Applied Physics*, vol. 130, no. 16, 2021.

[156] L. L. Su and B. Jorns, "Performance at High Current Densities of a Magnetically-Shielded Hall Thruster," in *AIAA Propulsion and Energy 2021 Forum*, Reston, Virginia: American Institute of Aeronautics and Astronautics, Aug. 2021, ISBN: 978-1-62410-611-8.

[157] Z. Wang *et al.*, "Simulation of Pole Erosion in Magnetically Shielded and Unshielded Hall Thrusters," *IEEE Transactions on Plasma Science*, vol. 49, no. 4, 2021.

[158] Y. Wu, C. Limbach, and R. B. Miles, "Spatially and temporally resolved electron temperature and number density measurements in 100-kHz nanosecond pulse burst discharges using Laser Thomson scattering," in *AIAA Scitech 2021 Forum*, 2021, p. 1377.

[159] J. Foust, "SpaceX passes 2,000 Starlink satellites launched," *https://spacenews.com*, Jan. 2022.

[160] P. J. Roberts, B. A. Jorns, and V. H. Chaplin, "Experimental Characterization of Wave-Induced Azimuthal Ion Velocities in a Hollow Cathode Plume," in *AIAA Scitech 2022 Forum*, Reston, Virginia: American Institute of Aeronautics and Astronautics, Jan. 2022, ISBN: 978-1-62410-631-6.

[161] S. Tsikata, T. Dubois, and K. Hara, "Coexistence of small-scale instabilities in Hall thrusters and hollow cathodes," in *37th International Electric Propulsion Conference Massachusetts Institute of Technology, Cambridge, MA USA*, Electric Rocket Propulsion Society, 2022.

[162] J. Bak *et al.*, "High resolution spatially extended 1D laser scattering diagnostics using volume Bragg grating notch filters," *Review of Scientific Instruments*, vol. 94, no. 2, p. 023 003, Feb. 2023.

[163] S. J. Grauer, T. A. Sipkens, P. J. Hadwin, and K. J. Daun, "Statistical Inversion, Uncertainty Quantification, and the Optimal Design of Optical Experiments," in *Optical Diagnostics for Reacting and Non-Reacting Flows: Theory and Practice*, Reston, VA: American Institute of Aeronautics and Astronautics, Inc., Jan. 2023, pp. 1137–1202.

[164] NASA, *Psyche Mission to a Metal-Rich World*, 2023.

[165] P. J. Roberts and B. A. Jorns, "Laser Measurement of Anomalous Electron Diffusion in a Crossed-Field Plasma," *Physics of Plasmas*, 2023.

[166] P. J. Roberts and B. Jorns, "Characterization of Electron Mach Number in a Hollow Cathode with Thomson Scattering," in *AIAA Scitech 2023 Forum*, Reston, Virginia: American Institute of Aeronautics and Astronautics, Jan. 2023, pp. 1–1, ISBN: 978-1-62410-699-6.

[167] A. Steinberg and A. K. Patnaik, "Light-Matter Interactions and Their Measurement: A Primer for Optical Diagnostics," in *Optical Diagnostics for Reacting and Non-Reacting Flows: Theory and Practice*, Reston, VA: American Institute of Aeronautics and Astronautics, Inc., Jan. 2023, pp. 15–74.

[168] L. L. Su *et al.*, "Operation and Performance of a Magnetically Shielded Hall Thruster at Ultrahigh Current Densities on Xenon and Krypton," in *AIAA Scitech 2023 Forum*, Reston, Virginia: American Institute of Aeronautics and Astronautics, Jan. 2023, ISBN: 978-1-62410-699-6.

[169] Chhavi C. and M. L. R. Walker, "Review of Non-conventional Hall Effect Thrusters," *Journal of Electric Propulsion*, Feb. 2024.

[170] D. Lee, J. L. Suazo Betancourt, D. Lev, and M. L. R. Walker, "Nitrogen admixture-driven electron cooling and plasma bullet dynamics in atmospheric-pressure dc nanosecond-pulsed argon jet plasmas," *Journal of Applied Physics*, vol. 135, no. 6, Feb. 2024.

[171] J. Lopez-Uricoechea, J. L. Suazo Betancourt, N. Butler-Craig, and M. L. R. Walker, "Spatially resolved laser Thomson scattering measurements in a negative glow and

cathode presheath to investigate a 1D sheath model," *Physics of Plasmas*, vol. 31, no. 3, Mar. 2024.

[172] P. J. Roberts and B. A. Jorns, "Laser measurement of anomalous electron diffusion in a crossed-field plasma," *Physical Review Letters*, Apr. 2024.

[173] P. J. Roberts and B. Jorns, "Inferring Electron Heat Flux in a High-Power Hall Thruster with Incoherent Thomson Scattering," in *AIAA Scitech 2023 Forum*, Reston, Virginia: American Institute of Aeronautics and Astronautics, Jan. 2024, ISBN: 978-1-62410-711-5.

[174] J. L. Suazo Betancourt, S. J. Grauer, J. Bak, A. M. Steinberg, and M. L. R. Walker, "Bayesian plasma model selection for Thomson scattering," *Review of Scientific Instruments*, vol. 95, no. 4, Apr. 2024.

[175] J. L. Suazo Betancourt, J. Lopez-Uricoechea, N. Butler-Craig, A. M. Steinberg, and M. L. R. Walker, "An incoherent Thomson scattering system for measurements near plasma boundaries," *Review of Scientific Instruments*, vol. 95, no. 4, Apr. 2024.

[176] J. L. Suazo Betancourt *et al.*, "Thomson scattering measurements in the krypton plume of a lanthanum hexaboride hollow cathode in a large vacuum test facility," *Journal of Applied Physics*, vol. 135, no. 8, Feb. 2024.